QUANTUM TRANSPORT IN NANOSTRUCTURES

Dissertation
zur Erlangung des Doktorgrades
des Fachbereichs Physik
der Universität Hamburg

vorgelegt von
Dietmar Weinmann
aus Stuttgart

Universität Hamburg

1994

Physikalisch-Technische Bundesanstalt, PTB-Bericht PTB-PG-4
ISBN 3-89429-542-2

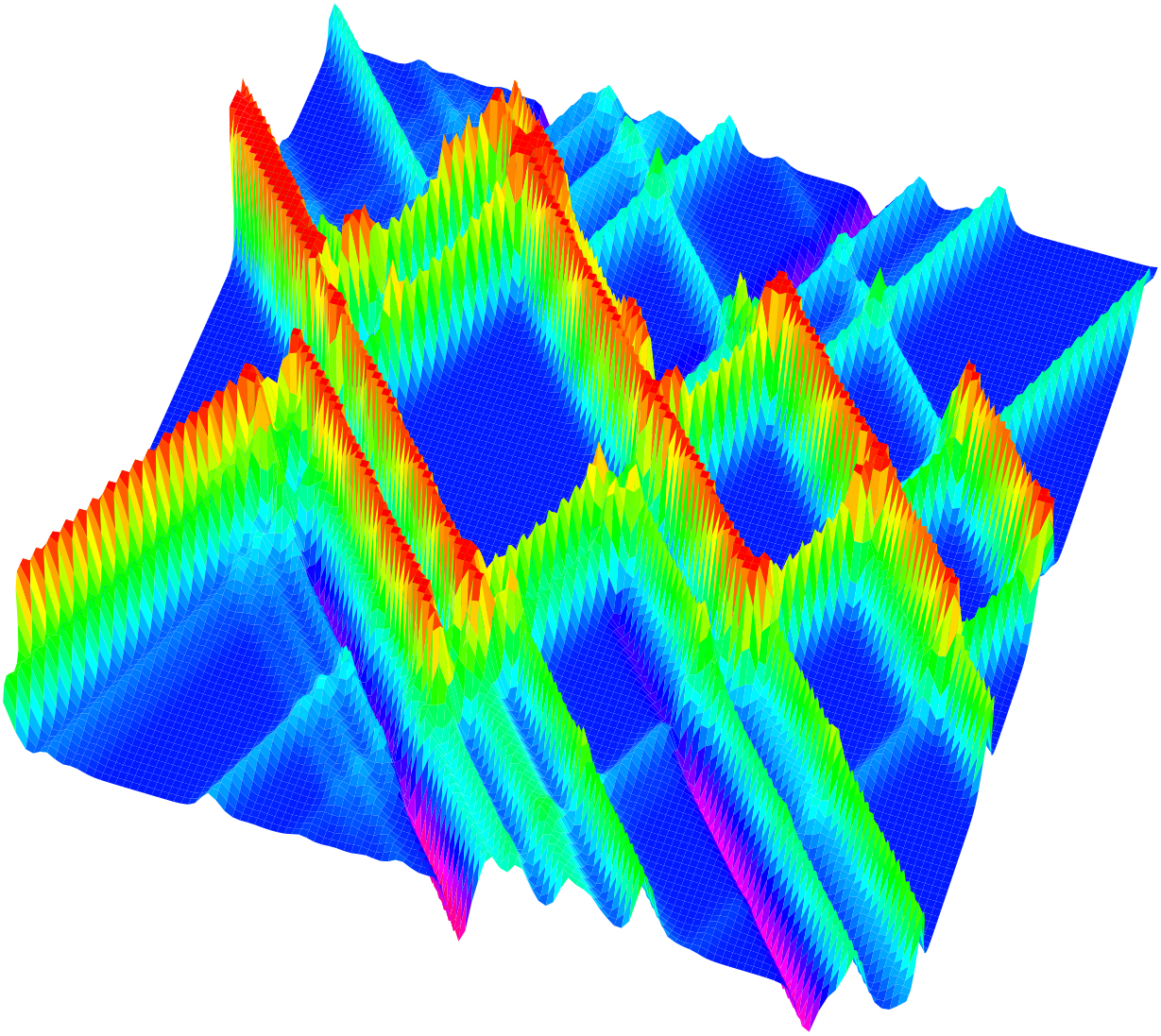

Abstract

This thesis treats some problems in the field of quantum transport in nanostructures.

In the first part, the ac–conductance of a tunnel junction is calculated in linear response. For the junction, a quasi–one dimensional model involving a potential barrier is used. The dependence of the frequency dependent conductance on the barrier parameters is studied. Its low frequency behavior is interpreted in terms of a dynamical capacitance. The influence of phase breaking electron–phonon interactions is investigated. It is argued that the Coulomb interaction between the electrons is of minor importance at higher frequencies. The argument provides a high frequency limit for turnstile operation.

Furthermore, the ac–conductance of a resonant tunneling diode is calculated yielding sharp resonances at frequencies depending on the distance between the barriers. The calculation of the exact scattering eigenfunctions of systems containing barriers with generalized boundary conditions gives contributions to the theory of persistent currents.

In the second part, linear and nonlinear transport through a quantum dot that is weakly coupled to perfect semi–infinite leads is investigated in the parameter regime where charging effects and geometrical quantization effects coexist. A master equation is combined with the exact quantum states of a finite number of strongly correlated electrons within the dot yielding the current in the regime of sequential tunneling. Different models for the dot are used. For an Anderson impurity, an analytic solution can be given. The phenomenological charging model for the dot is compared with a quantum mechanical model for interacting electrons in one and two dimensions. The current–voltage curve shows Coulomb blockade and additional finestructure that is related to the excited states of the correlated electrons. At finite transport–voltage, unequal coupling to the leads causes asymmetric splitting of the conductance peaks.

Negative differential conductances occur due to the existence of excited states with different spins. The spin selection rules lead to a 'spin blockade' decreasing the current when certain states become involved in transport. In two–dimensional square dots the spectrum is qualitatively different leading to new features like suppressions of linear conductance peaks at low temperatures. In a magnetic field, an electron number parity effect due to the different spins of the many–electron ground states is predicted as well as a vanishing of the spin blockade effect. All of the features discussed in the second part are consistent with recent experiments.

Zusammenfassung (Abstract in German)

Diese Arbeit behandelt einige Aspekte des Quantentransports in Nanostrukturen.

Im ersten Teil wird der frequenzabhängige Leitwert eines quasi–eindimensionalen Tunnelkontaktes im Rahmen der linearen Antworttheorie berechnet. Dabei wird ein Potentialmodell für die Tunnelbarriere verwendet und der Einfluß der Modellparameter auf den Leitwert untersucht. Seine Frequenzabhängigkeit wird benutzt, um eine dynamische Kapazität des Kontaktes zu definieren. Auch die Auswirkungen phasenbrechender Elektron–Phonon Wechselwirkungen werden untersucht. Es werden Hinweise dafür gefunden, daß die Coulomb–Wechselwirkung bei hohen Frequenzen von untergeordneter Bedeutung ist. Daraus kann eine Obergrenze für die Betriebsfrequenz des als Stromstandard vorgeschlagenen sogenannten Elektronen–turnstile gefolgert werden.

Desweiteren wird der frequenzabhängige Leitwert eines Doppelbarrierensystems im Bereich des resonanten Tunnelns berechnet. Dabei treten scharfe Maxima bei Frequenzen auf, die vom Abstand der Barrieren abhängen. Schließlich führt die Berechnung der exakten Eigenfunktion von Ringsystemen, die Barrieren enthalten, zu einem Beitrag zur Theorie der Dauerströme.

Im zweiten Teil der Arbeit werden lineare und nichtlineare Transporteigenschaften schwach kontaktierter künstlicher Atome (Quantentöpfe) untersucht. Eine Master–Gleichung erlaubt zusammen mit den exakten quantenmechanischen Zuständen einiger stark korrelierter Elektronen die Berechnung des Stroms bei beliebiger Transportspannung im Rahmen des sequentiellen Tunnelns. Verschiedene Modelle für das künstliche Atom werden verwendet. Für eine Anderson–Störstelle kann eine analytische Lösung angegeben werden. Ein phänomenologisches Ladungsmodell wird mit voll quantenmechanischen Modellen wechselwirkender Elektronen in einer und zwei Dimensionen verglichen. Die Strom–Spannungs Charakteristik zeigt Coulomb Blockade und weist zusätzliche Feinstruktur auf, die auf angeregte Zustände der korrelierten Elektronen zurückgeführt werden kann. Bei endlicher Transportspannung führt eine ungleiche Kopplung an die Zuleitungen zu asymmetrischen Leitwertpeaks.

Aufgrund angeregter Zustände mit verschiedenem Gesamtspin treten Bereiche mit negativem differentiellen Leitwert auf. Die Spinauswahlregeln führen zu einer 'Spin Blockade', die den Strom verringert, wenn bestimmte Zustände zum Strom beitragen. Das Spektrum von zweidimensionalen quadratischen künstlichen Atomen ist qualitativ verschieden von dem eindimensionaler Modelle und führt zu weiteren neuartigen Effekten wie etwa der Unterdrückung linearer Leitwertmaxima. Für quasi–eindimensionale Systeme in einem Magnetfeld wird aufgrund der verschiedenen Gesamtspins der Vielelektronenzustände ein Elektronenzahlparitätseffekt vorausgesagt. Außerdem wird die Spin Blockade durch das Anlegen eines Magnetfeldes unterdrückt. Alle im zweiten Teil diskutierten Eigenschaften stehen im Einklang mit neuesten Experimenten.

Contents

Preface

Due to immense progress in nanostructure fabrication technology, the physics of mesoscopic systems has attracted a lot of interest in the last ten years. Systems, in which typical geometrical length scales are small as compared to the phase coherence length L_φ, show a great variety of new quantum phenomena [1, 2].

Examples are the weak localization in disordered films [3, 4], the quantization of the conductance through quantum point contacts [5, 6], and Aharonov–Bohm oscillations of the magnetoresistance in tiny metallic cylinders [7] and in gold rings [8]. The role of phase coherence effects is strikingly demonstrated in experiments where a ring being externally connected to one of the leads introduces similar oscillations in the magnetoresistance of a small wire [9]. Recently, even persistent currents in single rings have been observed in metallic [10] and in semiconductor based [11] rings.

In view of possible applications of the novel effects, some new devices have been proposed that could appear in high technology products in the future. Among the most prospective ones are the single electron transistors [12, 13] which can be used as highly sensitive electrometers. They could represent the basis of the next generation of computers providing the ultimate step in the miniaturization of information technology hardware. In single electron tunneling devices, a controlled transfer of electrons can be achieved [14] by applying ac–voltages [15, 16, 17, 18]. This could open the way to a new current standard which is based on counting electrons that pass the sample per unit of time [19, 20, 21].

Thus, transport properties of mesoscopic systems are highly interesting in view of possible future applications. The main problems to overcome are the very low temperatures needed to operate such devices as well as the still quite high production costs. However, charging effects have recently been observed in ultrasmall systems at room temperature [22].

Additionally, the behavior of mesoscopic systems lies between the properties of the classical macroscopic world of every day life, and the microscopic world of atoms and molecules governed by the laws of quantum mechanics. Investigating mesoscopic systems is therefore fundamentally interesting. It allows to study the transition from quantum to classical behavior. Further, the typically low number of particles in small systems allows to treat few–particle systems experimentally as well as theoretically and therefore to enlarge the general understanding of many–particle problems [23]. It is possible to create artificial atoms [13] by confining electrons in potential wells, the so–called quantum dots and to tune the parameters by applying external gate–voltages. Using nonlinear transport experiments, the spectrum of quantum dots being weakly coupled to reservoirs can be investigated [24, 25]. Very recently, even coupled dots have been realized [26] representing artificial molecules.

In this thesis, we address questions that are of relevance for applications as well as for fundamental research. In the first part, we investigate the frequency dependent conductance of a single barrier and compare it to the behavior of a classical circuit. Working in the limit of low transport voltage, we use the general linear response formalism to calculate the conductance at arbitrary frequency. This is related to the turnstile effect where, using ac driving fields, electrons are transferred through the device one by one [21, 27].

In the second part, the influence of excited levels inside a quantum dot being weakly connected to semi–infinite leads on the transport properties is studied. A rate equation method allows to calculate the dc–current at arbitrary transport voltage. We trace back the transport properties to the spectra of correlated electrons in low dimensional systems and find striking results. They are consistent with recent experiments [24, 28, 29, 30, 31, 32, 33, 34, 36].

Publications

Some of the main results contained in this thesis have been published in the following articles:

- T. Brandes, D. Weinmann and B. Kramer, *Europhys. Lett.* **22**, 51, (1993).
- T. Brandes, W. Häusler, K. Jauregui, B. Kramer, D. Weinmann, *Physica* **B 189**, 16 (1993).
- D. Weinmann, W. Häusler, W. Pfaff, B. Kramer, U. Weiss, *Europhys. Lett.* **26**, 467 (1994).
- W. Häusler, K. Jauregui, D. Weinmann, T. Brandes, B. Kramer, *Physica* **B 194-196**, 1325 (1994).
- W. Pfaff, D. Weinmann, W. Häusler, B. Kramer, U. Weiss, to appear in *Z. Phys.* **B**, (1994).
- D. Weinmann, W. Häusler, B. Kramer, to be submitted (1994).
- B. Kramer, T. Brandes, W. Häusler, K. Jauregui, W. Pfaff, D. Weinmann, to be published in the proceedings of the winterschool in Mauterndorf (1994).
- D. Weinmann, *Physik in unserer Zeit* **25/4**, 158, (1994).

Acknowledgements

The work leading to this thesis has been carried out in an extremely favorable environment and benefited from the support of many people. It is a pleasure to acknowledge all those, without whom the work would have been less fun and consequently this thesis would have been much worse than it is.

I am very grateful to my supervisors Bernhard Kramer and Uli Weiß for their continuous support. They both provided very important and positive parts of my education and I enjoyed the pleasant atmosphere working with them and in their groups at the PTB

Braunschweig/Uni Hamburg and Uni Stuttgart, respectively. I am particularly indebted to Bernhard Kramer for numberless discussions and many contributions to this thesis. Thanks also for sending me to numerous workshops and conferences and therewith teaching me to give talks and allowing me to meet many of the researchers in the very active field.

The first part of this thesis arose from a very fruitful collaboration with Tobias Brandes. I thank him for many discussions and the good atmosphere. The results presented in Chapter 5 are due to him.

A special thanks goes to Walter Pfaff with whom many aspects of transport through quantum dots within the charging model (Chapter 11) have been developed in an intensive collaboration before he moved to Frankfurt in order to explore the stock exchange.

I want to thank Wolfgang Häusler for a very extensive collaboration over almost two years leading to the second part of this thesis. This contained a huge number of discussions, especially a late–night one about reference [29] which triggered the work on nonlinear transport through quantum dots.

I am indebted to Kristian Jauregui who worked out the properties of interacting electrons in one dimension together with Wolfgang Häusler and provided me with important data for the spectra of quantum dots.

Walter Apel, Avi Cohen, Dirk Endesfelder, Martin Hennecke, Marcus Kasner, Peter Markos, Wolfgang Pogrzeba, Ludwig Schweitzer and Wolfgang Wöger have contributed to a good atmosphere in the group of theoretical physics of the PTB in Braunschweig, where I worked from october 1991 to september 1993. Discussions with all of them are appreciated.

At the Universität Hamburg, I benefited from the presence of Markus Batsch and Isa Zharekeshev who were always willing to discuss.

I am very grateful to my roommates Tobias Brandes and Kristian Jauregui for an extremely friendly and pleasant atmosphere in which we passed a lot of time together. A great memory remains the great three day trekking tour through the Dovrefjell national park (Norway) in the summer of 1992.

I'm indebted to R. Haug, J. Weis for discussions about experimental results on transport through quantum dots prior to publication. Further, I acknowledge discussions with many researchers in the field, in particular D. Braun, C. Bruder, M. Büttiker, K. Frahm, H. Grabert, P. Hänggi, T. Heinzel, F. Hekking, H. Heyszenau, G.–L. Ingold, A. Odintsov, J. Palacios, J.–L. Pichard, G. Platero, D. Pfannkuche, H. Schoeller, G. Schön, K. Slevin, C. Tejedor, S. Ulloa and D. Wharam.

Anja Mohr at the II. Institut für Theoretische Physik of the Universität Stuttgart, where I was employed throughout this thesis deserves my gratitude for dealing with the administrative things. I thank the head of the institute Wolfgang Weidlich for accepting me as a member of the institute and all the other members for the nice atmosphere during my rare stays in Stuttgart.

I have to thank the Physikalisch–Technische Bundesanstalt in Braunschweig, where a part of this work was performed, and the I. Institut für Theoretische Physik of the Universität Hamburg, where this thesis was completed, for kind hospitality.

The numerical calculations have been performed on IBM RISC and DEC ALPHA workstations at the university of Hamburg and on another IBM RISC and on the CYBER

2000 supercomputer at the PTB in Braunschweig. Wolfgang Pogrzeba, Axel Puskeppel and Jürgen Stockburger have provided expert help with Computer problems.

Financial support of the Deutsche Forschungsgemeinschaft via grant We 1124/4–1 is gratefully acknowledged. The support of the Helmholtz–Fond that allowed me to participate in a conference in Trondheim is appreciated as well as a travel grant of the EC for a stay at the ICTP in Trieste and support from the EC within the Science program, grant SCC*–CT90–0020 and within the HCM program, grant CHRX–CT93–0136 for a stay at the CEA, Saclay and several conferences.

Last in this list, but most important, it is a pleasure to thank my best friend Anke Wichmann and my parents Paul and Klara Weinmann for their continuous optimism and patient support.

Part I

FREQUENCY-DEPENDENT CONDUCTANCE

Introduction

The capacitance of mesoscopic systems is an important quantity in the context of tiny tunnel junctions and small grains. If their capacitance C is very small (of the order of 10^{-15} F, the energy needed to charge them with one single electron, the charging energy E_{C} can exceed the energy of thermal fluctuations $k_{\mathrm{B}}T$ at subkelvin temperatures.

Thus, consequences of the discreteness of the electronic charge can be observed experimentally. Among the most striking ones is the Coulomb blockade [37, 38, 39, 40] which suppresses tunneling through small junctions of low capacitance when the applied voltage is not high enough to provide the charging energy. The current–voltage characteristic shows a voltage offset $V_{\mathrm{C}} = e/2C$ which can be used to determine the capacitance of the junction.

However, in single junctions it is extremely difficult to detect these effects. If there is not an impedance high enough to avoid fast discharging of the junction on a timescale $\tau = h/E_{\mathrm{C}}$, the Coulomb blockade effect will be unobservable [41]. For the same reason, the tunneling resistance of the junction R_{T} has to be large. Since the time needed to discharge a capacitor connected to a resistor is given by $\tau_{\mathrm{d}} = RC$, this yields the condition $R \gg h/e^2$ for both, the tunneling resistance and the impedance of the environment. Experimentally, the second requirement is very difficult to fulfill and the Coulomb blockade in single junction systems could be observed only recently in normal metal [42] and in superconducting systems [43].

On the other hand, the confinement of electrons to a box between two tunnel junctions with high enough resistance allows for the investigation of the Coulomb blockade without a dissipative environment (the effect is still influenced by the surrounding fluctuations [44]). The first observation was reported in the context of tunneling through small tin particles [45]. In the meantime, controlled fabrication of small enough islands is possible and allows for systematic investigations of the effect [12, 19]. In tunneling through ultrasmall particles, using the tip of a scanning tunneling microscope to form one of the barriers, the Coulomb blockade has been observed even at room temperature [22].

In a large part of the literature, the capacitance of a tunnel junction is treated as a phenomenological parameter. Only few authors tackle the problem to justify the concept of a capacitance starting from a microscopic quantum mechanical model [46]. Corrections to the classical value have been found [47, 48] within a path integral formulation of tunneling between superconductors.

We investigate the question of the justification of the capacitance in very small quantum systems by considering their dynamical properties. Using the frequency dependent conductance one can define a capacitance of a tunnel junction modeled by a potential barrier without referring to the Coulomb energy. We will demonstrate that in certain

regions of Fermi energy E_{F} and barrier parameters one can simulate the behavior of the quantum system by a circuit involving resistors and a capacitor. The 'dynamical' capacitance defined in this way is a genuine quantum feature. This is demonstrated by studying the dependence of the ac–conductance on inelastic processes using a simplified model involving electron–phonon coupling. The capacitive behavior is suppressed as temperature is increased when inelastic scattering is present. A similar effect has been found recently [49, 50, 51] using a semiclassical approach yielding the current–voltage characteristic at zero frequency.

Transport properties of mesoscopic systems are particularly interesting in the context of double barrier structure where Fabry–Perot like resonances are expected and observed experimentally [52] if the phase of the electrons is conserved. We will show that this leads to interesting phenomena in frequency dependent transport.

Chapter 1

Linear response theory

In the following we use quantum mechanical linear response theory. It provides a general formalism for the calculation of the frequency dependent conductance that allows, at least in principle, to treat inelastic processes and interactions in mesoscopic systems in a systematic manner [53, 54].

The linear response theory for the electrical conductivity is presented in numerous textbooks, e. g. in [55, 56]. However, in mesoscopic systems the electric field is varying over the spatial extension of the sample and geometrical confinement effects dominating the behavior destroy the translational invariance of the problem. This requires a nonstandard form of the Kubo formula [57]. For tutorial reasons, we derive the conductance formula needed for calculating the frequency dependent conductance of mesoscopic systems in linear response to an electric field applied to a finite part of the sample following the references [58, 59] and [60].

1.1 General formalism

We start from the total Hamiltonian

$$H_{\mathrm{tot}} = H + H' \,, \tag{1.1}$$

where

$$H = \sum_i \left(\frac{1}{2m^*} \vec{p}_i^{\,2} + V(\vec{x}_i) \right) \tag{1.2}$$

fully describes the system considered with the potential $V(\vec{x})$. H' takes into account the interaction with the electric field that will be assumed to be infinitesimally weak and shall be treated in lowest order. The sum runs over all the electrons in the system. e and m^* are the charge and the effective mass of the electrons, respectively. Expressing the electric field

$$\vec{E}(\vec{x},t) = -\frac{\partial \vec{A}(\vec{x},t)}{\partial t} \tag{1.3}$$

via the vector potential, we use the Coulomb gauge $\nabla \vec{A} = 0$ and set the electrostatic potential $\Phi = 0$. The current density operator can be written in the form

$$\vec{j}(\vec{x}) = \frac{e}{2m^*} \sum_i \left[\vec{p}_i, \delta(\vec{x} - \vec{x}_i) \right]_+ \,, \tag{1.4}$$

where $[\ldots,\ldots]_+$ denotes the antikommutator. We have to mention that we have omitted a diamagnetic term which is of no importance for the dissipative conductance we're going to calculate. This form of the current density operator leads to the usual result for the matrix elements in space representation

$$\vec{j}_{ij}(\vec{x}) := \langle i \mid \vec{j}(\vec{x}) \mid j \rangle = \frac{e\hbar}{2im^*} \left(\psi_j(\vec{x})\nabla\psi_i^*(\vec{x}) - \psi_i^*(\vec{x})\nabla\psi_j(\vec{x})\right) \tag{1.5}$$

with the eigenfunctions of the unperturbed Hamiltonian ψ_i. The lowest order term in the vector potential entering the perturbing Hamiltonian is

$$H' = -\frac{e}{m}\sum_i \left(\vec{p}_i\vec{A} + \vec{A}\vec{p}_i\right) \tag{1.6}$$

and can be expressed as

$$H' = -\int d^3x \vec{A}(\vec{x},t)\vec{j}(\vec{x})\,. \tag{1.7}$$

To calculate the thermal expectation value of the current, we use the density operator ρ, whose time evolution is governed by the Liouville–von Neumann equation

$$i\hbar\frac{\partial\rho}{\partial t} = [H_{\mathrm{tot}},\rho]\,. \tag{1.8}$$

We assume adiabatic switching on of the perturbation by a monochromatic field

$$\vec{A}(\vec{x},t) = \frac{i}{\omega+i\eta}\vec{E}(\vec{x})e^{i\omega t}\,. \tag{1.9}$$

The (infinitesimal) imaginary part of the frequency $i\eta$ guarantees the vanishing of the electric field at $t\to-\infty$. Therefore, the appropriate initial condition at $t=-\infty$ for the solution of (1.8) is thermal equilibrium described by

$$\rho_0 = \sum_i f(E_i) \mid i\rangle\langle i \mid \tag{1.10}$$

with the eigenstates $\mid i\rangle$ and the corresponding eigenenergies E_i of the unperturbed Hamiltonian H, where

$$f(E) = \frac{1}{\exp[\beta(E-E_{\mathrm{F}})]+1} \tag{1.11}$$

is the Fermi–Dirac distribution function with the inverse temperature $\beta = 1/(k_{\mathrm{B}}T)$ and the Fermi energy E_{F}. Writing $\rho(t) = \rho_0 + \rho'(t)$, and keeping only terms linear in the perturbation, the Fourier transform of (1.8) gives

$$\hbar\omega\rho'(\omega) = [H,\rho'(\omega)] + [H'(\omega),\rho_0]\,. \tag{1.12}$$

Solving for $\rho'(\omega)$ in the basis of the unperturbed eigenstates, one finds the matrix elements

$$\rho'_{ij}(\omega) = \frac{f(E_j)-f(E_i)}{E_j-E_i+\hbar(\omega+i\eta)}H'_{ij}(\omega)\,. \tag{1.13}$$

The thermal expectation value for the current density is the trace over the current density operator weighted with the density operator

$$\langle \vec{j}(\vec{x},t)\rangle = \mathrm{Tr}\left(\rho_0 j(\vec{x},t)\right) + \mathrm{Tr}\left(\rho'(t) j(\vec{x},t)\right) . \tag{1.14}$$

The first (equilibrium) term can be shown to vanish and the evaluation of the second one using (1.13) with (1.7) and (1.9) gives the result

$$\langle \vec{j}(\vec{x},\omega)\rangle = \int d^3x' \tilde{\sigma}(\vec{x},\vec{x}',\omega)\vec{E}(\vec{x}',\omega) \tag{1.15}$$

with the nonlocal and frequency dependent conductivity tensor

$$\tilde{\sigma}(\vec{x},\vec{x}',\omega) = (-i)\sum_{i,j} \frac{f(E_j)-f(E_i)}{\omega+i\eta} \frac{\vec{j}_{ij}(\vec{x})\vec{j}_{ji}(\vec{x}')}{E_j - E_i + \hbar(\omega+i\eta)} . \tag{1.16}$$

This result containing two current density matrix elements representing a current–current correlation function can be interpreted in terms of electron–hole excitations created at x', propagating through the system and recombining at x. The full conductivity tensor can in principle be used to discuss inductance effects. However, the evaluation of the imaginary part of the current is highly nontrivial because of principal part integrals arising from the energy denominator in the continuum limit. Only in very simple cases some results have been obtained [61]. The dissipative conductivity can be defined using the density of absorbed power averaged over one period

$$p(\vec{x},\omega) = \frac{\omega}{2\pi} \int_{t_0}^{t_0+2\pi/\omega} dt\, \vec{E}(\vec{x},t)\langle \vec{j}(\vec{x},t)\rangle . \tag{1.17}$$

Solely the real part of the conductivity contributes to the absorbed power. Thus, the dissipative conductivity is

$$\sigma(\vec{x},\vec{x}',\omega) = \mathrm{Re}[\tilde{\sigma}(\vec{x},\vec{x}',\omega)] . \tag{1.18}$$

For any finite frequency, the real part of (1.16) is given by

$$\sigma(\vec{x},\vec{x}',\omega) = -\pi \sum_{i,j} \frac{f(E_j)-f(E_i)}{\omega} \vec{j}_{ij}(\vec{x})\vec{j}_{ji}(\vec{x}')\delta(E_j - E_i + \hbar\omega) \tag{1.19}$$

in the limit $\eta \longrightarrow 0$. This quite general formula will be applied below for a quasi–one dimensional situation.

1.2 Definition of the conductance

To determine the conductance, the spatial shape of the applied electric field has to be fixed. Then, the frequency dependent current can be calculated and related to the voltage drop.

We now consider a quasi–one dimensional wire and the electric field is always taken in the longitudinal direction described by the coordinate x ($\vec{x} = (x, x_\perp)$). For simplicity, the electric field

$$E(x,t) = E_0\,\Theta(l/2 - |\,x\,|)\,,\cos(\omega t) \tag{1.20}$$

where

$$\Theta(x) = \begin{cases} 1 & \text{for} \quad x > 0 \\ 0 & \text{for} \quad x < 0 \end{cases} \tag{1.21}$$

is the usual step function, is assumed to be constant on a finite interval l of an infinitely long wire and zero outside. The conductance is defined via the absorbed power [58, 63, 64, 65]

$$\Gamma(\omega) = \frac{2P(\omega)}{U^2}\,. \tag{1.22}$$

The energy absorption rate

$$P(\omega) = \frac{\omega}{2\pi} \int\limits_{t_0}^{t_0+2\pi/\omega} dt \int dx\, E(x,t)\langle j(x,t)\rangle \tag{1.23}$$

is an average over one period $T = 2\pi/\omega$ of the driving field and the voltage is $U = E_0 l$. Inserting the general linear response relation (1.15), we find our definition to be equivalent to the spatial average of the real (absorptive) part of the conductivity

$$\Gamma(\omega) = \frac{1}{l^2}\int_{-l/2}^{l/2} dx dx' \mathrm{Re}\,\tilde{\sigma}(x,x';\omega) \quad . \tag{1.24}$$

The only space dependence in the real part of the conductivity is contained in the matrix elements of the current density. Thus, we define the current matrix elements

$$J_{ij} := \int\limits_{-l/2}^{l/2} dx\, j_{ij}(x) = \frac{e\hbar}{2im^*} \int\limits_{-l/2}^{l/2} dx \left(\frac{\partial \psi_i^*}{\partial x}\psi_j - \psi_i^* \frac{\partial \psi_j}{\partial x}\right) . \tag{1.25}$$

With (1.19), the average (1.24) gives

$$\begin{aligned} \Gamma(\omega) &= \frac{h}{2l^2} \int\limits_0^\infty dE\, \frac{f(E) - f(E+\hbar\omega)}{\hbar\omega} \\ &\times \sum_{i,j} |J_{ij}|^2\, \delta(E - E_i)\delta(E + \hbar\omega - E_j)\,, \end{aligned} \tag{1.26}$$

where the energy integral has been introduced together with a δ–function for convenience.

Chapter 2

The single barrier model

We consider a quasi–one dimensional system confined by a parabolic potential in transversal direction, without Coulomb interaction. A rectangular potential barrier of length b and height V in the longitudinal direction serves as a model for a tunnel junction (Figure 2.1). This description is more suitable for a discussion of the dependence on barrier parameters than the extensively used tunneling Hamiltonian which was introduced in the context of superconducting tunneling [66]. It allows to investigate also the regime of high transmission where the tunneling Hamiltonian breaks down [67]. We shall solve the Schrödinger equation

$$\left(-\frac{\hbar^2}{2m^*}\,\nabla^2 + V(x,x_\perp)\right)\Psi(x,x_\perp) = E\,\Psi(x,x_\perp) \tag{2.1}$$

with the potential

$$V(x,x_\perp) = V\Theta(b/2-|x|) + \frac{1}{2}m^*\omega_\perp^2 x_\perp^2\,, \tag{2.2}$$

where $\vec{x} = (x, x_\perp)$. Since the potential term in the Hamiltonian is a sum of the longitudinal and the transversal potential terms, the Schrödinger equation can be separated.

We assume the wire to be narrow enough ($\hbar\omega_\perp > m^*/2v_{\rm F}^2$) to allow for the restriction to the lowest band with transversal wave function

$$\chi(x_\perp) \propto \exp -(x_\perp/2\lambda)^2\,, \tag{2.3}$$

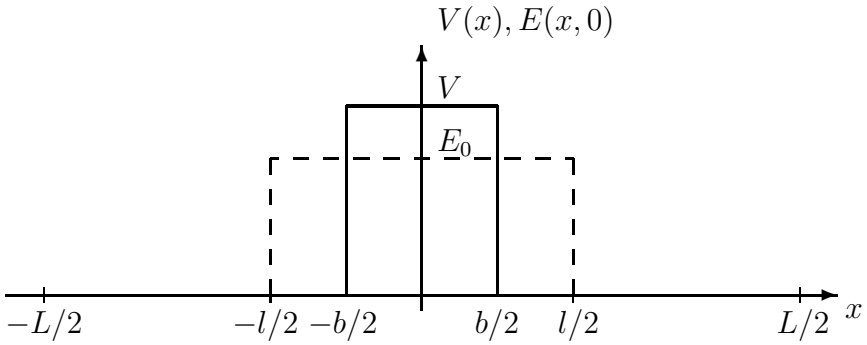

Figure 2.1: Model potential and space dependence of electric field (dashed).

where $\lambda = \sqrt{\hbar/(2m\omega)}$ is the effective transversal width. $\chi(x_\perp)$ is the usual and well known ground state wave function of the harmonic oscillator problem in transversal direction. The total wave function is given by

$$\Psi(x, x_\perp) = \psi(x)\,\chi(x_\perp)\,. \tag{2.4}$$

2.1 Longitudinal eigenfunctions

For a system of total length L we calculate the exact longitudinal eigenfunctions $\psi(x)$ using periodic boundary conditions at $x = \pm L/2$ and evaluate the conductance in the limit $L \longrightarrow \infty$. It is worth mentioning that the boundary conditions do not affect any of the results of our calculations because we will always take the thermodynamic limit $L \longrightarrow \infty$ first. In fact, a calculation using hard walls at $x = \pm L/2$ yields identical results for the conductance in linear response.

For periodic boundary conditions, the longitudinal part of the Schrödinger equation is solved by the set of symmetric and antisymmetric eigenfunctions

$$\psi_k^{\rm s}(x) = \begin{cases} A\sin(-kx + \phi_k^{\rm s}) & \text{for } x < -b/2 \\ B_k^{\rm s}\cosh(\kappa x) & \text{for } |x| < b/2 \\ A\sin(kx + \phi_k^{\rm s}) & \text{for } x > b/2 \end{cases} \tag{2.5}$$

and

$$\psi_k^{\rm a}(x) = \begin{cases} -A\sin(-kx + \phi_k^{\rm a}) & \text{for } x < -b/2 \\ B_k^{\rm a}\sinh(\kappa x) & \text{for } |x| < b/2 \\ A\sin(kx + \phi_k^{\rm a}) & \text{for } x > b/2 \end{cases}\,, \tag{2.6}$$

respectively, with the abbreviations

$$\begin{aligned} k &= \sqrt{2m^*E}/\hbar \\ \text{and}\quad \kappa &= \sqrt{2m^*(V-E)}/\hbar\,. \end{aligned}$$

Imposing periodic boundary conditions

$$\begin{aligned} \psi_k(L/2) &= \psi_k(-L/2) \\ \lim_{x\to L/2-0}\frac{\partial\psi_k(x)}{\partial x} &= \lim_{x\to -L/2+0}\frac{\partial\psi_k(x)}{\partial x} \end{aligned} \tag{2.7}$$

on the symmetric/antisymmetric wave functions yields the conditions

$$\begin{aligned} \cos\left(\frac{kL}{2} + \phi_k^{\rm s}\right) &= 0 \\ \sin\left(\frac{kL}{2} + \phi_k^{\rm a}\right) &= 0\,, \end{aligned} \tag{2.8}$$

being satisfied by wave vectors k solving $kL/2 + \phi_k^{\rm s} = \pi(n + 1/2)$ and $kL/2 + \phi_k^{\rm a} = \pi n$, respectively, with $n = 1, 2, \ldots, \infty$. The phases $\phi_k^{\rm s/a}$ modify the density of states due to the presence of the barrier.

However, in the continuum limit $L \longrightarrow \infty$ their importance vanishes $\sim 1/L$ at a given k and one finds for both, symmetric and antisymmetric states the same density of states

$$\rho(k) = \frac{L}{2\pi\hbar v(k)}\,. \tag{2.9}$$

Here, $v(k) = \hbar k/m^*$ is the classical velocity corresponding to the wave number k.

In the limits $kL \longrightarrow \infty$ and $L/b \longrightarrow \infty$, the normalization condition leads to

$$A = \sqrt{2/L} \tag{2.10}$$

while the matching conditions at $x = \pm b/2$ yield

$$B_k^{\mathrm{s/a}} = \gamma_k^{\mathrm{s/a}} A \tag{2.11}$$

with

$$\gamma_k^{\mathrm{s}} = \frac{\sin(kb/2 + \phi_k^{\mathrm{s}})}{\cosh \kappa b/2} \tag{2.12}$$

and

$$\gamma_k^{\mathrm{a}} = \frac{\sin(kb/2 + \phi_k^{\mathrm{a}})}{\sinh \kappa b/2}\,. \tag{2.13}$$

The phases $\phi_k^{\mathrm{s/a}}$ are the solutions of the equations

$$\tan(kb/2 + \phi_k^{\mathrm{s}}) = \frac{k}{\kappa} \coth \kappa b/2 \tag{2.14}$$

and

$$\tan(kb/2 + \phi_k^{\mathrm{a}}) = \frac{k}{\kappa} \tanh \kappa b/2\,. \tag{2.15}$$

2.2 Conductance

As shown in Chapter 1, linear response theory yields the general formula (1.26)

$$\begin{aligned} \Gamma(\omega) &= \frac{h}{2l^2} \int_0^\infty dE\, \frac{f(E) - f(E + \hbar\omega)}{\hbar\omega} \\ &\times \sum_{i,j} |J_{ij}|^2\, \delta(E - E_i)\delta(E + \hbar\omega - E_j) \end{aligned} \tag{2.16}$$

with the current matrix elements

$$J_{ij} = \frac{e\hbar}{2im^*} \int_{-l/2}^{l/2} dx \left(\frac{\partial \psi_i^*}{\partial x}\psi_j - \psi_i^* \frac{\partial \psi_j}{\partial x} \right)\,. \tag{2.17}$$

In the continuum limit we can replace the sums over the eigenstates by integrals with the density of states from (2.9) according to the rule

$$\sum_i \longrightarrow \int dE_i \rho(E_i)\,. \tag{2.18}$$

Then, one can perform the integrations due to the delta functions in (2.16). Inserting the exact expressions (2.5) and (2.6) for the wave functions into the conductance formula (2.16), the calculation of the current matrix elements (2.17) is lengthy but straightforward. The resulting expression for the conductance of our system is given by

$$\begin{aligned}\Gamma(\omega) &= \frac{h}{2l^2}\int_0^\infty dE\,\frac{f(E)-f(E+\hbar\omega)}{\hbar\omega} \\ &\times \left(\frac{m^*L}{2\pi\hbar^2}\right)^2 \frac{1}{k\,k_\omega}\left(\left|J^{\rm sa}_{kk_\omega}\right|^2+\left|J^{\rm sa}_{k_\omega k}\right|^2\right)\end{aligned} \tag{2.19}$$

with

$$k_\omega = \sqrt{2m^*(E+\hbar\omega)}/\hbar\,. \tag{2.20}$$

$J^{\rm sa}_{k_1k_2}$ are the current matrix elements between symmetrical states characterized by the wave number k_1 and antisymmetric states that correspond to k_2. For symmetry reasons, the current matrix elements between two symmetric states must vanish as those between antisymmetric states. This is due to integrating over a symmetrical interval in (2.17), where all of the terms in the integrand become antisymmetric functions. For the case $l \geq b$, when the barrier is shorter than the region of nonzero electric field, we find from (2.17) with (2.5) and (2.6) using standard integrals [68]

$$J^{\rm sa}_{k_1k_2} = \frac{e\hbar}{im^*L}\left(\xi_{k_1k_2}(l)-\xi_{k_1k_2}(b)+\gamma^{\rm s}_{k_1}\gamma^{\rm a}_{k_2}\zeta_{k_1k_2}(b)\right)\,, \tag{2.21}$$

while the result for $l < b$ is

$$J^{\rm sa}_{k_1k_2} = \frac{e\hbar}{im^*L}\,\gamma^{\rm s}_{k_1}\gamma^{\rm a}_{k_2}\zeta_{k_1k_2}(l)\,. \tag{2.22}$$

Here, we have introduced the functions

$$\begin{aligned}\xi_{k_1k_2}(x) &= \cos\left[k^-x/2+\phi^-\right]k^+/k^- - \cos\left[k^+x/2+\phi^+\right]k^-/k^+ \\ \zeta_{k_1k_2}(x) &= \sinh\left[\kappa^+x/2\right]\kappa^-/\kappa^+ - \sinh\left[\kappa^-x/2\right]\kappa^+/\kappa^-\end{aligned} \tag{2.23}$$

with

$$\begin{aligned}\kappa_{1,2} &= [2mV/\hbar^2-k^2_{1,2}]^{1/2} \\ k^\pm &= k_1 \pm k_2 \\ \kappa^\pm &= \kappa_1 \pm \kappa_2 \\ \phi^\pm &= \phi^{\rm s}_{k_1} \pm \phi^{\rm a}_{k_2}\,.\end{aligned} \tag{2.24}$$

They arise from spatial regions inside the electric field without and with the presence of the barrier, respectively, contributing to the conductance.

Chapter 3

Results

3.1 Numerical evaluation of the conductance

The evaluation of the formally exact expression (2.19) can be done using a computer in the general case. We did the energy integration numerically using Mathematica^{TM} routines on IBM RISC workstations.

The conductance $\Gamma(\omega)$ at zero temperature is plotted in Figure 3.1 for various values of the Fermi energy $E_{\rm F}$. For the lowest curves, $E_{\rm F} < V$ and the dc–current is strongly suppressed by the tunneling barrier. Finite (not too high) frequencies increase the conductance. Around $E_{\rm F} \approx V$ the behavior changes qualitatively. At $E_{\rm F} > V$, the dc–conductance is of the order of the quantum conductance e^2/h and increasing frequencies tend to decrease the absorptive conductance as in ideal quantum wires.

Similar results have been obtained for a two dimensional tight binding model with a constriction acting like a tunnel barrier [62]. At low energy, a maximum in the conductance appears at a frequency where roughly $\hbar\omega = 2(V - E_{\rm F})$. This can be understood from the description of transport in terms of electron hole pairs being implicitly included in the Kubo formula. A high conductance can be achieved when at least the electron can propagate above the barrier.

3.2 Limiting cases

In spite of the complicated general result, analytic expressions can be found for some limiting cases. It is instructive to consider the following situations.

3.2.1 Free quantum wire

The general result (2.19) contains the conductance of a free quantum wire. Setting $b = 0$ or $V = 0$ yields the simple current matrix elements

$$J^{\rm sa}_{k_1k_2} = \frac{e\hbar}{im^*L}\xi_{k_1k_2}(l)\,. \tag{3.1}$$

Inserting them into the general conductance formula, one finds the exact result

$$\begin{aligned}\Gamma_{\rm free}(\omega) &= \frac{h}{2l^2}\int_0^\infty dE \frac{f(E)-f(E+\hbar\omega)}{\hbar\omega}\frac{2e^2}{4\pi^2\hbar^2}\frac{1}{kk_\omega} \\ &\times \left[\left(\frac{k+k_\omega}{k-k_\omega}\sin[(k-k_\omega)l/2]\right)^2+\left(\frac{k-k_\omega}{k+k_\omega}\sin[(k+k_\omega)l/2]\right)^2\right].\end{aligned} \tag{3.2}$$

At not too high frequencies, $\hbar\omega \ll E_{\rm F}$, the second term in big brackets can be neglected as compared to the first one. Expanding k_ω up to linear order in $\hbar\omega/E_{\rm F}$, the well known [63, 64, 65] conductance of a free quantum wire

$$\Gamma_{\rm free}(\omega) = \frac{e^2}{h}\left(\frac{\sin(\omega l/2v_{\rm F})}{\omega l/2v_{\rm F}}\right)^2 \tag{3.3}$$

in the regime $\hbar\omega \ll E_{\rm F}$ is reproduced. This result shows a decreasing conductance with frequency and oscillations at higher frequencies. These oscillations as well as the frequency scale on which the conductance decreases, depend on the length of the irradiated region of the sample and the Fermi velocity. The first minimum occurs at

$$\omega_{\rm m} = \frac{2\pi v_{\rm F}}{l}\,. \tag{3.4}$$

This frequency can be interpreted in terms of a 'traversal time', an electron at the Fermi edge needs to travel through the irradiated region. At $\omega_{\rm m}$, the electron passes the length l of the wire in exactly one period $2\pi/\omega$ and the net effect of the field vanishes. Along this line, all the further minima can be explained by using integer multiples of a period.

Studying other spatial distributions of the electric field [60, 63] it has been shown that the conductance is determined by the autocorrelation function of the electric field.

By means of the Kramers–Kronig relation [69]

$$\Gamma'_{\rm free}(\omega) = -\frac{1}{\pi}\,P\int d\omega'\left(\frac{1}{\omega'-\omega}\right)\Gamma(\omega')\,, \tag{3.5}$$

where $P\int$ denotes a principal part integral, one obtains from the real (absorptive) part (3.3) an approximation for the imaginary (reactive) part

$$\Gamma'_{\rm free}(\omega) = \frac{e^2}{h}\frac{2v_{\rm F}}{\omega l}\left(1-\frac{\sin(\omega l/v_{\rm F})}{\omega l/v_{\rm F}}\right) \tag{3.6}$$

which is correct at low frequencies[1]. The behavior of $\Gamma_{\rm free}(\omega)$ and $\Gamma'_{\rm free}$ at low frequencies is very close to the conductance of a classical resistance h/e^2 and an inductance $(h/e^2)l/3v_{\rm F}$ in series. The dc–conductance, being determined by the resistor is just the quantum conductance, while the decrease of the (absorptive) conductance is a consequence of the presence of the inductance. The sign of the reactive part of the conductance describes the phase shift between current and voltage induced by the inductance.

[1] After performing a decomposition into partial fractions, the remaining integrals leading to (3.6) can be found in [68]

3.2.2 Low barrier

In the case of a low barrier, lower than the Fermi energy, the behavior of a free quantum wire is affected by the existence of the barrier. Nevertheless, some significant features remain valid. The curvature of the conductance plotted over the frequency is always negative at $\omega = 0$. The position of the first minimum of the conductance is altered. It can be interpreted by using the time $\tau_{\rm t}$ the electron needs to travel through the region in which the electric ac field is applied. $\tau_{\rm t}$ is increased in the presence of the barrier. We want to emphasize, that this concept breaks down at higher barriers, when we have to tackle a tunneling problem. It is not within the scope of this work to treat the problem of tunneling times, which is a topic of intensive discussion [70, 71, 72].

The exact conductance is plotted versus the frequency for different barrier parameters in Figure 3.2. We see that the decrease of the conductance with frequency is not very much influenced by the barrier width but by the length l on which the field is applied. In fact the heuristic formula for the time 'the electron stays in the field' $\tau_{\rm t} = b/v_{\rm B} + (l-b)/v_F$ with the 'Fermi velocity over the barrier' $v_{\rm B} = \sqrt{2(E_F - V)/m^*}$ gives with $\omega = 2\pi/\tau_{\rm t}$ (at this frequency, the electron passing through the field 'sees' a whole period of the field) a rough approximation for the first minimum in the graphs.

3.2.3 DC–conductance

To obtain the dc–conductance, we perform the limit $\omega \longrightarrow 0$ in the general expression for the conductance (2.19). At zero temperature, the term containing the Fermi distribution functions collapses to a delta function centered at $E_{\rm F} - \hbar\omega/2$ and the energy integration yields

$$\Gamma(\hbar\omega \ll E_{\rm F}) = \frac{h}{2l^2}\left(\frac{m^* L}{2\pi\hbar^2}\right)^2 \frac{1}{k^- k^+}\left(|J^{\rm sa}_{k^- k^+}|^2 + |J^{\rm sa}_{k^+ k^-}|^2\right) \tag{3.7}$$

with the abbreviations

$$k^{+/-} = \sqrt{2m^*(E_{\rm F} \pm \hbar\omega)}/\hbar\,. \tag{3.8}$$

Performing the lengthy but straightforward calculations of the limiting procedure $\omega \longrightarrow 0$ in the expression (3.7) yields the dc–conductance of a single barrier

$$\Gamma^{\rm DC} = \frac{e^2}{h} T(E_F)\,, \tag{3.9}$$

where

$$T(E) = \frac{4E(V-E)}{4E(V-E) + V^2 \sinh^2 \kappa b} \tag{3.10}$$

is the well known transmission coefficient of a rectangular potential barrier [73].

The equation (3.9) is the 'two terminal' Landauer formula. Some years ago, there have been intensive discussions whether or not in the genuine 'four terminal' Landauer formula [75, 76, 77] $G = (e^2/h)\, T/(1-T)$ the denominator should be used. The different formulas were found to correspond to different experimental setups [74]. While the latter describes a disordered conductor connected via ideal one dimensional leads to reservoirs and the voltage is measured across the sample without the leads, the first one corresponds

to measuring both, voltage and current via contacts well inside the reservoirs. The 'four terminal' Landauer formula has never been justified by a decent linear response calculation. In contrast, the 'two terminal' version (without the denominator $1-T$) is nothing but the dc–limit of linear response theory. This can be shown for very general situations [59].

Due to the presence of quantum coherence, (3.9) does not depend at all on the details of the electric field applied and only the voltage drop between the reservoirs determines the current. The result is independent of the region where the driving field is applied. Even if the voltage drop occurs far from the barrier, (3.9) remains unchanged [78]. In contrast, at finite frequencies, the conductance depends sensitively on the shape of the electric field applied as well as on the relation between the irradiated region and the barrier region.

3.2.4 Low frequency expansion

The behavior of the conductance at low frequencies is particularly interesting for the discussion of the capacitive properties of the tunnel junction. We perform the expansion

$$\Gamma(\omega) = \Gamma^{\mathrm{DC}} + \Gamma_2 \omega^2 + O[\omega^4] \tag{3.11}$$

exactly up to second order in the frequency. Due to the complex dependence of the conductance (2.19) on the frequency in the general situation, we calculated the second order coefficient Γ_2 in the case $b = l$ using the program Mathematica^{TM} for algebraic computations running on an IBM RISC workstation. The result is given in Appendix A. In spite of being quite lengthy and difficult to deal with, the expression is nevertheless an exact result which can be plotted (see Figure 3.3).

The first of the interesting features is an increase of Γ_2 starting just below $E_{\mathrm{F}} = V$. For not too low barrier length b, the coefficient Γ_2 is positive at $E_{\mathrm{F}} < V$. It will be interpreted in terms of a dynamical capacitance of the junction in Chapter 4.

Above the barrier, at $E_{\mathrm{F}} > V$, oscillations occur and the barrier no longer exhibits the behavior of a genuine capacitor.

Very high barrier

For a nearly impenetrable barrier, keeping only the leading term in $\exp(-\kappa b)$, we expand (3.7) with respect to ω for $k_{\mathrm{F}} \ll \kappa_{\mathrm{F}}$ and find

$$\begin{aligned} \Gamma(\omega) &= \frac{e^2}{h} T(E_{\mathrm{F}}) + \frac{e^2 (m^*)^2}{2\,\pi\,\hbar^3\, k_{\mathrm{F}}^2\, l^2} \left(\left(\frac{l-b}{2} + \frac{1}{\kappa_{\mathrm{F}}} \right)^2 - \left(\frac{1}{\kappa_{\mathrm{F}}} \right)^2 \right. \\ &+ \left. \frac{1}{2\,k_{\mathrm{F}}^2} \left(\cos\left[2\,k_{\mathrm{F}} \left(\frac{l-b}{2} + \frac{1}{\kappa_{\mathrm{F}}} \right) \right] - \cos\left[\frac{2\,k_{\mathrm{F}}}{\kappa_{\mathrm{F}}} \right] \right) + \frac{k_{\mathrm{F}}^2}{\kappa_{\mathrm{F}}^4} \right)^2 \omega^2 + \mathrm{O}[\omega^4] \quad . \end{aligned} \tag{3.12}$$

A numerical evaluation of this formula in comparison with the exact result for the second order term in the frequency (Appendix A) shows that the relative error of the coefficient in (3.12) is less than 10^{-3} if we choose $k_{\mathrm{F}}/\kappa_{\mathrm{F}} < 0.03$ and $\kappa_{\mathrm{F}}\, b > 15$. When the voltage

drop occurs just over the length of the barrier, we can set $b = l$ in (3.12) and obtain the much shorter expression

$$\Gamma(\omega) = \frac{e^2}{h} T(E_{\mathrm{F}}) + \frac{e^2 (m^*)^2}{2\pi\hbar^3 b^2} \frac{k_{\mathrm{F}}^2}{\kappa_{\mathrm{F}}^8} \omega^2 + \mathrm{O}[\omega^4] \quad . \tag{3.13}$$

This is nothing but the 17th term in the exact result (A.3).

Setting $b = l$ intuitively seems to be a reasonable assumption not only when the electric field is introduced by shining light onto the sample, but also if voltages are applied to the reservoirs with not too high frequencies.

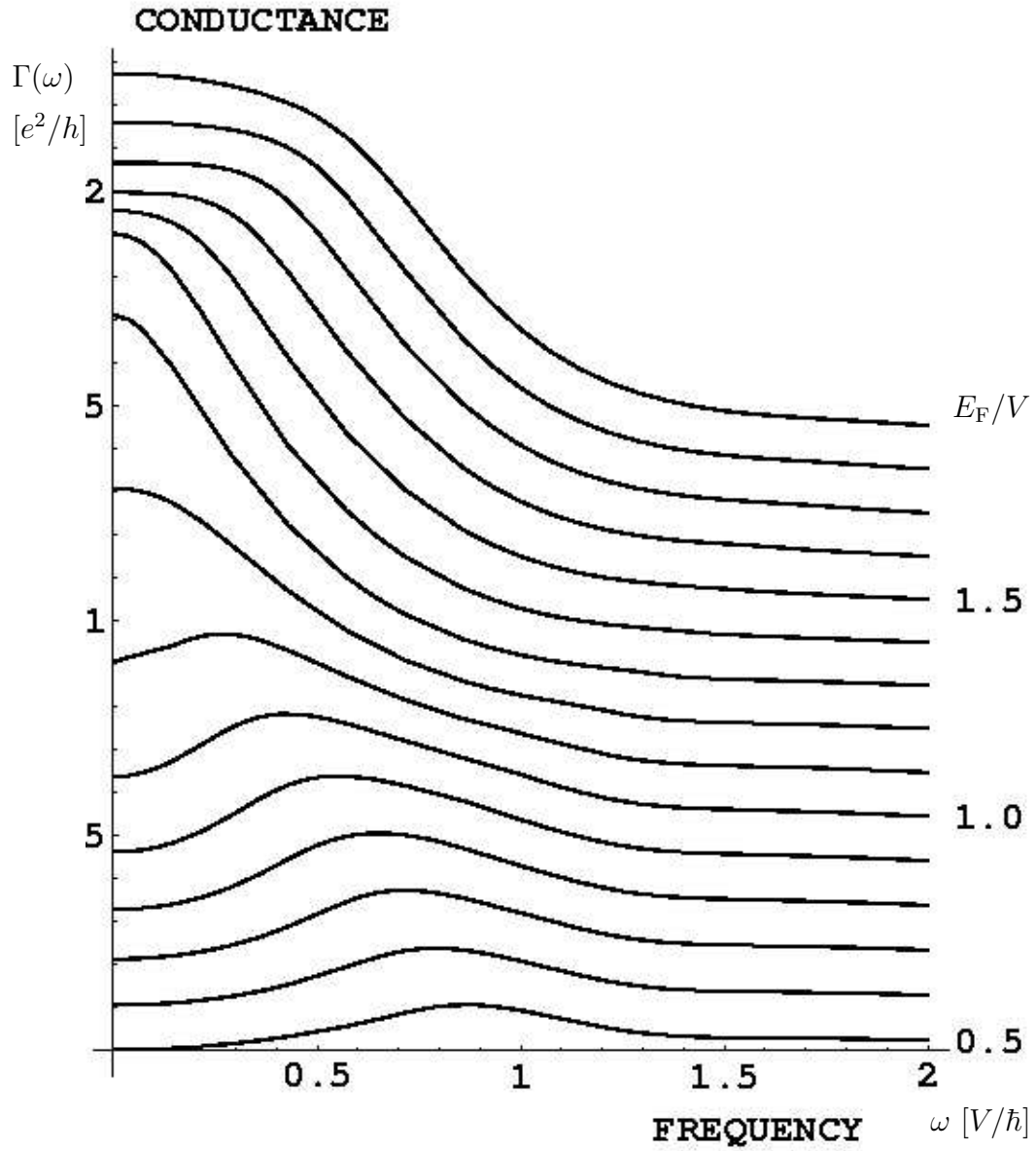

Figure 3.1: ac–Conductance of the one–dimensional system with a barrier of length $b = 5\hbar(2m^*V)^{-1/2}$ and field length $l = 7\hbar(2m^*V)^{-1/2}$ at zero temperature for various values of E_F (the curves are offset for clarity).

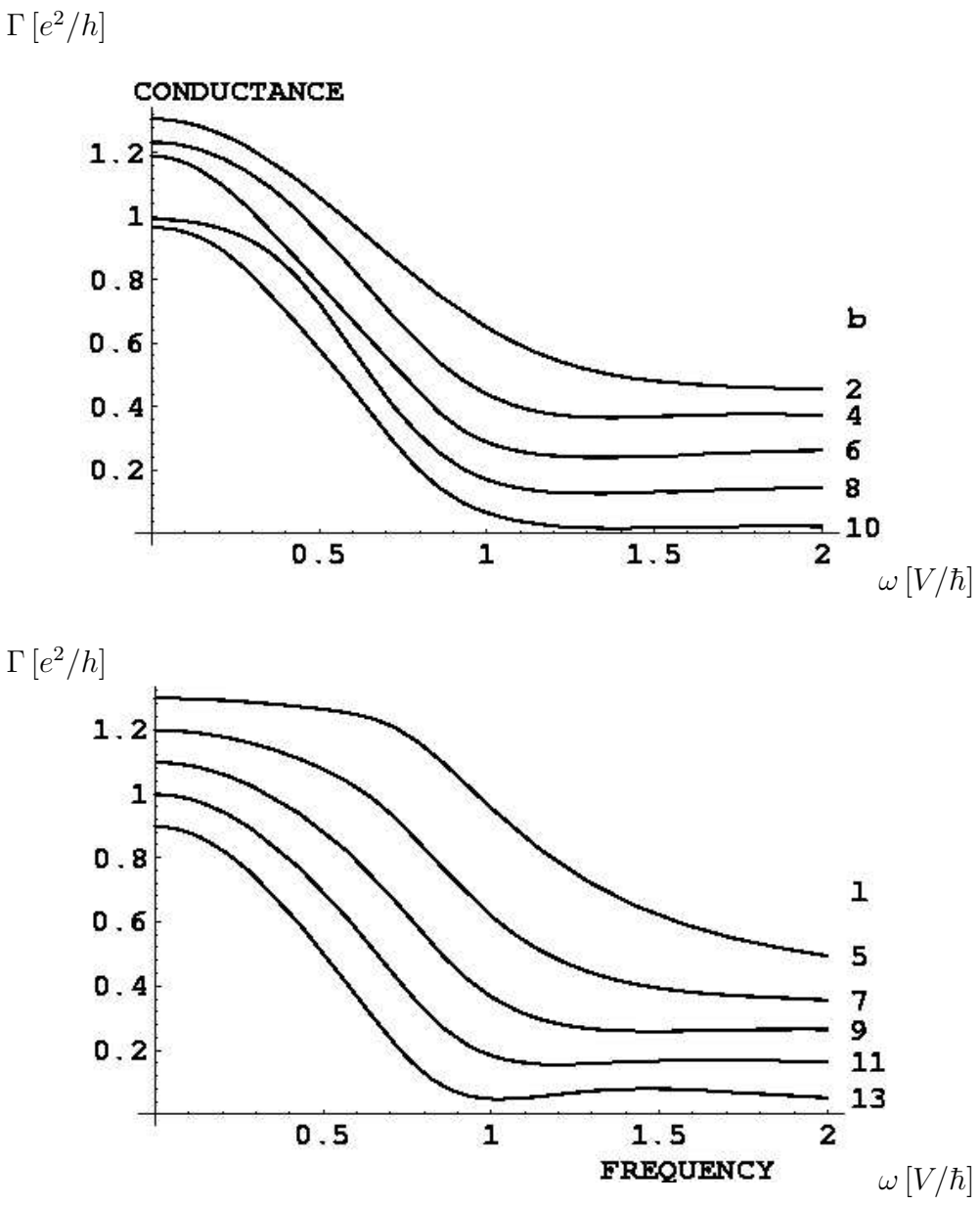

Figure 3.2: The ac–conductance of the system at high Fermi energy ($E_F = 2V$) for constant length of field irradiation ($l = 10\hbar(2m^*V)^{-1/2}$) and different values of the barrier width b (above) and for constant barrier width ($b = 5\hbar(2m^*V)^{-1/2}$) and different values of l (below). The lengths l and b are indicated in units of $\hbar(2m^*V)^{-1/2}$ at the right of the curves, which are offset for clarity.

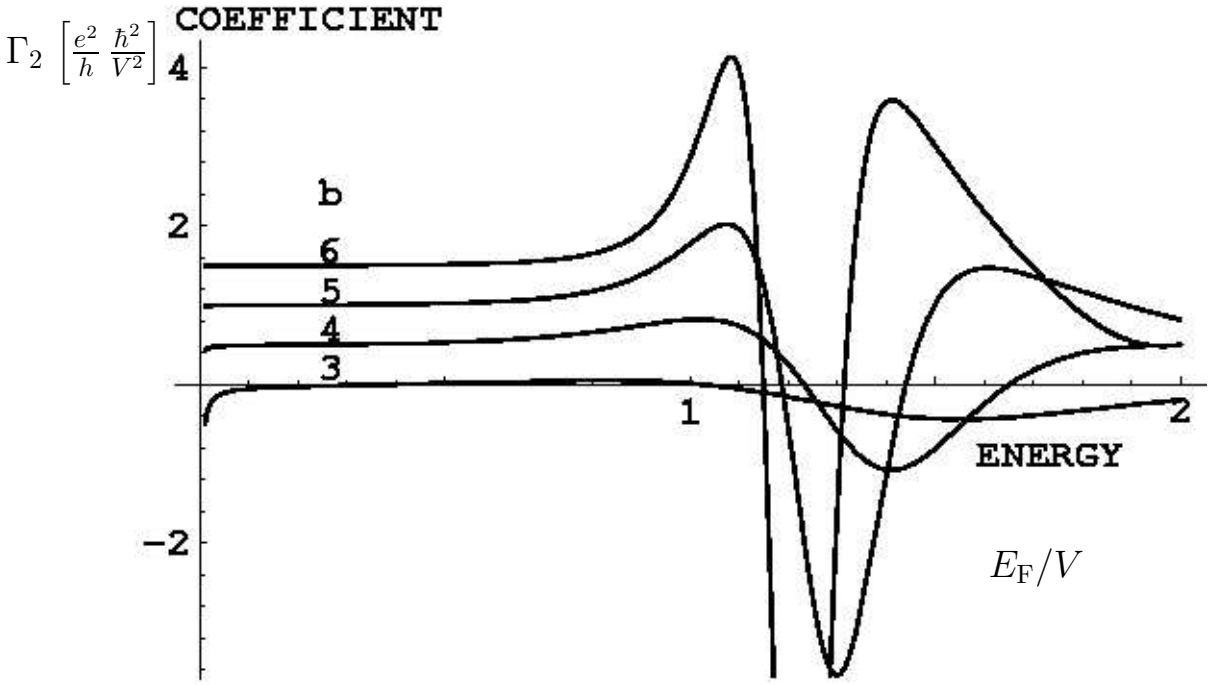

Figure 3.3: The exact result for the coefficient of the ω^2–term in the low frequency expansion of the zero temperature conductance for $l = b$ is plotted in units of $(e^2/h)(\hbar/V)^2$ as a function of the Fermi energy E_F/V for different values of b which are indicated in units of $\hbar(2m^*V)^{(-1/2)}$. The curves are offset by $0.5\,(b-3)$.

Chapter 4

Comparison to the behavior of a classical circuit

It is well known from elementary classical electrodynamics [69], that the frequency dependent conductance of a circuit containing coils and capacitors depends crucially on the values of their inductance and capacitance, respectively. In the case of circuits which are dominated by capacitors, an increase of the conductance with frequency is not unusual.

Since our quantum mechanical model is supposed to describe a tunnel junction which can be interpreted in the dc–limit roughly as a resistor and a capacitor in parallel [38, 79], it is tempting to compare its frequency dependent conductance with a classical model and to define its dynamical capacitance from the increase of the conductance with frequency. The second order term in the frequency of (3.13) shall be interpreted in this direction.

4.1 Classical model

We propose a very simple classical system (Figure 4.1) whose conductance will be compared with our results for the tunnel junction. It consists of an ohmic conductor with very low conductance Γ_{T} in parallel with an ideal capacitor of capacitance C. This arrangement corresponds to the tunnel junction which behaves like a capacitor but has nevertheless a low transmission at zero frequency. The leads are represented by the shunt impedance Z_{V} in series to the tunnel junction.

The complex conductance of the classical circuit (Figure 4.1) is

$$\Gamma_{\mathrm{c}}(\omega) = \left[Z_{\mathrm{V}} + \frac{1}{\Gamma_{\mathrm{T}} - i\omega C} \right]^{-1} . \tag{4.1}$$

We take the limit $\Gamma_{\mathrm{T}} \ll 1/|Z_{\mathrm{V}}|$ and expand the real part of (4.1) for low frequencies. Using for the impedance Z_{V} the results for the free quantum wire (3.3) and (3.6), we find

$$\mathrm{Re}\,\Gamma_{\mathrm{c}}(\omega) = \Gamma_{\mathrm{T}} + \frac{h}{e^2} C^2 \omega^2 + \mathrm{O}[\omega^4] \quad . \tag{4.2}$$

The imaginary part of Z_{V} does not enter the lowest order terms and contributes only in fourth order to (4.2). To take the real part of the conductance corresponds to our way to define the quantum conductance via the absorbed power (1.22).

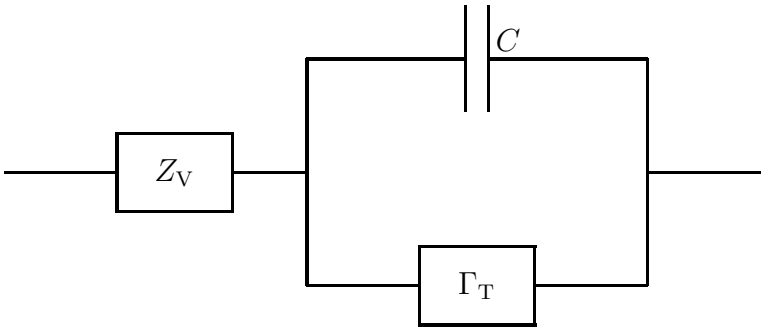

Figure 4.1: Classical circuit with a low frequency behavior close to the properties of a quasi–one dimensional tunnel junction

4.1.1 Dynamical capacitance

The comparison of the equations (4.2) and (3.11) yields the dynamical capacitance $C_D = \sqrt{(e^2/h)\,\Gamma_2}$ leading with (3.13) to

$$C_D = \frac{e^2 m^*}{2\pi\hbar^2}\,\frac{k_F}{\kappa_F^4}\,\frac{1}{b} \tag{4.3}$$

which is valid in the regime of very high barriers.

One can see from Figure 3.3 that a well behaved capacitance can only be defined when the Fermi energy is below the top of the barrier. Thus, a junction in which the electrons do not have to tunnel cannot behave capacitively.

4.2 The role of electron–electron interactions

In order to decide whether or not the dynamical capacitance is the same as the static capacitance needed to understand the Coulomb blockade, it is in principle necessary to consider the influence of electron–electron interactions. While Coulomb interactions are crucial at zero frequency, their importance for the conductance diminishes as ω is increased. This can be concluded [83] from the RPA result for the density–density correlation function [55] of a quantum wire where the interaction induced corrections to the noninteracting limit vanish as ω^{-2}.

A quantitative estimate of the frequency ω_0 above which Coulomb interactions have minor influence can be found using the tunneling Hamiltonian

$$H = H_L + H_R + H_T + H_C, \tag{4.4}$$

where H_L and H_R describe semi–infinite wires on the left and right hand side of the barrier. They are coupled by the tunneling term H_T and the Coulomb interaction is modeled by

$$H_C = \lambda(Q_L - Q_R)^2\,, \tag{4.5}$$

where Q_{L} and Q_{R} are the operators of the total charge in the left and the right wire, and λ parametrizes the interaction strength.

Applying linear response theory for $\lambda = 0$, one finds that the conductance consists of two contributions. The first is $\Gamma_{\mathrm{si}} = (e^2/h)(\omega l/4v_{\mathrm{F}})^2$ at low frequencies $\hbar\omega \ll E_{\mathrm{F}}$ and $k_{\mathrm{F}}l \gg 1$ and is due to the motion of the electrons in the semi–infinite wires. Here, l is again the interval where the electric field is applied, v_{F} and k_{F} are the Fermi velocity and wave vector, respectively. The second contribution is the dc–value $(e^2/h)T$, which is due to electrons tunneling through the barrier with transmission probability T. Taking into account the Coulomb interaction ($\lambda \neq 0$), the first contribution remains unchanged and H_{C} results only in a constant energy shift.

The second contribution to Γ arising from charge changing tunneling processes turns out to be suppressed [80]. We define ω_0 as the frequency above which the unchanged term $\sim \omega^2$ prevails over the (dc–) contribution at $\lambda = 0$ that is influenced by Coulomb interactions. While at low frequencies, interactions dominate the behavior [81], well above this frequency, which is given by

$$\omega_0 = (4v_{\mathrm{F}}/l)\sqrt{T}\,, \tag{4.6}$$

the total conductance is dominated by the semi–infinite wires, independent of the strength of the interaction λ. For high frequencies $\omega \gg \omega_0$ the investigation of frequency dependent transport properties of tunnel junctions neglecting electron–electron interactions should be a good approximation for the system even in the presence of interactions.

Of course, the model (4.4) is a severe simplification of the realistic situation. The interaction term does not take into account the decreasing charging energy when the electron leaves the region of the tunnel junction. Therefore, in this model no resistance is needed to observe the Coulomb blockade. Furthermore, for the critical frequency (4.6) we find a result that yields zero when the transmission of the contact vanishes. This would mean that there is no influence of the interaction at any finite frequency which seems to be somewhat unrealistic. Therefore, the investigation of more sophisticated models taking into account tunneling and electron–electron interaction effects [41] at high frequencies is highly desirable but outside the scope of this work.

4.3 Discussion

Using reasonable values of the parameters, suitable for instance for GaAs–AlGaAs heterostructures [53], we find that a barrier of length $b \approx 130\,\mathrm{nm}$ and height $0.75\,\mathrm{meV}$ has a dynamical capacitance of the order of $10^{-18}\,\mathrm{F}$ per conductance channel at $E_{\mathrm{F}} = 0.05\,\mathrm{meV}$. Furthermore, we see that the critical frequency ω_0, below which the influence of electron–electron interactions is of importance, is very small on the frequency scale $V/\hbar$ characteristic for the ac–conductance at low frequencies. Therefore the low frequency expansion remains valid well above ω_0.

For a wire of finite width the conductance is calculated from a sum over the contributions of the channels. The number of channels increases proportional to the cross–section A of the wire, when the potential representing the tunnel junction is independent of the

transverse coordinates. In the limit of many channels, one finds $C_{\mathrm{D}} \sim A/b$ as for a classical parallel–plate capacitor.

Since C_{D} depends on the shape of the electric field applied along the wire and across the barrier, we cannot conclude, that the dynamical capacitance defined above equals the static capacitance determined by the voltage offset of the current–voltage characteristic in a Coulomb blockade experiment [40, 82]. Nevertheless, if we require the capacitance of a quantum system to be a genuine property, its effects on static as well as on the dynamic properties should be the same. It is therefore highly desirable to investigate further the frequency dependent conductance of single tunnel junctions including electron–electron interactions and using a selfconsistent determination of the electric field dependence on the space coordinates.

We want to emphasize that the capacitance discussed above describes the behavior of the tunnel junction at high frequencies and is not a correction to the static capacitance like the one due to quasi–particle tunneling in Josephson junctions as calculated in [47].

Chapter 5

The influence of inelastic processes

To demonstrate that the capacitive behavior (3.13) is of quantum mechanical origin we investigate the influence of inelastic processes following the references [80, 83, 84]. We will see that they eventually lead to a vanishing of the effect.

We consider a simplified version of the above model, namely a barrier of the form

$$V(x) = V_0 \delta(x)\,. \tag{5.1}$$

The (retarded) single–electron Green's function is [85]

$$G(x,x';\omega) = G^0(x,x';\omega) + \frac{V_0}{1 - V_0 G^0(0,0;\omega)} G^0(x,0;\omega) G^0(0,x';\omega)\,, \tag{5.2}$$

where G^0 is the Green's function for $V_0 = 0$. The simplest approach to take into account phase breaking processes consists in renormalizing G^0 by a self-energy Σ caused by electron–phonon (e–p) interaction. We assume that electrons and phonons are coupled via a deformation potential [55, 86]

$$V_{\mathrm{e-p}}(x) = \frac{1}{\sqrt{\Omega}} \sum_Q V_Q F(Q_\perp) \exp(iqx)(a_Q + a^\dagger_{-Q}) \tag{5.3}$$

with phonon wave vector $Q = (q, Q_\perp)$, the deformation potential

$$|V_Q|^2 = V_{\mathrm{D}}^2 |Q| / Q_{\mathrm{D}}^4\,, \tag{5.4}$$

Debye cutoff Q_{D} and coupling parameter V_{D}, Ω being the total system volume ($\Omega \to \infty$). The form factor

$$F(Q_\perp) = \langle \chi | \exp(iQ_\perp x_\perp) | \chi \rangle \tag{5.5}$$

reflects the fact that although the phonons are three–dimensional the e–p coupling is affected by the confining potential.

In second order perturbation theory with respect to e–p coupling and close to E_{F}, we can restrict ourselves to $\mathrm{Im}\,\Sigma(k,\omega)$, numerical evaluation yielding only weak k– but strong ω–dependence around E_{F} similar to the results of Ref. [87]. Neglecting the k–dependence

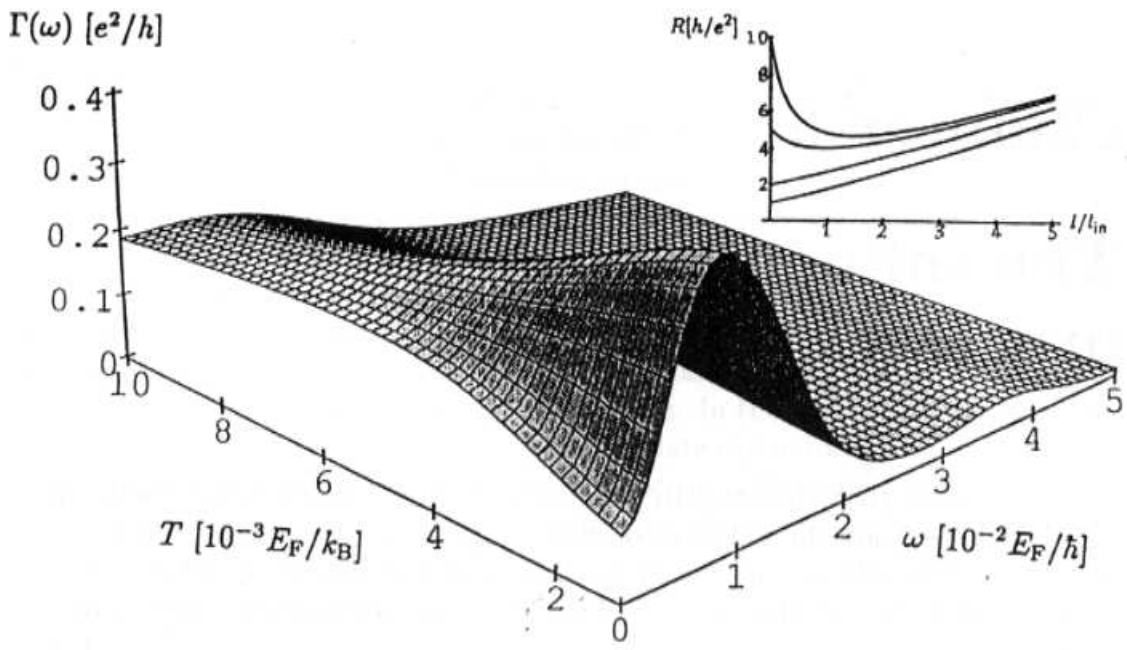

Figure 5.1: Conductance $\Gamma(\omega)$ for δ–barrier strength $k_F V_0/E_F = 7$ and $k_F l = 1000$. Self–energy parameters are $(V_D/E_F)^2 = 0.08\,\pi$, $Q_D/k_F = 1, \hbar\omega_D/E_F = 0.01$ and $k_F\lambda = 1$. In the inset, the resistance at $\omega = 0$ for δ-barrier strength $k_F V_0/E_F = 0, 2, 4, 6$ (from below) is shown as a function of l/l_{in}. The figure is taken from [83].

of Σ around the Fermi wave vector k_F we get

$$\begin{aligned} G^0 &= -\frac{im^*}{\hbar^2\gamma(\omega)} \exp(i\gamma(\omega) \mid x - x' \mid) \\ \gamma(\omega) &= \sqrt{\frac{2m^*}{\hbar^2}(\hbar\omega + E_F - i\,\mathrm{Im}\,\Sigma(k_F,\omega))} \end{aligned} \tag{5.6}$$

from which we calculate G and the corresponding spectral function $-(1/\pi)\mathrm{Im}\,G$. Neglecting vertex corrections, the dissipative nonlocal conductivity σ of the one–channel system can be calculated from the Kubo formula involving only products of the spectral functions at different energies [88].

From the general result (1.24) one finds the dc–limit of the conductance. The e–p interaction introduces an additional length scale, namely

$$l_{in}^{-1} := 2\ \mathrm{Im}\,[2m^*/\hbar^2(E_F - i\,\mathrm{Im}\,\Sigma(k_F,0))]^{1/2} \tag{5.7}$$

which is the decay length of the Green's function G^0 without the barrier. We evaluate the dc–resistance $R = \Gamma^{-1}(0)$ as a function of l/l_{in} for $k_B T \ll E_F$ and $k_F l_{in} \gg 1$ corresponding to weak e–p coupling (Figure 5.1). For $l_{in} = \infty$ we reproduce Landauer's result, for $l/l_{in} \gg 1$ we have ohmic behavior with R proportional to the effective length l of the wire. In the intermediate region the behavior of R depends on the δ–barrier strength V_0.

The evaluation of $\Gamma(\omega)$ (Figure 5.1) at nonzero frequency is again simplified when $\omega \ll E_{\mathrm{F}}/\hbar$ besides $k_{\mathrm{B}}T \ll E_{\mathrm{F}}$. The increase of conductance with frequency for small ω can again be interpreted as a capacitive behavior. The oscillatory decrease of $\Gamma(\omega)$ is similar to the free one–channel quantum wire (3.3).

The most important result is the suppression of oscillatory and capacitive behavior with increasing temperature as a result of the loss of phase coherence. Both effects are destroyed by the e–p interaction showing that the dynamical capacitance is a quantum mechanical property of the system.

Chapter 6

Frequency dependent resonant tunneling through quantum dots

In order to study the frequency dependent conductance of resonant tunneling systems, in which the phase coherence is conserved throughout the sample, in this chapter we shall treat a one dimensional double barrier model in linear response.

6.1 Double barrier model

We calculate the dissipative conductance of a system containing two rectangular barriers of height V and length b separated by the distance w, forming a quantum dot in between (Figure 6.1).

6.1.1 The wave functions

For this highly symmetric model potential it is possible to find a complete set of orthonormal eigenfunctions. As in the single barrier problem, they can be chosen purely symmetric

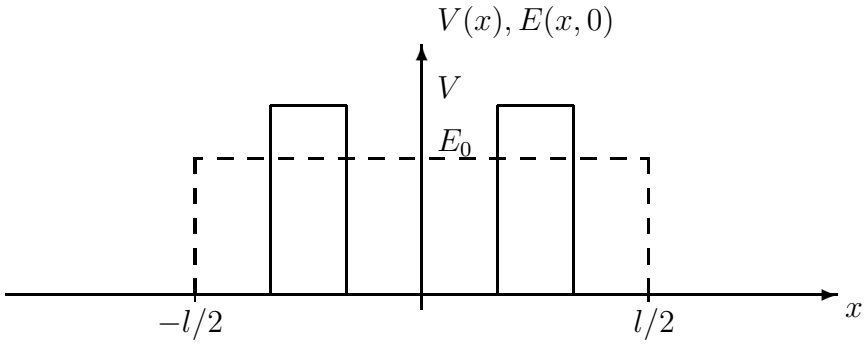

Figure 6.1: Model potential and spatial dependence of the electric field (dashed) describing a resonant tunneling system.

and antisymmetric. We use

$$\psi_k^{\rm s}(x) = \begin{cases} A\sin(-kx+\phi_k^{\rm s}) & \text{for } x < -w/2-b \\ B^{\rm s}e^{\kappa x} + C^{\rm s}e^{-\kappa x} & \text{for } -w/2-b < x < -w/2 \\ D_k^{\rm s}\cos(kx) & \text{for } |x| < w/2 \\ B^{\rm s}e^{-\kappa x} + C^{\rm s}e^{\kappa x} & \text{for } w/2 < x < w/2+b \\ A\sin(kx+\phi_k^{\rm s}) & \text{for } x > w/2+b \end{cases} \tag{6.1}$$

and

$$\psi_k^{\rm a}(x) = \begin{cases} -A\sin(-kx+\phi_k^{\rm a}) & \text{for } x < -w/2-b \\ -B^{\rm a}e^{\kappa x} - C^{\rm a}e^{-\kappa x} & \text{for } -w/2-b < x < -w/2 \\ D_k^{\rm a}\sin(kx) & \text{for } |x| < w/2 \\ B^{\rm a}e^{-\kappa x} + C^{\rm a}e^{\kappa x} & \text{for } w/2 < x < w/2+b \\ A\sin(kx+\phi_k^{\rm a}) & \text{for } x > w/2+b \end{cases} \tag{6.2}$$

with the abbreviations

$$\begin{aligned} k &= \sqrt{2m^*E}/\hbar \\ \text{and } \kappa &= \sqrt{2m^*(V-E)}/\hbar\,. \end{aligned}$$

From the matching conditions at $x = \pm w/2$ and $x = \pm(w/2+b)$, and the periodic boundary conditions at $\pm L/2$, one determines the coefficients. Introducing the abbreviation $y = w/2 + b$, one finds

$$\begin{aligned} B^{\rm s/a} &= A\frac{\sin(ky+\phi_k^{\rm s/a}) - \frac{k}{\kappa}\cos(ky+\phi_k^{\rm s/a})}{2\exp(-\kappa y)} \\ C^{\rm s/a} &= A\frac{\sin(ky+\phi_k^{\rm s/a}) + \frac{k}{\kappa}\cos(ky+\phi_k^{\rm s/a})}{2\exp(\kappa y)} \\ D^{\rm s/a} &= A\frac{\sin(ky+\phi_k^{\rm s/a})\cosh(\kappa b) - \frac{k}{\kappa}\cos(ky+\phi_k^{\rm s/a})\sinh\kappa b}{\cos\,/\,\sin(kw/2)} \end{aligned} \tag{6.3}$$

and the normalization condition yields $A = \sqrt{2/L}$ in the limit $L \gg b, w$. The angles $\phi_k^{\rm s/a}$ satisfy the conditions

$$\begin{aligned} \tan(kb+\phi_k^{\rm s}) &= \frac{\kappa k\coth(\kappa b) - V/2\sin(kw)}{V\cos^2(kw/2) - k^2} \\ \tan(kb+\phi_k^{\rm a}) &= \frac{k^2 - V\sin^2(kw/2)}{\kappa k\coth(\kappa b) + V/2\sin(kw)}\,. \end{aligned} \tag{6.4}$$

6.1.2 The conductance

As in chapter 2, we choose the spatial distribution of the electric field (Figure 6.1)

$$E(x,t) = E_0\,\Theta(l/2 - |\,x\,|)\cos(\omega t) \tag{6.5}$$

constant on a length l of the system and zero outside. Experimentally this could be realized by shining light on a sample through a mask exposing only a tiny fraction of the

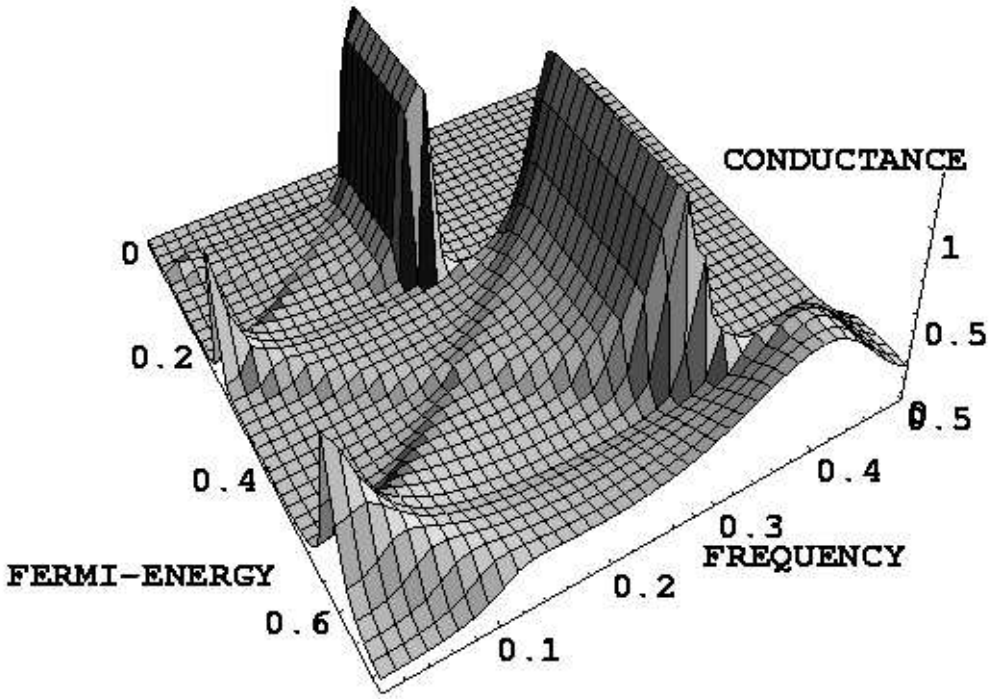

Figure 6.2: Plot of the conductance of a resonant tunneling diode with barriers of length $b = 2\hbar(2m^*V)^{-1/2}$, a length of the well $w = 10\hbar(2m^*V)^{-1/2}$ between the barriers and irradiated on a length $l = 20\hbar(2m^*V)^{-1/2}$. A rich structure can be observed showing resonances at sharp frequencies over distinct regions of the Fermi energy.

system. Then, the (dissipative) conductance can be computed using the same formalism as in Chapter 2.

Inserting the wave functions (6.1) and (6.2) into the expressions (2.17), and doing the integrals using standard tables [68] one finds quite lengthy analytical expressions for the current matrix elements. With these results, we calculate the conductance using the linear response formula (2.19), doing the energy integration numerically with the help of Mathematica^{TM} on an IBM RISC workstation. The zero temperature result is presented in Figure 6.2.

The dc–conductance shows peaks, when the Fermi energy is in resonance with a quasi–discrete level between the barriers. The width of the peaks is determined by the transparency of the barriers and the temperature.

This region of finite conductance is flattened and broadened at higher frequencies. At frequencies corresponding to energy differences between quasi–discrete states, there is a very strong peak in the frequency dependent conductance, when the Fermi energy lies between these two levels. Then, the lower one is occupied at thermal equilibrium and the higher one is empty. Thus, at the right frequency, electron–hole excitations are possible such that both, the electron and the hole can pass through the barriers resonantly yielding a maximum in the conductance. These features are consistent with [89], where

the same method was applied to a similar system. Important features like the resonances at finite frequencies can not be found when restricting the problem to a single resonant level between the barriers as in reference [61].

However, within this approach it is not obvious how to take into account the electron–electron interactions that are of crucial importance for nearly impenetrable barriers and low frequencies as well as inelastic processes destroying the phase coherence. Further, a generalization to arbitrary transport voltages is highly desirable in order to describe photon assisted tunneling [90].

In the second part of this thesis, a method allowing for the description of nonlinear transport through quantum dots with very high barriers in the presence of phase breaking processes is used. There, only the dc–limit is investigated in the regime of sequential tunneling. The crossover between the theories would be very interesting to study.

Chapter 7

Persistent currents

7.1 Background

Persistent currents in mesoscopic rings are a topic of high interest and are controversially discussed at the moment. These currents are equilibrium properties occurring in rings with circumferences L that are smaller than the phase coherence length. The groundstate of the electrons can carry a finite current depending on the magnetic flux threading the ring. It is interesting to study how this current changes as a function of the disorder and/or the electron–electron interaction strength.

The present situation is characterized by experiments on disordered gold rings [10, 91] disagreeing with theoretical estimates of the persistent current by almost two orders of magnitude. While the amplitude of the persistent current in clean rings is expected to be of the order of ev_{F}/L [92], in the presence of disorder a suppression to $ev_{\mathrm{F}}l/L$ with the mean free path $l = D/v_{\mathrm{F}}$ and the diffusion constant D was predicted in the framework of a theory ignoring electron–electron interactions [93]. Such a strong suppression has not been found in the experiments.

Attempts to explain the discrepancy by including electron–electron interactions [94, 95, 96, 97] have up to now not been completely convincing and do not yield the large missing factor. Investigating persistent currents in the presence of Luttinger type interactions even leads to a reduction of the current [98]. An interesting proposal [99] tries to explain the discrepancy with grain boundaries in the samples suppressing the persistent current considerably less than the conductance through a similar wire. Thus, the mean free path, determined experimentally from measuring the conductance could have been underestimated when assuming pointlike impurities as disorder.

In the clean regime, an experiment on a single ring defined in a semiconductor heterostructure [11] yields results agreeing with the theory of noninteracting electrons in ideal rings within the (very wide) error bars.

Here, we study the influence of tunnel barriers in the ring on the persistent current within a theory of noninteracting electrons. We contribute results that could be checked experimentally by introducing an electrostatic tunneling barrier in clean semiconductor rings using an additional gate. Such an experiment is an extension of a recently performed one [11], and could be done in principle [100].

7.2 Quasi–one dimensional ring

Persistent currents can be traced back to the dependence of the energy levels on the magnetic flux penetrating the ring. At zero temperature, the current can be calculated from

$$I_{\rm p} = -\sum_n \frac{\partial E_n}{\partial \phi}\,, \tag{7.1}$$

the sum running over all of the occupied single electron states of the system. At finite temperatures, the contributions have to be weighted with thermal equilibrium occupation probabilities.

We consider a one dimensional system of finite length L closed to a ring and threaded by the magnetic flux ϕ. The vector potential can be eliminated from the Hamiltonian by introducing a gauge transformation resulting in the generalized boundary conditions

$$\psi(L/2) = \psi(-L/2)\exp(2\pi i\varphi)\,, \tag{7.2}$$

where $\varphi = \phi/\phi_0$, $\phi_0 = h/e$ being the flux quantum. It is easy to see, that the wave functions in an ideal ring are

$$\psi_n^{\rm id} \sim \exp[2\pi\, i(n-\varphi)x/L)] \tag{7.3}$$

with integer quantum number n. The energy of these states is given by

$$E_n^{\rm id} = 2\pi^2 \frac{\hbar^2(n-\varphi)^2}{m^* L^2}\,. \tag{7.4}$$

Thus, the states carry the persistent current

$$I_{\rm p,n}^{\rm id} = 2e\pi \frac{\hbar(n-\varphi)}{m^* L^2}\,. \tag{7.5}$$

7.2.1 Single rectangular barrier

As before, we introduce a rectangular barrier potential

$$V(x) = V\Theta(b/2 - \mid x \mid) \tag{7.6}$$

for which one can calculate the exact single–electron eigenfunctions

$$\psi_k(x) = \begin{cases} Ae^{ikx} + Be^{-ikx} & \text{for } x < -b/2 \\ \alpha e^{\kappa x} + \beta e^{-\kappa x} & \text{for } |x| < b/2 \\ Ce^{ikx} + De^{-ikx} & \text{for } x > b/2 \end{cases} \tag{7.7}$$

and the corresponding eigenenergies

$$E = \frac{\hbar^2 k^2}{2m^*}\,. \tag{7.8}$$

The parameter

$$\kappa = \sqrt{2m^*(V-E)}/\hbar \tag{7.9}$$

depends on the height of the barrier and becomes imaginary when the energy exceeds V. Since this can be done at arbitrary magnetic flux one can find the contributions of the states to the persistent current. The matching conditions at $\pm b/2$ and at $\pm L/2$ together with the normalization of the wave function (7.7) yield a system of equations determining the prefactors. They have nonzero solutions only at particular wave vectors satisfying the transcendental equation

$$2k = \frac{V \sinh(\kappa b)\, \sin(kL - kb)}{\kappa[\cos(2\pi\varphi) - \cosh(\kappa b)\, \cos(kL - kb)]}\,. \tag{7.10}$$

In this result the $2\pi\varphi$ periodicity of the boundary conditions is reflected in the only flux dependent term in the denominator. As a consequence, the general periodicity of the persistent current is guaranteed.

7.2.2 Single delta–barrier

Simplifying the system further we take the limit $V = \tilde{g}/b \longrightarrow \infty$ yielding a delta–shaped barrier with strength $\tilde{g}$. Then, (7.10) takes the form

$$2k = g\frac{\sin(kL)}{\cos(2\pi\varphi) - \cos(kL)}\,, \tag{7.11}$$

where $g = 2m^*\tilde{g}/\hbar^2$.

7.2.3 Two delta–barriers

Introducing two delta–barriers having different strength $\tilde{g}_1$ and $\tilde{g}_2$ at positions $x \pm a/2$, we can even treat a problem containing two impurities. The method is as before and the resulting transcendental equation in this case is given by

$$2k = \frac{(g_1 + g_2)\sin(kL) - \frac{g_1 g_2}{2k}\left[\cos(kL) - \cos(kL - 2ka)\right]}{\cos(2\pi\varphi) - \cos(kL)}\,, \tag{7.12}$$

reflecting resonances due to quasi–bound states between the barriers at $g_1, g_2 >> k$. It is easy to check that by setting g_1 or g_2 to zero, one recovers (7.11). For $a = 0$, (7.11) is reproduced with $g = g_1 + g_2$.

7.3 Discussion

Using the transcendental equations of the previous section, one can find approximate solutions for the persistent current. A graphical solution is possible solving the equations for φ and plotting them as a function of k^2. Then, the slope of the branches of this plot at the intersection with a line of constant magnetic flux is inversely proportional to the contribution of the corresponding level to the persistent current. For the most simple model with one δ–barrier, one finds from (7.11)

$$\varphi = \frac{1}{2\pi}\arccos\left\{\frac{gL}{2kL}\sin kL + \cos kL\right\}\,. \tag{7.13}$$

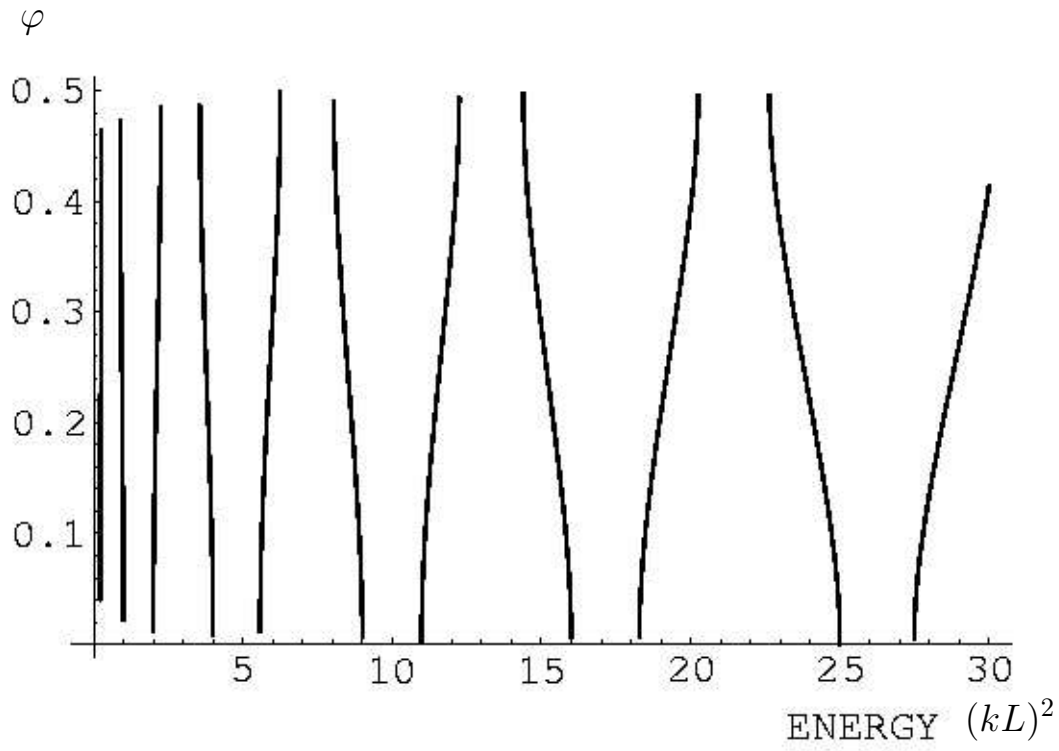

Figure 7.1: Plot of the flux φ from equation (7.13) at $gL = 10$. The energy is given in units of $\hbar^2/(2m^*L^2)$. Gaps in the spectrum appear connected with a suppression of the persistent current.

We plot φ as a function of $(kL)^2 = 2m^*L^2E/\hbar^2$ at $gL = 10$ in Figure 7.1. The suppression of the persistent current can be seen from the gaps in the spectrum. The effect is most striking at very low energy while at higher energies only a slight suppression remains. Since the persistent current depends mainly on the behavior of the highest occupied states, only weak influence on the total persistent current is expected. The wave functions calculated in the previous section can be used as a basis to study numerically the dependence of persistent currents on the strength of the electron–electron interaction in the presence of disorder, where the disorder is modeled by a single barrier [101].

Conclusions

We have calculated the frequency dependent conductance for a tunnel junction using a quasi–one dimensional model containing a rectangular tunneling barrier.

In the dc–limit, the transmission coefficient of the barrier dominates the conductance. Finite frequencieslead to a quadratic increase of the conductance at low Fermi energies. At higher E_{F}, the behavior changes qualitatively and becomes more similar to a free quantum wire where the corrections due to nonzero frequencies lead to a decrease of the (higher) dc–value.

We found that the ac–conductance of a quantum mechanical tunnel barrier can be simulated in a certain range of parameters by a classical circuit. This correspondence can be used to define a dynamical quantum mechanical capacitance of the tunnel contact. The latter depends not only on geometrical parameters like a classical capacitance but also on Fermi energy and effective mass of the charge carriers. Like the tunnel resistance the dynamical capacitance is of quantum mechanical origin. This was demonstrated using a model with electron–phonon interaction destroying quantum mechanical coherence.

We have further argued that the dynamical capacitance should not depend on the Coulomb interaction above a critical frequency ω_0. Thus if the capacitance is a genuine property of the system independent of the experiment which is used for its detection one may conclude that the dynamical capacitance has to be the same as the static capacitance used for the explanation of Coulomb blockade experiments. We want to mention that the results are also relevant in the context of conductivity in the presence of impurities [102]

The frequency ω_0 can also be considered to be an upper limit for the observation of the Coulomb blockade effect and, important for practical applications, the limiting frequency for turnstile devices [15, 20] proposed as current standard. Reasonable parameter values for GaAs–AlGaAs structures [53] ($V = 0.75\,\mathrm{meV}$, $E_{\mathrm{F}} = 0.05\,\mathrm{meV}$, $m^* = 0.07\,m_e$, $b = 130\,\mathrm{nm}$ and $l = 1\,\mu\mathrm{m}$) yield $\omega_0 \approx 1\,\mathrm{GHz}$. This would limit the highest achievable current in such a turnstile device with only one channel to about 25 pA. Using the estimate obtained in reference [20], $\omega_c = 2\pi/R_{\mathrm{T}}C \sim T/C$, one gets a frequency which is an order of magnitude smaller. Thus, the frequency ω_0 above which the Coulomb blockade is lifted in a quantum coherent system is still higher than the classical RC–time of the corresponding circuit.

Anyway, the achievable currents in turnstiles are very small and higher frequencies cannot be applied without reducing the accuracy. For the application as a current standard, a huge number of turnstiles have to be operated in parallel.

The frequency dependent conductance of a double barrier structure was investigated yielding sharp peaks at frequencies being in resonance with energy differences between quasi–discrete states in the dot. They occur in the range of Fermi energy between the

energies of the involved levels. The theory neglects electron–electron interactions as well as inelastic processes but, in contrast to approaches using the tunneling Hamiltonian yields a good description in the regime of highly penetrable barriers.

Finally, a contribution to the theory of persistent currents in the presence of disorder could be made using simple quasi–one dimensional models with barriers. A suppression of the persistent current with the strength of the barriers is found. At high Fermi energy, the suppression is much less effective because of the dominating role played by the highest of the occupied states and cancellations of the contributions of the lower levels to the persistent current.

Part II

NONLINEAR TRANSPORT

Introduction

In the last ten years, progress in nanostructure fabrication led to the possibility to create samples in which electrons are confined to very small spatial areas, the so–called quantum dots. They can be considered as 'artificial atoms' [13] with tunable parameters. Thus, it is possible to study the properties of few correlated electrons systematically.

In such situations of few electrons in very small dots, the Coulomb interaction between the electrons strongly influences the spectra. Spectroscopically investigating arrays of ultrasmall dots in infrared absorption experiments [103, 104, 105], dots with electron numbers down to one can be studied. According to Kohn's theorem [106] the effects of correlations are very difficult to observe [1].

Capacitance spectroscopy [107] has been used to investigate the spectra of ultrasmall single quantum dots down to very low electron numbers. Here, only equilibrium properties come into play and therefore, no information about excited states is obtained.

In contrast, using nonlinear transport experiments on single quantum dots, the full spectrum can be investigated. When the quantum dot and the reservoirs are only weakly coupled, the transport is dominated by the quantum mechanical properties of the isolated dot. If the dots are small enough, the charging energy E_{C} needed to add a single electron can exceed the thermal energy $k_{\mathrm{B}}T$ at experimentally accessible temperatures and lead to a suppression of the conductance through the dot at low voltages known as the Coulomb blockade effect [19]. For small voltages, and at low temperatures the current is blocked if for the chemical potentials μ_L and μ_R of the reservoirs on the left and on the right hand side of the dot, respectively, $\mu_{\mathrm{L}} \approx \mu_{\mathrm{R}} \neq E_0(n) - E_0(n-1)$. $E_0(n)$ is the ground state energy of n electrons in the isolated dot and the difference between the ground state energies of n and $n-1$ electrons represents the chemical potential of the quantum dot.

On the other hand, if $\mu_{\mathrm{L}} \approx \mu_{\mathrm{R}} = E_0(n) - E_0(n-1)$, the number of electrons inside the dot can oscillate between the two values n and $n-1$ (single electron tunneling (SET) oscillations), and the conductance is finite. The resulting periodic oscillations of the conductance through quantum dots [12, 52, 108, 110] are well established consequences of the charging energy. They can be observed at temperatures $k_{\mathrm{B}}T \ll E_{\mathrm{C}}$ low enough to suppress thermal smearing if the coupling to the leads (characterized by the tunneling resistance R_{T}) is weak enough $R_{\mathrm{T}} \gg h/e^2$ to avoid quantum smearing and therefore to assure the electron number in the dot n to be a good quantum number on a long enough timescale. The height and width of the peaks depends on temperature and the coupling

[1] In parabolic confinement potentials center of mass excitations decouple completely from the relative coordinates. Since in optical absorption experiments the perturbation couples to the center of mass only and the dot potentials are nearly parabolic in these arrays, only faint effects due to slight nonparabolicities can be detected.

to the leads [109]. In linear transport, the conductance oscillations are observed as a function of the carrier density in the system.

In semiconductor based heterostructures consisting of GaAs and GaAlAs layers, a two–dimensional electron gas of high mobility can be produced at the interface by properly doping the different materials. Depleting this electron gas by applying negative voltages to metallic gates on top of the sample which are separated from the electron gas by insulating layers, ultrasmall islands or quantum dots being weakly connected to leads can be formed [36]. Even the height of the barriers can be tuned by changing the voltages.

The electron density in semiconductors of reduced dimensionality is considerably lower than in metallic systems and even the excitation energies for a fixed number of particles can exceed the thermal energy at mK–temperatures which are available in ^{3}He–^{4}He dilution refrigerators. At bias voltages V larger than the differences between discrete excitation energies within the dot, a characteristic splitting of the conductance peaks emerges [24, 28, 29, 30, 31, 33, 34, 35]. We shall demonstrate unambiguously that this is related to transport involving transitions between the excited states of n and $n+1$ correlated electrons. The shape of the peaks depends strongly on the coupling between the quantum dot and the leads. Additional steps in the current occur when V is increased. This allows to investigate experimentally the spectrum of the energy levels of the excited states of a quantum dot [28, 29].

However, the current is not necessarily increased when, by increasing V, the number of transitions between n and $n-1$ electron states increases. Spin selection rules can suppress certain transitions and thus reduce the current. This happens if the electrons in the dot are spin–polarized, and the total spin $S = n/2$ takes its maximum value. Then, the electron number can only be decreased by simultaneously reducing the total spin [25]. Thus, regions of negative differential conductance occur due to a 'spin blockade' which is a consequence of the existence of excited states with different spins [25, 111, 112, 113]. The existence of such regions has been seen in recent experiments [24, 29]. Transport was investigated also in the presence of a magnetic field parallel to the current [24, 32]. Recently, negative differential conductances have also been found in the transport through a two–dimensional dot with parabolic confinement in the fractional quantum Hall effect (FQHE) regime without spin [114], where the origin of the effect are excited states for which the coupling to the leads is weaker than for the ground state.

Chapter 8

Model

8.1 The tunneling Hamiltonian

For systems in which particles can be in different spatial areas and where the coupling between the areas is very weak via high and/or wide tunneling barriers (as indicated in Figure 8.1), it was proposed to use the so–called tunneling Hamiltonian [66] which consists of a sum of terms describing the particles in the classically allowed areas and operators transferring particles between them. This kind of Hamiltonian has serious problems [67] because it is not possible to deduce it unambiguously from first principles using a model for the barrier potential. Only in lowest order in the tunneling some justification is possible.

However the tunneling Hamiltonian is very successful in describing situations with weak couplings and it allows to treat the tunneling in standard time dependent perturbation theory. Further, the different regions can be treated first as isolated problems and it is possible to account for interactions only in some of them. This treatment is an expansion in the small tunneling terms valid only for very weak coupling where the Hamiltonian can be justified.

As a model for a dot which is connected weakly to two semi–infinite leads (Figures 8.1 and 8.2), we consider therefore the double barrier Hamiltonian

$$H = H_{\mathrm{L}} + H_{\mathrm{R}} + H_{\mathrm{D}} + H_{\mathrm{L}}^{\mathrm{T}} + H_{\mathrm{R}}^{\mathrm{T}} + H_{\mathrm{Ph}} + H_{\mathrm{ep}}\,. \tag{8.1}$$

8.1.1 The semi–infinite leads

The terms

$$H_{\mathrm{L/R}} = \sum_{k,\sigma} \varepsilon_k^{\mathrm{L/R}} c^+_{\mathrm{L/R},k,\sigma} c_{\mathrm{L/R},k,\sigma} \tag{8.2}$$

describes free electrons in the left/right lead. The operators $c^+_{\mathrm{L/R},k,\sigma}$ and $c_{\mathrm{L/R},k,\sigma}$ create and destroy electrons with wave vector k and spin σ in the left/right lead, respectively.

The leads are assumed to be always large enough to be considered as reservoirs and we take them in thermal equilibrium described by the Fermi–Dirac distributions

$$f_{\mathrm{L/R}}(\varepsilon) = \frac{1}{\exp[\beta(\varepsilon - \mu_{\mathrm{L/R}})] + 1}\,. \tag{8.3}$$

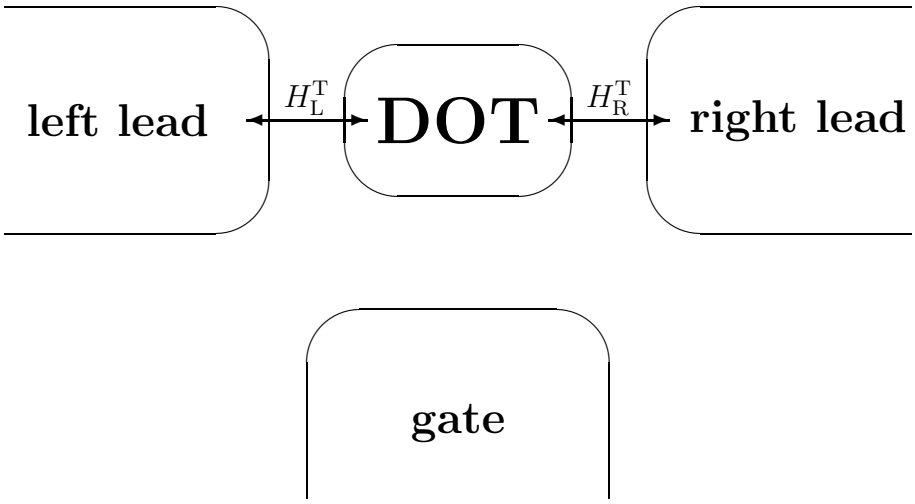

Figure 8.1: Schematic picture of the quantum dot, the left/right and the gate electrode. The tunneling junctions are modeled by the terms $H_{\mathrm{L/R}}^{\mathrm{T}}$.

The chemical potential in the left/right lead is given by $\mu_{\mathrm{L/R}}$ and $\beta = 1/k_{\mathrm{B}}T$ is the inverse temperature.

8.1.2 The effective Hamiltonian of the quantum dot

The general form for the effective Hamiltonian describing the interacting electrons with spin $\sigma = \pm 1/2$ inside the dot is

$$\begin{aligned} H_{\mathrm{D}} &= \sum_{m,\sigma} (\varepsilon_m - e\Phi + g\mu_{\mathrm{B}} B\sigma) c^+_{m,\sigma} c_{m,\sigma} \\ &+ \sum_{\substack{m_1,m_2,m_3,m_4 \\ \sigma_1,\sigma_2,}} V_{m_1 m_2 m_3 m_4}\, c^+_{m_1,\sigma_1} c^+_{m_2,\sigma_2} c_{m_3,\sigma_2} c_{m_4,\sigma_1}\,. \end{aligned} \tag{8.4}$$

Electrons in the noninteracting single–electron states m of the dot are created/destroyed by $c^+_{m,\sigma}/c_{m,\sigma}$. The magnetic field B is taken into account by the Zeeman term in the first summation. The energies of the noninteracting electrons are ε_m and $V_{m_1 m_2 m_3 m_4}$ the matrix–elements of the spin independent Coulomb interaction.

The interactions between the electrons outside the dot are neglected. There, we assume the electron density to be high enough that due to screening, we can effectively use a single–particle picture. The interactions between electrons in the dot and electrons in the leads and in the gate–electrode, respectively, are reduced to an influence of the voltages applied to the electrodes on the electrostatic potential Φ inside the dot (See Appendix B). The simplified situation is visualized in Figure 8.3 and seems to be a quite realistic

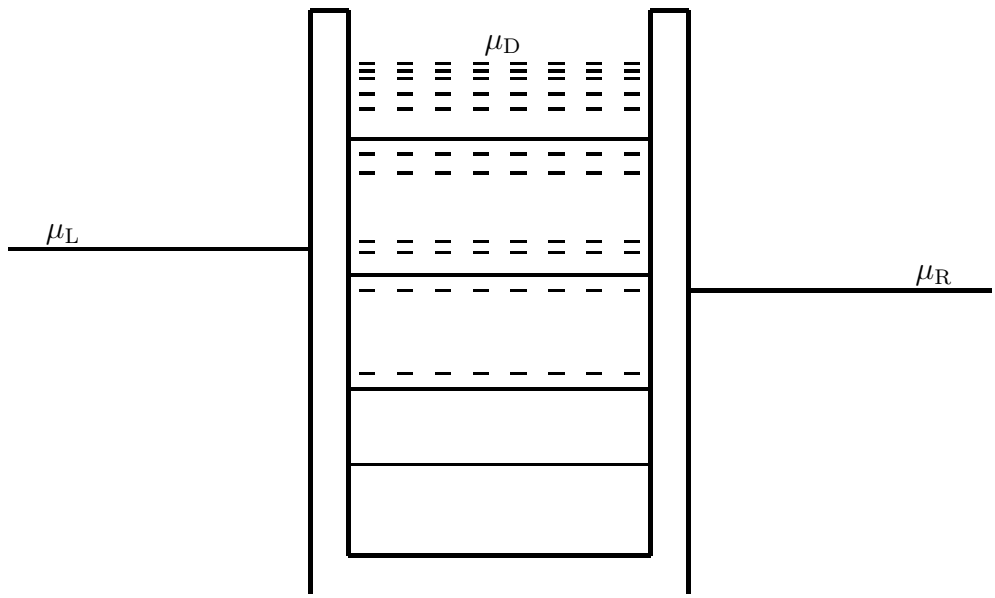

Figure 8.2: The double barrier potential model. There are electrons at both sides of the structure up to the chemical potentials $\mu_{\rm L/R}$. In the dot, energy differences between discrete states corresponding to subsequent electron numbers are indicated. Solid lines stand for ground state to ground state energy differences while dashed lines involve excited many–electron levels.

model for recent experiments [28]. From the assumption that the gate as well as the leads are capacitively coupled to the dot, we find the potential change in the dot due to the gate–voltage $V_{\rm G}$ and the transport voltages to be

$$\Phi = \frac{C_{\rm G}V_{\rm G} + C_{\rm L}V_{\rm L} + C_{\rm R}V_{\rm R}}{C_{\rm G} + C_{\rm L} + C_{\rm R}}\,, \tag{8.5}$$

where the voltages applied to the leads are connected to the chemical potentials by $\mu_{\rm L/R} = -eV_{\rm L/R}$ and the transport or bias voltage is $V = V_{\rm R} - V_{\rm L}$. The C's are the capacitances of the tunnel junctions and the gate capacitor, respectively. In the experiments, their ratios can be determined from the relative changes of voltages when following one conductance peak (see Section 12.7). In our theory their values lead to an influence of the chemical potentials on the eigenenergies of the dot. For all our calculations, we set $C_{\rm G} = C_{\rm L} = C_{\rm R}$. Other values just lead to a renormalization of the voltage scales.

In this procedure, we have implicitly assumed the form of the electronic wave functions within the dot not to be influenced by the applied voltages. This means that the voltage between the leads drops in the barriers without changing the potential landscape and only the electron number dependent energy $-en\Phi$ has to be added. This simplifies the calculation of the energies of the dot states considerably, since the dependence on the

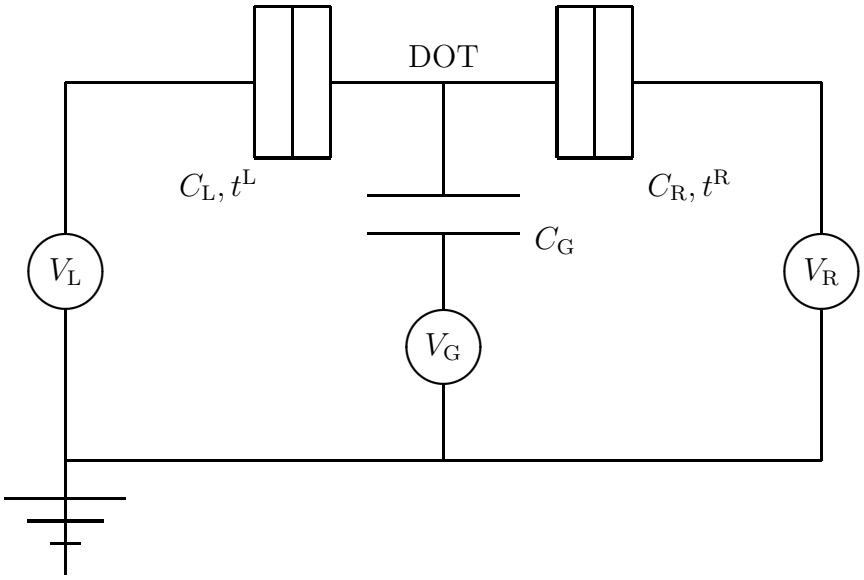

Figure 8.3: Equivalent circuit for the experimental setup we have in mind. The dot region is coupled capacitively to a gate. The tunneling barriers are assumed to behave as (weakly transmissive) capacitors.

voltages becomes trivial and the computation of the interacting many–electron states has to be done only once.

Formally, we can state that the Hamiltonian at $\Phi = 0$ and $B = 0$

$$\begin{aligned} H_{\rm D}^{\Phi=0,B=0} &= \sum_{m,\sigma} \varepsilon_m \, c^+_{m,\sigma} c_{m,\sigma} \\ &+ \sum_{\substack{m_1,m_2,m_3,m_4 \\ \sigma_1,\sigma_2,}} V_{m_1 m_2 m_3 m_4} \, c^+_{m_1,\sigma_1} c^+_{m_2,\sigma_2} c_{m_3,\sigma_2} c_{m_4,\sigma_1} \end{aligned} \tag{8.6}$$

commutes with both, the potential energy term

$$H_\Phi = \sum_{m,\sigma} (-e\Phi) c^+_{m,\sigma} c_{m,\sigma} \tag{8.7}$$

and the Zeeman energy term

$$H_B = \sum_{m,\sigma} g\mu_{\rm B} B\sigma c^+_{m,\sigma} c_{m,\sigma}. \tag{8.8}$$

Therefore, the two latter contributions do not change the electronic eigenstates of the dot but they do influence the eigenenergies. The full energy of the many–electron eigenstate $\mid \Psi_i^{\rm D} \rangle$ is then given by

$$E_i(\Phi, B) = E_i(\Phi = 0, B = 0) - e\Phi n_i + g\mu_{\rm B} B M_i \tag{8.9}$$

where n_i is the number of electrons in the dot and M_i the total magnetic quantum number of the correlated state.

8.1.3 Coupling to phonons

Further we couple the electronic system to a bosonic heat bath described by

$$H_{\rm Ph} = \sum_q \hbar\omega_q (a_q^+ a_q \ + \frac{1}{2}) \, . \tag{8.10}$$

A phononic heat bath and a Fröhlich type coupling [55]

$$H_{\rm ep} = \sum_{q,m_1,m_2,\sigma} \sqrt{g(q,m_1,m_2)} c^+_{m_1,\sigma} c_{m_2,\sigma} (a_q \ + a^+_{-q}) \tag{8.11}$$

where $\sqrt{g}$ is the coupling matrix element while a_q^+ and a_q creates and destroys phonons with wave vector q, respectively, is a microscopic model leading to such a term. For simplicity, we assume the product of the matrix element $g(q,m_1,m_2)$ and the density of bosonic states $\rho_{\rm ph}(q)$ to be independent of q, m_1 and m_2. This coupling to phonons allows for transitions between the dot levels without changing the electron number.

Further, we assume that the phase coherence between the eigenstates of H is destroyed on the time scale of the phase coherence time τ_φ, which is much larger than the semiclassical time an electron needs to travel from one barrier to the other[1]. Thus, the motion of the electrons inside the dot is sufficiently coherent to have Fabry–Perot like interference effects and therefore to allow for the existence of quasi–discrete levels.

8.1.4 Tunneling between the leads and the dot

The barriers are represented by the tunneling Hamiltonians

$$H^{\rm T}_{\rm L/R} = \sum_{k,m,\sigma} \left(T^{\rm L/R}_{k,m} c^+_{{\rm L/R},k,\sigma} c_{m,\sigma} + h.c. \right) \, , \tag{8.12}$$

where $T^{\rm L/R}_{k,m}$ are the transmission probability amplitudes. Within WKB, their dependence on energy might be approximated by

$$\mid T(\varepsilon) \mid^2 \propto \exp\left[-2b\sqrt{2m^*(V_{\rm max}-\varepsilon)}/\hbar \right] \, , \tag{8.13}$$

where m^* is the effective mass of the electron, $V_{\rm max}$ is the height and b the width of the barrier. However, the barrier height should always be much larger than the energy of the electron and we do not want to specify the properties of the barrier. To investigate the effects that are due to properties of the dot, we assume the transmission probability amplitudes in (8.12) to be independent of k, m and spin.

For simplicity, we take the tunneling rates through the barriers

$$t^{\rm L/R} = \frac{2\pi}{\hbar} \sum_k \left| T^{\rm L/R}_{k,m} \right|^2 \delta(\varepsilon^{\rm L/R}_k - E) \approx \frac{2\pi}{\hbar} \left| T^{\rm L/R} \right|^2 \rho^{L/R}(E) \tag{8.14}$$

[1]It is well known that strong dissipation can suppress tunneling [124]. This choice for the phase breaking rate τ_φ^{-1} guarantees that the renormalization of the tunneling rates through the barriers is negligible.

to be independent on energy E. The tunneling rates are a property of the barriers and in the limit of high barriers that is taken always in this work, only a slight energy dependence is expected. For simplicity and because we are not interested in the influence of this effect, we fix them to constant values.

If they are small as compared to the phase breaking rate τ_φ^{-1}, the phase correlations between subsequent tunneling processes need not to be taken into account. This is consistent with neglecting the k–dependence of the tunneling matrix elements. In this case, the nondiagonal elements of the reduced density matrix of the dot decay fast on the timescale of the tunneling events. The time evolution of the occupation probabilities of the many–electron states in the dot can be calculated using a master equation formalism taking into account only the effective transition rates between their diagonal elements P instead of the full von Neumann equation. The treatment of the von Neumann equation was mentioned before [115], but carried out only in special cases. In other words, our aim is to deal with sequential tunneling which yields the main effects in some of the experiments involving quantum dots. Our method is very well suited for this but does not allow us to take into account resonant tunneling.

Chapter 9

Method

We trace back the electronic transport through a quantum dot to transitions between many–electron eigenstates of the isolated dot corresponding to different electron numbers. These transitions are due to the weak coupling to the leads, where electrons can tunnel between the leads and the dot. Since the coupling is very weak, the transport properties are governed mainly by properties of the isolated dot and we can treat the tunneling terms in the Hamiltonian as a perturbation. They allow to transfer transfer electrons between the leads and the dot and therewith for transitions between the quantum mechanical eigenstates. These transitions are always connected with electron transport between the leads and the dot.

Our strategy consists of several steps. First, we determine the spectrum of the isolated dot. Then, we calculate the effective transition rates between the eigenstates of the isolated dot H_{D} using lowest order perturbation theory in the tunneling terms $H_{\mathrm{T}}^{\mathrm{L/R}}$ and the coupling to the bosonic heat bath H_{ep}. These rates strongly depend on temperature and on the voltages applied to the leads and the gate.

Finally we determine the current through the system by counting the electron tunnel processes out of the dot through one of the barriers and subtracting the tunneling processes into the dot through the same barrier.

Selfenergy contributions due to the coupling to the leads which would appear in higher orders in the tunneling term [53] and lead to a finite width of the conductance peaks at zero temperature are not taken into account. This means that the lineshape of our peaks is dominated by the finite width of the step in the Fermi–Dirac distributions which is correct for tunneling rates lower than the temperature $\hbar t^{\mathrm{L/R}} \ll k_{\mathrm{B}}T$. This is consistent with the assumption of weak coupling and the treatment of the tunneling terms as a perturbation to the isolated dot. In addition, in the experimental situation it is possible to tune the barriers such that the intrinsic linewidth due to the finite tunneling rate is negligible as compared to the broadening due to finite temperature [12, 36].

This is similar to an earlier approach [116] where linear transport properties and small deviations from equilibrium are addressed without considering spin effects. In contrast to [117, 118], where changes in the occupation probabilities for one–electron levels were considered, we take into account the populations P_i of all possible many–electron Fock states $\mid \Psi_i^{\mathrm{D}} \rangle$ of H_{D}. This allows to use of a more realistic model than the phenomenological charging model for the electron–electron interaction and to include spin selection rules

directly.

9.1 Energy spectrum

We start from the isolated dot and determine first the many–electron Fock states $\mid \Psi_i^{\mathrm{D}} \rangle$ of H_{D}. Each of the states $\mid \Psi_i^{\mathrm{D}} \rangle$ is associated with a certain electron number n_i, with an energy eigenvalue E_i and eventually with the total spin S_i and the magnetic quantum number M_i of the electrons in the dot. To do this, we have to specify a model for the quantum dot. The different models we use will be discussed in the following chapters together with the corresponding transport properties.

To be specific, we will deal in Chapter 10 with a simple Anderson model, consisting of two levels on one site with an on–site interaction term. Further, we shall discuss the phenomenological charging model in Chapter 11 where the electron–electron interaction is reduced to an electron number dependent additional energy term in the Hamiltonian. In these cases the determination of the dot spectra is easy.

To overcome the restrictions of the charging model, we will use a model of correlated electrons in a quasi–one dimensional dot including their spins in Chapter 12. For up to four Coulombically interacting electrons, the corresponding Hamiltonian has been diagonalized numerically [84, 119, 120] and the wave functions [135]. In the limit of low charge density, the most important energetically low energy excitations of the dot can be understood analytically in the framework of a pocket state description [121] where results have been obtained for up to six electrons. This method can also be applied to interacting electrons in a square shaped quasi–two dimensional dot [121]. We deal with the corresponding transport properties in Chapter 14.

In all cases we use the spectrum of the many–electron states in order to determine the nonlinear transport properties.

9.2 Transitions between many–electron states and electronic transport

Transitions between states with different electron number occur when an electron tunnels through a barrier while transitions between states with the same electron number are induced by the inelastic relaxation term H_{ep} of the Hamiltonian (8.1). Transitions between dot states that are connected with a change in the electron number of the dot are directly related to electronic transport. The electron that is added to or removed from the dot tunnels between the dot and one of the leads. Transport occurs when electrons induce transitions by entering mainly from one side and leaving to the other yielding a net current.

From very general considerations one can find some conditions for a transition to contribute to the current at $T = 0$.

- Energy has to be conserved (see Appendix C). Thus, an electron tunneling to the dot has to carry the energy difference $E = E_j - E_i$ between the many–electron states ($n_j = n_i + 1$). The transition can occur only if the chemical potential in the

involved lead is higher than E. Similarly, electrons that tunnel out of the dot need an empty state in a lead. Such processes can happen if the chemical potential in this lead is below E.

- In order to contribute to the current, transitions must be possible in the direction of increasing electron number induced by tunneling electrons from one side and the decrease must be possible by tunneling through the other barrier. At $T = 0$ this yields the condition $\max(\mu_{\rm L}, \mu_{\rm R}) > E > \min(\mu_{\rm L}, \mu_{\rm R})$.

- The transition between the ground states of the same electron numbers has to be in the energy window between the chemical potentials. Otherwise, the system will decay to one of the ground states and be blocked there. Only at very high voltages outside the SET regime, when transitions to more distant electron numbers are possible, also excited levels can be continuously occupied without significant population of the corresponding ground state.

- The states involved in the transition must be reachable by allowed transitions starting from one of the ground states of the corresponding electron numbers. Otherwise, the transition is 'disconnected' and cannot contribute to the current because none of the states is ever occupied.

From these rules, a rough understanding of the behavior of the system can be achieved and some of the effects can be explained qualitatively. It is nevertheless necessary to perform a quantitative investigation in order to find all of the features.

9.3 Transition rates

Due to the smallness of $H^{\rm T}$, simultaneous transitions of two or more electrons [122, 123] which are processes of higher order in $H^{\rm T}$ are strongly suppressed. We neglect them consistent with the tunneling Hamiltonian itself being an approximation for the behavior of a tunneling barrier holding only for almost impenetrable barriers [67].

In lowest order in the tunneling Hamiltonian $H^{\rm T}$, only one–electron processes occur. Further selection rules will be specified below. The transition rates between states $\mid \Psi_i^{\rm D}\rangle$ and $\mid \Psi_j^{\rm D}\rangle$ with $n_j = n_i + 1$ are denoted by $\Gamma_{i,j}^{\rm L/R,-}$ and $\Gamma_{j,i}^{\rm L/R,+}$, depending on whether an electron is leaving or entering the dot through the left/right barrier, respectively. Here, Fermi's golden rule or standard time dependent perturbation theory (see Appendix C) yields the rates

$$\begin{aligned}
\Gamma_{i,j}^{\rm L/R,-} &= \frac{1}{2}\left|\langle S_j, M_j, \frac{1}{2}, \pm\frac{1}{2} \mid S_i, M_i\rangle_{CG}\right|^2 t^{\rm L/R}[1 - f_{\rm L/R}(E)]\delta_{n_i,n_j-1}\,, \\
\Gamma_{j,i}^{\rm L/R,+} &= \frac{1}{2}\left|\langle S_i, M_i, \frac{1}{2}, \pm\frac{1}{2} \mid S_j, M_j\rangle_{CG}\right|^2 t^{\rm L/R} f_{\rm L/R}(E)\delta_{n_j,n_i+1}\,. \qquad (9.1)
\end{aligned}$$

The electron has to provide the energy difference $E = E_j - E_i$ between the energies of the many–electron states and the Clebsch–Gordan coefficients $\langle \ldots \rangle_{CG}$ arise from the consideration of the spin Hilbert space.

They introduce new spin selection rules for transitions between the dot states, the factor 1/2 accounting for the reduced density of states for a given electronic spin in the leads. In particular, transition rates between states whose difference in total spin or in the magnetic quantum number is not 1/2 vanish because the corresponding Clebsch–Gordan coefficients are zero. The numerical values of the squares of the Clebsch–Gordan coefficients are listed in Table 12.2.

The orbital part of the matrix element connected to the transition of the dot has been neglected in (9.1), but the important and very general spin part, which does not depend on the microscopic details of the sample, is kept and has crucial consequences when considering the models of correlated electrons.

Assuming a bosonic heat bath to be weakly coupled to the electrons, the (inelastic) transition rate between $\mid \Psi_i^{\mathrm{D}}\rangle$ and $\mid \Psi_j^{\mathrm{D}}\rangle$ (now states with the same electron number $n_i = n_j$, the same total spin $S_i = S_j$ and the same magnetic quantum number $M_i = M_j$) induced by H_{ep} is given by (see Appendix C)

$$\Gamma_{j,i}^{\mathrm{in}} = r[n_{\mathrm{B}}(|E|) + \Theta(E)]\,, \tag{9.2}$$

where we choose the product $r = g\,\rho_{\mathrm{ph}}$ to be constant for simplicity. This is the lowest order result quadratic in the electron–heat bath coupling strength $\sqrt{g}$. Here, ρ_{ph} is the boson density of states, and

$$n_{\mathrm{B}}(E) = \frac{1}{\exp(\beta E) - 1} \tag{9.3}$$

is the Bose–Einstein distribution.

The requirement of energy conservation during the tunneling process must not be fulfilled exactly in the presence of a bosonic heat bath [124] but we assume the coupling to the leads as well as to the phonons to be weak enough such that we can neglect the modifications of the tunneling due to dissipation. In our case the energy is dissipated in the reservoirs connected to the leads or due to electron–phonon processes in the dot. Thermal equilibrium in the leads is implicitly assumed by writing a Fermi–Dirac distribution for the occupation probabilities of the electronic levels there.

The full matrix of transition rates is the sum of all the contributions from the electronic tunneling processes through both of the barriers and the electron–phonon scattering processes

$$\Gamma = \Gamma^{\mathrm{L},+} + \Gamma^{\mathrm{R},+} + \Gamma^{\mathrm{L},-} + \Gamma^{\mathrm{R},-} + \Gamma^{\mathrm{in}}\,. \tag{9.4}$$

9.4 Occupation probabilities and the current

With these transition rates, we can write the master equation for the time evolution of the occupation probabilities P_i of the many–electron dot states

$$\frac{d}{dt}P_i = \sum_{j\,(j\neq i)} (\Gamma_{i,j}P_j - \Gamma_{j,i}P_i) \tag{9.5}$$

where the solutions have to satisfy the normalization condition

$$\sum_i P_i = 1\,. \tag{9.6}$$

This rate equation can be regarded as governing the propagation of one particle in a network of sites that represent the many–electron states of the dot. The connections between these sites are the possible transitions while the rates depend on the applied voltages.

Setting the left hand side of (9.5) to zero, and solving the system of linear equations

$$0 = \sum_{j\,(j\neq i)} (\Gamma_{i,j} P_j - \Gamma_{j,i} P_i) \tag{9.7}$$

for the occupation probabilities, one gets the stationary non–equilibrium populations $\bar{P}_i$ satisfying $d\bar{P}_i/dt = 0$.

Our method allows to determine the stationary non–equilibrium populations of all the states without further restrictions. While deviations from equilibrium linear in the applied voltage have been mentioned in [116], we can calculate exactly the occupation probabilities of all the many–electron states for arbitrary bias voltage.

In addition the exact many–electron states of the dot including spin can be taken into account without being restricted to the conventional charging model. A similar method was applied in the FQHE regime without spin [114].

However, the validity of the rate equation description (9.5) depends crucially on the presence of additional phase randomizing processes. They should provide the truncation of the density matrix to its diagonal elements (which are the populations P_i) on time scales τ_φ shorter than the lifetimes $(\sum_j \Gamma_{ji})^{-1}$ of individual states.

One determines the dc–current

$$I \equiv I^{\mathrm{L/R}} = (-/+)e \sum_{i,j\,(j\neq i)} \bar{P}_j (\Gamma_{i,j}^{\mathrm{L/R},-} - \Gamma_{i,j}^{\mathrm{L/R},+}) \tag{9.8}$$

by considering one of the barriers separately. The first term in (9.8) contains only processes where an electron leaves the dot through the left/right barrier, while in the second term processes involving electrons that enter the dot through the same barrier are subtracted.

Since we calculated the stationary occupation probabilities of the dot states which enter (9.8) using the full matrix of transition rates, including the contributions of tunneling through the other barrier, this equals the number of electrons that pass the system per unit of time. In the stationary limit, no currents that charge or discharge the dot can be flowing. Therefore the system is in dynamic equilibrium and the current through the left barrier equals the current through the right barrier and thus the current through the whole system.

9.5 Numerical solution of the stationary rate equation

The stationary rate equation (9.7) is a system of linear equations. The number of equations D equals the number of many–electron states of the dot being taken into account. Thus, for all but the simplest cases, (9.7) has to be solved numerically.

We rewrite it in the form

$$0 = \sum_{j=1}^{D} \Xi_{i,j} P_j \tag{9.9}$$

with the matrix

$$\Xi_{i,j} = \Gamma_{i,j} - \delta_{i,j} \sum_{k=1}^{D} \Gamma_{k,j} \,. \tag{9.10}$$

For physical reasons, there must exist a solution to (9.9) with nonzero stationary populations. Thus, the rank of Ξ is less than its dimensionality D.

We simply replace the first line of (9.9) by the normalization condition (9.6) setting

$$\Xi_{1,j} = 1 \tag{9.11}$$

and writing the new equation

$$\delta_{1,i} = \sum_{j=1}^{D} \Xi_{i,j} P_j \tag{9.12}$$

instead of (9.9).

Then, the inhomogeneous system of equations (9.12) has an unique normalized solution that is determined in a FORTRAN program using the NAG routine F04ARF (Appendix D). The computations have been performed on the CYBER 2000 supercomputer at the PTB in Braunschweig and on the DEC ALPHA workstation at the university of Hamburg.

At very low temperatures, some of the transition rates are exponentially small. This leads to numerical problems when the precision of the calculation no longer allows to distinguish them from zero. In some parameter ranges, the numerical realization of Ξ can contain so many zeroes that a unique solution of (9.12) becomes impossible. Then, some of the states do not contribute and the method can be used after the truncation of the basis to the important many–electron levels.

Chapter 10

Anderson Impurity

As a first step we consider the simplest nontrivial case of transport of spinless electrons through an Anderson impurity [126] which consists of two one–electron states and a Hubbard like interaction term providing a 'charging energy' U when both of the levels are occupied. Here, an analytical solution for the stationary occupation probabilities is possible. It is very instructive to demonstrate our method to determine the nonlinear transport properties using this simple example and therewith to generalize the results of a previous investigation [53] which is dealing with the linear transport through an Anderson impurity using a Landauer–type conductance formula.

The Hamiltonian for the dot region H_{D} is now given by

$$H_{\mathrm{D}}^{\mathrm{AI}} = (\varepsilon_1 - e\Phi)c_1^+ c_1 \; + (\varepsilon_2 - e\Phi)c_2^+ c_2 \; + U c_1^+ c_1 \, c_2^+ c_2 \; . \tag{10.1}$$

Here, $c_{1/2}^+$ and $c_{1/2}$ create and destroy spinless electrons in the state $1/2$ of the impurity, respectively. The parameter U accounts for the charging energy needed to overcome the Coulomb repulsion when both of the single electron levels are occupied.

In principle it can be calculated as

$$U = \int dx\, dx'\, V(x,x') \; \mid \psi_1(x) \mid^2 \mid \psi_2(x') \mid^2 \tag{10.2}$$

if the wave functions $\psi_m(x)$ of the single electron states in the dot are known and the interaction potential in configuration space $V(x,x')$ is specified. Since these details depend on the specific realization of the sample, we will treat U as a phenomenological parameter.

10.1 Spectrum

First, we have to determine the many–electron Fock states and the corresponding energies of the dot. This is easy because the Hamiltonian (10.1) contains only occupation number operators of the single electron levels. Thus the many–electron eigenstates of 10.1 are nothing but products of single electron states and the energies can be found immediately from the Hamiltonian. All of the many–electron states for the Anderson impurity are listed in Table 10.1.

Table 10.1: Electron numbers n_i, eigenenergies E_i and the eigenstates $\mid \Psi_i^{\mathrm{D}}\rangle$ of the four states for the Anderson model (10.1). The 'vacuum state' $|0\rangle$ denotes the empty dot.

i	n_i	E_i	$\mid \Psi_i^{\mathrm{D}}\rangle$
1	0	0	$\|0\rangle$
2	1	$\varepsilon_1 - e\Phi$	$c_1^+\|0\rangle$
3	1	$\varepsilon_2 - e\Phi$	$c_2^+\|0\rangle$
4	2	$\varepsilon_1 + \varepsilon_2 + U - 2e\Phi$	$c_1^+ c_2^+\|0\rangle$

10.2 Transition rates

Second, we have to find the transition rates arising from electron tunneling processes and electron–phonon scattering. This can be done as described in the Appendix C omitting the spin dependencies. The matrices $\Gamma^{\mathrm{L/R},+}$ can have nonzero elements only for transitions where one single electron enters the dot.

All of these possibilities are the transitions $\mid \Psi_1^{\mathrm{D}}\rangle \rightarrow \mid \Psi_2^{\mathrm{D}}\rangle$, $\mid \Psi_1^{\mathrm{D}}\rangle \rightarrow \mid \Psi_3^{\mathrm{D}}\rangle$, $\mid \Psi_2^{\mathrm{D}}\rangle \rightarrow \mid \Psi_4^{\mathrm{D}}\rangle$ and $\mid \Psi_3^{\mathrm{D}}\rangle \rightarrow \mid \Psi_4^{\mathrm{D}}\rangle$. The transition from $\mid \Psi_i^{\mathrm{D}}\rangle$ to $\mid \Psi_j^{\mathrm{D}}\rangle$ involves an electron which tunnels through the left/right barrier into the dot. Since the process has to satisfy energy conservation, the electron has to provide the energy difference $E = E_j - E_i$ between the states. Therefore, the probability to find an occupied state in the lead at energy E enters into the transition rates via the Fermi–Dirac distribution. For the transition rates, we find the expression

$$\Gamma_{j,i}^{\mathrm{L/R},+} = t^{\mathrm{L/R}} f_{\mathrm{L/R}}(E)\delta_{n_j,n_i+1}\,, \tag{10.3}$$

where the tunneling rates $t^{\mathrm{L/R}}$ contain all the information about the transmittivity of the barriers and the density of states in the leads. The chemical potentials and the temperature enter the Fermi–Dirac distributions $f_{\mathrm{L/R}}$.

The matrices $\Gamma^{\mathrm{L/R},-}$ arise from processes where an electron leaves the dot through one of the barriers. Here, only the inverse transitions from $\mid \Psi_j^{\mathrm{D}}\rangle$ to $\mid \Psi_i^{\mathrm{D}}\rangle$ of the case above can occur and the electron leaving the dot has to find an empty state in the lead. Therefore, these matrices contain the Pauli blocking factors and read

$$\Gamma_{i,j}^{\mathrm{L/R},-} = t^{\mathrm{L/R}}[1 - f_{\mathrm{L/R}}(E)]\delta_{n_i,n_j-1}\,. \tag{10.4}$$

We also have two different states with one electron in the dot between which inelastic relaxation processes involving phonons are possible. The transition rate between these states $\mid \Psi_2^{\mathrm{D}}\rangle$ and $\mid \Psi_3^{\mathrm{D}}\rangle$ is

$$\Gamma_{3,2}^{\mathrm{in}} = r n_{\mathrm{B}}(E) \tag{10.5}$$

for the phonon absorption process, where the population of the bosonic phonon states of energy E is the Bose–Einstein distribution. We find

$$\Gamma_{2,3}^{\mathrm{in}} = r[n_{\mathrm{B}}(E) + 1] \tag{10.6}$$

for the process involving the emission of a phonon. The energy difference is $E = E_3 - E_2$ which we take always positive.

10.3 Stationary occupation probabilities and current

With these informations we can construct the full matrix of transition rates by summing up the contributions from all of the possible processes and find

$$\Gamma = \begin{pmatrix} 0 & \zeta(\varepsilon_1) & \zeta(\varepsilon_2) & 0 \\ \xi(\varepsilon_1) & 0 & r[n_{\rm B}(\varepsilon_2-\varepsilon_1)+1] & \zeta(\varepsilon_2+U) \\ \xi(\varepsilon_2) & rn_{\rm B}(\varepsilon_2-\varepsilon_1) & 0 & \zeta(\varepsilon_1+U) \\ 0 & \xi(\varepsilon_2+U) & \xi(\varepsilon_1+U) & 0 \end{pmatrix}, \tag{10.7}$$

where we have defined the functions

$$\xi(E) := t^{\rm L} f_{\rm L}(E) + t^{\rm R} f_{\rm R}(E)\,, \tag{10.8}$$
$$\zeta(E) := t^{\rm L}[1-f_{\rm L}(E)] + t^{\rm R}[1-f_{\rm R}(E)]\,. \tag{10.9}$$

Now, we can write explicitly the master equation by inserting (10.7) into (9.5)

$$\begin{aligned} \partial P_1/\partial t &= -(\Gamma_{2,1}+\Gamma_{3,1})P_1 + \Gamma_{1,2}P_2 + \Gamma_{1,3}P_3 \\ \partial P_2/\partial t &= \Gamma_{2,1}P_1 - (\Gamma_{1,2}+\Gamma_{3,2}+\Gamma_{4,2})P_2 + \Gamma_{2,3}P_3 + \Gamma_{2,4}P_4 \\ \partial P_3/\partial t &= \Gamma_{3,1}P_1 + \Gamma_{3,2}P_2 - (\Gamma_{1,3}+\Gamma_{2,3}+\Gamma_{4,3})P_3 + \Gamma_{3,4}P_4 \\ \partial P_4/\partial t &= \Gamma_{4,2}P_2 + \Gamma_{4,3}P_3 - (\Gamma_{2,4}+\Gamma_{3,4})P_4 \end{aligned} \tag{10.10}$$

and set the left hand side expressions $\partial P_i/\partial t$ to zero in order to obtain the stationary occupation probabilities $\bar{P}_i$. In this case we have to deal with a system of only four linear equations which can be solved analytically.

The nontrivial solution of the homogeneous equation contains a free parameter which is fixed by the normalization condition $\sum_{i=1}^{4}\bar{P}_i = 1$ for the probabilities. After a lengthy but straightforward calculation, the stationary populations $\bar{P}_i$ with the property $\partial\bar{P}_i/\partial t = 0$ of the four dot states are found to be given by the analytical expressions

$$\begin{aligned} \bar{P}_1 &= (x_1 y + x_2)/\Sigma \\ \bar{P}_2 &= y/\Sigma \\ \bar{P}_3 &= 1/\Sigma \\ \bar{P}_4 &= (x_4 y + x_3)/\Sigma\,, \end{aligned} \tag{10.11}$$

where the abbreviations

$$\Sigma = x_1 y + x_2 + y + 1 + x_4 y + x_3 \tag{10.12}$$
$$y = \frac{\Gamma_{2,1}x_2 + \Gamma_{2,4}x_3 + \Gamma_{2,3}}{\Gamma_{3,1}x_1 + \Gamma_{3,4}x_4 + \Gamma_{3,2}} \tag{10.13}$$
$$x_{\left\{{1\atop 2}\right\}} = \frac{\Gamma_{1,\left\{{2\atop 3}\right\}}}{\Gamma_{2,1}+\Gamma_{3,1}} \tag{10.14}$$
$$x_{\left\{{3\atop 4}\right\}} = \frac{\Gamma_{4,\left\{{3\atop 2}\right\}}}{\Gamma_{3,4}+\Gamma_{2,4}} \tag{10.15}$$

have been introduced.

It can be shown that, independent of the inelastic relaxation rate, the stationary occupation probabilities satisfy a Gibbs distribution

$$P_i^{\mathrm{G}} = (\exp[-\beta(E_i - \mu n_i)])/\mathcal{Z} \tag{10.16}$$

in the equilibrium limit of zero voltage with $\mu = \mu_{\mathrm{L}} = \mu_{\mathrm{R}}$ and the inverse temperature β being equal to the one in the leads, while they can deviate drastically in the general situation.

The final expression for the current

$$\begin{aligned} I &= e\left[(\Gamma^{\mathrm{R},-}_{3,4} + \Gamma^{\mathrm{R},-}_{2,4})\bar{P}_4 + (\Gamma^{\mathrm{R},-}_{1,3} - \Gamma^{\mathrm{R},+}_{4,3})\bar{P}_3\right. \\ &+ \left.(\Gamma^{\mathrm{R},-}_{1,2} - \Gamma^{\mathrm{R},+}_{4,2})\bar{P}_2 - (\Gamma^{\mathrm{R},+}_{2,1} + \Gamma^{\mathrm{R},+}_{3,1})\bar{P}_1\right]. \end{aligned} \tag{10.17}$$

results from plugging (10.11) into (9.8).

10.4 Conductance peaks

As consistent with a recent calculation of the linear transport properties [53], in the (linear response) low voltage limit we find conductance peaks for the situations $\mu_{\mathrm{L}} = \mu_{\mathrm{R}} = \mu = \varepsilon_1 - e\Phi$ and $\mu = \varepsilon_2 + U - e\Phi$, thermally broadened by the finite width of the step of the Fermi functions entering the transition rates.

In reference [53], the current was calculated from a Landauer like formula involving the density of states of the dot. The density of states was determined from the imaginary part of the dot Green's function which was calculated using an equation of motion technique taking the coupling to the leads into account. This yielded a broadening of the peaks of the isolated system due to a selfenergy term to the width $\hbar t = \hbar t^{\mathrm{L}} + \hbar t^{\mathrm{R}}$. At very low temperatures, lower than the Kondo temperature and in the limit $U \longrightarrow \infty$, Kondo peaks in the density of states were found taking into account higher orders of the coupling to the leads [127]. However, it is questionable whether it is consistent to use the tunneling Hamiltonian in situations where higher orders have to be considered.

Anyway, we are working in the parameter regime, in which the coupling to the leads is the lowest energy scale in the system. Then, the Kondo temperature $T_{\mathrm{K}} \propto \sqrt{Ut}$ becomes very small and we will always have $T \gg T_{\mathrm{K}}$. Also, at $\hbar t^{\mathrm{L}}, \hbar t^{\mathrm{R}} \ll k_{\mathrm{B}}T$ the broadening due to the finite coupling to the leads is negligible as compared to the effect of finite temperature that leads to a width $k_{\mathrm{B}}T$ of the step at the chemical potential in the Fermi–Dirac functions. In this regime, we can calculate the current through the system for arbitrary voltages.

The conductance peaks as a function of the gate–voltage V_{G} which directly enters in the electrostatic potential Φ (8.5), are broadened at finite transport–voltage $V = (\mu_{\mathrm{L}} - \mu_{\mathrm{R}})/e$. Current can flow as long as a ground state to ground state transition energy E for transitions between adjacent electron numbers in the impurity (here $E = E_2 - E_1$ or $E = E_4 - E_2$) is between the chemical potentials in the leads. In the other case, the system remains in the stable ground state from which no transition is possible and transport is blocked (Coulomb blockade). At finite voltage the condition

$$\mu_{\mathrm{L}} \geq E \geq \mu_{\mathrm{R}} \tag{10.18}$$

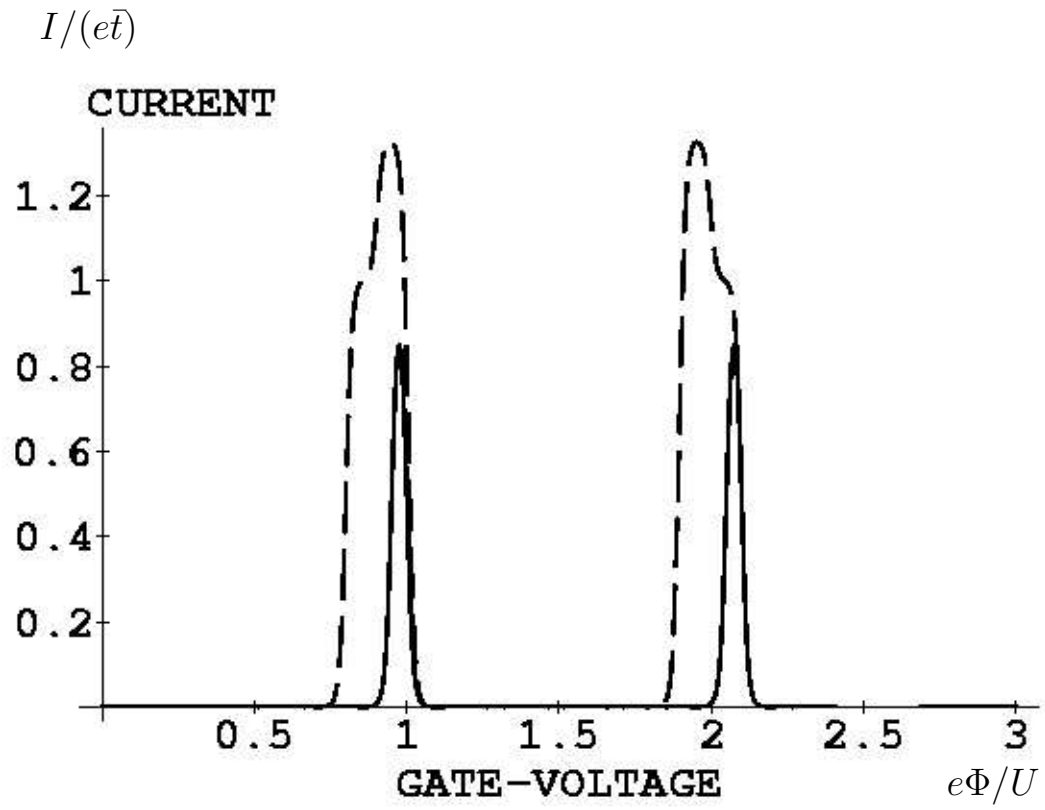

Figure 10.1: Conductance peaks in the transport through an Anderson impurity as a function of the gate–voltage. The energies of the single–electron levels are $\varepsilon_1 = U$ and $\varepsilon_2 = 1.1U$ and the transmittivities of the barriers have been chosen symmetric as $t = t_{\rm L} = t_{\rm R}$. The temperature $k_{\rm B}T = 0.01U$ is chosen considerably smaller than the level spacing. The right chemical potential is fixed at $\mu_{\rm R} = 0$ and the bias voltage is $eV = 0.02U$ and $eV = 0.2U$ for the solid and the dashed line, respectively. The current is given in units of the total transmission rate $\bar{t} = t^{\rm L}t^{\rm R}/(t^{\rm L} + t^{\rm R})$. The results are shown for $r = 0$.

is fulfilled for a nonvanishing interval of gate–voltage.

If the voltage is in the range of the excitation energies of the dot, high enough that in addition to the ground state to ground state transition also transitions between excited states that correspond to different electron numbers can fulfill (10.18), additional structure appears. The value of the current changes as the number of available transitions is altered.

This can be seen in Figure 10.1, where the conductance peaks are shown for different voltages. Since in the simple example of the Anderson impurity, we have only two states of the same electron number $n_2 = n_3 = 1$, the structure appearing at $eV \geq E_3 - E_2$ consists of one additional step representing the added transition involving only the excited state $\mid \Psi_3^{\rm D}\rangle$. The first peak corresponds to the transitions between the state $\mid \Psi_1^{\rm D}\rangle$ with $n_1 = 0$ electrons in the dot and the states $\mid \Psi_2^{\rm D}\rangle$ and $\mid \Psi_3^{\rm D}\rangle$ with $n_2 = n_3 = 1$ electron. First the ground state to ground state transition is moved between the chemical potentials and

carries current.

The second step arises when the gate voltage is raised further and the transition to the excited state enters the window (10.18). As soon as the transition between the ground states is below the lower chemical potential, the system is blocked in the one electron ground state $\mid \Psi_2^{\mathrm{D}}\rangle$ although the transition involving the excited state still fulfills (10.18). There is no way to leave the state $\mid \Psi_2^{\mathrm{D}}\rangle$ until the gate–voltage is raised to a value for which the transition to the two electron state $\mid \Psi_4^{\mathrm{D}}\rangle$ becomes available for transport.

Since the ground state to ground state transition between $\mid \Psi_2^{\mathrm{D}}\rangle$ and $\mid \Psi_4^{\mathrm{D}}\rangle$ is energetically higher than the transition involving the excited state $\mid \Psi_3^{\mathrm{D}}\rangle \longleftrightarrow \mid \Psi_4^{\mathrm{D}}\rangle$, immediately both transitions come into play and the current is increased to the maximum value. On the other side of the peak, however, the current decreases in two steps because the transition involving the excited state is pulled out of the range between the chemical potentials before the ground state to ground state transition leaves this window given in (10.18). For the models of the quantum dot consisting of more single electron levels the conductance peaks will show more structure due to different numbers of transitions involved.

10.5 Current–voltage characteristic

Figure 10.2 shows the current–voltage characteristic obtained from the exact solution for the current (10.17) through an Anderson impurity. At temperatures low enough to resolve the difference between the two one–electron levels, we observe finestructure in addition to the usual Coulomb steps which occur when the states with the next electron number become accessible.

The first step occurs when the lower of the states with $n_i = 1$ can be occupied and the transition between states $\mid \Psi_1^{\mathrm{D}}\rangle$ and $\mid \Psi_2^{\mathrm{D}}\rangle$ is responsible for the increase of the current, the transition energy $E_2 - E_1$ lying now between the chemical potentials in the leads. If the voltage is increased further, the transition between the states $\mid \Psi_1^{\mathrm{D}}\rangle$ and $\mid \Psi_3^{\mathrm{D}}\rangle$ can come into this range too and therefore contribute to the current. Since the empty dot can now be filled in two ways, the rate to add an electron from the side where the chemical potential is high enough is enhanced and a second step appears in the current.

The second Coulomb step appears when the transitions between the states with one and two electrons become accessible. First, the transition $\mid \Psi_3^{\mathrm{D}}\rangle \longrightarrow \mid \Psi_4^{\mathrm{D}}\rangle$ involving the excited state is opened and contributes to the current because the corresponding energy difference is lower than for the ground state to ground state transition. Then, the higher step announces the occupation of the (ground) state for $n = 2$.

10.6 Influence of the inelastic relaxation rate

It is tempting to define a voltage–dependent effective inverse temperature

$$\beta_{ij} = \frac{\ln(P_i/P_j)}{E_j - E_i - \mu_{\mathrm{eff}}(n_j - n_i)} \tag{10.19}$$

of the dot from the assumption that for the stationary occupation probabilities a Gibbs distribution holds with an effective chemical potential μ_{eff}. However, in general this

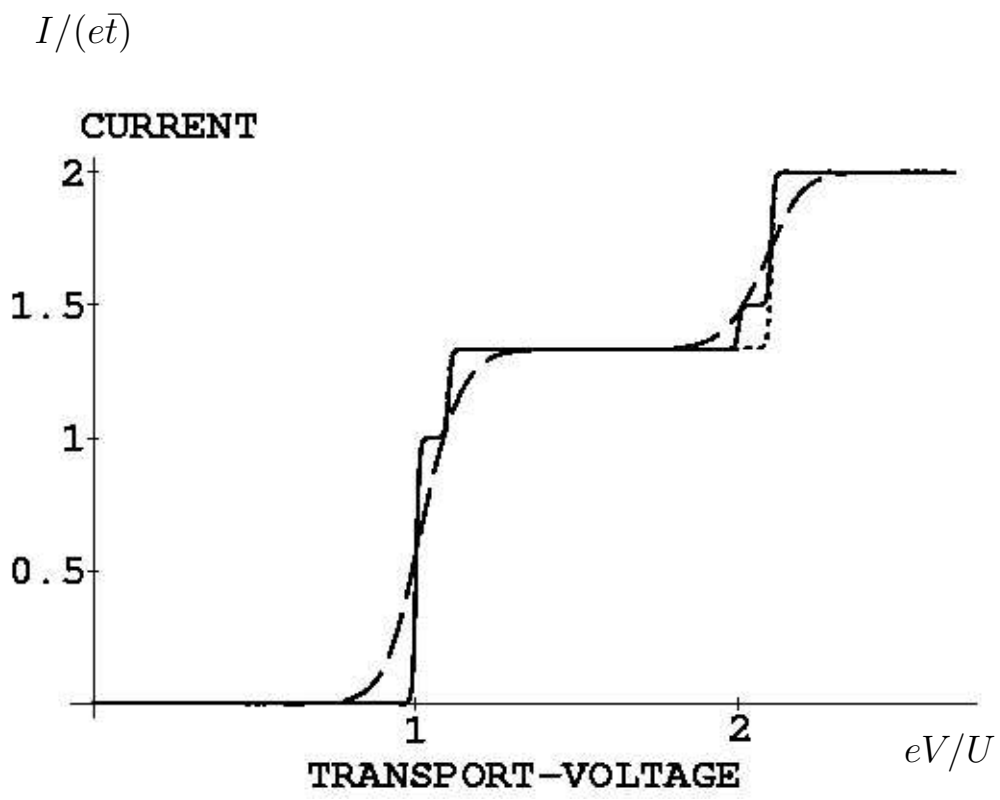

Figure 10.2: Current–voltage characteristic for the transport through an Anderson impurity. The parameters are chosen as in Figure 10.1. The chemical potential in the right lead and the electrostatical potential are always fixed at $\mu_{\rm R} = \Phi = 0$ while the left chemical potential is varied. Temperatures are $k_{\rm B}T = 0.005\,U$ and $k_{\rm B}T = 0.05\,U$ for the solid and the dashed line, respectively. While the latter curves show the situation for $r = 0$, the dotted line represents $k_{\rm B}T = 0.005U$ and $r = 50t$.

procedure does not lead to a unique temperature [128] $\beta_{\rm eff} = \beta_{12} = \beta_{23} = \beta_{34}$. It can be shown only in the limit of zero voltage that the dot is in thermal equilibrium with $\beta_{\rm eff} = \beta$ and $\mu_{\rm eff} = \mu_{\rm L} = \mu_{\rm R}$. The different effective temperatures usually increase with the transport voltage. However, exceptions to this rule have been found for some of the possible arrangements of the chemical potentials with respect to the single particle levels.

Only for the effective temperature β_{23}, which is defined via the two one–electron states, the equilibrium temperature can be reestablished even at high voltage. This happens, when the inelastic relaxation rate r between the two states becomes much larger than the tunneling rates through the barriers. Then, fast equilibration by the coupling to the bosonic heat bath leads to an equilibrium ratio of the populations. In the limit $r/t \to \infty$, the effective temperature β_{23} tends towards the temperature of the bosonic heat bath.

The only influence of the inelastic relaxation in the current–voltage characteristic appears at the second Coulomb step. The first finestructure step is due to the transition between the states $\mid \Psi_3^{\rm D}\rangle$ and $\mid \Psi_4^{\rm D}\rangle$ while after the second step, the transition between states $\mid \Psi_2^{\rm D}\rangle$ and $\mid \Psi_4^{\rm D}\rangle$ yields an additional contribution because it is possible to access

to the doubly occupied dot from two different initial states.

If the relaxation rate is very high as compared to the tunneling rate through the barrier connecting the dot and the lead with the lower chemical potential, the system relaxes to the lower one–electron state $\mid \Psi_2^{\mathrm{D}} \rangle$ after the first electron has entered the dot. This happens very fast on the timescale of the tunneling out of the dot. Therefore the excited state $\mid \Psi_3^{\mathrm{D}} \rangle$ is almost never occupied on the average. Consequently, the state $\mid \Psi_4^{\mathrm{D}} \rangle$ which can only be reached by transitions starting from $\mid \Psi_3^{\mathrm{D}} \rangle$ in the range

$$E_4 - E_3 \; < \; \max(\mu_{\mathrm{L}}, \mu_{\mathrm{R}}) \; < \; E_4 - E_2 \tag{10.20}$$

cannot be occupied neither. Thus the contribution of the transition between the states $\mid \Psi_3^{\mathrm{D}} \rangle$ and $\mid \Psi_4^{\mathrm{D}} \rangle$ which is responsible for the first finestructure step is suppressed by the influence of the inelastic relaxation in the dot (Figure 10.2).

Chapter 11

The charging model

As a second tutorial example we consider the spinless phenomenological charging model [111] for $B = 0$ used before [116, 117, 118] for N single–electron levels, where

$$V_{m_1 m_2 m_3 m_4} = (U/2)\delta_{m_1,m_4}\delta_{m_2,m_3}\,. \tag{11.1}$$

This means that the electron–electron interaction is taken into account via an enhanced energy depending solely on the number of electrons inside the dot. While in the case of an Anderson impurity the electron–electron interaction is taken into account exactly by enhancing the energy of the only two–electron state, here the parameter U should depend on the electron number in the dot and on the single electron levels between which the interaction is described. Furthermore, the exchange terms are ignored. Only for the metallic case where the electron density is very high and the charge distribution is a structureless function in configuration space, this can be justified. Indeed, the behavior of metallic samples can be very well described using the charging model with a continuum of single–electron levels inside the dot [19].

Taking the interaction matrix element to be constant is a rough approximation for low electron numbers, but nevertheless some of the characteristic features of the behavior can be observed using the charging model which allows to determine the many–electron states trivially. The dot Hamiltonian reads now

$$H_{\mathrm{D}} = \sum_{m=1}^{N} (\varepsilon_m - e\Phi) c_m^+ c_m + \frac{U}{2} \sum_{m_1 \neq m_2} c_{m_1}^+ c_{m_1} c_{m_2}^+ c_{m_2} \tag{11.2}$$

and describes spinless electrons that can occupy N different single electron levels and a phenomenological charging energy term which accounts for the electron–electron interactions between the electrons in the dot.

The transport properties have been investigated within this model using rate equations for the occupation of the single electron levels. While in the first work [117], it was assumed that the relative occupation probabilities of the single–electron levels equal the equilibrium value for states with the same electron number, the populations were calculated correctly in a subsequent paper [118]. Our treatment can be shown to be equivalent to the one in the latter work and has been used before in the same context [116] and in the FQHE regime [114]. It was pointed out that the populations of the many–electron states can

deviate from equilibrium at finite transport voltage V and deviations linear in V have been mentioned [116]. We calculate the populations numerically at arbitrary voltage and present various results for the current–voltage characteristic and the splitting of the conductance peaks.

11.1 Spectrum

Since the dot Hamiltonian still contains only occupation number operators and the interaction term commutes with the term of kinetic energy, the many–electron states can be constructed easily from the single–particle states as Slater determinants. The many–electron state $\mid \Psi_i^{\mathrm{D}}\rangle$ is characterized by the vector of single–electron level occupations $p_m(i)$ $(m = 1, 2, \ldots, N)$ which are either one or zero. Therefore, there are 2^N different states.

The many–electron state can be written in the form

$$\mid \Psi_i^{\mathrm{D}}\rangle = \prod_{m=1}^{N} \left(c_m^+\right)^{p_m(i)} \mid 0\rangle \tag{11.3}$$

and the eigenenergy of the state is

$$E_i = \sum_{m=1}^{N} p_m(i)(\varepsilon_m - e\Phi) + n_i(n_i - 1)U/2\,, \tag{11.4}$$

while the electron number is given by

$$n_i = \sum_{m=1}^{N} p_m(i)\,. \tag{11.5}$$

We see explicitly, that the charging energy in this model $E_{\mathrm{C}}(n) = n(n-1)U/2$ depends only on the number of electrons in the dot and not on the specific levels being occupied. Thus, the charging model represents a simple and trivially soluble model in which quantization and charging effects are contained in the energy of the many–electron states.

11.2 Transition rates

The values for the transition rates are calculated in the same way as the ones between the states of an Anderson impurity (10.3,10.4). As a reasonable selection rule, we take into account only transitions between states that differ in the occupation p_m of only one single–electron level. Transitions involving the rearrangement of electrons among the single–electron levels are omitted. That means that an electron which tunnels into the dot can occupy only empty states while the other electrons remain unaffected. In the same way, tunneling of an electron out of the dot is only possible by taking an electron from an occupied one–electron state in the initial arrangement without influencing the remaining electrons. These selection rules arise from the consideration of the transition matrix element

$$\langle \Psi_j^{\mathrm{D}} \mid c_m^+ \mid \Psi_i^{\mathrm{D}}\rangle \tag{11.6}$$

between the many–electron dot states which correspond to adjacent electron numbers (see Appendix C).

Therefore, we get the transition rates

$$\begin{aligned} \Gamma_{j,i}^{\mathrm{L/R},+} &= t^{\mathrm{L/R}} f_{\mathrm{L/R}}(E) \delta_{n_j,n_i+1} \delta_{1,(\vec{p}(j)-\vec{p}(i))^2} \,, \\ \Gamma_{i,j}^{\mathrm{L/R},-} &= t^{\mathrm{L/R}} [1 - f_{\mathrm{L/R}}(E)] \delta_{n_i,n_j-1} \delta_{1,(\vec{p}(i)-\vec{p}(j))^2} \,, \end{aligned} \tag{11.7}$$

where the energy $E = E_j - E_i$ is the energy difference between the eigenstates of the isolated dot Hamiltonian (11.2).

11.3 Stationary occupation probabilities

The stationary (but non–equilibrium) solution of (9.5) is obtained by solving numerically the system of 2^N linear equations [111].

At zero bias voltage, the stationary state is the equilibrium state and the occupation probabilities of the n–electron states are given by a Gibbs distribution

$$P_i^{\mathrm{G}} = (\exp[-\beta(E_i - \mu n_i)])/\mathcal{Z} \tag{11.8}$$

with the constant chemical potential $\mu = \mu_{\mathrm{L}} = \mu_{\mathrm{R}}$. With $\mathcal{Z}$, we denote the grand canonical partition function. It can be shown that P_i^{G} solves the rate equation (9.5) for arbitrary inelastic relaxation rate r.

For temperatures lower and voltages higher than the level spacings, the stationary occupation probabilities $\bar{P}_i$ deviate from their equilibrium values P_i^{G}. For $r \gg t^{\mathrm{L/R}}$, when the dot states decay fastly on the timescale of the tunneling events via electron–phonon scattering, the ratios $\bar{P}_i/\bar{P}_j$ can be satisfactorily approximated using the Gibbs distribution by $P_i^{\mathrm{G}}/P_j^{\mathrm{G}}$ for fixed electron number $n_i = n_j$. This can be seen in Figure 11.1 where the data points for $\ln \bar{P}_i$ versus E_i for a given n_i lie on straight lines with slope $-\beta$. This confirms the assumptions of a Gibbs distribution among states with given electron number in [116, 117] in this parameter regime.

For different electron numbers $n_i \neq n_j$, $\bar{P}_i/\bar{P}_j$ can be far from equilibrium. It is impossible to scale all of the points onto one common curve by defining an effective chemical potential for the dot. The linear correction to the Gibbs distribution calculated in [116] vanishes for the case shown in Figure 11.1. We show exact results valid for arbitrary transport voltages.

11.4 Current–voltage characteristic

The current–voltage characteristics (Figure 11.2) for temperatures lower than the level spacing shows finestructure in the Coulomb staircase consistent with recent experiments [24, 29] and earlier theoretical predictions using a slightly different approach [117, 118]. To avoid artifacts arising from the finite number of one–electron levels we do not plot the part arising from states with $n > 3$ and discuss only the realistic case $n < N$.

Intra–dot relaxation ($\sim r$) suppresses the lowest of the finestructure steps because the electron that contributes to the current at the n–th Coulomb step has to enter the

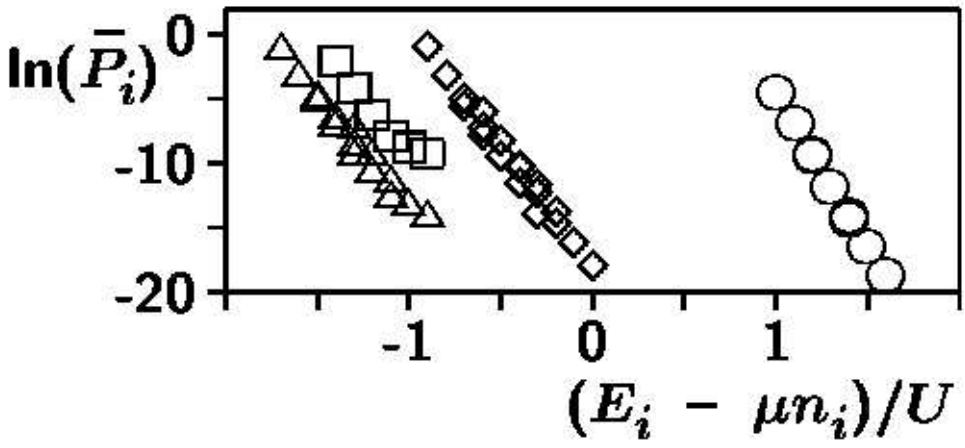

Figure 11.1: Stationary occupation probabilities $\bar{P}_i$ for a dot containing $N = 6$ one–electron levels. Electron numbers are $n_i = 1$ ($\square$), $n_i = 2$ ($\triangle$), $n_i = 3$ ($\Diamond$) and $n_i = 4$ ($\bigcirc$). We used $t^{\rm L} = t^{\rm R}$, $\Phi = 0$, $\mu_{\rm L} = 1.5U$, $\mu_{\rm R} = -0.3U$ and $\mu = (\mu_{\rm L} + \mu_{\rm R})/2$. Energies of the one–electron levels are $\varepsilon_1 = 0.1U$, $\varepsilon_2 = 0.2U$, $\varepsilon_3 = 0.3U$, $\varepsilon_4 = 0.4U$, $\varepsilon_5 = 0.5U$ and $\varepsilon_6 = 0.6U$. Inverse temperature is $\beta = 25/U$ and the relaxation rate $r = 100\bar{t}$. This figure is taken from [111].

n–th or a higher one–electron level when the strong relaxation leads to the situation with all the lower states occupied. For $r \gg t^{\rm L/R}$ the $n-1$ other electrons occupy with high probability all of the lower one–electron levels.

Asymmetric coupling to the leads changes the height of the steps in the I–V curve. This can be explained for the nth Coulomb step as follows. If $t^{\rm L} > t^{\rm R}$ ($\mu_{\rm L} > \mu_{\rm R}$) the stationary occupation probabilities favor the n–electron levels, while for $t^{\rm L} < t^{\rm R}$ the $(n-1)$–electron states are preferred. Since there are more n–electron levels than $(n-1)$–electron levels, the probability for an electron to escape is reduced in the former case as compared to the probability for an electron to enter in the latter case. These processes limit the current. They lead to a reduction and an enhancement of the current in the first and second case, respectively.

The occurrence of regions of negative differential conductance in the experiments [24, 29], however, cannot be explained within the charging model.

11.5 Conductance peaks

For fixed V, the conductance shows peaks when $V_{\rm G}$ and consequently the electrostatic potential Φ is varied. The linear response limit simply reproduces the periodic conductance peaks in agreement with [53]. For finite bias voltage, $eV = \mu_{\rm L} - \mu_{\rm R}$, larger than the level spacing, transitions involving excited states can occur. The number of levels that contribute to the current varies when $V_{\rm G}$ is changed. This leads to the splitting of the conductance peaks observed experimentally and explained qualitatively in [29, 30, 34, 35]. A fit of the ortodox theory within the charging model [117, 118] to experimental data yields quite good agreement [34, 35].

From the quantitative treatment of the charging model using (9.5) for $T = 0$, i.e. only constant nonvanishing or vanishing $\Gamma_{i,j}$'s, we obtain that the number of transitions contributing to the current according to the rules given in Section 9.2 varies with $V_{\rm G}$ as $0-6-4-12-4-6-0$ in the specific example shown for finite temperature in Figure 11.3. Taking into account the stationary $\bar{P}_i$'s the sequence of current values is $0-3/2-4/3-2-4/3-3/2-0$ [129]. If the difference $E_0(n) - E_0(n-1)$ between the energies of the many electron ground states lies outside the interval $[\mu_{\rm R}, \mu_{\rm L}]$ the transport via other energetically allowed transitions is Coulombically blocked. While the relaxation rates have almost no influence on the conductance, asymmetric coupling to the leads changes the shape of the peaks considerably.

We propose to explain the slight asymmetry observed experimentally [29, 30] by the asymmetry of the barriers and we predict that the asymmetry in the finestructure of the observed conductance peaks will be reversed if the sign of the bias voltage is changed. This has been observed experimentally in [30]. Such asymmetric conductance properties can be used to construct a mesoscopic rectifier. Similar effects were inferred earlier from the high frequency properties of mesoscopic systems containing asymmetric disorder [130].

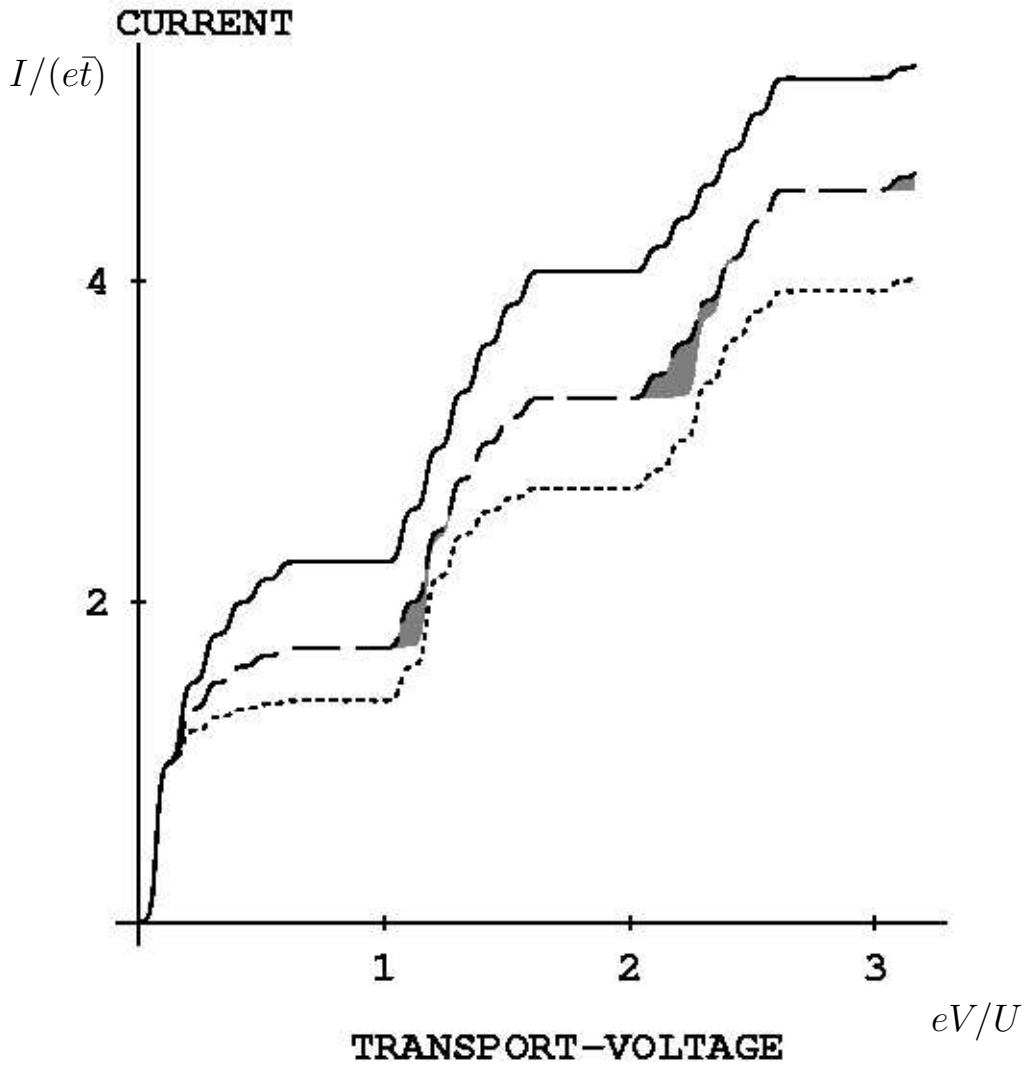

Figure 11.2: Current–voltage characteristic of a dot represented by $N = 6$ one–electron levels. Model parameters are as in Figure 11.1. Inverse temperature is $\beta = 100/U$ and $\mu_{\rm R} = 0$, $\Phi = 0$ was chosen. Dashed lines: results for $r = 0$ and equal barriers, dotted and solid lines: $t^{\rm R}/t^{\rm L} = 0.5$ and 2, respectively. Shaded regions: suppressions of steps induced by relaxation $r/\bar{t} = 100$ at $t^{\rm L} = t^{\rm R}$. The Figure is taken from [111].

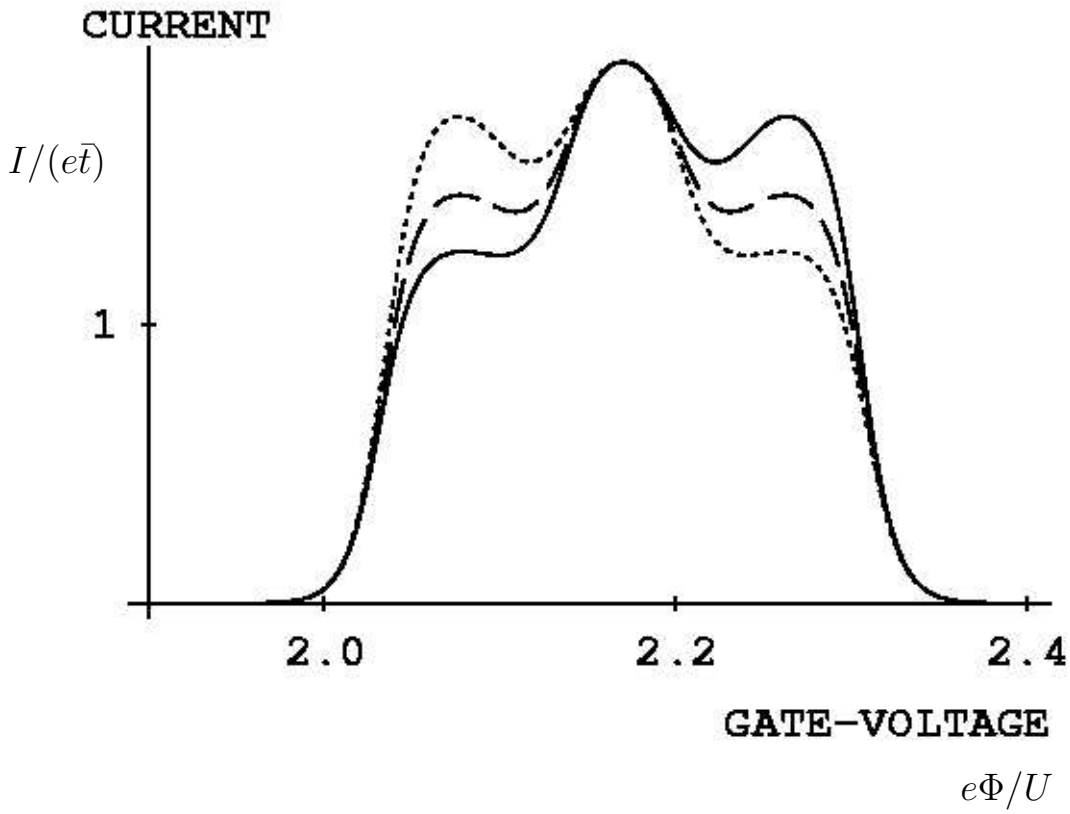

Figure 11.3: Current versus $V_{\rm G}$ for $\mu_{\rm L} = 0.26U$ and $\mu_{\rm R} = 0$ through a dot represented by $N = 6$ one–electron levels. Model parameters are as in Figure 11.1. Inverse temperature is $\beta = 100/U$. $V = 0.26U/e$ is between the double and the triple of the bare level spacing such that the conductance peaks are modulated as explained in the text. Dashed lines: results for $r = 0$ and equal barriers, dotted and solid lines: $t^{\rm R}/t^{\rm L} = 0.5$ and 2, respectively. The Figure is taken from [111].

Chapter 12

Correlated electrons in quasi–one dimension

The charging model is a severe simplification for interacting electrons, neglecting many important features especially for systems with reduced dimensionality and low electron density. Therefore, we consider now as a third example a model of Coulombically interacting electrons where the correlations are fully taken into account.

12.1 Dot spectrum

Theoretical calculations of electronic spectra which include correlations are restricted to very low electron numbers. In two dimensional dots with parabolic confinement, situations with two electrons [131] and even effects of nonparabolicity [132] and magnetic fields [133] have been investigated analytically. For few electrons, numerical investigations demonstrate the importance of correlation effects [134].

For our purpose, reliable data for several different electron numbers are necessary. Therefore we use here a quasi–one dimensional (1D) square well of length L as a model for the dot and include the spin degree of freedom. For this system, numerical results for up to four electrons are available [84, 119, 120]. In the low density limit, an analytical solution exists [121] which describes the lowest excitations for even higher electron numbers. This system is described by the full dot Hamiltonian (8.4)

$$\begin{aligned} H_{\mathrm{D}} &= \sum_{m,\sigma} (\varepsilon_m - e\Phi + g\mu_{\mathrm{B}} B\sigma) c^+_{m,\sigma} c_{m,\sigma} \\ &+ \sum_{\substack{m_1,m_2,m_3,m_4 \\ \sigma_1,\sigma_2,}} V_{m_1 m_2 m_3 m_4}\, c^+_{m_1,\sigma_1} c^+_{m_2,\sigma_2} c_{m_3,\sigma_2} c_{m_4,\sigma_1}\,. \end{aligned} \tag{12.1}$$

The exact eigenvalues E_i [84, 119, 120] and the corresponding n–electron eigenstates $\mid \Psi_i^{\mathrm{D}}\rangle$ [135] for up to $n = 4$ electrons in this correlated electron model have been calculated numerically. The interaction potential

$$V(x, x') \propto ((x - x')^2 + \lambda^2)^{-1/2} \tag{12.2}$$

was chosen to be Coulombically for large spatial separations and cut off at small distances $\mid x - x' \mid < \lambda$ in order to avoid divergences in the interaction matrix elements

$$V_{m1,m2,m3,m4} = \int dx\, dx'\, V(x,x') \psi^*_{m1,\sigma_1}(x) \psi^*_{m2,\sigma_2}(x') \psi_{m3,\sigma_2}(x') \psi_{m4,\sigma_1}(x)\,. \tag{12.3}$$

The cutoff parameter λ ($\ll L$) is due to a lateral spread in the lowest transversal state of the electronic wave functions ψ_m corresponding to one–electron states in the well. It allows the particles to pass each other due to the finite height λ^{-1} of the Coulomb barrier. Only if such processes which involve electrons interchanging their position in the line are possible, the fermionic nature of the particles plays a role. These processes are crucial for the understanding of the energetically lowest excitations [121]. If, on the other hand, the particles are ordered on the only relevant spatial degree of freedom and their order cannot be changed due to impenetrable Coulomb barriers, the statistics of the particles is irrelevant. We shall deal with genuine fermions.

Since the interaction (12.3) is spin independent, the n–electron total spin S and its projection onto one spatial direction M, the total magnetic quantum number, is conserved during electron–electron scattering events and therefore is a good quantum number for the classification of the states of the interacting dot.

This feature of the model is realistic with respect to experimental situations if spin–orbit scattering processes and other effects which are able to violate the conservation of spin, are slow on the timescale of the inverse tunneling rates. In the experiments [24, 29], the order of magnitude of the current through the dot is 1 nA. This means that about 10^{10} electrons pass the dot per second. Thus, the lifetime of the spin has to be larger than 100 ps in order to allow for using a spin conserving model. There is no evidence for shorter spin relaxation times in semiconductor based quantum dots. Only in the presence of inhomogeneous magnetic fields induced by magnetic impurities nearby or when ESR radiation is applied, the spin conservation might be violated affecting some of the most striking results presented below.

Within our model, the total spin and the magnetic quantum number of the dot can only be changed by electrons tunneling through the barrier. The spin of the total system including the leads is conserved during tunneling processes, but the spin carried by the electrons is transported into or out of the dot.

The properties of the correlated states and the energy spectrum are discussed in detail in the references [84, 119, 120]. For not too large electron densities $L/(n-1) > a_{\mathrm{B}}$, when the mean separation of two electrons becomes larger than the Bohr radius a_{B}, the charge density in the dot develops n distinct peaks and indicates a tendency towards Wigner crystallization [84, 135]. The few correlated electrons in the dot then form a 'Wigner molecule'. The charge density distribution is shown in Figure 12.1 (taken from [135]) for three electrons and different system lengths L.

In the limit of very dilute electrons, $L/(N-1) \gg a_{\mathrm{B}}$, the ground state energy is well described by a model of equidistant classical point charges on a line of length L [84]. In the intermediate regime, the excitation spectrum (Figure 12.2) consists of well separated multiplets, each containing 2^n states.

The energetic differences between adjacent multiplets decrease algebraically with electron density. They correspond to vibrational excitations of the Wigner molecule. The

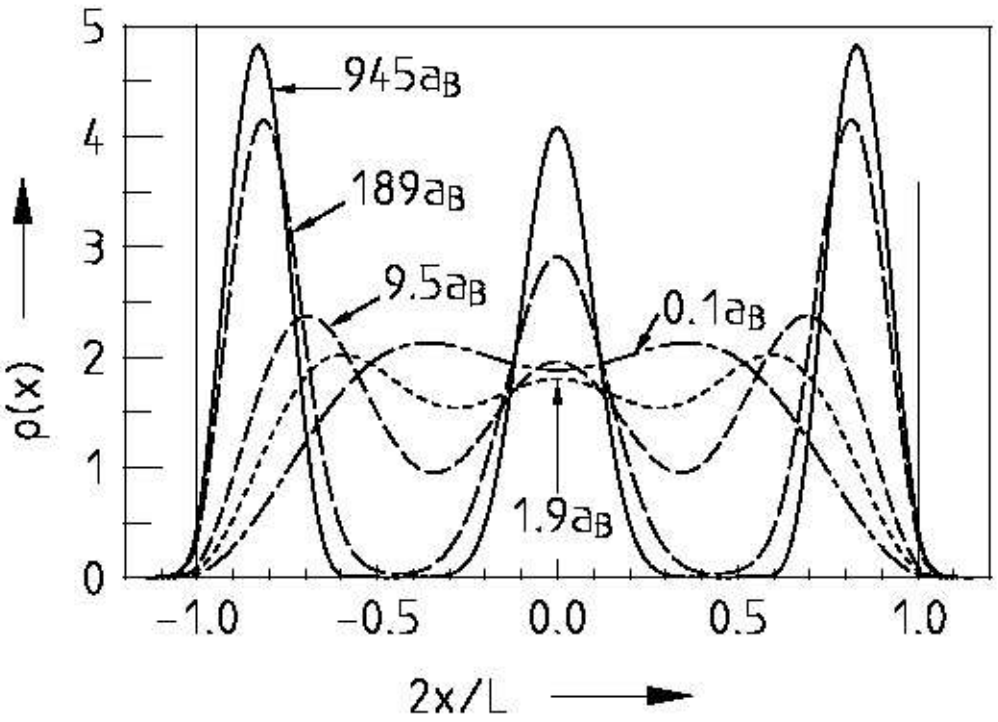

Figure 12.1: The charge density $\rho(x)$ in a quasi–one dimensional dot for the the ground state of $n = 3$ electrons in the dot. The corresponding system lengths L are indicated in units of the Bohr radius $a_{\rm B}$. Clearly, for larger systems ($\rightarrow$ lower densities), there are strong deviations from the purely kinetic behavior and the interaction effects lead to distinct peaks with regions of zero charge density in between. This figure is taken from [135].

considerably smaller intra–multiplet energy differences decrease exponentially. They are due to tunneling between different configurations of the n electrons in the well. The wave functions of individual levels within a given multiplet differ in symmetry and S.

In the limit of low density, the excitation energies in the lowest multiplet can be calculated analytically [121] starting from a pocket state basis that already takes into account the peaked structure of the interacting many–electron wave functions. The excitation energies depend only on one tunneling integral t_n (Table 12.1) between adjacent configurations of the n electrons. This tunneling integral can be calculated in principle and depends heavily on the cutoff parameter λ [121]. We have chosen reasonable values leading to excitation energies that can be compared with the experimental situation.

For the explicit numerical calculations of the current we estimated the values of the tunneling integrals to be $t_2 = 0.03E_{\rm H}$, $t_3 = 0.07E_{\rm H}$ and $t_4 = 0.09E_{\rm H}$ ($E_{\rm H} \equiv e^2/a_{\rm B}$ is the Hartree energy) . The ground state energies of the isolated dot were determined numerically for $n \in \{1, 2, 3, 4\}$ and $L = 15\, a_{\rm B}$ [136]. The resulting energy values of the states in the lowest multiplet are given in Table 12.3.

In summary, two different energy scales characterize the n–electron excitations. We will demonstrate that they can in principle be detected by nonlinear transport experi-

Table 12.1: Spin and energies of low lying excitations of the correlated electron model at sufficiently large mean electron distances $r_s \equiv L/(n-1) \gg a_B$. The tunneling integrals t_n decrease exponentially with r_s.

n_i	S_i	$E_i - E_0(n)$
2	0	0
2	1	$2t_2$
3	1/2	0
3	1/2	$2t_3$
3	3/2	$3t_3$
4	0	0
4	1	$(1-\sqrt{2}+\sqrt{3})t_4$
4	1	$(1+\sqrt{3})t_4$
4	0	$(2\sqrt{3})t_4$
4	1	$(1+\sqrt{2}+\sqrt{3})t_4$
4	2	$(3+\sqrt{3})t_4$

ments.

Neglecting the effect of space dependent electrostatic potentials due to the electric fields, we use the results for the properties of the dot states at arbitrary transport voltage by adjusting the eigenenergies of the many–electron states according to the potential change Φ in the dot induced by the voltages applied to the electrodes (Appendix B).

12.2 Transition rates

In this section the full expressions for the transition rates (9.1) are important. They are calculated in Appendix C and read

$$\begin{aligned}
\Gamma_{i,j}^{\mathrm{L/R},-} &= \frac{1}{2}\left|\langle S_j, M_j, \frac{1}{2}, \pm\frac{1}{2} \mid S_i, M_i\rangle_{CG}\right|^2 t^{\mathrm{L/R}}[1-f_{\mathrm{L/R}}(E)]\delta_{n_i,n_j-1}\,, \\
\Gamma_{j,i}^{\mathrm{L/R},+} &= \frac{1}{2}\left|\langle S_i, M_i, \frac{1}{2}, \pm\frac{1}{2} \mid S_j, M_j\rangle_{CG}\right|^2 t^{\mathrm{L/R}} f_{\mathrm{L/R}}(E)\delta_{n_j,n_i+1}\,. \qquad (12.4)
\end{aligned}$$

The rates contain Clebsch–Gordan coefficients. The probability factor entering the transition rates is the square of the Clebsch–Gordan coefficients listed in Table 12.2. They account for the combination of the spin of the incoming or leaving electron with the spin of the initial dot state to generate the spin of the final dot state and introduce spin selection rules. The quantum numbers S and M, denoting the total spin and the total magnetic quantum number of the correlated electrons in the dot, respectively, can be changed only by $\pm 1/2$ when one electron enters or leaves. These spin selection rules are a consequence of using the exact correlated many–particle states in the rate equation (9.5).

This is a drastic restriction for the transitions and completely different from the selection rules used within the charging model, where only processes are allowed, in which electrons enter or leave one–electron states. Here, the correlated many–electron states

Table 12.2: The squares of the vector coupling Clebsch–Gordan coefficients $\langle S_i, M_i, \frac{1}{2}, \pm\frac{1}{2} \mid S_j, M_j\rangle_{CG}$ for the combination of the total spin S_i and magnetic quantum number M_i of the dot state, with the spin 1/2 of an electron needed to form a final dot state with spin S_j and magnetic quantum number M_j. For $S_j - S_i \neq \pm 1/2$ or $M_j - M_i \neq \pm 1/2$, the Clebsch–Gordan coefficients vanish.

	$S_j = S_i + 1/2$	$S_j = S_i - 1/2$
$M_j = M_i + 1/2$	$(S_i + M_i + 1)/(2S_i + 1)$	$(S_i - M_i)/(2S_i + 1)$
$M_j = M_i - 1/2$	$(S_i - M_i + 1)/(2S_i + 1)$	$(S_i + M_i)/(2S_i + 1)$

are linear combinations of many noninteracting basis states with contributions of all the one–electron levels. Thus, it makes no sense to introduce selection rules for the occupation of one–electron levels.

If the exact eigenstates are known, one can determine the overlap matrix element of a one–electron creation operator applied to a n–electron dot state with an $n+1$–electron dot state [138]. These matrix elements

$$\langle \Psi_j^{\mathrm{D}} \mid c_{m,\sigma}^{+} \mid \Psi_i^{\mathrm{D}} \rangle \tag{12.5}$$

with $n_j = n_i + 1$ enter the transition rates (see Appendix C) weighted with the transition tunneling matrix elements. They depend strongly on details of the microscopic realization of the dot such as impurities and the geometrical form, while the spin effects yield very general selection rules. In a first approximation, we ignore the influence of the spatial effects of the correlated wave functions by using solely the selection rules induced by the Clebsch–Gordan coefficients which arise from the consideration of the spin Hilbert space and discuss the influence of the full transition matrix elements in Section 12.8.

Anyway, the correlations play an important role for the transport properties. The order of the states with different spins on the energy axis is strongly influenced by the electron–electron interactions and leads to highly nontrivial new effects. Together with taking into account the spin selection rules it influences not only quantitatively but also qualitatively the transport properties. In addition to the Coulomb blockade, further blocking mechanisms occur as will be discussed in the following.

12.3 Effective master equation

At zero magnetic field the problem is completely isotropic with respect to spin and the states with different magnetic quantum numbers M_i are perfectly degenerate. Thus, their stationary population does not depend on M_i but only on their total spin. Therefore one can consider transitions between states of total spin and arbitrary magnetic quantum number in the rate equation (9.5). We define the total occupation probability

$$P_\alpha^{\mathrm{T}} = \sum_{M=-S_\alpha}^{+S_\alpha} P_{\alpha,M} = (2S_\alpha + 1) P_{\alpha,M}\,, \tag{12.6}$$

where the index α contains all the quantum numbers needed to characterize the state except the magnetic quantum number M. Then, the master equation (9.5) becomes

$$\frac{d}{dt}P_\alpha^{\mathrm{T}} = \sum_{\beta\,(\beta\neq\alpha)} (\Gamma_{\alpha,\beta}^{\mathrm{T}} P_\beta^{\mathrm{T}} - \Gamma_{\beta,\alpha}^{\mathrm{T}} P_\alpha^{\mathrm{T}}) \tag{12.7}$$

where the total transition rates

$$\Gamma_{\alpha,\beta}^{\mathrm{T}} = \sum_{M_1=-S_\alpha}^{+S_\alpha} \sum_{M_2=-S_\beta}^{+S_\beta} \frac{\Gamma_{\alpha M_1;\beta M_2}}{2S_\beta+1} \tag{12.8}$$

are an average over the transition rates between the individual levels. Since the states with different M are degenerate, the only dependence on the magnetic quantum number is contained in the Clebsch–Gordan coefficients such that the total transition rates are given by

$$\begin{aligned} \Gamma_{\beta,\alpha}^{\mathrm{L/R},-} &= \gamma_{\beta,\alpha}\, t^{\mathrm{L/R}}[1-f_{\mathrm{L/R}}(E)]\delta_{n_\beta,n_\alpha-1}\,, \\ \Gamma_{\alpha,\beta}^{\mathrm{L/R},+} &= \gamma_{\alpha,\beta}\, t^{\mathrm{L/R}} f_{\mathrm{L/R}}(E)\delta_{n_\alpha,n_\beta+1}\,, \end{aligned} \tag{12.9}$$

with the effective spin dependent factors

$$\gamma_{\beta,\alpha} = \sum_{M_1=-S_\alpha}^{+S_\alpha} \sum_{M_2=-S_\beta}^{+S_\beta} \frac{1}{2} \left| \langle S_\alpha, M_\alpha, \frac{1}{2}, \pm\frac{1}{2} \mid S_\beta, M_\beta\rangle_{CG} \right|^2 . \tag{12.10}$$

Evaluating the sums using the values from Table 12.2 one finds

$$\gamma_{\beta,\alpha} = \frac{S_\alpha+1}{2S_\alpha+1}\delta_{S_\beta,S_\alpha+1/2} + \frac{S_\alpha}{2S_\alpha+1}\delta_{S_\beta,S_\alpha-1/2} \tag{12.11}$$

that has been used in reference [25]. These effective spin dependent factors favor an increase of the total spin in the case of correlated electrons.

Transitions due to electron phonon scattering events conserve both, total spin and magnetic quantum number as well as the number of electrons inside the dot. Therefore, there are not many transitions available for this kind of processes and the influence of inelastic processes is even weaker than in the framework of the charging model. In all of the calculations, we will use $r = \bar{t}$.

12.4 Current–voltage characteristics

The stationary occupation probabilities are similar as for the charging model but modified by spin effects.

The Current–voltage characteristic calculated by using the excitation energies given in Table 12.3 is shown in Figure 12.3. First of all, we observe that the lengths of the steps in the Coulomb staircase and accordingly the distances of the conductance peaks are no longer equal since the exact n–electron ground state energy is not proportional to $n(n-1)$ for small ε_m's as in the charging model. The deviation from the classical behavior

Table 12.3: The values used in the actual calculations.

α	n_α	S_α	$E_\alpha/E_{\rm H}$
1	0	0	0
2	1	1/2	0.0225
3	2	0	0.2972
4	2	1	0.3572
5	3	1/2	0.9654
6	3	1/2	1.1054
7	3	3/2	1.1754
8	4	0	2.1480
9	4	1	2.2666
10	4	1	2.3939
11	4	0	2.4598
12	4	1	2.5212
13	4	2	2.5739

is related to the inhomogeneity of the quantum mechanical charge density of the ground state [84, 120, 135]. Second, the heights of the finestructure steps are more random as compared to those in Figure 11.2 due to the non–regular sequence of total spins (cf. Table 12.1) and the spin dependent factors in the transition rates. In certain cases finestructure steps in the I–V characteristic may even be completely suppressed.

12.5 Spin blockade type I

Strikingly, regions of negative differential conductance occur in Figure 12.3. They are related to the reduced possibility for the states of maximal spin $S = n/2$ to decay into states of lower electron number via the transitions

$$n\,;\,S \longrightarrow n-1\,;\,S'\,. \tag{12.12}$$

If $S = n/2$, $S' = S - 1/2$ is the only available spin at the lower electron number $n - 1$.

Since this effect is due to spin selection rules we call it 'spin blockade'. In the context of the spectrum of the quasi–one dimensional model we shall discuss the spin blockade of type I related to states with maximum spin being highly excited within the lowest multiplet. The second kind of spin blockade is due to states with high (not necessarily maximum) spin being the ground state or energetically close to the ground state. Such situations occur for correlated electrons in two dimensions and will be discussed in Chapter 14.

Within the quasi–one dimensional model, the states with maximal spin occur only once in each multiplet for given electron number. Therefore only one finestructure step with negative differential conductance can occur within each Coulomb step. The peak in the I–V curve becomes less pronounced if $t^{\rm L} < t^{\rm R}$, because then the dot is mostly empty

and the $(n-1) \rightarrow n$ transitions determine the current. The spin selection rules reduce the probability for some of the $n \rightarrow (n-1)$ transitions (especially important for $t^{\mathrm{L}} > t^{\mathrm{R}}$) and the negative differential conductance becomes more pronounced (Figure 12.3).

To illustrate this, we concentrate on the first region of negative differential conductance in the third conductance peak around the voltage of about $eV/E_{\mathrm{H}} = 0.8$. This voltage is high enough to allow for all the transitions between the states with lower electron numbers $0 \leq n \leq 2$ and the finestructure steps in Figure 12.3 occur when the voltage is raised to values that open a transition between two states with $n = 2$ and $n = 3$, respectively. Then the transition can contribute to the current through the system. This can be verified by plotting the stationary occupation probabilities of the corresponding states together with the current as a function of the transport voltage V (Figure 12.4). Every step in the current is accompanied by a change in the stationary occupation probabilities of the many–electron states involved.

In order to understand the steps, we sketch the energy levels of the dot for $n = 2$ and $n = 3$ and the transitions allowed by the spin selection rules (Figures 12.5 and 12.6). The chemical potential in the right lead is kept fixed at $\mu_{\mathrm{R}} = 0$ such that at $T = 0$ electrons can leave the dot to the right side with any positive energy. This means that all the decays to lower electron number are possible by tunneling of an electron through the right barrier. The chemical potential in the left lead is raised making electrons available at energies up to μ_{L}. A transition between an n–electron state with energy E_α and an $n+1$–electron state with energy $E_\beta > E_\alpha$ can contribute to the current when the chemical potentials are such that the transition can occur in the direction of increasing electron number by tunneling of an electron through one lead and in the direction of decreasing electron number by tunneling through the other lead.

While the 'exit' to the right is possible for all of the transitions, the 'entry' through the left barrier is opened one after the other by increasing the left chemical potential to the value $\mu_{\mathrm{L}} = E_\beta - E_\alpha$. At low μ_{L}, only the states with $n \leq 2$ can be occupied. As soon as the voltage is high enough ($eV/E_{\mathrm{H}} \approx 0.6$) to allow for the $n = 2 \rightarrow 3$ transition that needs the lowest amount of energy in the lead, $\mu_{\mathrm{L}} = E_{\mathbf{c}} - E_{\mathbf{b}}$, the lowest state with $n = 3$ (**c**) appears with a finite stationary population. This happens at the expense of the highest state for $n = 2$ (**b**) which is depopulated by this process. In the same time, the $n = 2$ ground state (**a**) slightly gains occupation probability because the ground state with $n = 3$ (**c**) can decay into this state of lower electron number. At the next step, the ground state to ground state transition becomes accessible in both directions. Then, at the step around $eV/E_{\mathrm{H}} \approx 0.75$, the transition from state **b** to **d** comes into play, further decreasing the population of the excited $n = 2$ electron state **b** and populating the first excited $n = 3$ electron state (**d**). All these steps are accompanied by increasing values of the current.

For voltages slightly higher than $eV/E_{\mathrm{H}} \approx 0.8$, the transition to the energetically highest state with $n = 3$ (**e**) becomes available and this state attracts considerable stationary occupation probability at the expense of all the other populations. Strikingly, the current is decreased. There are two or three possible transitions to states with another electron number starting from any but the state **e** with highest spin for $n = 3$ (The transitions to states with $n = 4$ are disregarded in the moment, because the voltage is not high enough to allow for them). Thus, due to the spin selection rules the system has a reduced

probability to leave the state **e** lowering the electron number. Therefore, the lifetime of this state is exceptionally large leading to the high population and the spin blockade of the current because the total number of transitions per unit of time is decreased when state **e** can be occupied.

For asymmetric barriers, when the tunneling rate through the right lead t^{R} is lower than t^{L}, electron number decreasing transitions are relatively slow. Thus, the transition into the 'dead end' **e** becomes almost a 'one way road' and the spin blockade is drastically enhanced (Figure 12.3). If, on the other hand, electron number decreasing processes are fast ($t^{\mathrm{R}} > t^{\mathrm{L}}$), the state (**e**) loses its trap–like properties and the spin blockade is suppressed .

Negative differential conductances can in fact be seen in the experimental data [24, 29] but certainly need much more elaborate further investigations. They can in principle be used to construct a mesoscopic oscillator. The influence of asymmetric coupling to the leads [30] is consistent with our results.

12.6 Splitting of the conductance peaks

The splitting of the conductance peaks (Figure 12.7) shows similar effects as for the charging model. The regularity of the peaks is lost due to the more irregular sequence of total spins on the energy scale and the unequal transition rates. We expect that for higher electron numbers, $n \approx 20$, the more regular shape could be reestablished. The dependence on the asymmetry of the barriers discussed in Section 10.4 however remains.

12.7 Transport spectroscopy

The spectra of quantum dots have been investigated using infrared absorption spectroscopy [103, 104, 105] on samples containing an array of many dots in order to get observable signal intensity. The wavelength of the radiation needed to probe the spectrum is very long as compared to the spatial extension of the dots. Thus, the perturbing radiation couples only to the center of mass coordinate of all the electrons and does not affect the degrees of freedom corresponding to other excitations. According to Kohn's theorem [106] the center of mass motion decouples completely from the other degrees of freedom in perfectly parabolic confinement potentials.

The Hamiltonian for the center of mass motion however is identical with the one–electron Hamiltonian in the given potential and the excitation energies detected with optical methods do not show signatures of the electron–electron interactions entering only the difference terms. Due to deviations from parabolic confinement potentials, weak signals of the almost forbidden transitions can be detected.

In contrast, nonlinear transport experiments are a powerful tool to investigate the full spectra of interacting electrons in quantum dots. The current is determined by transitions between all the states of the dot, including excited ones and the influence of the electron–electron correlations on the spectra is crucial for the results. The addition spectrum can in principle be deduced from the experimental data [24, 36] opening a way to study interacting few–electron systems systematically.

To gain more insight on the structure of the conductance peaks, we shall plot the differential conductance $\partial I/\partial V$ as a function of the transport voltage V and the gate voltage V_{G}. Such a representation of the experimental data [24] together with the investigation of the magnetic field effects could allow to get informations about the spectrum of quantum dots in the experiments if the relation between the peaks in the differential conductance and the properties of the spectrum is known.

12.7.1 Expected peaks

The transition rates are the only quantities that enter the rate equation and the current formula. The stationary occupation probabilities are determined as a function of these rates. Therefore, the current can change only when at least one of the transition rates changes.

The transition rates between two different many–electron states $\mid \Psi_i^{\mathrm{D}}\rangle$ and $\mid \Psi_j^{\mathrm{D}}\rangle$ of the quantum dot have a simple dependence on the voltages applied to the leads. The voltages are assumed to capacitively influence the energy of the many–electron levels and therefore change the energy difference associated with the transition. The only factors in the transition rates depending on this energy difference $E = E_j - E_i$ are the Fermi–Dirac distribution functions

$$f_{\mathrm{L/R}}(E) = \frac{1}{\exp[\beta(E-\mu_{\mathrm{L/R}})]+1}\,, \tag{12.13}$$

depending also explicitly on the chemical potentials in the leads.

At zero temperature ($\beta \to \infty$), they are particularly simple and jump discontinuously from unity to zero at $E - \mu_{\mathrm{L/R}} = 0$. This means that the rate for the electron number increasing transition ($\propto f$) drops to zero while the rate for the electron number decreasing transition ($\propto [1-f]$) becomes nonvanishing. A transition between many–electron levels can contribute to the current if it is open for transitions in both directions. This means that the energy difference must be smaller than one of the chemical potentials and larger than the other

$$\min(\mu_{\mathrm{L}}, \mu_{\mathrm{R}}) < E < \max(\mu_{\mathrm{L}}, \mu_{\mathrm{R}})\,. \tag{12.14}$$

Thus, the current can change, if one of the lines in the V–V_{G} plane, given by

$$\mu_{\mathrm{L}} = E \tag{12.15}$$

and

$$\mu_{\mathrm{R}} = E\,, \tag{12.16}$$

respectively, is crossed. At zero temperature the differential conductance $\partial I/\partial V$ can be nonzero only on these lines. In the experiment [24, 36], the chemical potential in one of the leads is kept constant while the other is swept through. To account for this, we choose $\mu_{\mathrm{L}} = 0$ and the transport voltage is $eV = \mu_{\mathrm{L}} - \mu_{\mathrm{R}} = -\mu_{\mathrm{R}}$. Using the explicit dependence of the energy of the many–electron states on the electrostatic potential due to the voltages in the leads (8.9) together with (8.5), the conditions (12.15) and (12.16) yield the explicit formulae

$$\frac{e}{C_\Sigma}\left(C_{\mathrm{G}}V_{\mathrm{G}} + C_{\mathrm{R}}V\right) = E_j^0 - E_i^0 \tag{12.17}$$

and

$$\frac{e}{C_\Sigma}\left(C_{\rm G}V_{\rm G} - (C_{\rm L}+C_{\rm G})V\right) = E_j^0 - E_i^0\,, \tag{12.18}$$

respectively, where $E_i^0 = E_i(\Phi = 0, B = 0)$ is the eigenenergy of the many–electron state $\mid \Psi_i^{\rm D}\rangle$ at zero electrostatic electric potential and tero magnetic field, and $C_\Sigma = C_{\rm L} + C_{\rm R} + C_{\rm G}$ is the total capacitance between the dot and the environment. They describe the lines in the V–$V_{\rm G}$ plane on which we expect significant nonzero values of the differential conductance at low temperatures due to the transition between the many–electron states $\mid \Psi_i^{\rm D}\rangle \leftrightarrow \mid \Psi_j^{\rm D}\rangle$ with different electron number $n_j = n_i + 1$.

The slopes of the lines depend only on the properties of the circuit (the ratios of the capacitances) while the position of the intersection with the $V_{\rm G}$–axis, which is the same for both of the lines, is determined by the energy eigenvalues of the isolated dot and the gate capacitance. We can see immediately from (12.17) and (12.18) that the slopes of the lines depend on the capacitances of the barriers in the model circuit (Figure 8.3). They are intrinsically asymmetric, even for completely symmetric barriers with equal capacitances. This is due to the asymmetric way of applying the transport voltage. In all our calculations, we use $C_{\rm L} = C_{\rm R} = C_{\rm G}$. Different values lead to nothing but a renormalization of the voltage scales.

All the lines arising from considering all of the states listed in Table 12.3 taking into account the spin selection rules are schematically shown in Figure 12.8.

12.7.2 Differential conductance

The overall behavior of the differential conductance versus gate– and transport–voltage, $V_{\rm G}$ and V, is shown in Figure 12.9 in a greyscale representation. Along the $V = 0$ axis the linear conductance peaks [108] can be observed with the intervals of the Coulomb blockade in between. Lines that intersect at the positions of the peaks of the linear conductance correspond to ground state to ground state transitions. The regions of the Coulomb blockade are the diamond shaped areas between these lines. The lines parallel to the edges of the Coulomb blockade areas reflect the dot spectrum [36, 112]. Qualitatively similar features have been observed experimentally [24, 36]. In Figure 12.9 the energy spectrum of a 1D quantum dot with values according to Table 12.3 has been used.

When either $V_{\rm G}$ or V are changed, the set of the dot states that are involved in the transport changes. At zero temperature, $T = 0$, this leads to jumps in the current. In general, a finite transport voltage V broadens the conductance peaks and leads to finestructure which is characteristic for the dot spectrum and is in general asymmetric [29, 34, 35].

The asymmetry is reversed when reversing the voltage [111] if the barriers are not equally transparent, in agreement with experimental findings [30]. Bright regions that correspond to negative differential conductances occur preferably when the lower chemical potential is attached to the less transmitting barrier and the transitions of the type (12.12) limit the current.

In Figure 12.10, results for different ratios of barrier transparencies are shown. Transitions through the less transmitting barrier lead to more pronounced steps in the current,

including the features of the spin blockade. This is consistent with experimental findings [36].

12.8 The influence of the orbital transition matrix elements

Having neglected the orbital part of the transition matrix elements in the previous part of this chapter, we shall treat the tunneling to and from the dot more precisely in this section. In a recent work, the total tunneling rate to and from a one–dimensional Wigner lattice was calculated within a path integral approach [137]. However, we need all the individual matrix elements between all of the many electron states.

For the model of correlated electrons in quasi–one dimension discussed in this chapter, the orbital part of the exact transition matrix elements between dot states of different electron number which enter the transition rates (see Appendix C) have very recently been calculated numerically [138]. For a regular barrier that allows for the assumption $T_{k,m} \equiv T$ in the tunneling Hamiltonian, the relevant quantity is

$$\left| \sum_m \langle \Psi_j^{\mathrm{D}} \mid c_{m,\sigma}^{+} \mid \Psi_i^{\mathrm{D}} \rangle \right|^2 . \tag{12.19}$$

The spin part of this matrix element was used throughout this chapter. The corresponding spin selection rules were discussed above. They led to striking effects in the transport properties.

The orbital part has been neglected so far. In contrast to the spin part, it depends sensitively on the microscopic realization of the sample and the shape of the wave functions. In our example, there are strong fluctuations in the values yielding 'weak selection rules' in addition to the spin selection rules. Thus, some of the lines corresponding to transitions between many–electron states of the dot are additionally suppressed. Such effects have been proposed [144] to explain the low number of transitions observed in the experiments [24] in the framework of rotational symmetric dots. At present, the importance of the orbital part of the transition matrix elements is not completely clear.

Including the orbital part in our calculations, we can no longer use the effective master equation (12.7) but have to consider all of the individual states. Using the full description of equation (9.5), we find that the main features of our results are unaffected.

One can see from Figure 12.11 that the orbital part of the transition matrix elements reduces the structure in the plot by suppressing some of the lines. Nevertheless, the qualitative aspects remain unchanged. In particular, the occurrence of negative differential conductances is still due to the spin blockade effect induced by the spin selection rules.

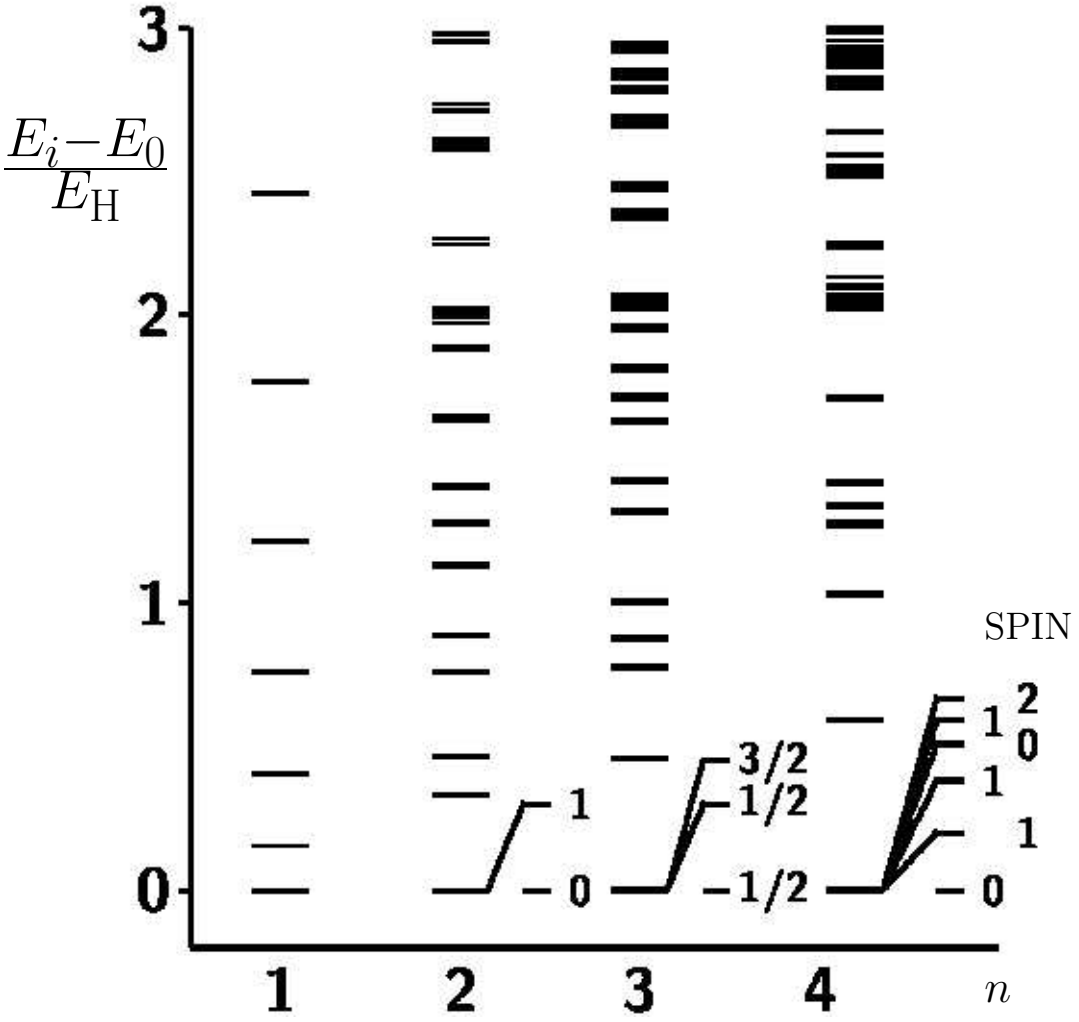

Figure 12.2: The excitation spectrum of a quasi–one dimensional dot for up to four electrons in a dot of length $L = 9.45\, a_B$. For $n \geq 2$ the low lying eigenvalues form multiplets containing a total number of states being equal to the dimension of the spin Hilbert space 2^n. The lowest multiplets are magnified in order to resolve the individual states which are labeled according to their total spin. The figure is taken from [84].

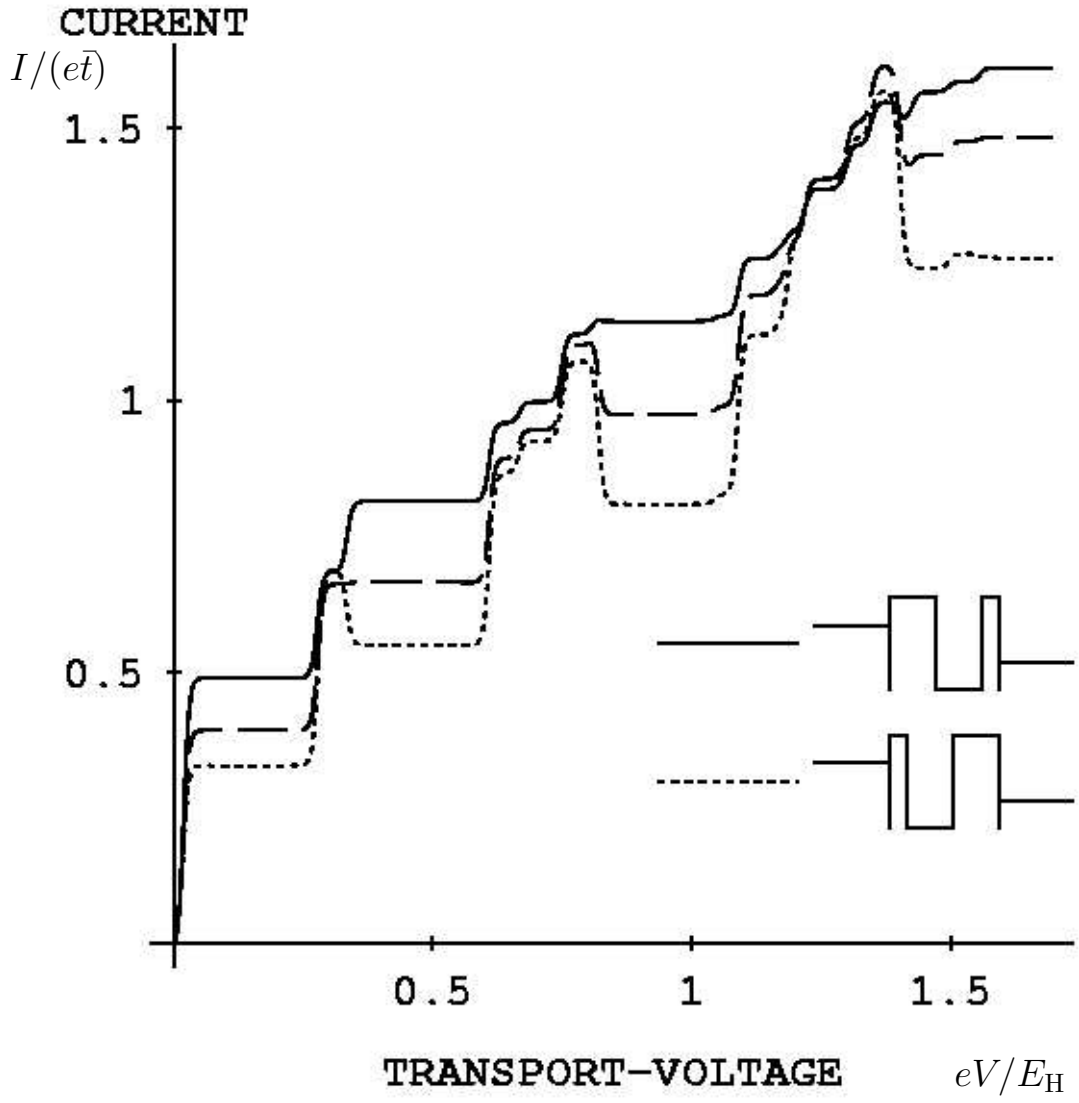

Figure 12.3: Current–voltage characteristic ($\mu_{\mathrm{R}} = 0$, $\Phi = 0$) of a dot described by the quasi–one dimensional correlated electron model with energy values from Table 12.3 for inverse temperature $\beta = 200/E_{\mathrm{H}}$ and $r = \bar{t}$. Dashed, dotted and solid lines correspond to different ratios of coupling to the leads with $t^{\mathrm{R}}/t^{\mathrm{L}} = 1$, 0.5 and 2, respectively.

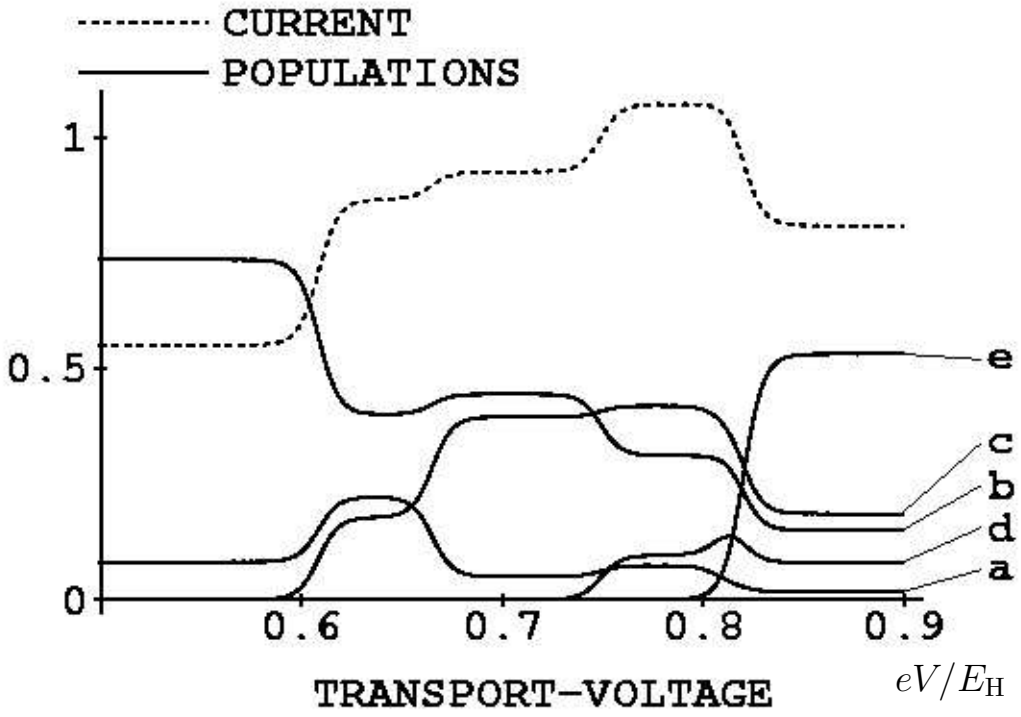

Figure 12.4: The most prominent feature in Figure 12.3 for $t^{\mathrm{L}} > t^{\mathrm{R}}$ is enlarged. The current in units of $e\bar{t}$ (dotted) and the populations of the most relevant dot states **a** : $n = 2$, $S = 0$, **b** : $n = 2$, $S = 1$, **c** : $n = 3$, $S = 1/2$ (ground state), **d** : $n = 3$, $S = 1/2$ (first excited state), **e** : $n = 3$, $S = 3/2$ versus bias voltage are shown. The populations shown here do not sum up to unity because of the occupation of other states.

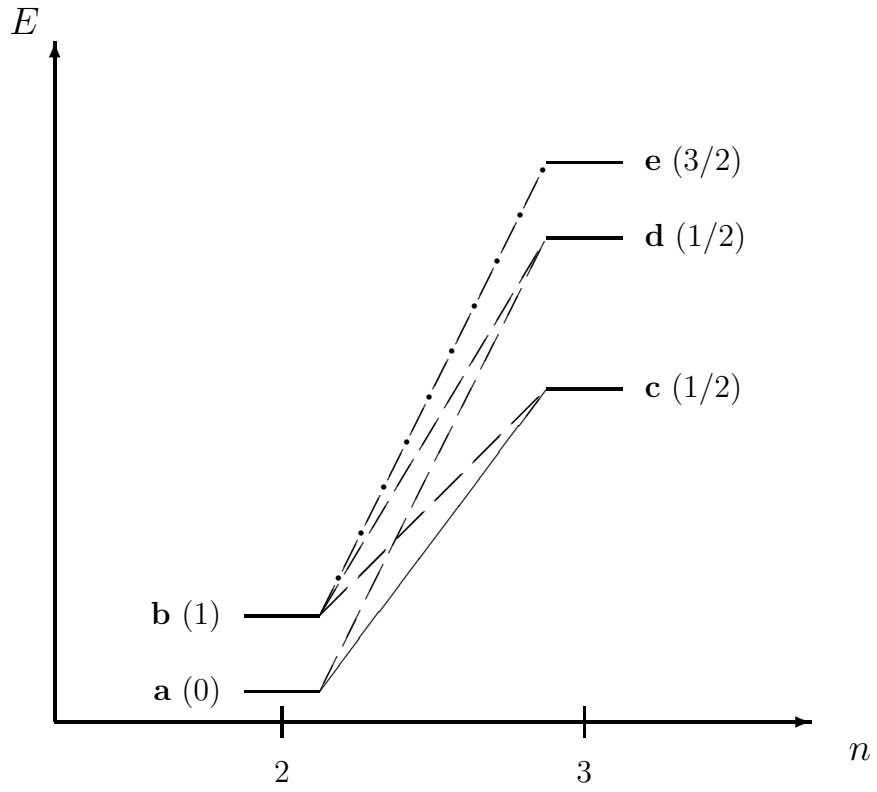

Figure 12.5: Dot states for $n = 2$ and $n = 3$. The total spins S of the states are indicated in brackets next to the lines representing the level. Transitions being allowed by the selection rules are sketched. In linear transport, only the ground state to ground state transition (solid line) contributes to the conductance. At finite transport voltage, additional transitions between excited states contribute. Since the transition to the highest state (dotted–dashed) is a 'dead end', the current is reduced when the voltage is raised to a value that allows the system to enter state **e**.

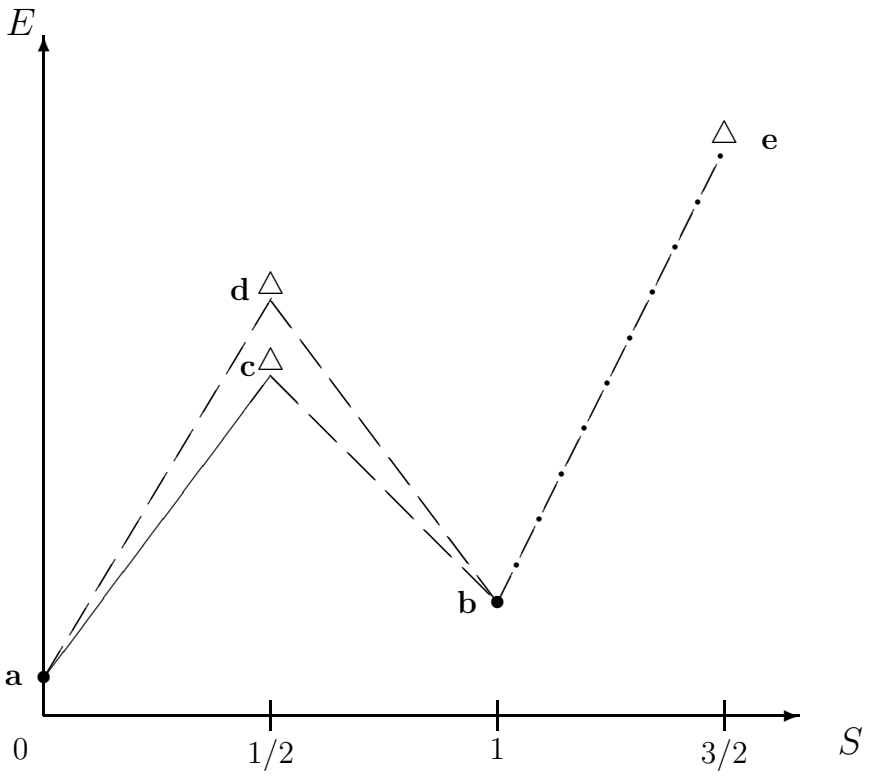

Figure 12.6: Dot states for $n = 2$ and $n = 3$, versus total spin and energy. The lines represent transitions being allowed by the selection rules. Since the transition to the highest state is a 'dead end', the current is reduced when the voltage is raised to a value that allows to enter the highest state.

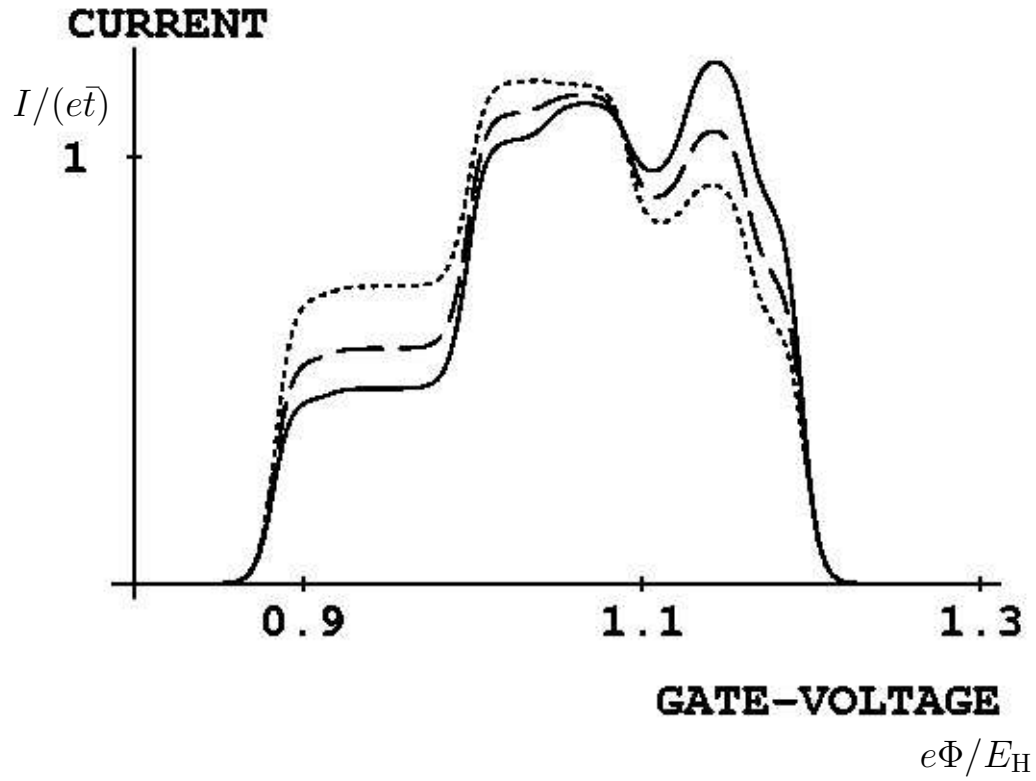

Figure 12.7: The splitting of the fourth conductance peak at $\mu_{\rm L} = 0.3E_{\rm H}$ and $\mu_{\rm R} = 0$ of a dot described by the correlated electron model (parameters as in Figure 12.3). Dashed, dotted and solid lines correspond to $t^{\rm R}/t^{\rm L} = 1$, 0.5 and 2, respectively.

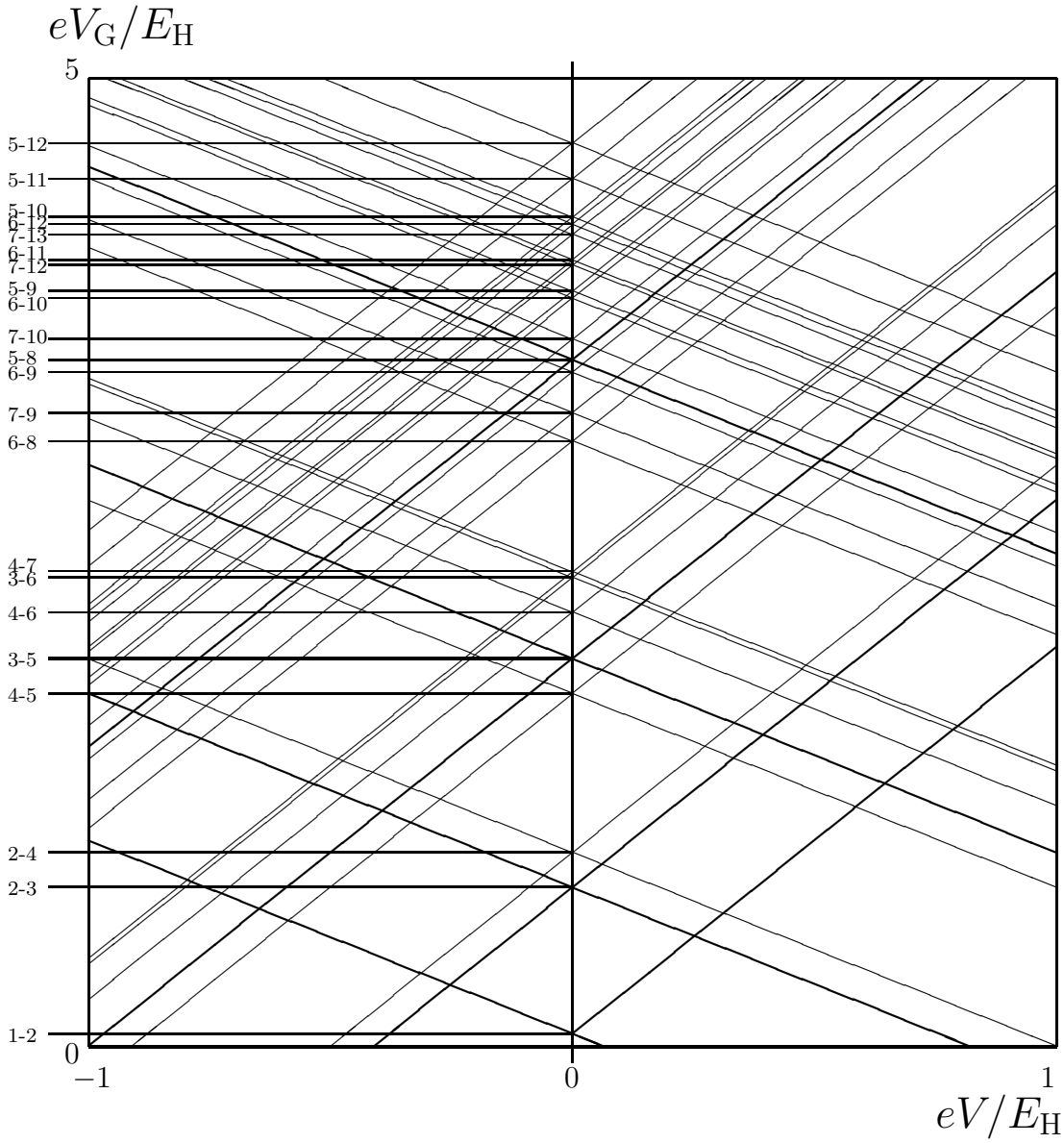

Figure 12.8: The lines corresponding to the energetic distances between the many–electron levels in the V–V_G plot. Thick lines represent ground state to ground state transitions while thin lines involve excited levels. The numbers at the left indicate the states (according to Table 12.3) between which the corresponding transition takes place.

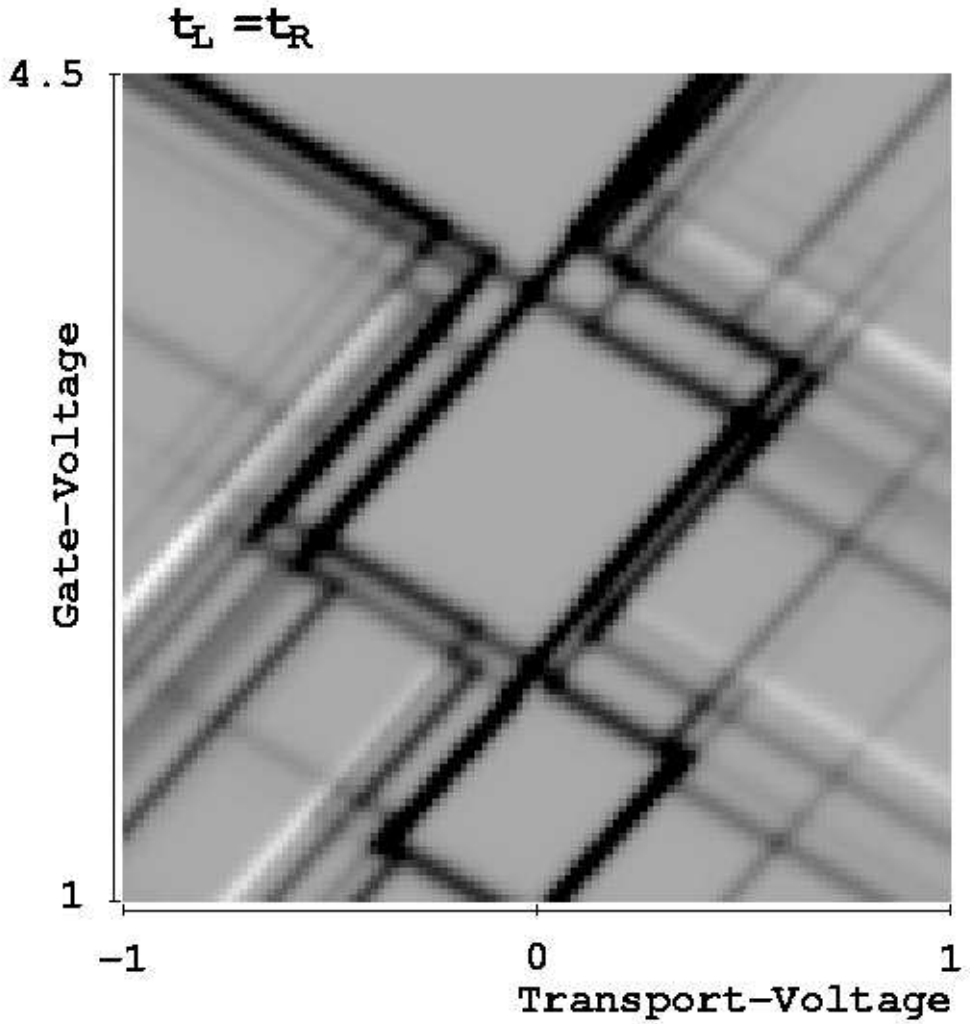

Figure 12.9: Differential conductance versus gate– $V_{\rm G}$ and transport–voltage V in units of $E_{\rm H}/e$ for symmetrical coupling to the leads. The zero value inside the diamond shaped Coulomb blockade regions corresponds to grey. Dark and bright parts indicate positive and negative differential conductances, respectively.

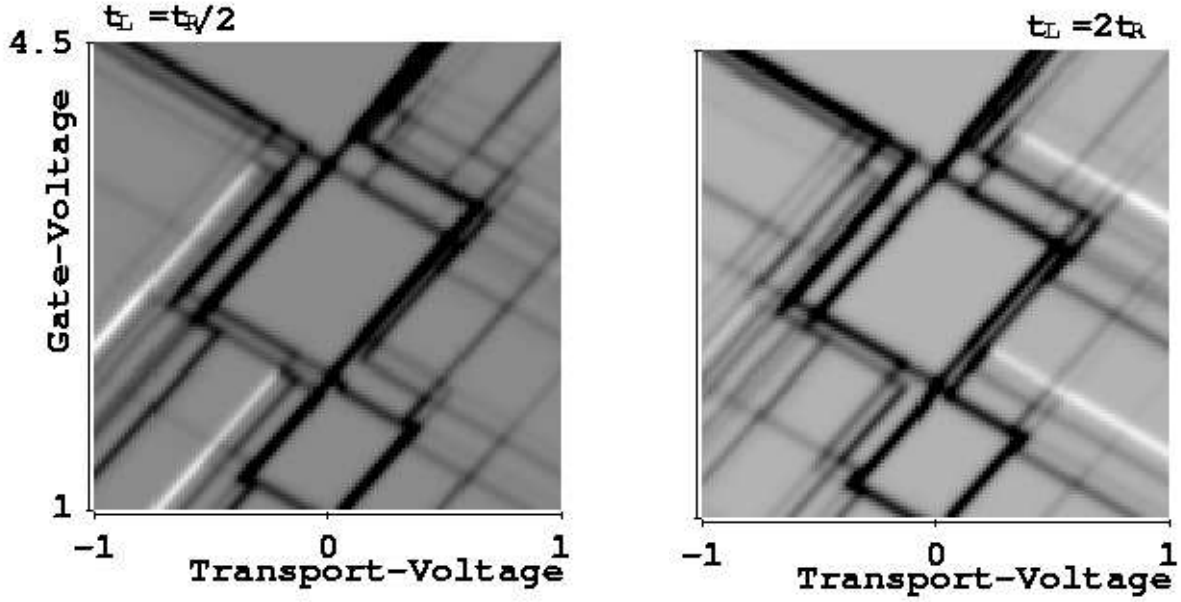

Figure 12.10: Differential conductance versus gate–voltage $V_{\rm G}$ and transport–voltage V in units of $E_{\rm H}/e$. The zero value inside the diamond shaped Coulomb blockade regions corresponds to grey. Dark and bright parts indicate positive and negative differential conductances, respectively. The couplings between the dot and the leads have been assumed to be unequal $t_{\rm L} = t_{\rm R}/2$ (left) and $t_{\rm L} = 2t_{\rm R}$ (right). Thus, the transitions through the left/right barrier limit the current and bright regions occur mainly when the less transmitting barrier is attached to the lower of the chemical potentials.

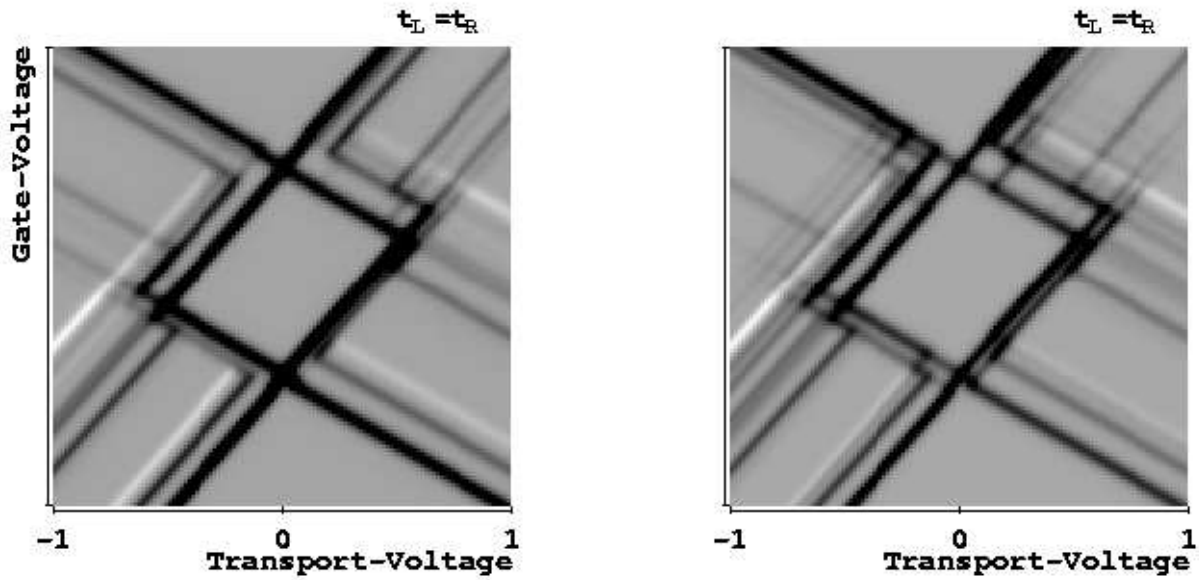

Figure 12.11: The differential conductance through a quasi–one dimensional quantum dot is calculated taking into account the exact transition matrix elements between the many–electron dot states and plotted as a function of the gate– and the transport–voltage in units of $E_{\rm H}/e$ (left). For comparison, the result using only the spin Hilbert space part in determining the transition rates is shown (right). Only transitions between states with 2, 3, and 4 electrons in the dot have been taken into account.

Chapter 13

Magnetic field effects

Investigating the influence of a magnetic field can provide more informations about the electronic states in the system. In particular, the Zeeman effect changes the energies of states with different magnetic quantum numbers and allows to compare the predictions of the spin blockade theory with the experimental data.

Since we are dealing with a one dimensional model, the magnetic field can influence solely the magnetic moments of the electrons only and is accounted for by a Zeeman term in the Hamiltonian. This is a reasonable model for the situation in the experiments of reference [32] if the effects of spin–orbit coupling can be neglected. There, the dots are quasi–two dimensional. In contrast to experiments, where Landau levels emerge [35] and even tunneling between them can be observed in a strong perpendicular magnetic field [140], the field is applied in a direction parallel to the plane of the interface in which the two dimensional electron gas is formed. A magnetic field parallel to the 2D plane has only weak influence on the spatial part of the dot electron wave functions if the magnetic length remains large as compared to the thickness of the 2D electron gas.

The main effect, a Zeeman splitting of the quantum dot levels is observed [24, 32, 36] by nonlinear transport spectroscopy, where two slopes can be seen in the dependence of the dot excitations on the magnetic field [24, 32]. If Zeeman and finestructure energies become comparable in magnitude, level crossings change the spin values of the ground states. This may occur either in the n or in the $n-1$ electron ground state leading to oscillatory motions of the linear conductance peak with magnetic field as observed in reference [33]. In this particular experiment, the dot has been defined under a gate tip and its geometry is quite unclear. Nevertheless, the measurements suggest, that the Zeeman splitting is the main effect of the magnetic field at least for low fields.

However, the quantization energy connected with the constriction in the transversal direction of the two–dimensional electron gas depends on the magnetic field in the plane [141] causing the main effect in the experiment of references [32, 36]. We take into account only the influence of the interaction of the spin of the electrons with the magnetic field. The only effect of the magnetic field in the Hamiltonian of the dot (8.4) can be written in the form of the additional Zeeman term

$$H_{\mathrm{Z}} = \sum_i g\mu_{\mathrm{B}} B M_i |\Psi_i^{\mathrm{D}}\rangle\langle\Psi_i^{\mathrm{D}}| \,, \tag{13.1}$$

where g is the Landé factor, μ_{B} is the Bohr magneton, B the magnetic field and M_i the

magnetic quantum number of the many–electron state $\mid \Psi_i^{\mathrm{D}} \rangle$.

This term leads to a splitting of the energy levels of the many–electron states which differ only in the magnetic quantum number and are degenerated in the absence of a magnetic field. In the reservoirs, outside the quantum dot, the influence of the magnetic field changes slightly the density of states at the Fermi energy for the different spin directions but the Fermi energy itself which is determined by the externally applied voltages is not modified. In the experimentally relevant regime $E_{\mathrm{F}} \gg g\mu_{\mathrm{B}}B$, this effect of the magnetic field on the densities of states can be neglected.

13.1 Linear Transport

For linear transport, only the many–electron ground states are relevant. Now, depending on the magnetic field, the energy of the states changes according to

$$E_i(B) = E_i(0) + g\mu_{\mathrm{B}}BM_i\,. \tag{13.2}$$

States with high spin and negative magnetic quantum number eventually become lower in energy than the ground state at zero magnetic field. According to a theorem by Lieb and Mattis [145], the ground state is a state with lowest total spin.

A schematic view of the dependence of the energies of the two–electron states and the three–electron states on the magnetic field is shown in Figure 13.1. Several level crossings occur and it can be seen how the ground state to ground state transition energy depends on the magnetic field. This is reflected in the numerical result of Figure 13.2 where we calculated the differential conductance as a function of the gate–voltage and the magnetic field at zero bias–voltage.

The result shows oscillatory behavior of the peak position as a function of the magnetic field as observed experimentally [33]. At high magnetic fields, the spin polarized states are ground states for all electron numbers leading to a decreasing energy difference with increasing magnetic field. Since in one–dimensional correlated systems the ground state spin at $B = 0$ is zero or $1/2$ depending on the parity of the electron number, the energy difference between ground states decreases with low increasing B when the lower electron number is even. If, on the other hand, the lower of the two electron numbers is odd, the energy difference increases with increasing magnetic field and the corresponding conductance peak moves to higher values of the gate–voltage. This parity effect can be seen in the numerical data presented in Figure 13.2.

13.2 Finite Voltage

At finite voltages, not only the ground state to ground state transitions occur. Between the lines which appear when the ground state to ground state transition energy crosses the chemical potential in the left and right lead the transitions still lead to structure even when one of the states is no longer the ground state for the given magnetic field.

The results are shown in Figure 13.3. Plotting the differential conductance as a function of gate– and transport–voltage at different magnetic fields shows how the energy

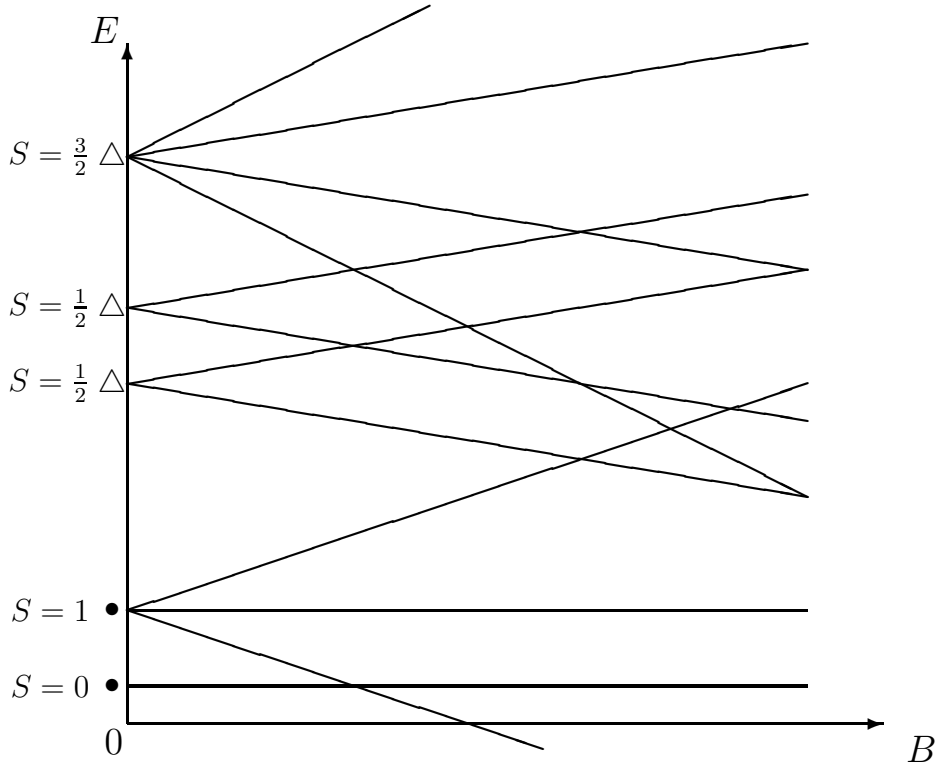

Figure 13.1: The energy dependence of dot states for $n_i = 2$ (•) and $n_i = 3$ (△) on the magnetic field (schematically). The Zeeman splitting leads to level crossings and therewith changes the ground state.

differences $E_j - E_i$ which correspond to transitions between (excited) eigenstates $\mid \Psi_i^{\mathrm{D}}\rangle$ and $\mid \Psi_j^{\mathrm{D}}\rangle$ of the dot with different electron numbers $n_j = n_i + 1$ change with the Zeeman splitting.

In our model, the shift of the lines with nonzero differential conductance is directly connected to the differences in magnetic quantum numbers $\Delta M = M_j - M_i = \pm 1/2$. For $\Delta M = +1/2$, the energy difference is increased and the line corresponding to the transition is shifted upwards in the direction of positive gate–voltage. For $\Delta M = -1/2$, the contrary is the case and the line of resonance is shifted to lower gate–voltages.

Since the change in the energy of an eigenstate of the dot induced by the magnetic field depends on the magnetic quantum number of the state, the field influences the order of the states with different spins on the energy scale. Therefore, the weight of some of the transitions is changed. The most spectacular effects of this kind are transitions entering the Coulomb blockade regime which consequently become completely suppressed as can be seen in Figure 13.3.

Furthermore, the spin blockade leading to negative differential conductance is sup-

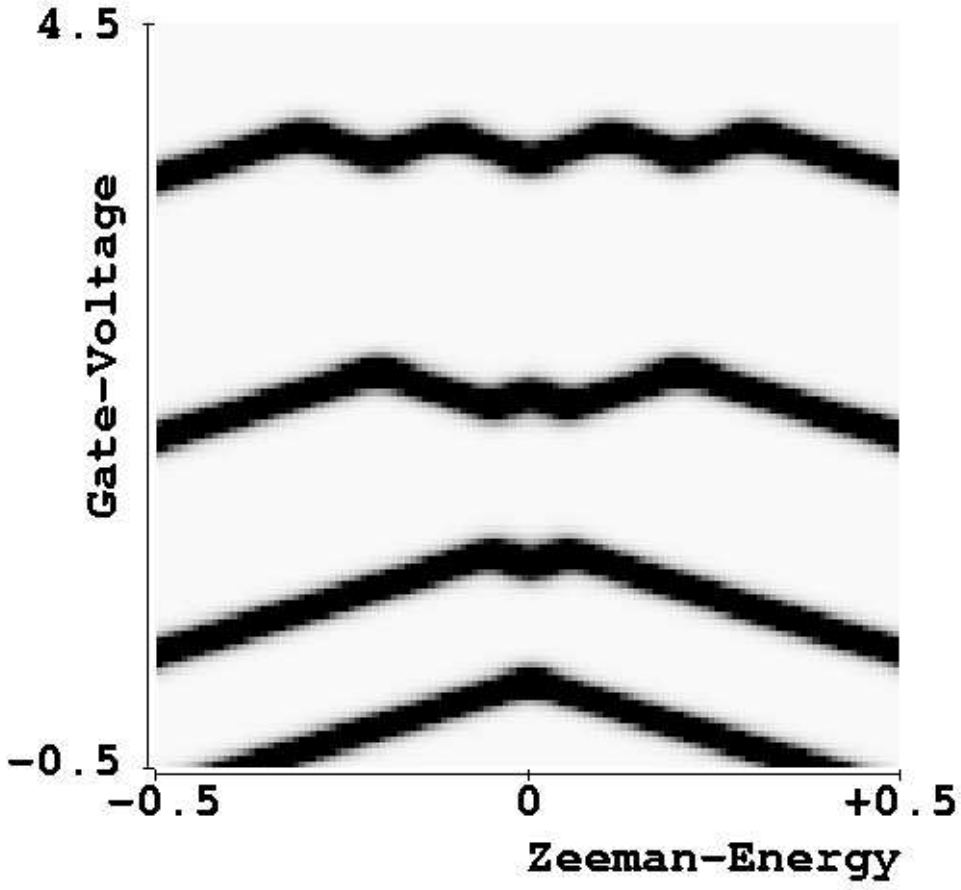

Figure 13.2: Differential Conductance at zero bias voltage as a function of the Zeeman energy $g\mu_{\mathrm{B}}B$ and the gate–voltage in units of E_{H} and E_{H}/e, respectively.

pressed by high magnetic fields. As soon as the component of the state with maximum spin $n/2$ becomes the ground state for a given electron number, the ground state to ground state transition is among the ones that contribute only poorly to the current. Then the increase of the voltage opens the transitions to other (excited) states which can contribute more and do not lead to a decrease of the current occurring only if the added transitions are weaker than the transitions that were present before. A series of greyscale plots of the differential conductance at different magnetic fields is shown in Appendix E.

As expected the negative differential conductances decrease considerably when the Zeeman energy exceeds the level spacing. This is consistent with recent experiments [36], where, due to the two–dimensionality of the dot, the states with highest spin are not the energetically highest states at zero magnetic field and the negative differential conductances appear quite close to the linear voltage regime [24]. Therefore, the Zeeman splitting needed to suppress the regimes of negative differential conductance is lower in their situation.

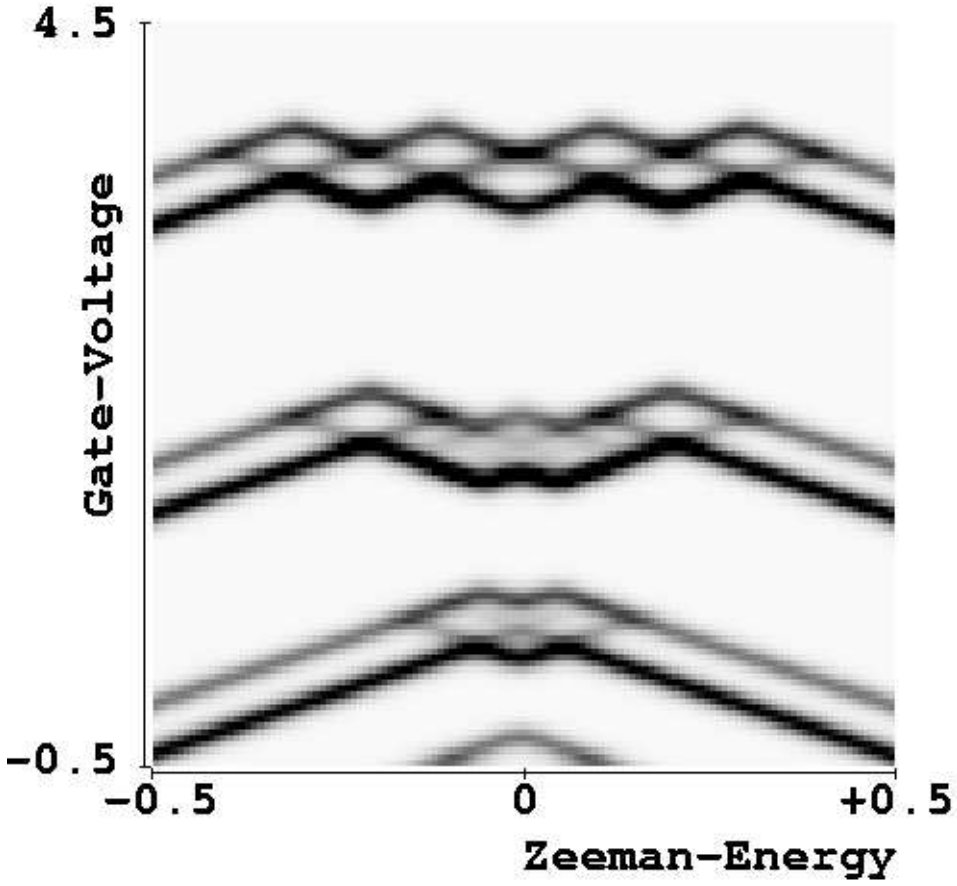

Figure 13.3: Differential Conductance at bias voltage $V = 0.1\,E_{\rm H}$ as a function of the Zeeman energy and the gate–voltage in units of $E_{\rm H}$ and $E_{\rm H}/e$, respectively.

Chapter 14

Two–dimensional square shaped dots

The basic mechanism of the spin blockade effect was discovered by using a one–dimensional (1D) model to determine the electronic spectrum of the quantum dot [25] as described in Chapter 12.

In this chapter we consider square quantum dots in order to investigate the influence of the dimensionality on this blockade effect. The spectrum of two dimensional square shaped dots shows qualitative differences as compared to the one dimensional model. We present novel results which are associated with low lying excited states that do not necessarily have maximum spin. We show that even in the linear transport regime the current may be suppressed by spin effects, namely if the total spins of the ground states of successive electron numbers differ by more than 1/2. This leads to characteristic temperature and transport–voltage dependences of the conductance peaks. Finally, we demonstrate that negative differential conductances can occur close to a conductance peak already at very low transport–voltages, if an excited state with large (not necessarily maximum) total spin lies energetically close to the ground state.

14.1 Spectrum of correlated electrons in two dimensions

There are several papers treating correlated electrons in two–dimensional systems. Most of them are dealing with dots having rotational symmetry and are restricted to very low electron numbers as e.g. [147] or the investigations of ground states only [146].

In the low density regime the low lying excitation spectrum can be calculated for Coulombically interacting electrons including their spin degree of freedom in square shaped quantum dots using the pocket state approximation [121]. There, results for up to five electrons are available. Roughly speaking, this approach takes into account the quantum corrections arising from tunneling between different minimum energy configurations of classical point charges. The low energy excitation spectrum for interacting electrons in a square shaped dot with hard wall boundaries calculated in the low electron density limit [121] is listed in Table 14.1. The ground state energies can be estimated in this limit using point charges in the clasically most favorable configurations. For the numerical calculations of the conductance, we used $E_0(1) = 0.23\,E_{\mathrm{H}}$, $E_0(2) = 0.30\,E_{\mathrm{H}}$,

Table 14.1: Analytical values [121] for the fine structure excitation spectrum $E_\alpha - E_0(n)$ of a square–shaped quantum dot in the low electron density limit for $n \leq 5$. S refers to the total spin. The energy units t_n (tunneling integrals) are explained in [121]. In some cases, states with different total spin are degenerate due to the high symmetry of the problem.

n_α	S_α	$E_\alpha - E_0(n)$
2	0	0
2	1 , 1	$2t_2$
2	0	$4t_2$
3	1/2 , 1/2 , 3/2	0
3	1/2 , 1/2 , 1/2 , 1/2 , 3/2 , 3/2	$2t_3$
3	1/2 , 1/2 , 3/2	$4t_3$
4	0	0
4	1	$2t_4$
4	1 , 1 , 0	$4t_4$
4	2	$6t_4$
5	3/2	0
5	1/2 , 1/2 , 1/2	t_5
5	1/2 , 1/2	$3t_5$
5	3/2 , 3/2 , 3/2	$4t_5$
5	5/2	$5t_5$

$E_0(3) = 0.97\,E_\mathrm{H}$, $E_0(4) = 1.90\,E_\mathrm{H}$ and $E_0(5) = 3.40\,E_\mathrm{H}$ for the ground state energies. The tunneling integrals have been estimated to be $t_2 = 0.015\,E_\mathrm{H}$, $t_3 = 0.04\,E_\mathrm{H}$, $t_4 = 0.05\,E_\mathrm{H}$ and $t_5 = 0.065\,E_\mathrm{H}$.

14.2 Spin blockade type II

The 'spin blockade of the first kind' has been discussed in chapter 12. It is related to the occupation of states with maximal spin $S = n/2$. They occur as excited states both in 1D [120] and in 2D [121] quantum dots. This spin blockade phenomenon appears at transport–voltages of the order of the excitation energies of the $S = n/2$ states.

The 'spin blockade of the second kind' occurs if the total spins of the ground states that correspond to successive electron numbers n and $n \pm 1$ differ by more than 1/2. It can even be observed in linear transport, namely when

$$(n,\ \text{ground state},\ S) \longrightarrow (n \pm 1\,,\ \text{ground state},\ S') \quad \text{with} \quad |S - S'| > 1/2\,. \tag{14.1}$$

Then the dot is blocked in the n– or the $n-1$–electron ground state and the corresponding peak in the linear conductance is missing at zero temperature. At finite temperatures and/or transport–voltages excited states with appropriate spin values can be occupied. This can lead to the recovery of a spin forbidden conductance peak with temperature that was indeed observed experimentally [33]. The spin blockade of the second kind (14.1) is

specific for 2D quantum dots. In 1D the Lieb and Mattis theorem [145] guarantees that the spins of the ground states are always 0 or 1/2 (depending of the parity of n). Thus in a 'slim' quantum dot no linear conductance peak should be missing in contrast to 2D dots.

Figure 14.1 shows the grey scale plot of the differential conductance through a square, hard wall quantum dot. One prominent feature is the missing of the linear conductance peak corresponding to the transition between $n = 4$ and $n = 5$ electrons. The reason is that the spins of the ground states are $S = 0$ ($n = 4$) and $S = 3/2$ ($n = 5$). Either finite transport voltages or finite temperatures can reestablish the conductance via transport through excited states with spins $S = 1$ ($n = 4$) and $S = 1/2$ ($n = 5$). The voltage– or temperature–induced recovery of the conductance is shown in Figure 14.2.

In addition, states with high spin but not necessarily completely spin–polarized ($S = n/2$), which are energetically situated close to the ground state, can cause blocking phenomena. This is demonstrated for the transition between $n = 3$ and $n = 4$ in Figure 14.3a. In contrast to the spin blockade of the first kind, (14.1) can lead to negative differential conductances even close to the linear conductance peak. The reason is that the $n = 3$ ground states for $S = 3/2$ and $S = 1/2$ are (almost) degenerate in a square dot.

The most important levels are shown schematically in Figure 14.4. Within the Coulomb blockade region all transition rates that increase the electron number are exponentially small. At $V = 0$ the system is in thermal equilibrium and the three electron ground states are populated according to their degeneracies. Already a slightly increased voltage changes the ratio between them by orders of magnitude, thus favoring the occupation of the $S = 3/2$ state **b** (cf. Figure 14.3b). This is due to a delicate interplay between multiple transitions that connect eventually the $n = 3$ ground states via at least three intermediate states. There is a competition between processes like **a**→**d**→**c**→**e**→**b** transferring the system in the spin polarized ground state with the process **b**→**e**→**a**. Direct transitions from the $S = 3/2$ state to the $n = 4$ ground state are spin forbidden which causes the pronounced negative differential conductance at low voltages.

Since this degeneracy is an artifact of the high symmetry of the model considered, we can lift it by enhancing slightly the energy of the lowest $n = 3; S = 3/2$ state. Figure 14.5 shows (a) the differential conductance and (b) the stationary occupation probability of this state.

Now, the region of negative differential conductance is shifted in V by the excitation energy of the $S = 3/2$ state **b**. When the $(n = 3; S = 3/2)$ state starts to contribute to the transport, it attracts a large portion of the population at the expense of the $(n = 3; S = 1/2)$ ground state **a**. This suppresses the ground state to ground state transition. Only at even higher voltages the $S = 3/2$ state can again be depopulated and the line corresponding to transport involving the ground states is recovered. Striking features like this can also be detected in the greyscale representations of the experimental results [24, 36].

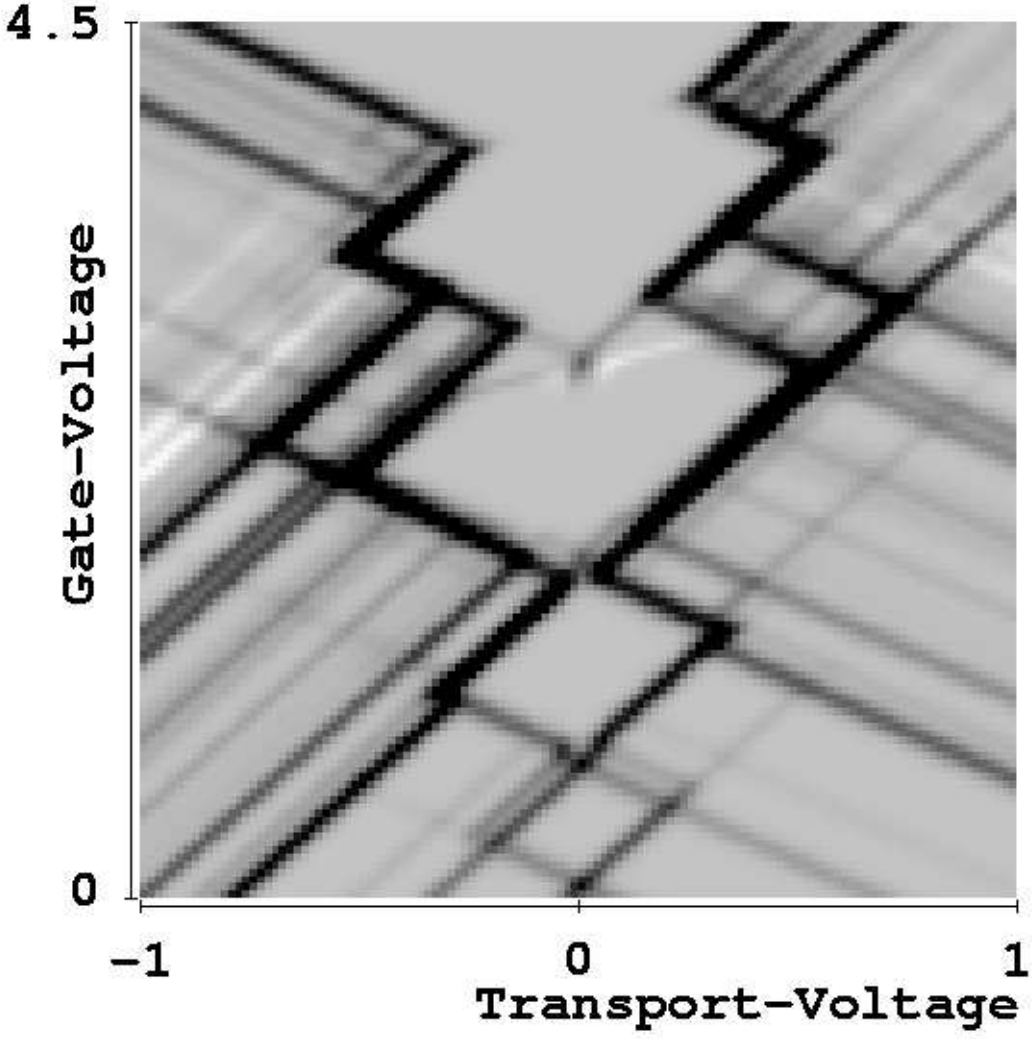

Figure 14.1: Differential conductance versus gate–voltage $V_{\rm G}$ and transport–voltage V in units of $E_{\rm H}/e$. The spectrum for a 2D square–shaped dot is used. The transition between the ground states for $n = 4$ and $n = 5$ is forbidden by the spin selection rules and the corresponding lines that should cross on the $V_{\rm G}$–axis are missing.

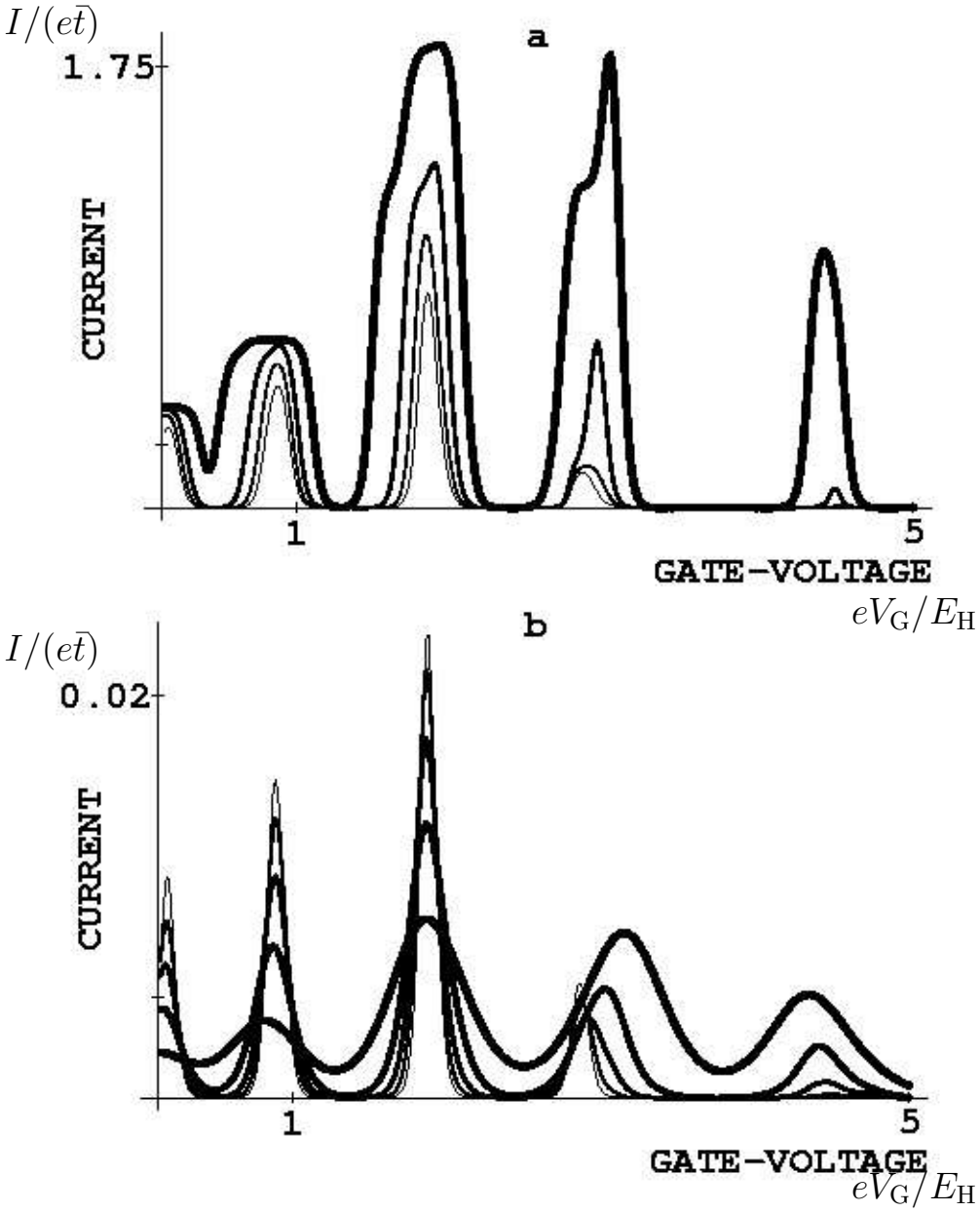

Figure 14.2: Current versus gate voltage for a square–shaped quantum dot containing few electrons. In a) the transport voltage is increased. According to the thickness of the lines, it takes the values $V = 0.04, 0.06, 0.1, 0.2E_H/e$. In b) the temperature is increased. Thin to thick lines correspond to $\beta E_H = 100, 80, 60, 40, 20$. The missing peak in linear conductance corresponding to oscillations between $n = 4$ and $n = 5$ electrons is recovered. The peak corresponding to the transition between $n = 3$ and $n = 4$ electrons behaves un–normally because the ground state to ground state coupling is very weak and the increased temperature/voltage allows to involve many excited levels.

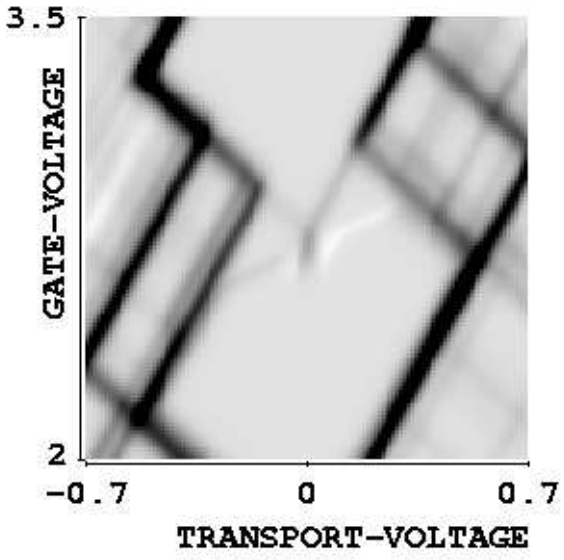

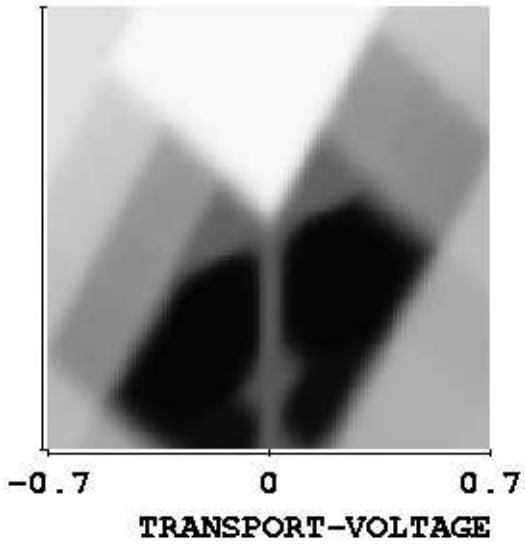

Figure 14.3:
a) : Region around the transition between $n = 3$ and $n = 4$, magnified and with the energy of the $S = 3/2$ state being degenerate with the $n = 3$ $S = 1/2$ ground state. At low but finite transport voltage the $S = 3/2$ ground state becomes populated. Transitions to the $n = 4$ ground state are spin forbidden. Negative differential conductances appear.

b) : Same region as in a) but now showing the relative population of the $n = 3$, $S = 3/2$ state (**b** in Figure 14.4 in dark. If the transport voltages are sufficient to occupy the $S = 3/2$ state it is easily populated but depopulation is difficult.

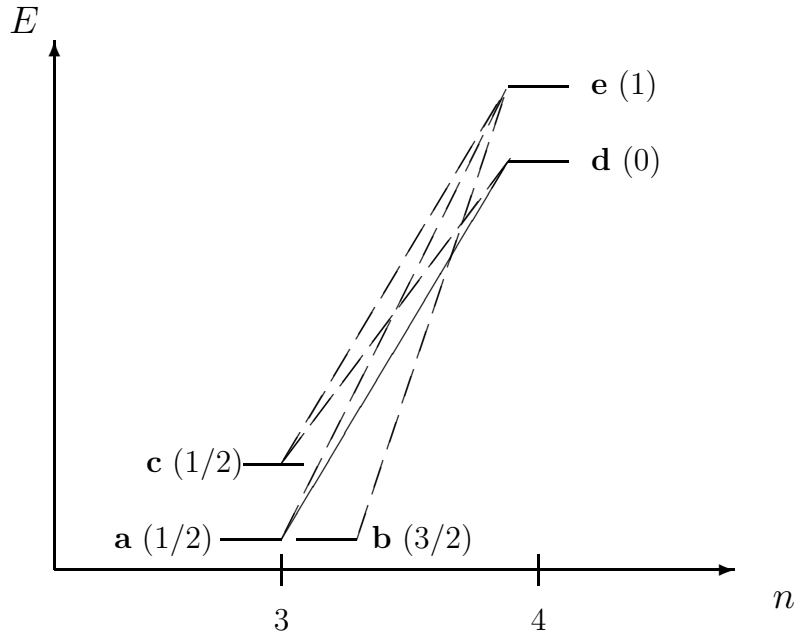

Figure 14.4: Some dot states for $n = 3$ and $n = 4$. The total spins S of the states are indicated in brackets next to the lines that represent the level. The lines represent transitions that are allowed by the selection rules. Note that the transition between one of the three electron ground states (**b**) to the four electron ground state **d** is forbidden. The unusual behavior in the vicinity of the corresponding linear conductance peak is due to these five levels. It is necessary to include them all to find the main features of Figure 14.3. Whether or not one includes further states in the calculations does not change the result qualitatively.

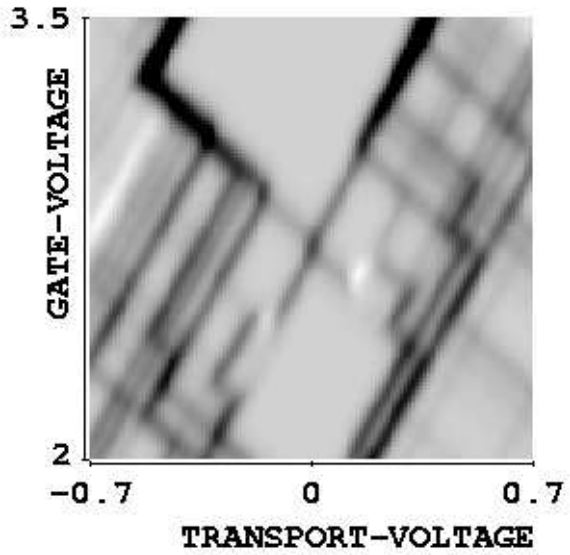

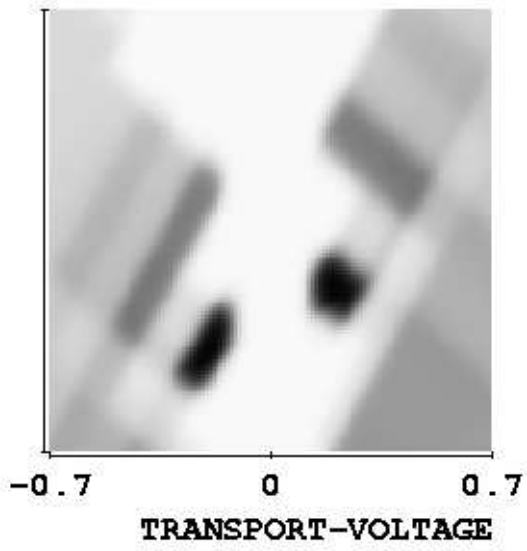

Figure 14.5:
a) : Region around the transition between $n = 3$ and $n = 4$, magnified and with the energy of the $S = 3/2$ state **b** being slightly increased so that the degeneracy of the $n = 3$ ground states is lifted. At low but finite transport voltage the ground state to ground state transition is blocked because state **b** attracts almost all of the stationary occupation probability. Thus, negative differential conductances appear.

b) : Same region as in a) but now showing the relative population of the $n = 3$, $S = 3/2$ state (**b**) in dark. If the transport voltages are sufficient to occupy the $S = 3/2$ state it is easily populated but depopulation is difficult.

Summary and conclusions

In summary, we have investigated nonlinear transport through a small quantum dot being weakly coupled to reservoirs taking into account Coulomb interactions, spin, magnetic field and in particular non–equilibrium effects. The studies have been carried out in the parameter regime where charging and geometrical quantization effects coexist.

For different model Hamiltonians occupation probabilities, current–voltage characteristics and conductances versus gate–voltage at finite bias voltage have been calculated using a master equation approach.

Within the conventional charging model, we investigated thermally induced intra–dot relaxation processes. They lead to a suppression of the n lowest finestructure steps in the n–th Coulomb step of the I–V curve. At finite bias voltages, the intra–dot relaxation results in thermal equilibrium only among the states with equal dot electron number. We have demonstrated explicitly that the stationary non–equilibrium populations cannot be described by a Gibbs distribution. Consistent with previous studies we find additional steps in the Coulomb staircase corresponding to transitions involving excited levels when the temperature is lower and the transport voltage higher than the excitation energies. We find pronounced asymmetries in the conductance peaks versus gate–voltage caused by asymmetric barriers, consistent with experimental findings.

Taking into account the quantum mechanics of Coulombically interacting electrons including their spins, we have demonstrated that spin selection rules can strongly influence the transport properties of semiconducting quantum dots where electron correlations are important. The excitations of the n–electron system cannot be described by the occupation of single electron states, and the spins of all electrons are influenced by the entering or leaving electrons. The transition amplitude between spin states is proportional to the square of the vector coupling (Clebsch–Gordan) coefficients. The corresponding selection rules lead to a spin blockade effect and explain in a natural way various experimentally observed features which qualitatively cannot be accounted for within the charging model where excitations are treated like single particle excitations.

We have proposed two qualitatively different types of spin blockades. They influence the heights of the linear conductance peaks and lead to nonlinear differential conductances which may even become negative. While the spin blockade of the first kind is connected with highly excited spin–polarized states, the spin blockade of the second kind is a more general mechanism which leads to qualitative changes even in linear transport, and is particularly relevant for 2D quantum dots.

The effects of an in–plane magnetic field have been discussed and are in agreement with recent experiments [24, 32, 33, 36]. The positions of the conductance peaks on the gate–voltage axis change with magnetic field and exhibit a parity depending behavior at low

fields in quasi–one dimensional quantum dots. Level crossings lead to oscillating positions with magnetic field. The typical spin blockade phenomena disappear at sufficiently high magnetic fields when the spin polarized states of the dot become the ground states.

All of the theoretically predicted features described above are qualitatively consistent with experiments [24, 28, 29, 30, 31, 34, 35, 33]. Thus, the spin blockade effect is very likely to be the mechanism which causes negative differential conductances. Further experiments, in particular using 'slim quantum dots', are however necessary in order to clarify the quantitative aspects.

In experimental situations where the total spin of the electrons in the dot is not stable over timescales being long as compared to the tunneling time, the spin blockade is expected to disappear. Introducing an inhomogeneous magnetic field in the dot region (e.g. using type II superconductors on top of the structure) or irradiating the sample with the proper ESR frequencies might be a way to confirm unambiguously the relevance of the spin blockade mechanism for transport. Such experiments are highly desirable and can in principle be carried out [148].

Appendix A

The coefficient of the second order term in the low frequency expansion of the conductance

The formally exact expression (2.19) for the frequency dependent conductance of a single rectangular barrier is calculated in chapter 1. For $b = l$, the expansion with respect to the frequency has been performed using the algebraic formula manipulation program Mathematica^{TM} on an IBM RISC workstation. The zero temperature result for the coefficient of the second order term is

$$\Gamma_2 = \frac{8}{\pi b^2}\left(\frac{Z_1}{N_1} + \frac{Z_2}{N_2} + \frac{Z_3}{N_3}\right), \tag{A.1}$$

where

$$\begin{aligned}
Z_1 \;=\;& 4\,b^2\,\kappa_{\rm F}^3\,k_{\rm F}^2\,\cosh^4 a - 2\,b^3\,\kappa_{\rm F}^4\,k_{\rm F}^2\,\cosh a\,\sinh a \\
&+2\,b^3\,\kappa_{\rm F}^2\,k_{\rm F}^4\,\cosh a\,\sinh a - 8b\,\kappa_{\rm F}^2\,k_{\rm F}^2\,\cosh^5 a\,\sinh a \\
&-b^4\,\kappa_{\rm F}^3\,k_{\rm F}^4\,\sinh^2 a - 8b\,k_{\rm F}^4\,\cosh^3 a\,\sinh^3 a \\
&+4\,b^2\,\kappa_{\rm F}^3\,k_{\rm F}^2\,\cosh^2 a\,\sinh^4 a + 4\,b^2\,\kappa_{\rm F}\,k_{\rm F}^4\,\cosh^2 a\,\sinh^4 a \qquad \text{(A.2)} \\
Z_2 \;=\;& -24\,b^2\,\kappa_{\rm F}^6\,k_{\rm F}^4\,\cosh^2 a + 3\,b^4\,\kappa_{\rm F}^6\,k_{\rm F}^6\,\cosh^2 a \\
&-12\,b^2\,\kappa_{\rm F}^6\,k_{\rm F}^4\,\cosh^4 a + 2\,b^4\,\kappa_{\rm F}^8\,k_{\rm F}^4\,\cosh^4 a \\
&+24\,b^2\,\kappa_{\rm F}^{10}\,\cosh^6 a - 24\,b^3\,\kappa_{\rm F}^5\,k_{\rm F}^6\,\cosh a\,\sinh a \\
&-24\,b^3\,\kappa_{\rm F}^7\,k_{\rm F}^4\,\cosh^3 a\,\sinh a - 30\,b^3\,\kappa_{\rm F}^5\,k_{\rm F}^6\,\cosh^3 a\,\sinh a \\
&+96\,b\,\kappa_{\rm F}^5\,k_{\rm F}^4\,\cosh^5 a\,\sinh a - 12\,b^3\,\kappa_{\rm F}^7\,k_{\rm F}^4\,\cosh^5 a\,\sinh a \\
&-9\,b^4\,\kappa_{\rm F}^4\,k_{\rm F}^8\,\sinh^2 a - 2\,b^4\,\kappa_{\rm F}^6\,k_{\rm F}^6\,\cosh^2 a\,\sinh^2 a \\
&+48\,b^2\,\kappa_{\rm F}^8\,k_{\rm F}^2\,\cosh^4 a\,\sinh^2 a + 36\,b^2\,\kappa_{\rm F}^6\,k_{\rm F}^4\,\cosh^4 a\,\sinh^2 a \\
&-4\,b^4\,\kappa_{\rm F}^8\,k_{\rm F}^4\,\cosh^4 a\,\sinh^2 a + 72\,b^2\,\kappa_{\rm F}^4\,k_{\rm F}^6\,\cosh^4 a\,\sinh^2 a \\
&-48\,\kappa_{\rm F}^4\,k_{\rm F}^4\,\cosh^8 a\,\sinh^2 a - 6\,b^3\,\kappa_{\rm F}^3\,k_{\rm F}^8\,\cosh a\,\sinh^3 a \\
&+96\,b\,\kappa_{\rm F}^3\,k_{\rm F}^6\,\cosh^3 a\,\sinh^3 a - 24\,b^3\,\kappa_{\rm F}^5\,k_{\rm F}^6\,\cosh^3 a\,\sinh^3 a \\
&-8\,b^4\,\kappa_{\rm F}^6\,k_{\rm F}^6\,\cosh^2 a\,\sinh^4 a + 60\,b^2\,\kappa_{\rm F}^2\,k_{\rm F}^8\,\cosh^2 a\,\sinh^4 a \\
&-4\,b^4\,\kappa_{\rm F}^4\,k_{\rm F}^8\,\cosh^2 a\,\sinh^4 a - 96\,\kappa_{\rm F}^2\,k_{\rm F}^6\,\cosh^6 a\,\sinh^4 a
\end{aligned}$$

$$
\begin{aligned}
& -12\,b^3\,\kappa_{\rm F}^3\,k_{\rm F}^8\,\cosh a\,\sinh^5 a - 48\,k_{\rm F}^8\,\cosh^4 a\,\sinh^6 a && \text{(A.3)}\\
Z_3 \;=\;& 6\,b^3\,\kappa_{\rm F}\,k_{\rm F}^4\,\cosh^3 a\,\sinh a + 10\,b^3\,\kappa_{\rm F}^3\,k_{\rm F}^2\,\cosh a\,\sinh a\\
& +6\,b^3\,\kappa_{\rm F}^3\,k_{\rm F}^2\,\cosh^3 a\,\sinh a + b^4\,\kappa_{\rm F}^2\,k_{\rm F}^4\,\cosh^2 a\\
& -2\,b^4\,\kappa_{\rm F}^2\,k_{\rm F}^4\,\cosh^2 a\,\sinh^2 a - 16\,b^2\,\kappa_{\rm F}^2\,k_{\rm F}^2\,\cosh^2 a\\
& -3\,b^4\,\kappa_{\rm F}^4\,k_{\rm F}^2\,\sinh^2 a - 2\,b^4\,\kappa_{\rm F}^4\,k_{\rm F}^2\,\sinh^4 a && \text{(A.4)}\\
N_1 \;=\;& 256\,\kappa_{\rm F}\,\cosh^2 a\left(\kappa_{\rm F}^2\,k_{\rm F}^2 + \left(\kappa_{\rm F}^2 + k_{\rm F}^2\right)^2\cosh^2 a\,\sinh^2 a\right)^2 && \text{(A.5)}\\
N_2 \;=\;& -3072\,\kappa_{\rm F}^4\,k_{\rm F}^2\,\cosh^2 a\left(k_{\rm F}^2\cosh^2 a + \kappa_{\rm F}^2\sinh^2 a\right)\\
& \times\left(\kappa_{\rm F}^2\cosh^2 a + k_{\rm F}^2\sinh^2 a\right)^3 && \text{(A.6)}\\
N_3 \;=\;& -1024\,\cosh^2 a\left(k_{\rm F}^2\cosh^2 a + \kappa_{\rm F}^2\sinh^2 a\right)^3\left(\kappa_{\rm F}^2\cosh^2 a + k_{\rm F}^2\sinh^2 a\right). && \text{(A.7)}\\
& && \text{(A.8)}
\end{aligned}
$$

For brevity, we have set $e = 2m^* = \hbar = 1$ and used the abbreviations

$$
\begin{aligned}
a &= b\,\frac{\kappa_{\rm F}}{2}\\
k_{\rm F} &= \sqrt{E_{\rm F}}\\
\kappa_{\rm F} &= \sqrt{V - E_{\rm F}}\,. && \text{(A.9)}
\end{aligned}
$$

We want to stress again that this is an exact result within linear response theory.

Appendix B

Interactions between the electrons in the structure

In this appendix, we start from the Hamiltonian taking fully into account the interactions between all of the electrons in the structure. We give some rough arguments for the reduction of the problem to an effective Hamiltonian where only the interaction between the electrons in the dot remains in its explicit form. The interaction with the electrons in the leads is reduced to an electrostatic potential for the dot electrons and included in the Hamiltonian of the dot. Being interested in the behavior of the system in the presence of very weak coupling to the leads, we treat the tunneling in lowest order perturbation theory and therefore do not have to take the tunneling terms into account in this investigation concerned with properties of the unperturbed system.

B.1 Full Hamiltonian of interacting electrons

The full Hamiltonian for all the electrons in all of the electrodes including the gate and the dot reads (without tunneling terms)

$$H = H^0_{\mathrm{L}} + H^0_{\mathrm{R}} + H^0_{\mathrm{G}} + H^0_{\mathrm{D}} + H^{\mathrm{e-e}}\,, \tag{B.1}$$

where $H^0_{\mathrm{L/R}}$, H^0_{G} and H^0_{D} describe noninteracting electrons in the left/right lead, the gate and in the dot, respectively. The situation is shown schematically in Figure 8.1. The electron–electron interactions between all of the electrons in all the parts of the structure are represented by

$$H^{\mathrm{e-e}} = H^{\mathrm{e-e}}_{\mathrm{DD}} + H^{\mathrm{e-e}}_{\mathrm{LL}} + H^{\mathrm{e-e}}_{\mathrm{RR}} + H^{\mathrm{e-e}}_{\mathrm{GG}} + H^{\mathrm{e-e}}_{\mathrm{LD}} + H^{\mathrm{e-e}}_{\mathrm{RD}} + H^{\mathrm{e-e}}_{\mathrm{GD}} + H^{\mathrm{e-e}}_{\mathrm{LG}} + H^{\mathrm{e-e}}_{\mathrm{RG}} + H^{\mathrm{e-e}}_{\mathrm{LR}}\,, \tag{B.2}$$

which consists of many parts that are classified with respect to the electrodes in which the interacting electrons are located ($H^{\mathrm{e-e}}_{\mathrm{XY}}$ includes all the interactions between electrons in X and electrons in Y).

B.2 Interactions inside the leads

We assume to have very high electron densities in all of the electrodes such that they can be considered to be metallic regions of the sample where effective screening takes

place (see e.g.[86]). Therefore the 'diagonal' terms $H_{\mathrm{XX}}^{\mathrm{e-e}}$, $\mathrm{X} \in \{\mathrm{L}, \mathrm{R}, \mathrm{G}\}$ emerging from the interactions between electrons in the same electrode lead to a Fermi–liquid picture of effectively noninteracting particles with a slightly modified dispersion relation which will be described by the Hamiltonians

$$H_{\mathrm{X}} = H_{\mathrm{X}}^{0} + H_{\mathrm{XX}}^{\mathrm{e-e}} \tag{B.3}$$

with

$$H_{\mathrm{X}} = \sum_{k,\sigma} \varepsilon_{k,\sigma} c_{\mathrm{X},k,\sigma}^{+} c_{\mathrm{X},k,\sigma} \,. \tag{B.4}$$

Therefore it makes sense to speak about single particle levels in the leads. The chemical potentials there can be modified experimentally by applying external voltages.

B.3 Interactions inside the dot

In the dot, the electron–electron interactions are very important and lead to qualitative effects. Therefore, we take them into account exactly with the full Hamiltonian of the dot

$$H_{\mathrm{D}} = H_{\mathrm{D}}^{0} + H_{\mathrm{DD}}^{\mathrm{e-e}} \,, \tag{B.5}$$

where the explicit form is

$$H_{\mathrm{D}} = \sum_{m,\sigma} \varepsilon_{m} c_{m,\sigma}^{+} c_{m,\sigma} + \sum_{\substack{m_1,m_2,m_3,m_4 \\ \sigma_1,\sigma_2,}} V_{m_1 m_2 m_3 m_4} \, c_{m_1,\sigma_1}^{+} c_{m_2,\sigma_2}^{+} c_{m_3,\sigma_2} c_{m_4,\sigma_1} \tag{B.6}$$

with the single particle energies ε_m determined by the external confinement potential and the Coulomb matrix elements $V_{m_1 m_2 m_3 m_4}$.

B.4 Interactions between electrons in different spatial areas

The last three terms in (B.2) deal with interactions between electrons in different electrodes. They determine the capacitances between the electrodes and therefore the energy needed to establish the stationary state corresponding to the given voltages by charging these capacitors. Since, in contrast to time dependent problems [125], this effect is not relevant for our problem, and the distance between the different electrodes is large as compared to the distance between the dot region and the electrodes, we neglect these terms.

The interactions between electrons in the dot and electrons in the electrodes are however very important for the behavior of the structure. They are represented by the Hamiltonians

$$H_{\mathrm{XD}}^{\mathrm{e-e}} = \sum_{\substack{m_1,m_2,k_1,k_2 \\ \sigma_1,\sigma_2,}} V_{m_1 m_2 k_1 k_2}^{\mathrm{XD}} \, c_{\mathrm{X},k_1,\sigma_1}^{+} c_{m_1,\sigma_2}^{+} c_{m_2,\sigma_2} c_{\mathrm{X},k_2,\sigma_1} \tag{B.7}$$

with the Coulomb matrix elements which can be written in spatial representation as

$$V^{\mathrm{XD}}_{m_1 m_2 k_1 k_2} = e^2 \int_{\substack{x\in \mathrm{X}\\ x'\in \mathrm{D}}} dx\, dx' \, \frac{\psi^+_{\mathrm{X},k_1}(x)\psi_{\mathrm{X},k_2}(x)\, \psi^+_{\mathrm{D},m_1}(x')\psi_{\mathrm{D},m_2}(x')}{|x-x'|}\,. \tag{B.8}$$

Here, $e \approx -1.6 \times 10^{-19}\mathrm{C}$ is the elementary charge and $\psi_{\mathrm{X},k}(x)$ is the wavefunction in spatial representation in the electrode X corresponding to the wavevector k. Since the distance $|x-x'|$ is very large on the scale of the Fermi–wavelength, the interaction is weak and the matrix elements with $m_1 \neq m_2$ or $k_1 \neq k_2$ can be neglected as compared to the diagonal elements leading to the classical result

$$H^{\mathrm{e-e}}_{\mathrm{XD}} = e^2 \int_{\substack{x\in \mathrm{X}\\ x'\in \mathrm{D}}} dx\, dx' \, \frac{\rho_{\mathrm{X}}(x)\, \rho_{\mathrm{D}}(x')}{|x-x'|}\,, \tag{B.9}$$

where ρ_{D} and ρ_{X} are the electron densities in the dot and the electrode X, respectively.

If we assume the charge density in the dot to be of spherical symmetry with center at x_{D}, we can perform the integration over x' in (B.9) and obtain

$$H^{\mathrm{e-e}}_{\mathrm{XD}} = Ne^2 \int_{x\in \mathrm{X}} dx\, \frac{\rho_{\mathrm{X}}(x)}{|x-x_{\mathrm{D}}|}\,, \tag{B.10}$$

where N is the number of electrons in the dot. The integral in (B.10) now depends solely on the electron distribution in the lead X. We assume the shape of $\rho_{\mathrm{X}}(x)$ to be depending only on the geometry of the lead being controlled by the chemical potential μ_{X}, which introduces a prefactor

$$\rho_{\mathrm{X}}(x) = f_{\mathrm{X}}(\mu_{\mathrm{X}})\rho^0_{\mathrm{X}}(x)\,. \tag{B.11}$$

The factor $f_{\mathrm{X}}(\mu_{\mathrm{X}})$ is a monotonic function which may be assumed to be linear over reasonable parameter ranges. Further, we neglect the influence of the electron number in the dot and of the charges on the other leads on the charge distribution in the lead X. Linearizing the function

$$f_{\mathrm{X}}(\mu_{\mathrm{X}}) \approx \gamma_{\mathrm{X}}\rho^0_{\mathrm{X}}(x)\,, \tag{B.12}$$

we find

$$H^{\mathrm{e-e}}_{\mathrm{XD}} = Ne^2\mu_{\mathrm{X}}\gamma_{\mathrm{X}}I_{\mathrm{X}}\,, \tag{B.13}$$

where

$$I_{\mathrm{X}} = \int_{x\in \mathrm{X}} dx\, \frac{\rho^0_{\mathrm{X}}(x)}{|x-x_{\mathrm{D}}|} \tag{B.14}$$

is an integral depending on the form of the electronic distribution function in the lead. We include all of these energies arising from interactions involving the electrons inside the dot in an effective dot Hamiltonian

$$\begin{aligned} H_{\mathrm{D}} &= H^0_{\mathrm{D}} + H^{\mathrm{e-e}}_{\mathrm{DD}} + \sum_{\mathrm{X}} H^{\mathrm{e-e}}_{\mathrm{DX}} \\ &= H^0_{\mathrm{D}} + H^{\mathrm{e-e}}_{\mathrm{DD}} + Ne^2\left[\mu_{\mathrm{G}}\gamma_{\mathrm{G}}I_{\mathrm{G}} + \mu_{\mathrm{L}}\gamma_{\mathrm{L}}I_{\mathrm{L}} + \mu_{\mathrm{R}}\gamma_{\mathrm{R}}I_{\mathrm{R}}\right]\,. \end{aligned} \tag{B.15}$$

Comparing this result with the one of classical electrostatics for the potential on an island between capacitors (Fig. 8.3), we can identify the parameters with the capacitances

$$e^2\gamma_{\mathrm{X}}I_{\mathrm{X}} = \frac{C_{\mathrm{X}}}{C_\Sigma}\,, \tag{B.16}$$

where

$$C_\Sigma = C_\mathrm{G} + C_\mathrm{L} + C_\mathrm{R}\,. \tag{B.17}$$

Since the interaction terms with the leads contain only the electron number in the dot, one can include these terms in the single particle term of the dot Hamiltonian. We therefore rewrite the effective dot Hamiltonian in the form

$$H_\mathrm{D} = \sum_{m,\sigma}(\varepsilon_m - e\Phi)c^+_{m,\sigma}c_{m,\sigma} + \sum_{\substack{m_1,m_2,m_3,m_4\\ \sigma_1,\sigma_2,}} V_{m_1m_2m_3m_4}\, c^+_{m_1,\sigma_1}c^+_{m_2,\sigma_2}c_{m_3,\sigma_2}c_{m_4,\sigma_1}\,, \tag{B.18}$$

where

$$\Phi = \frac{C_\mathrm{G}V_\mathrm{G} + C_\mathrm{L}V_\mathrm{L} + C_\mathrm{R}V_\mathrm{R}}{C_\mathrm{G} + C_\mathrm{L} + C_\mathrm{R}} \tag{B.19}$$

is the electrostatic potential introduced by the voltages $V_\mathrm{X} = -\mu_\mathrm{X}/e$ applied to the electrodes.

Appendix C

Transition rates between the many–electron eigenstates of the isolated system

In this appendix, we show in detail how the transition rates (9.1) between the many–electron Fock–states of the correlated electrons in the dot are calculated using standard time–dependent perturbation theory in lowest order in the tunneling terms. The same method can be applied to determine the rates in the case of the Anderson impurity (10.4,10.3) and the charging model (11.7).

C.1 Time–dependent perturbation theory

Time–dependent quantum mechanical problems are described by the time–dependent Schrödinger–equation

$$i\hbar\frac{\partial}{\partial t} \mid \Psi(t)\rangle = H \mid \Psi(t)\rangle \,, \tag{C.1}$$

where $\mid \Psi(t)\rangle$ is the time–dependent state–vector of the total system. The time–evolution of the statevector can be written in the form

$$\mid \Psi(t_f)\rangle = U(t_f, t_i) \mid \Psi(t_i)\rangle \,. \tag{C.2}$$

An integration of (C.1) directly leads to the formally exact expression for the propagator

$$U(t_f, t_i) = \exp[-i \int_{t_i}^{t_f} dt\, H(t)/\hbar] \,, \tag{C.3}$$

which reduces to

$$U(t_f, t_i) = \exp[-iH(t_f - t_i)/\hbar] \tag{C.4}$$

if the Hamiltonian is not explicitly depending on time. However, (C.4) contains an operator in the exponent and the expression is defined only via the expansion of the exponential function in powers of the argument. In general, it is a very difficult task to evaluate the propagator directly.

If one can split up the Hamiltonian into two parts,

$$H = H_0 + H_{\rm p}\,, \tag{C.5}$$

where the stationary Schrödinger–equation of the time–independent first term H_0

$$H_0 \mid \Psi_i^{(0)}\rangle = E_i^{(0)} \mid \Psi_i^{(0)}\rangle \tag{C.6}$$

can be solved exactly, yielding the eigenstates $\mid \Psi_i^{(0)}\rangle$ and the corresponding eigenenergies $E_i^{(0)}$, a systematic expansion of the propagator in terms of the second part of the Hamiltonian is possible in the basis of the eigenstates of H_0. The part $H_{\rm p}$ is then treated as a (weak) perturbation to the system which leads to a (small) coupling of the eigenstates of H_0.

Standard time–dependent perturbation theory (see e.g. [142]) yields the total propagator in the form of a series

$$U(t_f, t_i) = U_0(t_f, t_i) + \sum_{n=1}^{\infty} \left(\frac{1}{i\hbar}\right)^n U_n(t_f, t_i) \tag{C.7}$$

where

$$U_0(t_f, t_i) = \exp[-iH_0(t_f - t_i)/\hbar] \tag{C.8}$$

is the propagator of the unperturbed system and

$$U_n(t_f, t_i) = \int_{t_i}^{t_f} dt_n \int_{t_i}^{t_n} dt_{n-1} \cdots \int_{t_i}^{t_2} dt_1 U_0(t_f, t_n) H_{\rm p}(t_n) U_0(t_n, t_{n-1}) H_{\rm p}(t_{n-1}) \ldots H_{\rm p}(t_1) U_0(t_1, t_i) \tag{C.9}$$

the n–th order correction due to the presence of the perturbation. If the perturbation (e.g. the matrix elements of $H_{\rm p}$) is small, and the time–evolution in short time periods is considered,

$$\langle \Psi_{i_2}^{(0)} \mid H_{\rm p} \mid \Psi_{i_1}^{(0)}\rangle (t_f - t_i)/\hbar \ll 1\,, \tag{C.10}$$

the series (C.7) converges very fast and can be approximated by the lowest terms.

Since our goal is to treat the tunneling as a perturbation to the isolated dot and the leads and we always assume the tunneling terms to be very weak as compared to all the other energy scales in the problem, we proceed now by considering solely the first order term in $H_{\rm p}$. Further, our perturbation does not explicitly depend on time such that the propagator depends only on the time difference $t = t_f - t_i$.

We start by considering the probability amplitude $A(t)$ for the event, that the system, which is in the initial state $\mid \Psi_i^{(0)}\rangle$, is found after the time t in the final state $\mid \Psi_f^{(0)}\rangle$. The general expression for this quantity is

$$A_{f,i}(t) = \langle \Psi_f^{(0)} \mid U(t) \mid \Psi_i^{(0)}\rangle\,. \tag{C.11}$$

Acting on an eigenstate, the unperturbed propagator (C.8), which is the 0–th order term in the perturbation, generates only the trivial time–dependence

$$\mid \Psi_i^{(0)}(t)\rangle = \exp[-iE_i^{(0)}t/\hbar] \mid \Psi_i^{(0)}(0)\rangle. \tag{C.12}$$

and does not allow for transitions between the eigenstates of H_0. We are interested in the transitions between different eigenstates and from now on, we imply $i \neq f$ for the rest of this section. From (C.7) and (C.9), keeping only the first order term in the perturbation, the lowest order result for the amplitude is

$$A^{(1)}_{f,i}(t) = \langle \Psi^{(0)}_f \mid \frac{1}{i\hbar} \int_0^t dt_1 U_0(t-t_1) H_{\rm p} U_0(t_1) \mid \Psi^{(0)}_i \rangle \,. \tag{C.13}$$

Using (C.8), and performing the integration over t_1, one gets

$$A^{(1)}_{f,i}(t) = M_{f,i} \frac{1}{E^{(0)}_f - E^{(0)}_i} \left(\exp[-iE^{(0)}_f t/\hbar] - \exp[-iE^{(0)}_i t/\hbar] \right) \tag{C.14}$$

with the matrix element of the eigenfunctions of the unperturbed Hamiltonian with the perturbation

$$M_{f,i} = \langle \Psi^{(0)}_f \mid H_{\rm p} \mid \Psi^{(0)}_i \rangle. \tag{C.15}$$

The probability $W^{(1)}_{f,i}(t)$, that the perturbation has caused the transition from the initial to the final eigenstate within the time interval t (in lowest order in the perturbation) is the absolute square of the transition amplitude (C.14)

$$W^{(1)}_{f,i}(t) = \mid M_{f,i} \mid^2 \frac{1}{\hbar^2} \frac{2 - 2\cos[(E^{(0)}_f - E^{(0)}_i)t/\hbar]}{[(E^{(0)}_f - E^{(0)}_i)/\hbar]^2} \,. \tag{C.16}$$

For times that are long as compared to $\hbar/(E^{(0)}_f - E^{(0)}_i)$, the last fraction can be approximated by

$$\frac{2 - 2\cos[(E^{(0)}_f - E^{(0)}_i)t/\hbar]}{[(E^{(0)}_f - E^{(0)}_i)/\hbar]^2} \approx 2\pi\delta((E^{(0)}_f - E^{(0)}_i)/\hbar)t \tag{C.17}$$

and guarantees energy conservation.

The condition of long enough times reflects the uncertainty relation between time and energy. On the other hand, the time t must be short according to (C.10). We have chosen the parameters for our system such that the mean time between tunneling events is many orders of magnitude longer than $\hbar$ over the energy difference between the discrete levels of the dot Hamiltonian. Therefore we can satisfy (C.10) and consider energy conservation on an energy scale that is much smaller than the energy differences of the dot at the same time.

Thus, we get for the transition rate, which is defined by

$$\gamma_{f,i} = \lim_{t \to 0} W_{f,i}(t)/t \tag{C.18}$$

the final result

$$\gamma_{f,i} = \mid M_{f,i} \mid^2 \frac{2\pi}{\hbar} \delta(E^{(0)}_f - E^{(0)}_i) \,. \tag{C.19}$$

C.2 Effective transition rates between the many–electron dot states

Now, we specify the model to calculate the transition rates from the general expression derived above. We integrate over the lead states to find effective transition rates for the transitions between the eigenstates of the dot Hamiltonian.

First we have to remember that the state–vector used in the previous paragraph describes the whole system. In the unperturbed problem given by $H_0 = H_{\rm D}+H_{\rm L}+H_{\rm R}+H_{\rm Ph}$, the dot, the leads and the heat bath are completely decoupled and the Schrödinger–equation can be separated. Then, the total state–vector

$$\mid \Psi_i^{(0)}\rangle = \mid \Psi_{d_i}^{\rm D}\rangle \mid \Psi_{l_i}^{\rm L}\rangle \mid \Psi_{r_i}^{\rm R}\rangle \mid \Psi_{Q_i}^{\rm Ph}\rangle \tag{C.20}$$

is given by a product of the state–vector of the dot $\mid \Psi_{d_i}^{\rm D}\rangle$ and the ones describing the left/right lead $\mid \Psi_{l/r_i}^{\rm L/R}\rangle$ and the phonons $\mid \Psi_{Q_i}^{\rm Ph}\rangle$. The energies satisfying

$$\begin{aligned} H_{\rm D} \mid \Psi_{d_i}^{\rm D}\rangle &= E_{d_i}^{\rm D} \mid \Psi_{d_i}^{\rm D}\rangle \\ H_{\rm L/R} \mid \Psi_{l/r_i}^{\rm L/R}\rangle &= E_{l/r_i}^{\rm L/R} \mid \Psi_{l/r_i}^{\rm L/R}\rangle \\ H_{\rm Ph} \mid \Psi_{Q_i}^{\rm Ph}\rangle &= E_{Q_i}^{\rm Ph} \mid \Psi_{Q_i}^{\rm Ph}\rangle \end{aligned} \tag{C.21}$$

are additive yielding

$$E_i^{(0)} = E_{d_i}^{\rm (D)} + E_{l_i}^{\rm (L)} + E_{r_i}^{\rm (R)} + E_{Q_i}^{\rm (Ph)} \, . \tag{C.22}$$

The small tunneling terms and the weak electron–phonon interaction in the Hamiltonian (8.12) are considered as the perturbation $H_{\rm p} = H_{\rm L}^{\rm T} + H_{\rm R}^{\rm T} + H_{\rm ep}$ allowing for transitions between the eigenstates of the isolated dot and the reservoirs. Since they lead to different transitions changing the state of different leads, we can treat the tunneling to and from the different leads and transitions involving no electron tunneling but phononic excitations separately. The tunneling terms can be written as a sum of two parts $H_{\rm L/R}^{\rm T} = H_{\rm L/R}^{\rm T,-}+H_{\rm L/R}^{\rm T,+}$ where the first,

$$H_{\rm L/R}^{\rm T,-} = \sum_{k,m,\sigma} T_{k,m}^{\rm L/R} c_{{\rm L/R},k,\sigma}^{+} c_{m,\sigma} \tag{C.23}$$

describes tunneling of electrons out of the dot and the second part

$$H_{\rm L/R}^{\rm T,+} = \sum_{k,m,\sigma} \left(T_{k,m}^{\rm L/R}\right)^{*} c_{m,\sigma}^{+} c_{{\rm L/R},k,\sigma} \tag{C.24}$$

corresponds to electrons entering the dot. These parts contain a sum over all the one–electron states in the leads and in the quantum dot while the conservation of the spin of the tunneling electron is assumed as experimentally verified for not too wide barriers [143].

The electron–phonon interaction terms can be written as a sum of two terms $H_{\rm ep} = H_{\rm ep}^{-} + H_{\rm ep}^{+}$ where the first,

$$H_{\rm ep}^{-} = \sum_{q,m_1,m_2,\sigma} \sqrt{g(q,m_1,m_2)} c_{m_1,\sigma}^{+} c_{m_2,\sigma} a_q \tag{C.25}$$

describes the absorption of a phonon and the second part

$$H_{\rm ep}^{+} = \sum_{q,m_1,m_2,\sigma} \sqrt{g(q,m_1,m_2)}\, c_{m_1,\sigma}^{+} c_{m_2,\sigma} a_{-q}^{+} \tag{C.26}$$

corresponds to the emission of a phonon. For simplicity, we assume the prefactor to be independent of all the parameters $g(q,m_1,m_2) \equiv g$.

C.2.1 Transitions with a reduction of the electron number in the dot

First, we treat the case of a transition in which an electron tunnels from the dot to the left/right lead. These transitions occur due to the first part of the tunneling Hamiltonian (C.23), which we insert in the expression for the transition matrix elements (C.15) and using (C.20), one gets the matrix elements

$$M_{f,i}^{\rm L/R,-} = \tag{C.27}$$
$$\sum_{k,m,\sigma} T_{k,m}^{\rm L/R} \langle \Psi_{Q_f}^{\rm Ph} \mid \langle \Psi_{l_f}^{\rm L} \mid \langle \Psi_{r_f}^{\rm R} \mid \langle \Psi_{d_f}^{\rm D} \mid c_{{\rm L/R},k,\sigma}^{+} c_{m,\sigma} \mid \Psi_{d_i}^{\rm D} \rangle \mid \Psi_{r_i}^{\rm R} \rangle \mid \Psi_{l_i}^{\rm L} \rangle \mid \Psi_{Q_i}^{\rm Ph} \rangle \,.$$

This expression contains a product of an operator acting on the left/right lead Hilbert space only ($c_{\rm L/R,k,\sigma}^{+}$) and an operator acting exclusively in the dot Hilbert space ($c_{m,\sigma}$). We can write the matrix elements in the form

$$M_{f,i}^{\rm L/R,-} = \sum_{m,\sigma} \sum_{k} T_{k,m}^{\rm L/R} D_{d_f,d_i;m,\sigma}^{-} A_{l/r_f,l/r_i;k,\sigma}^{\rm L/R,-} B_{r/l_f,r/l_i}^{\rm R/L} C_{Q_f,Q_i}^{\rm Ph} \tag{C.28}$$

as a product of four matrix elements, where

$$\begin{aligned} D_{d_f,d_i;m,\sigma}^{-} &= \langle \Psi_{d_f}^{\rm D} \mid c_{m,\sigma} \mid \Psi_{d_i}^{\rm D} \rangle \\ A_{l/r_f,l/r_i;k,\sigma}^{\rm L/R,-} &= \langle \Psi_{l/r_f}^{\rm L/R} \mid c_{\rm L/R,k,\sigma}^{+} \mid \Psi_{l/r_i}^{\rm L/R} \rangle \\ B_{r/l_f,r/l_i}^{\rm R/L} &= \langle \Psi_{r/l_f}^{\rm R/L} \mid \Psi_{r/l_i}^{\rm R/L} \rangle \\ C_{Q_f,Q_i}^{\rm Ph} &= \langle \Psi_{Q_f}^{\rm Ph} \mid \Psi_{Q_i}^{\rm Ph} \rangle \end{aligned} \tag{C.29}$$

are the terms which are connected to the different Hilbert spaces involved. The spin summation in (C.28) runs over the values $\sigma = \pm 1/2$ of the magnetic quantum number of the tunneling electron. Since the matrix element connected to the dot Hilbert space contains also a Clebsch–Gordan coefficient for the coupling of the spin of the initial dot state with the spin of the tunneling electron to the spin of the final state, it can be nonzero only if the difference between the magnetic quantum numbers $M_{d_f} - M_{d_i} = \pm 1/2$ and the selection rule $\sigma = -\tilde{\sigma} := M_{d_f} - M_{d_i}$ is fulfilled. Therefore, (C.28) can be simplified to

$$M_{f,i}^{\rm L/R,-} = \sum_{m} \sum_{k} T_{k,m}^{\rm L/R}\, D_{d_f,d_i;m,-\tilde{\sigma}}^{-}\, A_{l/r_f,l/r_i;k,-\tilde{\sigma}}^{\rm L/R,-}\, B_{r/l_f,r/l_i}^{\rm R/L}\, C_{Q_f,Q_i}^{\rm Ph} \,. \tag{C.30}$$

To obtain the effective rates for transitions between the dot states

$$\Gamma_{d_f,d_i}^{-} := < \sum_{l_f,r_f,Q_f} \gamma_{f,i}^{-} >_{{\rm th}(l_i,r_i,Q_i)} \,, \tag{C.31}$$

we sum over all the final states of the leads which are assumed to be coupled to reservoirs and the phonons. Matrix elements of the initial states of the leads and the phonons are evaluated assuming thermal equilibrium denoted by $< \cdots >_{\mathrm{th}(l_i,r_i,Q_i)}$. Using (C.19) and (C.30) with (C.29), one gets

$$\begin{aligned}\Gamma^{-}_{d_f,d_i} &= \frac{2\pi}{\hbar} < \sum_{l_f,r_f,Q_f} \sum_{m,m'} \sum_{k,k'} \left(T^{\mathrm{L/R}}_{k,m}\right)^* T^{\mathrm{L/R}}_{k',m'} \left(D^{-}_{d_f,d_i;m,-\tilde{\sigma}}\right)^* D^{-}_{d_f,d_i;m',-\tilde{\sigma}} \\ &\times \left[\langle \Psi^{\mathrm{L/R}}_{l/r_i} \mid c_{\mathrm{L/R},k',-\tilde{\sigma}} \mid \Psi^{\mathrm{L/R}}_{l/r_f}\rangle\langle \Psi^{\mathrm{L/R}}_{l/r_f} \mid c^{+}_{\mathrm{L/R},k,-\tilde{\sigma}} \mid \Psi^{\mathrm{L/R}}_{l/r_i}\rangle\right] \\ &\times \langle \Psi^{\mathrm{R/L}}_{r/l_i} \mid \Psi^{\mathrm{R/L}}_{r/l_f}\rangle\langle \Psi^{\mathrm{R/L}}_{r/l_f} \mid \Psi^{\mathrm{R/L}}_{r/l_i}\rangle\langle \Psi^{\mathrm{Ph}}_{Q_i} \mid \Psi^{\mathrm{Ph}}_{Q_f}\rangle\langle \Psi^{\mathrm{Ph}}_{Q_f} \mid \Psi^{\mathrm{Ph}}_{Q_i}\rangle >_{\mathrm{th}(l_i,r_i,Q_i)} \\ &\times \delta(E^{(0)}_f - E^{(0)}_i)\,. \end{aligned} \tag{C.32}$$

Since the set of orthonormal eigenfunctions $\mid \Psi^{\mathrm{L/R}}_{l/r_i}\rangle$ of the lead Hamiltonian $H_{\mathrm{L/R}}$ is complete, the sums over the final states of the leads give identity matrices and the two last factors in $< \cdots >$ yield unity reflecting the fact that neither the right/left lead nor the phonons are affected by the process at all. Using the equilibrium expression

$$< \langle \Psi^{\mathrm{L/R}}_{l/r_i} \mid c_{\mathrm{L/R},k',-\tilde{\sigma}} c^{+}_{\mathrm{L/R},k,-\tilde{\sigma}} \mid \Psi^{\mathrm{L/R}}_{l/r_i}\rangle >_{\mathrm{th}(l/r_i)} = [1 - f_{\mathrm{L/R}}(\varepsilon^{\mathrm{L/R}}_{k,-\tilde{\sigma}})]\delta_{k,k'}\,, \tag{C.33}$$

for the occupation number operator, where the Fermi–Dirac distribution function

$$f_{\mathrm{L/R}}(\varepsilon) = (\exp[\beta(\varepsilon - \mu_{\mathrm{L/R}})] + 1)^{-1} \tag{C.34}$$

contains the temperature and the chemical potential of the reservoir, and using (C.22), which yields

$$E^{(0)}_f - E^{(0)}_i = E^{(\mathrm{D})}_{d_f} + \varepsilon^{\mathrm{L/R}}_{k,-\tilde{\sigma}} - E^{(\mathrm{D})}_{d_i} \tag{C.35}$$

in the argument of the Delta–function in (C.32) selects the value $k = k_{\mathrm{E}}$ for the wave–vector in the left/right lead. We finally find

$$\Gamma^{-}_{d_f,d_i} = \frac{2\pi}{\hbar} \left| \sum_m T^{\mathrm{L/R}}_{k_{\mathrm{E}},m} D^{-}_{d_f,d_i;m,-\tilde{\sigma}} \right|^2 \frac{\rho_{\mathrm{L/R}}(E)}{2} [1 - f_{\mathrm{L/R}}(E)] \tag{C.36}$$

with the energy of the tunneling electron $E = E^{(\mathrm{D})}_{d_i} - E^{(\mathrm{D})}_{d_f}$ and the density of states in the left/right lead $\rho_{\mathrm{L/R}}$. A factor of 1/2 arises because of the reduced density of states for a given electronic spin.

C.2.2 Transitions with an increase of the electron number in the dot

Now, we deal with an electron that tunnels from the left/right lead into the dot. Such transitions are due to the presence of the tunneling term (C.24). The calculation of the rates is analogous to the case of an electron tunneling out of the dot. Inserting (C.24) in (C.15) using (C.20), one gets the matrix elements for the increase of the electron number in the dot

$$M^{\mathrm{L/R},+}_{f,i} = \sum_m \sum_k \left(T^{\mathrm{L/R}}_{k,m}\right)^* D^{+}_{d_f,d_i;m,\tilde{\sigma}}\, A^{\mathrm{L/R},+}_{l/r_f,l/r_i;k,\tilde{\sigma}}\, B^{\mathrm{R/L}}_{r/l_f,r/l_i}\, C^{\mathrm{Ph}}_{Q_f,Q_i} \tag{C.37}$$

with

$$\begin{aligned} D^{+}_{d_f,d_i;m,\sigma} &= \langle \Psi^{\mathrm{D}}_{d_f} \mid c^{+}_{m,\sigma} \mid \Psi^{\mathrm{D}}_{d_i} \rangle \\ A^{\mathrm{L/R},+}_{l/r_f,l/r_i;k,\sigma} &= \langle \Psi^{\mathrm{L/R}}_{l/r_f} \mid c_{\mathrm{L/R},k,\sigma} \mid \Psi^{\mathrm{L/R}}_{l/r_i} \rangle \,. \end{aligned} \tag{C.38}$$

Again, we proceed by calculating the effective rates for transitions between the states of the dot and using now

$$< \langle \Psi^{\mathrm{L/R}}_{l/r_i} \mid c^{+}_{\mathrm{L/R},k',\tilde{\sigma}} c_{\mathrm{L/R},k,\tilde{\sigma}} \mid \Psi^{\mathrm{L/R}}_{l/r_i} \rangle >_{\mathrm{th}(l/r_i)} = f_{\mathrm{L/R}}(\varepsilon_k)\delta_{k,k'} \,, \tag{C.39}$$

one finds the result

$$\Gamma^{+}_{d_f,d_i} = \frac{2\pi}{\hbar} \left| \sum_m \left(T^{\mathrm{L/R}}_{k_{\mathrm{E}},m} \right)^{*} \, D^{+}_{d_f,d_i;m,\tilde{\sigma}} \right|^2 \frac{\rho_{\mathrm{L/R}}(E)}{2} f_{\mathrm{L/R}}(E) \,. \tag{C.40}$$

C.2.3 Approximations

For the sake of simplicity, we neglect the dependence of the tunneling matrix elements on the electronic states involved and put

$$T^{\mathrm{L/R}}_{k,m} \equiv T^{\mathrm{L/R}} \tag{C.41}$$

and introduce the abbreviations

$$t^{\mathrm{L/R}} = \frac{2\pi}{\hbar} \left| T^{\mathrm{L/R}} \right|^2 \rho_{\mathrm{L/R}}(E) \,, \tag{C.42}$$

neglecting the dependence of the density of states on the energy.

Thus, the effective transition rates between the eigenstates of the isolated dot take the simple form

$$\begin{aligned} \Gamma^{-}_{d_f,d_i} &= \frac{t^{\mathrm{L/R}}}{2} \left| \sum_m D^{-}_{d_f,d_i;m,-\tilde{\sigma}} \right|^2 \left[1 - f_{\mathrm{L/R}}(E) \right] \\ \Gamma^{+}_{d_f,d_i} &= \frac{t^{\mathrm{L/R}}}{2} \left| \sum_m D^{+}_{d_f,d_i;m,\tilde{\sigma}} \right|^2 f_{\mathrm{L/R}}(E) \,. \end{aligned} \tag{C.43}$$

Further, we extract the spin part of the state–vector describing the quantum dot, which is of very general nature and yields rich structure. From the consideration of the spin Hilbert space we find the squares of the vector coupling Clebsch–Gordan coefficients $\left| \left\langle S_{d_f}, M_{d_f}, \frac{1}{2}, \pm\frac{1}{2} \mid S_i, M_i \right\rangle_{CG} \right|^2$ for the combination of the initial spin (S_{d_i}, M_{d_i}) with the spin of the tunneling electron $(1/2, \pm 1/2)$ to the spin of the final state (S_{d_f}, M_{d_f}) (for the values, see table (12.2). To determine the orbital part of the matrix elements $D^{+/-}$, we have to go back to a microscopic model of the dot to calculate the orbital part of the many–electron wave–functions of the dot states, where the results will depend strongly on the details of the model. In principle, this can be done [135, 138], but in a first approach, we neglect this influence and approximate the dot matrix elements by

$$\left| \sum_m D^{+/-}_{d_f,d_i;m,\tilde{\sigma}} \right|^2 = \left| \left\langle S_{d_f}, M_{d_f}, \frac{1}{2}, +/-\tilde{\sigma} \mid S_i, M_i \right\rangle_{CG} \right|^2 \delta_{n_f,n_i\pm 1} \,. \tag{C.44}$$

C.2.4 Transitions between dot states with the same electron number

The electron–phonon coupling leads to transitions between the dot states which do not change the electron number in the dot. Nevertheless, the state of the correlated electrons can be affected by the emission or absorption of a phonon.

We start with electron absorption processes which are due to the presence of (C.25). Inserting (C.25) in (C.15) using (C.20), one gets the matrix elements for this process

$$M_{f,i}^{\mathrm{Ph},-} = \sqrt{g} D_{d_f,d_i}^{\mathrm{Ph}} B_{l_f,l_i}^{\mathrm{L}} B_{r_f,r_i}^{\mathrm{R}} C_{Q_f,Q_i}^{\mathrm{Ph},-} \tag{C.45}$$

with

$$\begin{aligned} D_{d_f,d_i}^{\mathrm{Ph}} &= \sum_{m_1,m_2,\sigma} \langle \Psi_{d_f}^{\mathrm{D}} \mid c_{m_1,\sigma}^{+} c_{m_2,\sigma} \mid \Psi_{d_i}^{\mathrm{D}} \rangle \\ C_{Q_f,Q_i}^{\mathrm{Ph},-} &= \sum_{q} \langle \Psi_{Q_f}^{\mathrm{Ph}} \mid a_q \mid \Psi_{Q_i}^{\mathrm{Ph}} \rangle . \end{aligned} \tag{C.46}$$

The thermal average over the initial states of the phononic heat bath yields

$$< \langle \Psi_{Q_i}^{\mathrm{Ph}} \mid a_q^{+} a_{q'} \mid \Psi_{Q_i}^{\mathrm{Ph}} \rangle >_{\mathrm{th}(Q_i)} = n_{\mathrm{B}}(\hbar\omega_q)\delta_{q,q'} , \tag{C.47}$$

due to the bosonic nature of the phonons and one finds the result

$$\Gamma_{d_f,d_i}^{\mathrm{Ph}+} = \frac{2\pi}{\hbar} g \mid D_{d_f,d_i}^{\mathrm{Ph}} \mid^2 \rho_{\mathrm{L/R}}(E) n_{\mathrm{B}}(E) . \tag{C.48}$$

The processes of phonon emission are induced by (C.26). Inserting (C.26) in (C.15) using (C.20), one gets the matrix elements for this process

$$M_{f,i}^{\mathrm{Ph},+} = \sqrt{g} D_{d_f,d_i}^{\mathrm{Ph}} B_{l_f,l_i}^{\mathrm{L}} B_{r_f,r_i}^{\mathrm{R}} C_{Q_f,Q_i}^{\mathrm{Ph},+} \tag{C.49}$$

with

$$C_{Q_f,Q_i}^{\mathrm{Ph},-} = \sum_{q} \langle \Psi_{Q_f}^{\mathrm{Ph}} \mid a_q^{+} \mid \Psi_{Q_i}^{\mathrm{Ph}} \rangle . \tag{C.50}$$

Now using

$$< \langle \Psi_{Q_i}^{\mathrm{Ph}} \mid a_q \, a_{q'}^{+} \mid \Psi_{Q_i}^{\mathrm{Ph}} \rangle >_{\mathrm{th}(Q_i)} = [1 + n_{\mathrm{B}}(\hbar\omega_q)]\delta_{q,q'} , \tag{C.51}$$

one finds the result

$$\Gamma_{d_f,d_i}^{\mathrm{Ph}+} = \frac{2\pi}{\hbar} g \mid D_{d_f,d_i}^{\mathrm{Ph}} \mid^2 \rho_{\mathrm{L/R}}(E)[1 + n_{\mathrm{B}}(-E)] , \tag{C.52}$$

where the energy difference due to the phonon emission $E = -\hbar\omega_q$ is now negative. The rates (C.48) and (C.52) can be cast into one expression

$$\Gamma_{d_f,d_i}^{\mathrm{in}} = \frac{2\pi}{\hbar} g \mid D_{d_f,d_i}^{\mathrm{Ph}} \mid^2 \rho_{\mathrm{Ph}}(E)[n_{\mathrm{B}}(\mid E \mid) + \Theta(-E)] . \tag{C.53}$$

We neglect the dependence of the rate on the particular shape of the dot wavefunctions and the phononic density of states. For simplicity we set $r = (2\pi/\hbar) g \rho_{\mathrm{Ph}}$ and $\mid D \mid^2 = 1$.

The general case of the results (C.36), (C.40) and (C.53) is known in the literature as Fermi's Golden rule.

Appendix D

The FORTRAN source code for the numerical solution of the master equation

The master equation (9.7) was solved numerically for all the models except the Anderson impurity.

For different situations, we have used different versions of the program. Here we append the most general form taking into account the full master equation in presence of a magnetic field. The spectrum of the dot is read from the file ENERGY.DAT and the Mathematica^{TM} readable results are written to the file MOUTBDI.DAT. The parameters are read from MINBDI.DAT. The program runs on the VAX-Cluster at the university of Hamburg and in particular on the DEC ALPHA workstation.

D.1 FORTRAN source code

```
      program MEXBDI
c     ************************************************************
c     * Program for the computation of the differential          *
c     * Conductance including a magnetic field.                  *
c     * Input of energy levels from ENERGY.DAT.                  *
c     * Input of parameters from MINBDI.DAT.                     *
c     * Output of Mathematica readable results to MOUTBDI.DAT.   *
c     * A greyscale plot can be generated with ListDensityPlot.  *
c     * Dietmar Weinmann 6.4.1993                                *
c     * The program is based on an earlier version written by    *
c     * Walter Pfaff.                                            *
c     ************************************************************
        parameter(MaxDim=200)    ! dimension of matrix

      parameter(MaxPVolt=120)  ! Number of plot-points
c
      Integer  Numb0, nn0(MaxDim)
```

```
      Integer  IFail, Numb, nn(MaxDim), diff
c ********************************************************
c    ************** VARIABLES *********************************
c    ****  Ilinks : Current through left barrier             ***
c    ****  TL/TR : Tunneling rate through left/right barrier ***
c    ****  CL/CR : Capacitance of the left/right junction    ***
c    ****  CG : Capacitance to the gate                      ***
c    ****  CS : total Capacitance                            ***
c    ****  G : Coupling to phonons                           ***
c    ****  Beta : inverse temperature                        ***
c    ****  B : Magnetic field                                ***
c    ****  VoltLinks : Voltage applied to the left lead      ***
c    ****  VoltRechts : Voltage applied to the right lead    ***
c    ****  VG : Gate-voltage                                 ***
c    ****  VGAnf/End : Begin/end of gate-voltage loop        ***
c    ****  VoltLinksAnf/End : .. of left voltage loop        ***
c    ****  VoltLinksMitt : Average of left voltages          ***
c    ****  deltaVolt : voltage difference for difference     ***
c    ****  ss0, ss : total spin of the levels                ***
c    ****  e_nu0, e_nu, e_nu1, e_nu2 : energy of the levels  ***
c    ****  ms : magnetic quantum number                      ***
c    ****  str : current at differnt voltage positions       ***
      real  Ilinks
      real  TL, TR, G, CL, CR, CG, CS, B
      real   VoltLinks, VoltRechts, VG, VGAnf, VGEnd, Beta
      real   VoltLinksAnf, VoltLinksEnd, VoltLinksMitt
      real   deltaVolt
      real   ss0(MaxDim), e_nu(MaxDim), e_nu0(MaxDim), str(2)
      real   ms(MaxDim), ss(MaxDim), e_nu1(MaxDim), e_nu2(MaxDim)
c
c       ** P(.) population of many-electron states ***
c       ** Pein(.) population entering NAG Routine ***
      double precision  p(MaxDim)
      double precision  pein(MaxDim)
c     *******  Total Rates Sq for transitions ******
c     *******  Different rates  ******
      double precision  GammaSq(MaxDim,MaxDim)
      double precision  GammaL(MaxDim,MaxDim)
      double precision  GammaR(MaxDim,MaxDim)
      double precision  GammaIn(MaxDim,MaxDim)
c     ***** Reduced matrix for normalization ********
      double precision  MatrLeq(MaxDim,MaxDim)
c
c     ** computation array for nag-routine f04arf **
      double precision rechenv(MaxDim)
```

```
c
c     ******* Commonblocks ***************************
      Common /Kapazitaet/  VoltLinks, VoltRechts, beta
      Common /Widerst/TL,TR,G
      Common/Gamms/GammaL, GammaR, GammaIn, Numb
c
c     ************** Main Programm ******************************
c
      print *,' '
        print *,'Master equation for exact energy levels'
      print *,'with relaxation and magnetic field'
      print *,'Version 2.1'
c
c     ****** Reading of the parameters **********************
      print *,'Reading of data from MINBDI.DAT'
      open(12,file='MINBDI.DAT',status='old')
c     ************************************************************
c     *** in MINBDI.DAT the parameter beta, TL, TR, CL, CR, B, G,*
c     *** VGAnf, VGEnd, CG, VoltLinksAnf, VoltLinksEnd,          *
c     *** VoltRechts, deltaVolt have to be given.                *
c     ************************************************************
      read(12,*)beta
      read(12,*)TL
      read(12,*)TR
      read(12,*)CL
      read(12,*)CR
      read(12,*)B
      read(12,*)G
      read(12,*)VGAnf
      read(12,*)VGEnd
      read(12,*)CG
      read(12,*)VoltLinksAnf
      read(12,*)VoltLinksEnd
      read(12,*)VoltRechts
      read(12,*)deltaVolt
      close(12,status='keep')
c     *** Reading of the energy levels ***
      print*,'Reading the data from ENERGY.DAT'
      open(13,file='ENERGY.DAT',status='old')
c     ************************************************************
c     *** in ENERGY.DAT the energy levels have to be given in the*
c     *** form electron number, total spin, energy               *
c     ************************************************************
        do 198 ii = 1, 200
        read (13,*,END=888)  nn0(ii), ss0(ii), e_nu0(ii)
```

```
 198    Numb0 = ii ! <---------------- Remember number of levels !
 888   close(13,status='keep')
c      *** Write the parameter of the states with the
c      *** magnetic quantum numbers.
        i=0
        do 199 ii = 1, Numb0
         do 201 s=-ss0(ii), ss0(ii)
          i=i+1
          e_nu1(i)=e_nu0(ii)
          nn(i)=nn0(ii)
          ss(i)=ss0(ii)
          ms(i)=s
 201    continue
 199    continue
        Numb = i  ! <--------- Remember the total number of levels
       open(11,file='MOUTBDI.DAT',status='OLD')
      write(11,*)'(* Modell using exact levels+phonons'
      write(11,*)' The differential conductance ist given as a'
      write(11,*)' funktion of gate- and transport-voltage.'
      write(11,*)' This file was created by MEXBDI.FOR.'
      write(11,*)'beta=',beta
      write(11,*)'TL=',TL
      write(11,*)'TR=',TR
      write(11,*)'CL=',CL
      write(11,*)'CR=',CR
      write(11,*)'B=',B
      write(11,*)'CG=',CG
      write(11,*)'Phonon Coupling G=',G
       write(11,*)'VGAnf=',VGAnf
      write(11,*)'VGEnd=',VGEnd
      write(11,*)'VLAnf=',VoltLinksAnf
      write(11,*)'VLEnd=',VoltLinksEnd
      write(11,*)'V Rechts=',VoltRechts
      write(11,*)'delta V=',deltaVolt
       write(11,*)'================== *)'
      write(11,*)'{{'
c
c      ************* Total capacitance ****************************
      CS=CL+CR+CG
c
c      *** Include the Zeeman energy and write the ***
c      *** parameters for the states                ***
        do 203 i = 1, Numb
          e_nu2(i)=e_nu1(i) + B*ms(i)
 203    continue
```

```
c
c     ********* Loop gate-voltage *****************
       do 2 ivolt=0,MaxPVolt-1
       VG = VGAnf +(VGEnd-VGAnf)*ivolt/MaxPVolt
c
c     **** Loop transport-voltage *******
      do 3 ibias=0,MaxPVolt-1
       VoltLinksmitt = VoltLinksEnd
     1 -(VoltLinksEnd-VoltLinksAnf)*ibias/MaxPVolt
        vb=VoltLinksmitt-VoltRechts
c    ************************************************************
c    *  For the differential conductance, two values for the     *
c    *  current at voltages separated by deltaVolt are computed. *
c    ************************************************************
      do 4 diff=1,2
       VoltLinks=VoltLinksmitt +(diff-1.5)*deltaVolt
c     *** Take into account the gate-voltage and the capacitive
c     *** influence of the transport-voltage. ***
c     ***  (Elektrons have negative charge)  ***
      do 205 ii = 1, Numb
        e_nu(ii) = e_nu2(ii)
     1   - float(nn(ii))
     1   *(VG*CG-VoltLinks*CL-VoltRechts*CR)/CS
 205    continue
c     ****** Determination of the different transition rates *****
c     ****** CALL subroutine gammas ***************
           call gammas(nn,ss,e_nu,ms)
c     ** Calculation of GammaSq between many-particle states **
c       ********** Initialize all Gamma's ! ********
        do 7 i=1,MaxDim
           do 8 ii=1,MaxDim
      GammaSq(i,ii)=0.
8          continue
7       continue


c
c     ******* Vary final level ito ***************
        do 9 ito=1,Numb
c     ******* Vary initial level ifrom ***************
           do 12 ifrom=1,Numb
            if (ito.eq.ifrom) then   ! continue for ito=ifrom
             Goto 211
            endif
c    **** generate the effective matrix ******
         GammaSq(ito,ifrom) =
```

```
     1 GammaL(ito,ifrom)+GammaR(ito,ifrom)+GammaIn(ito,ifrom)
         GammaSq(ito,ito) =  GammaSq(ito,ito)
     1 -GammaL(ifrom,ito)-GammaR(ifrom,ito)-GammaIn(ifrom,ito)
211      continue
12       continue
9       continue
c     ******* MatrLeq runs from 1. to Numb ******
        do 18 i=1,Numb
           do 19 ii=1,Numb
      MatrLeq(i,ii)= GammaSq(i,ii)
19         continue
18      continue
c       **** Normalization condition in the first line ***
        do 20 ii=1,Numb
       MatrLeq(1,ii) = 1.
20      continue
c    *** Replace the left hand side of the matrix equation by **
c    *** Pein (1,0,0,...)                                      **
       do 234 ii=1,Numb
        Pein(ii)=0.
 234   continue
       Pein(1)=1.
c
c *********** CALL of the NAG routine **************
      IFail = 1
      call F04ARF( MatrLeq, MaxDim, Pein, Numb, P,
     *                    Rechenv, IFail )
      if (ifail.eq.1) then
      print*,'Matrix singular at VG=',VG
      endif
c     ********** Calculation of the current **********
c     ********** Current through the left barrier ****
      Ilinks=0
      do 31 ito=1,Numb
      do 32 ifrom=1,Numb
      if (ito.eq.ifrom) then
      goto 32
      endif
              Ilinks=Ilinks
     *         +GammaL(ito,ifrom)*P(ifrom)*(nn(ito)-nn(ifrom))
32     continue
31     continue
        str(diff)=Ilinks
4     continue
c     ******** Evaluate the difference *****
```

```
        diffcond=(str(2)-str(1))/deltaVolt
       IF (abs(diffcond).lt.1E-6) THEN
         diffcond=0.
       END IF
c      ******* Output **********************************
       IF (ibias.gt.(MaxPVolt-1.5))THEN
        write(11,'(F8.4)')diffcond
        ELSE
      write(11,'(F8.4,A1)')diffcond,','
      ENDIF
3     continue
       IF (ivolt.gt.(MaxPVolt-1.5))THEN
        write(11,*)'}}'
        ELSE
       write(11,*)'},{'
      ENDIF
2     continue
      close(11,status='keep')
      end
c     ***************************************************************
c     ********     END main program   ***************************
c     ***************************************************************
c
c     ***************************************************************
c     ********* Function  Fermi distribution *********************
c     ***************************************************************
      real function Fermi(x)
c
      real  x
      real  beta
      Common /Kapazitaet/ VoltLinks, VoltRechts, beta
c
c     ****** Cut off at high energies ******
      if (beta*x.gt.32) then
      Fermi=0.
      return
      endif
      Fermi = 1/( exp(beta*x) +1)
        end
c
c     ***************************************************************
c     ******** Function  Bose distribution  **********************
c     ***************************************************************
      real function Bose(y)
c
```

```
      real  y, x
      real  beta
      Common /Kapazitaet/ VoltLinks, VoltRechts, beta
c
c     ****** Cut off at to high exponents *******
      X = beta * Y
      IF  (ABS(X) .LT. 3E-04)  THEN
         BOSE = 1. / X
         RETURN
      END IF
      IF  (X .GT. 32.)  THEN
         BOSE = 0.
         RETURN
      END IF
      IF  (X .LT. -32.)  THEN
         BOSE = -1.
         RETURN
      END IF
      BOSE = 1. / (EXP(X) - 1.)
      RETURN
      END
c
c     ************************************************************
c     *Subroutine 'Gammas' for the computation of transition rates*
c     ************************************************************
c
      SUBROUTINE Gammas(NN,SS,E_NU,MS)
      parameter(MaxDim=200)
      integer NN(MaxDim)

      real SS(MaxDim), E_NU(MaxDim), MS(MaxDim)
      double precision GammaL(MaxDim,MaxDim)
      double precision GammaR(MaxDim,MaxDim)
      double precision GammaIn(MaxDim,MaxDim)
      Common /Kapazitaet/ VoltLinks, VoltRechts, beta
      Common /Widerst/TL,TR,G
      Common/Gamms/GammaL, GammaR, GammaIn, Numb
      DO  90  I1 = 1, Numb
       DO  90  I2 = 1, Numb
        GammaL(I1,I2) = 0.
        GammaR(I1,I2) = 0.
 90     GammaIn(I1,I2) = 0.
      DO  100  Ifrom = 1, Numb
       DO  100  Ito = 1, Numb
        IF (ito .EQ. ifrom)  THEN
```

```
          GOTO 100
        END IF
c   ************************************************************
c     calculation of the transition rates considering the      *
c     Clebsch-Gordan coefficients                              *
c   ************************************************************
        IF  (NN(Ifrom)-NN(Ito) .EQ. 1)  THEN
          IF  (ABS(SS(Ifrom)-SS(Ito)-0.5) .LT. 1E-08)  THEN
             IF  (ABS(MS(Ifrom)-MS(Ito)-0.5) .LT. 1E-08) THEN
          GammaL(Ito,Ifrom) =
     *     TL * ((SS(Ifrom)+MS(Ifrom))/(2.*SS(Ifrom)+1.)) *
     *         (1.-Fermi(E_NU(Ifrom)-E_NU(Ito)-VoltLinks))
          GammaR(Ito,Ifrom) =
     *     TR * ((SS(Ifrom)+MS(Ifrom))/(2.*SS(Ifrom)+1.)) *
     *         (1.-Fermi(E_NU(Ifrom)-E_NU(Ito)-VoltRechts))
            ELSE IF (ABS(MS(Ifrom)-MS(Ito)+0.5) .LT. 1E-08) THEN
          GammaL(Ito,Ifrom) =
     *     TL * ((SS(Ifrom)-MS(Ifrom))/(2.*SS(Ifrom)+1.)) *
     *         (1.-Fermi(E_NU(Ifrom)-E_NU(Ito)-VoltLinks))
          GammaR(Ito,Ifrom) =
     *     TR * ((SS(Ifrom)-MS(Ifrom))/(2.*SS(Ifrom)+1.)) *
     *         (1.-Fermi(E_NU(Ifrom)-E_NU(Ito)-VoltRechts))
          END IF
           ELSE IF (ABS(SS(Ifrom)-SS(Ito)+0.5) .LT. 1E-08)  THEN
             IF  (ABS(MS(Ifrom)-MS(Ito)-0.5) .LT. 1E-08) THEN
           GammaL(Ito,Ifrom) =
     *       TL * ((SS(Ifrom)-MS(Ifrom)+1.)/(2.*SS(Ifrom)+1.))*
     *         (1.-Fermi(E_NU(Ifrom)-E_NU(Ito)-VoltLinks))
           GammaR(Ito,Ifrom) =
     *       TR * ((SS(Ifrom)-MS(Ifrom)+1.)/(2.*SS(Ifrom)+1.))*
     *         (1.-Fermi(E_NU(Ifrom)-E_NU(Ito)-VoltRechts))
             ELSE IF  (ABS(MS(Ifrom)-MS(Ito)+0.5) .LT. 1E-08) THEN
           GammaL(Ito,Ifrom) =
     *       TL * ((SS(Ifrom)+MS(Ifrom)+1.)/(2.*SS(Ifrom)+1.))*
     *         (1.-Fermi(E_NU(Ifrom)-E_NU(Ito)-VoltLinks))
           GammaR(Ito,Ifrom) =
     *       TR * ((SS(Ifrom)+MS(Ifrom)+1.)/(2.*SS(Ifrom)+1.))*
     *         (1.-Fermi(E_NU(Ifrom)-E_NU(Ito)-VoltRechts))
             END IF
          END IF
        END IF
        IF  (NN(Ifrom)-NN(Ito) .EQ. -1)  THEN
          IF  (ABS(SS(Ifrom)-SS(Ito)-0.5) .LT. 1E-08)  THEN
            IF  (ABS(MS(Ifrom)-MS(Ito)-0.5) .LT. 1E-08)  THEN
          GammaL(Ito,Ifrom) =
```

```
*         TL * ((SS(Ifrom)+MS(Ifrom))/(2.*SS(Ifrom)+1.)) *
*         Fermi(E_NU(Ito)-E_NU(Ifrom)-VoltLinks)
      GammaR(Ito,Ifrom) =
*         TR * ((SS(Ifrom)+MS(Ifrom))/(2.*SS(Ifrom)+1.)) *
*         Fermi(E_NU(Ito)-E_NU(Ifrom)-VoltRechts)
        ELSE IF  (ABS(MS(Ifrom)-MS(Ito)+0.5) .LT. 1E-08)  THEN
      GammaL(Ito,Ifrom) =
*         TL * ((SS(Ifrom)-MS(Ifrom))/(2.*SS(Ifrom)+1.)) *
*         Fermi(E_NU(Ito)-E_NU(Ifrom)-VoltLinks)
      GammaR(Ito,Ifrom) =
*         TR * ((SS(Ifrom)-MS(Ifrom))/(2.*SS(Ifrom)+1.)) *
*         Fermi(E_NU(Ito)-E_NU(Ifrom)-VoltRechts)
        END IF
       ELSE IF (ABS(SS(Ifrom)-SS(Ito)+0.5) .LT. 1E-08)  THEN
         IF  (ABS(MS(Ifrom)-MS(Ito)-0.5) .LT. 1E-08)  THEN
       GammaL(Ito,Ifrom) =
*        TL * ((SS(Ifrom)-MS(Ifrom)+1.)/(2.*SS(Ifrom)+1.))*
*         Fermi(E_NU(Ito)-E_NU(Ifrom)-VoltLinks)
       GammaR(Ito,Ifrom) =
*        TR * ((SS(Ifrom)-MS(Ifrom)+1.)/(2.*SS(Ifrom)+1.))*
*         Fermi(E_NU(Ito)-E_NU(Ifrom)-VoltRechts)
        ELSE IF  (ABS(MS(Ifrom)-MS(Ito)+0.5) .LT. 1E-08)  THEN
       GammaL(Ito,Ifrom) =
*        TL * ((SS(Ifrom)+MS(Ifrom)+1.)/(2.*SS(Ifrom)+1.))*
*         Fermi(E_NU(Ito)-E_NU(Ifrom)-VoltLinks)
       GammaR(Ito,Ifrom) =
*        TR * ((SS(Ifrom)+MS(Ifrom)+1.)/(2.*SS(Ifrom)+1.))*
*         Fermi(E_NU(Ito)-E_NU(Ifrom)-VoltRechts)
        END IF
      END IF
    END IF
    IF  (NN(Ifrom) .EQ. NN(Ito))  THEN
      IF  (ABS(SS(Ifrom)-SS(Ito)) .LT. 1E-08)  THEN
        IF  (ABS(MS(Ifrom)-MS(Ito)) .LT. 1E-08)  THEN
     GammaIn(Ito,Ifrom) = G * ABS(Bose(E_NU(Ito)-E_NU(Ifrom)))
        END IF
      END IF
    END IF
100  CONTINUE
     RETURN
     END
```

Appendix E

Differential conductance at different magnetic fields

In this appendix, we present plots of the differential conductance $\partial I/\partial V$ through a quantum dot represented by the correlated model in quasi–one dimension (Chapter 12) as a function of the transport– and the gate–voltage (in units of E_{H}/e) at different magnetic field values. The structures that appear are shifted towards higher or lower gate–voltages, depending on the difference in total magnetic quantum number of the states involved. At high magnetic fields when the spin polarized states become ground states, the spin blockade effect is suppressed. One observes decreasing structure in the plots when the magnetic field is increased. Gaps appear between lines that correspond to transitions between excited states. These features can also be detected in the experimental data [36].

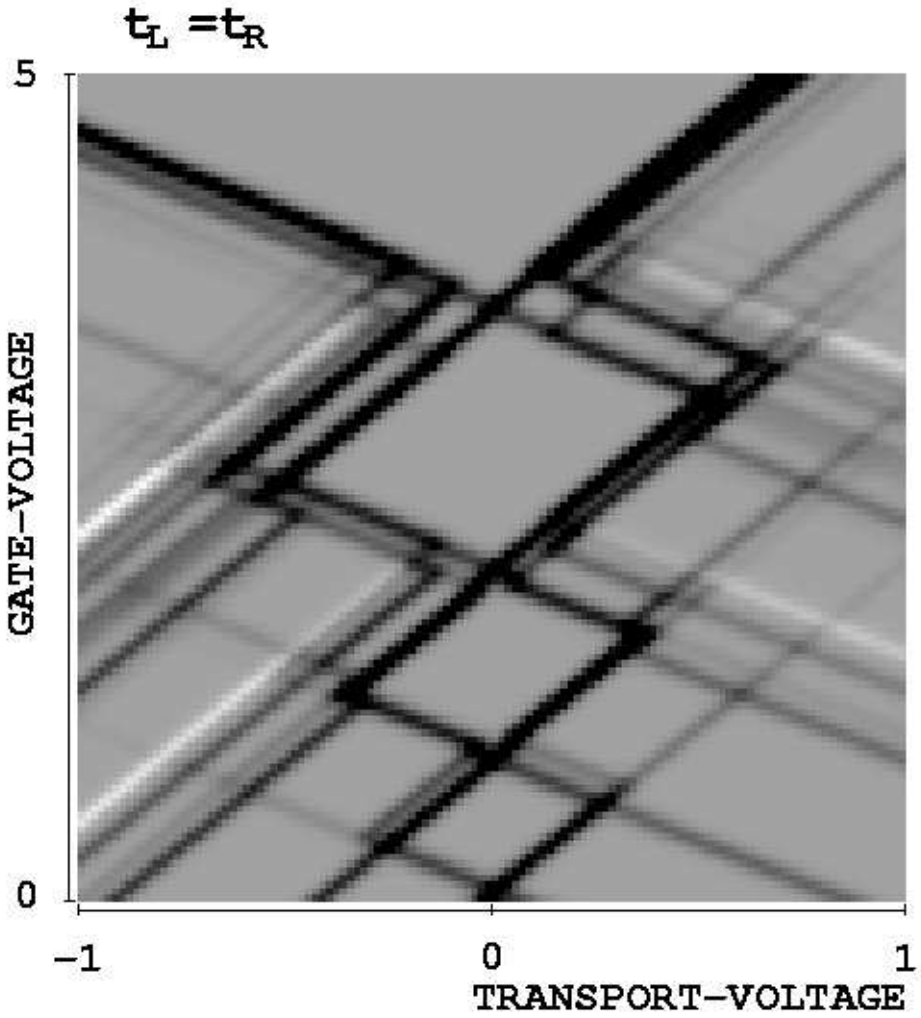

Figure E.1: The differential conductance as a function of the transport– and the gate–voltage is shown for symmetric barriers and zero magnetic field.

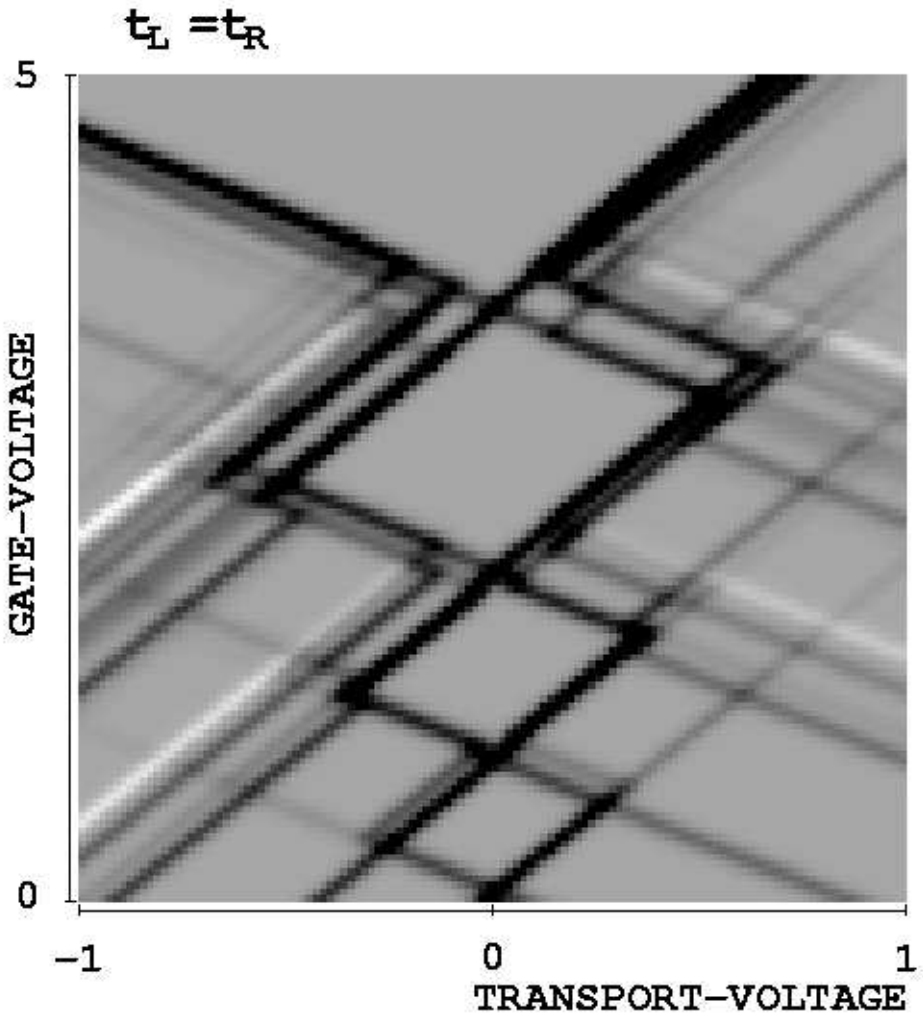

Figure E.2: The differential conductance as a function of transport– and gate–voltage at Zeeman energy $E_{\mathrm{Z}} = g\mu_{\mathrm{B}}B = 0.01\,E_{\mathrm{H}}$.

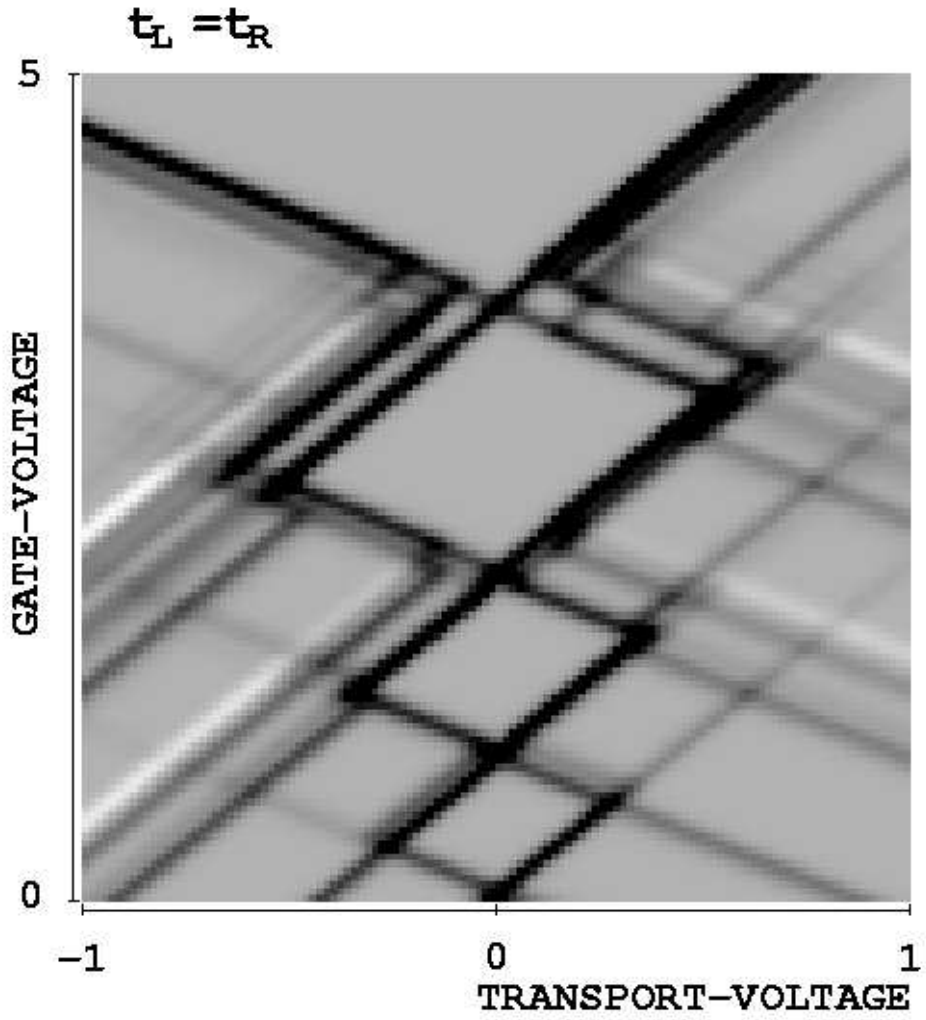

Figure E.3: The differential conductance as a function of transport– and gate–voltage at Zeeman energy $E_{\mathrm{Z}} = g\mu_{\mathrm{B}}B = 0.02\,E_{\mathrm{H}}$.

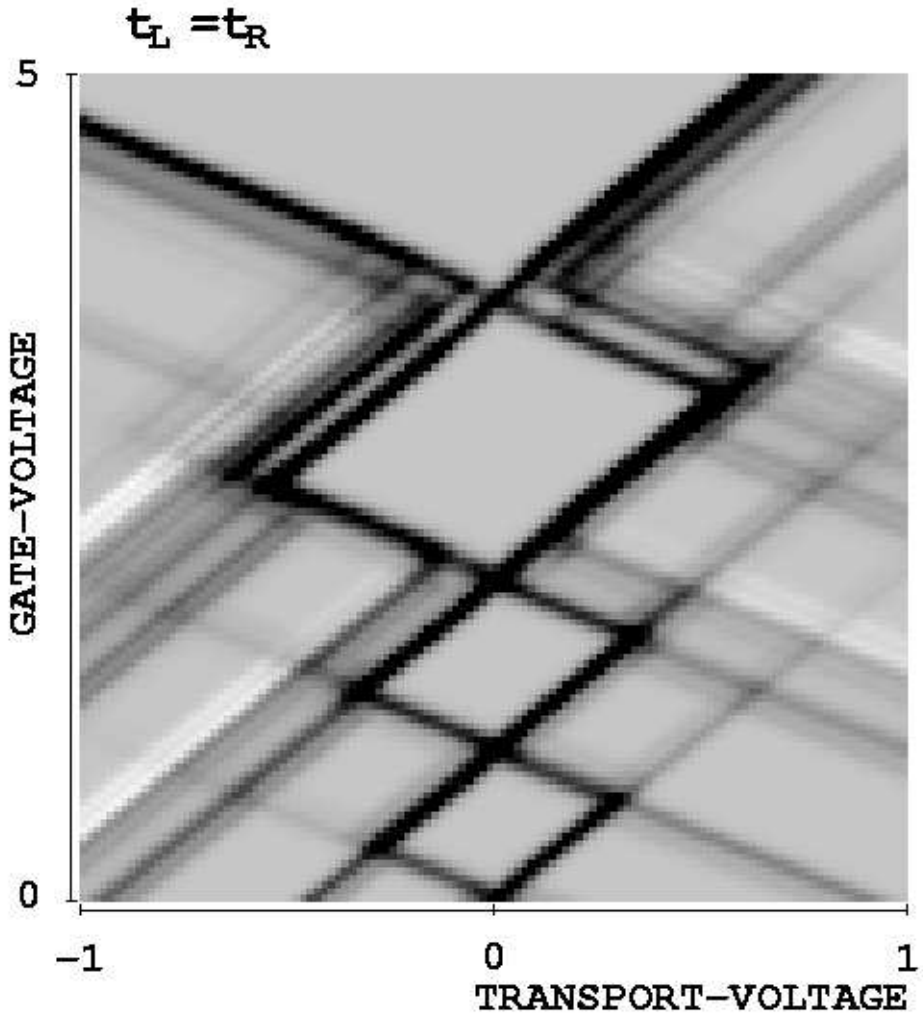

Figure E.4: The differential conductance as a function of transport– and gate–voltage at Zeeman energy $E_{\mathrm{Z}} = g\mu_{\mathrm{B}}B = 0.04\,E_{\mathrm{H}}$.

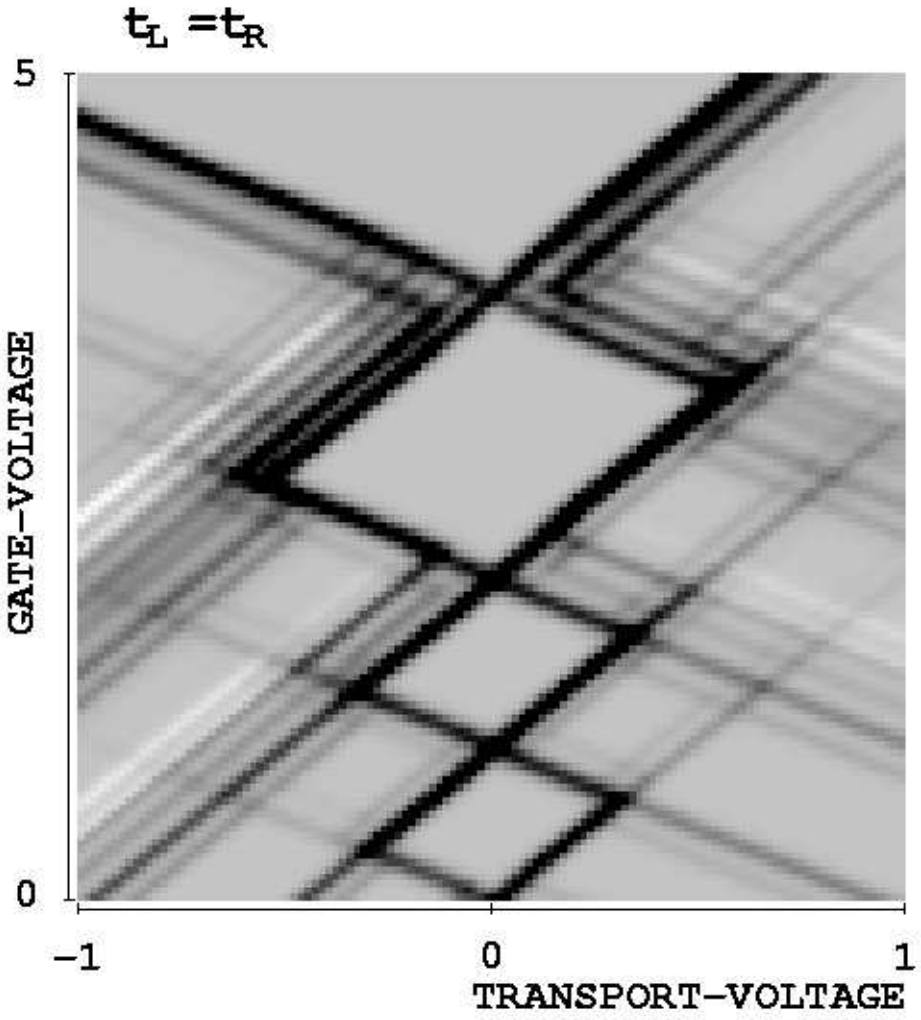

Figure E.5: The differential conductance as a function of transport– and gate–voltage at Zeeman energy $E_{\mathrm{Z}} = g\mu_{\mathrm{B}}B = 0.06\,E_{\mathrm{H}}$.

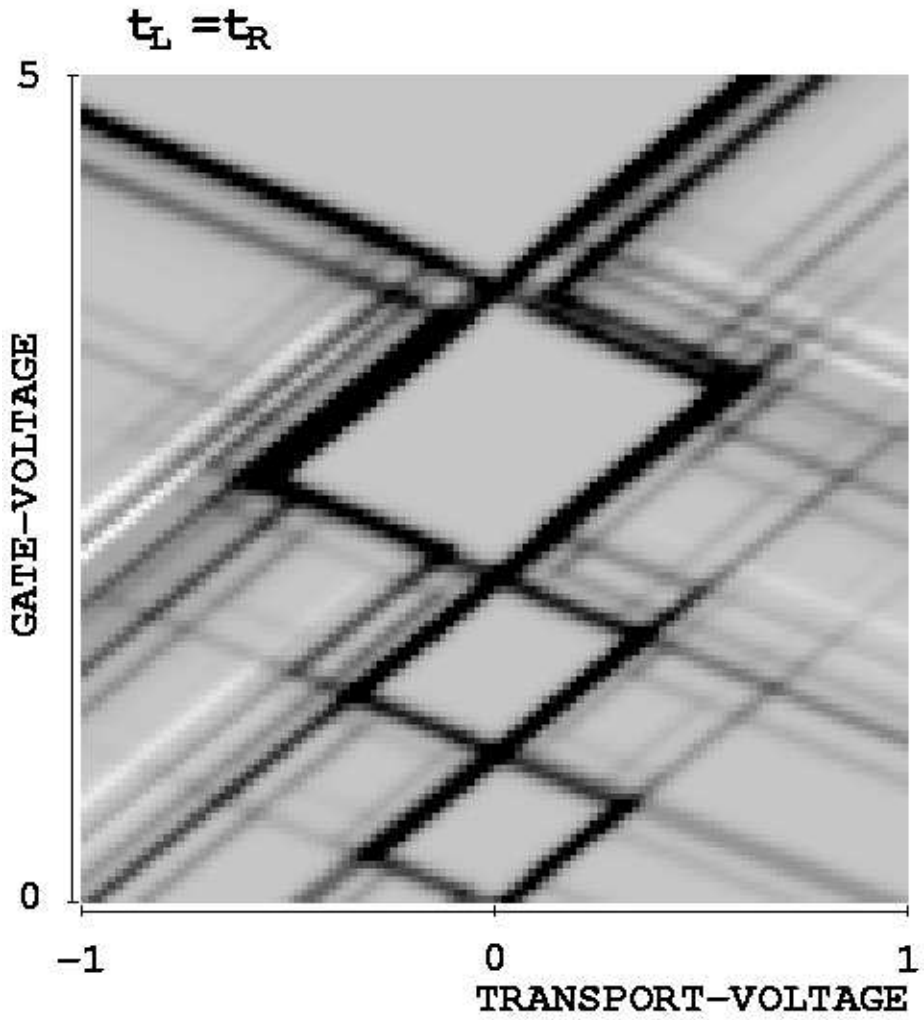

Figure E.6: The differential conductance as a function of transport– and gate–voltage at Zeeman energy $E_{\mathrm{Z}} = g\mu_{\mathrm{B}}B = 0.08\,E_{\mathrm{H}}$.

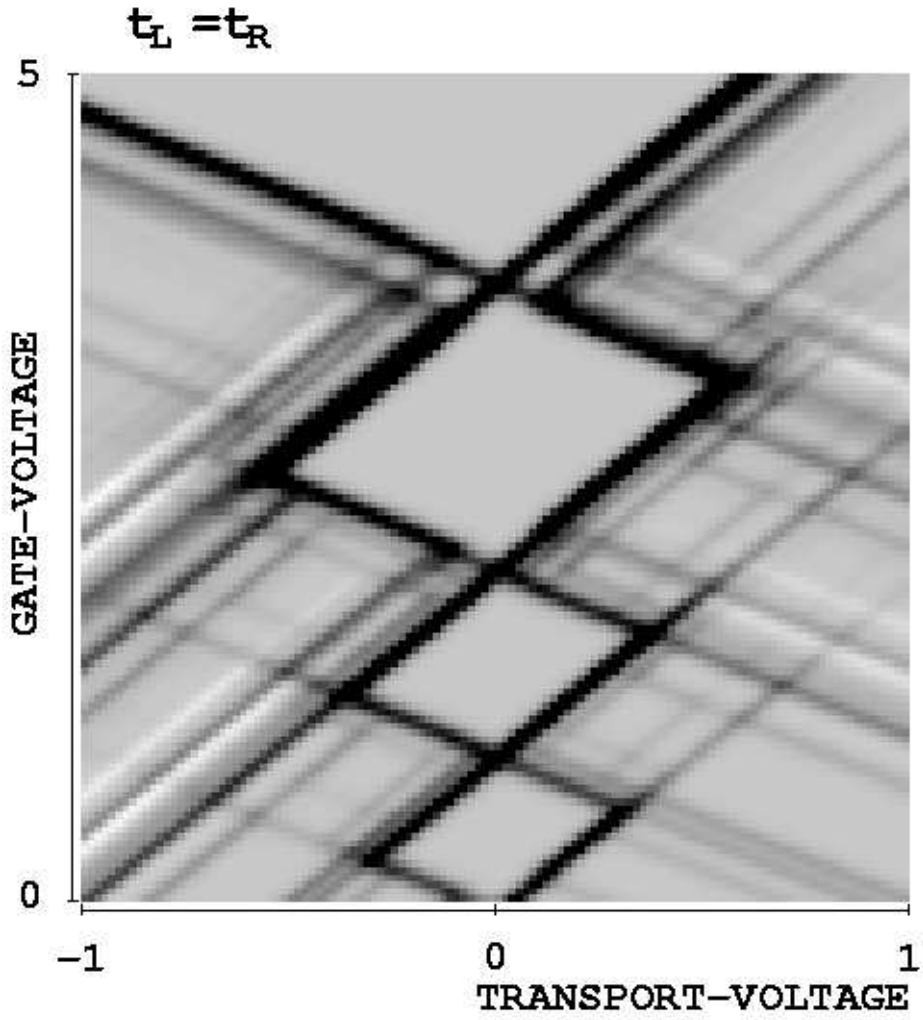

Figure E.7: The differential conductance as a function of transport– and gate–voltage at Zeeman energy $E_{\mathrm{Z}} = g\mu_{\mathrm{B}}B = 0.1\,E_{\mathrm{H}}$.

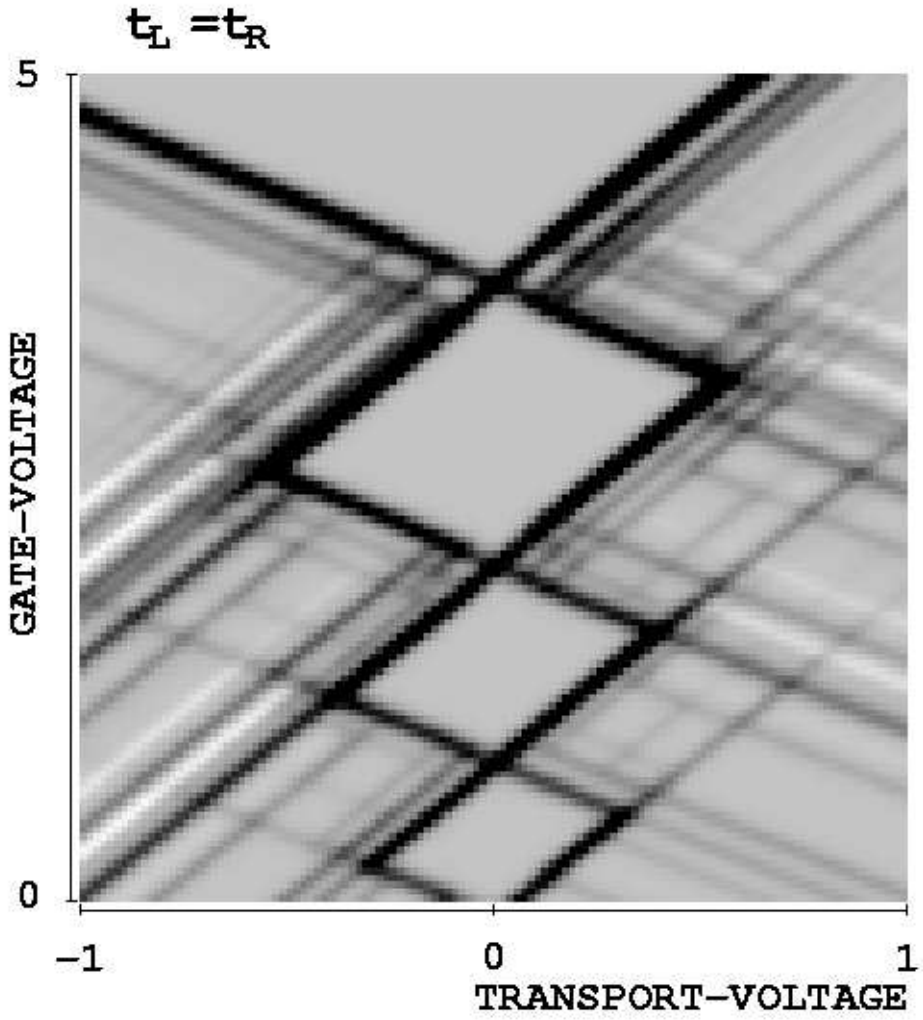

Figure E.8: The differential conductance as a function of transport– and gate–voltage at Zeeman energy $E_{\mathrm{Z}} = g\mu_{\mathrm{B}}B = 0.12\,E_{\mathrm{H}}$.

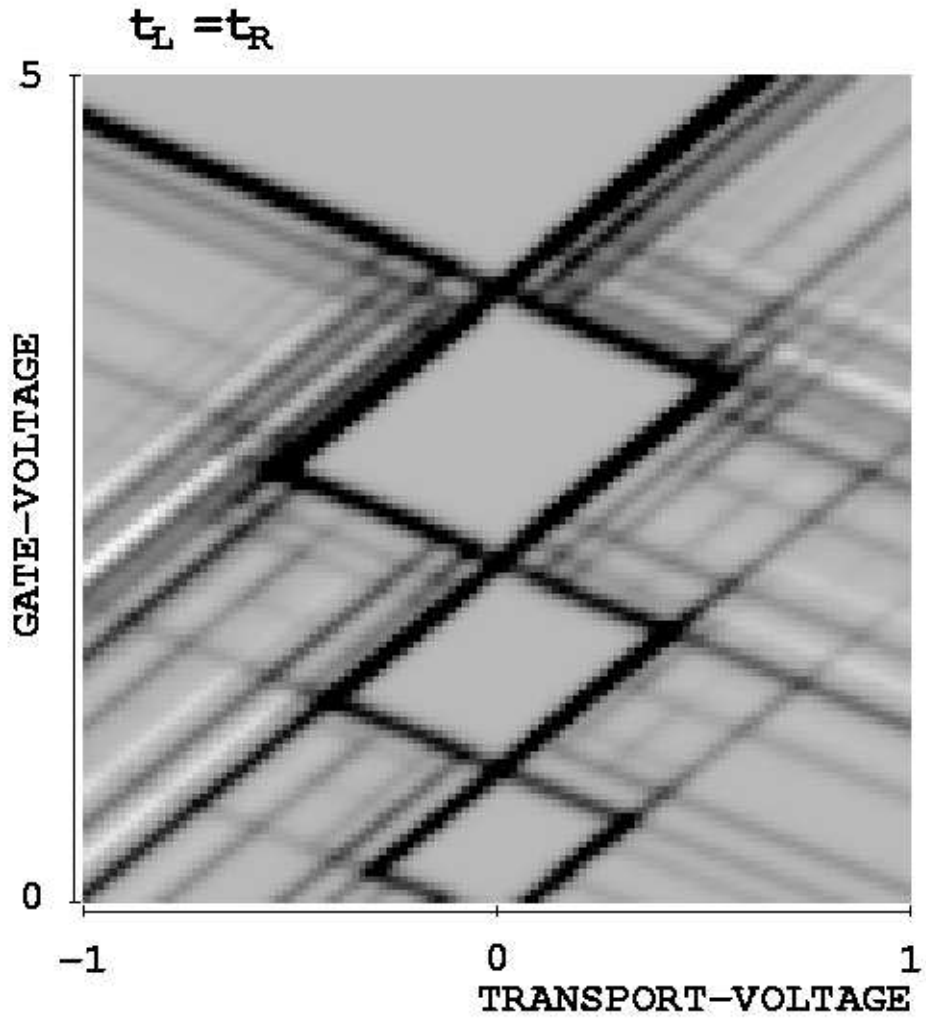

Figure E.9: The differential conductance as a function of transport– and gate–voltage at Zeeman energy $E_{\mathrm{Z}} = g\mu_{\mathrm{B}}B = 0.14\,E_{\mathrm{H}}$.

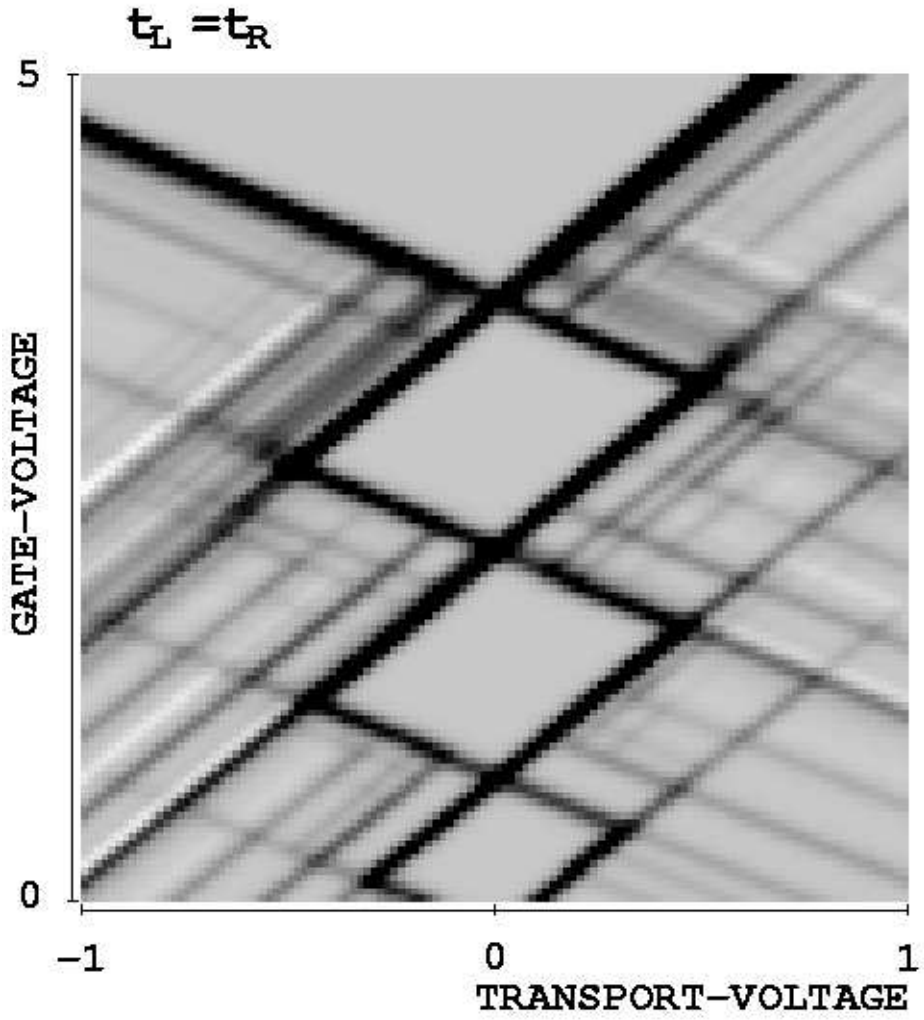

Figure E.10: The differential conductance as a function of transport– and gate–voltage at Zeeman energy $E_{\mathrm{Z}} = g\mu_{\mathrm{B}}B = 0.18\,E_{\mathrm{H}}$.

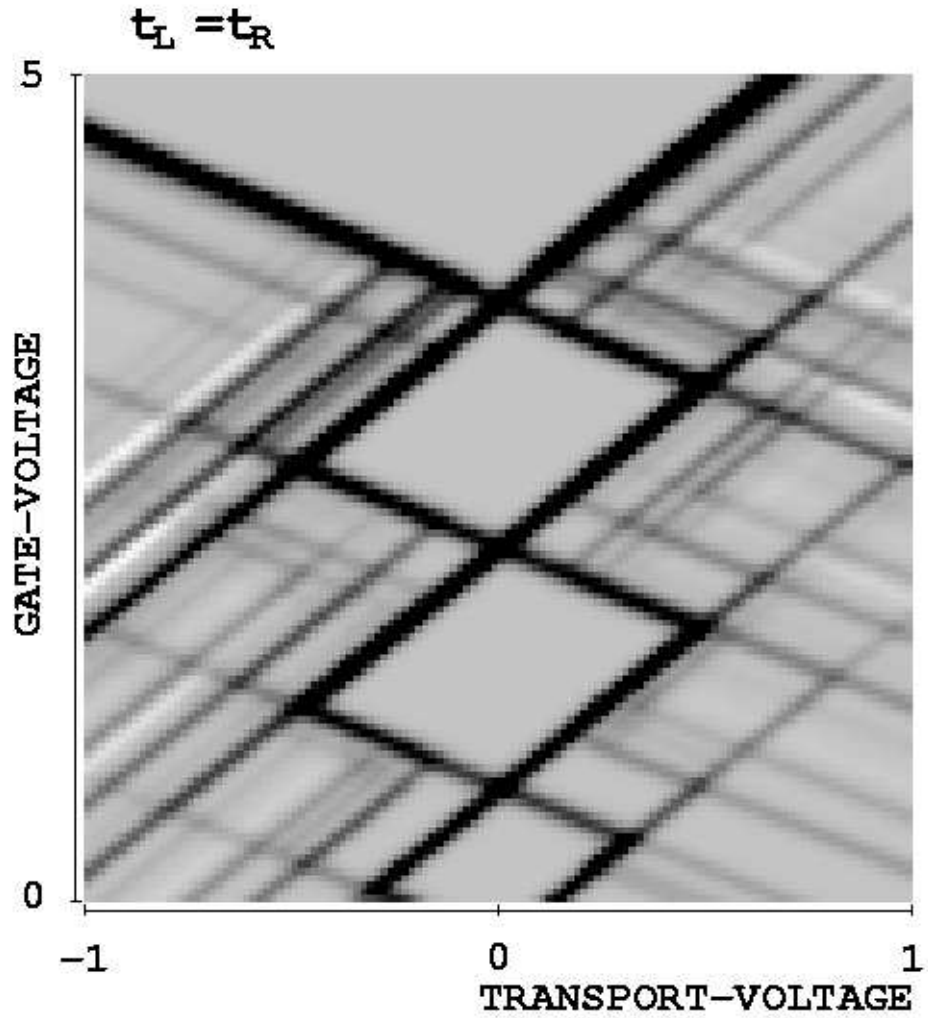

Figure E.11: The differential conductance as a function of transport– and gate–voltage at Zeeman energy $E_{\rm Z} = g\mu_{\rm B}B = 0.22\,E_{\rm H}$.

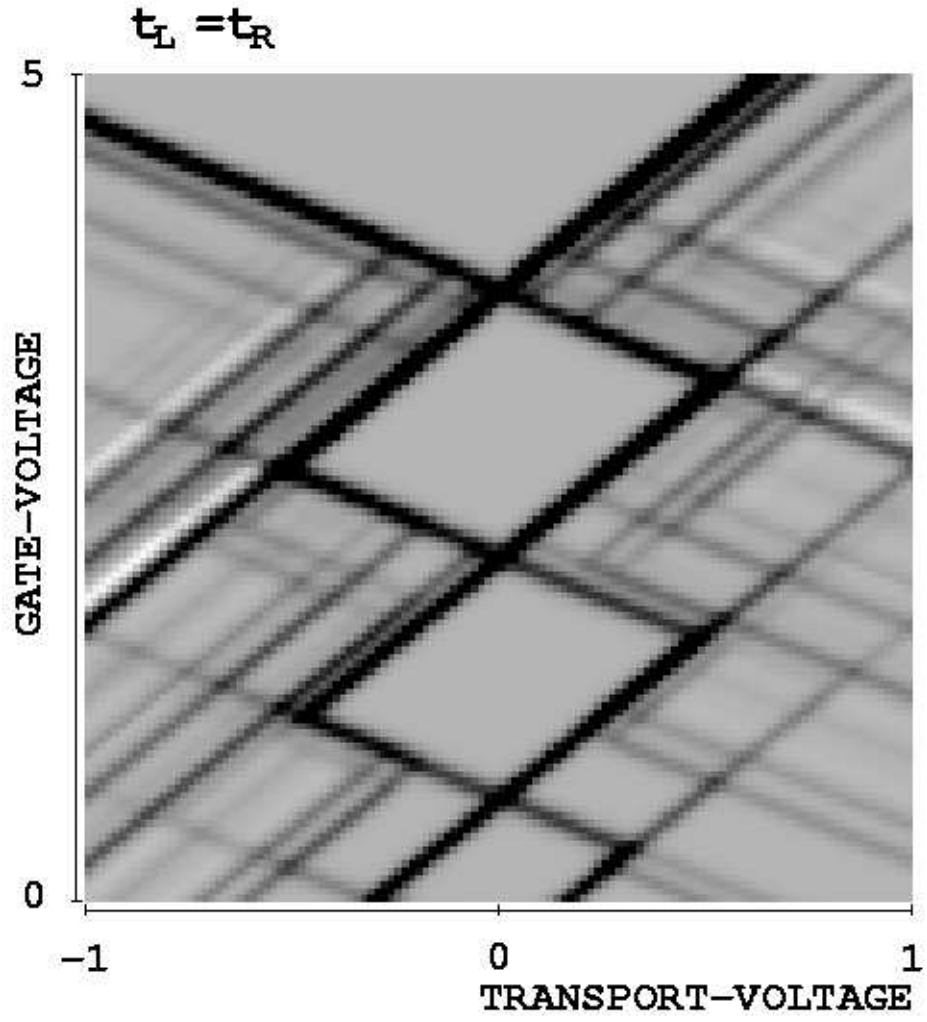

Figure E.12: The differential conductance as a function of transport– and gate–voltage at Zeeman energy $E_{\mathrm{Z}} = g\mu_{\mathrm{B}}B = 0.26\,E_{\mathrm{H}}$.

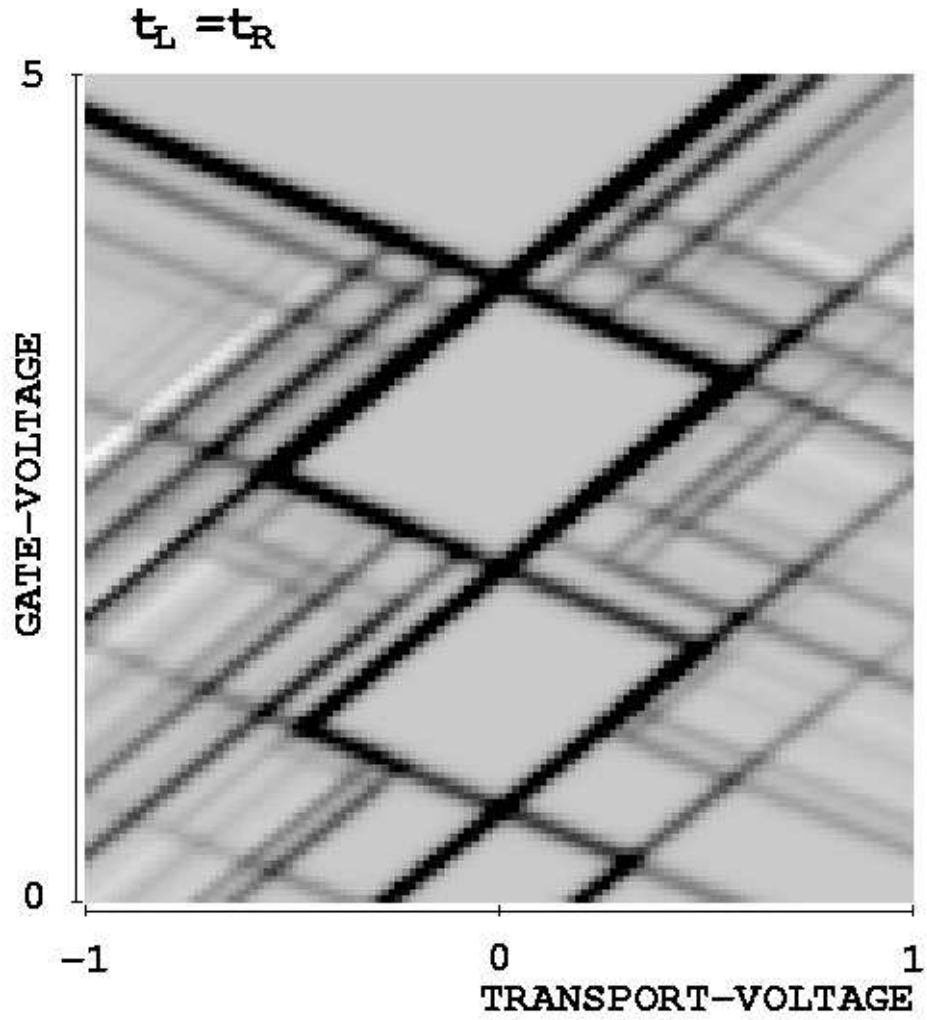

Figure E.13: The differential conductance as a function of transport– and gate–voltage at Zeeman energy $E_{\mathrm{Z}} = g\mu_{\mathrm{B}}B = 0.3\,E_{\mathrm{H}}$.

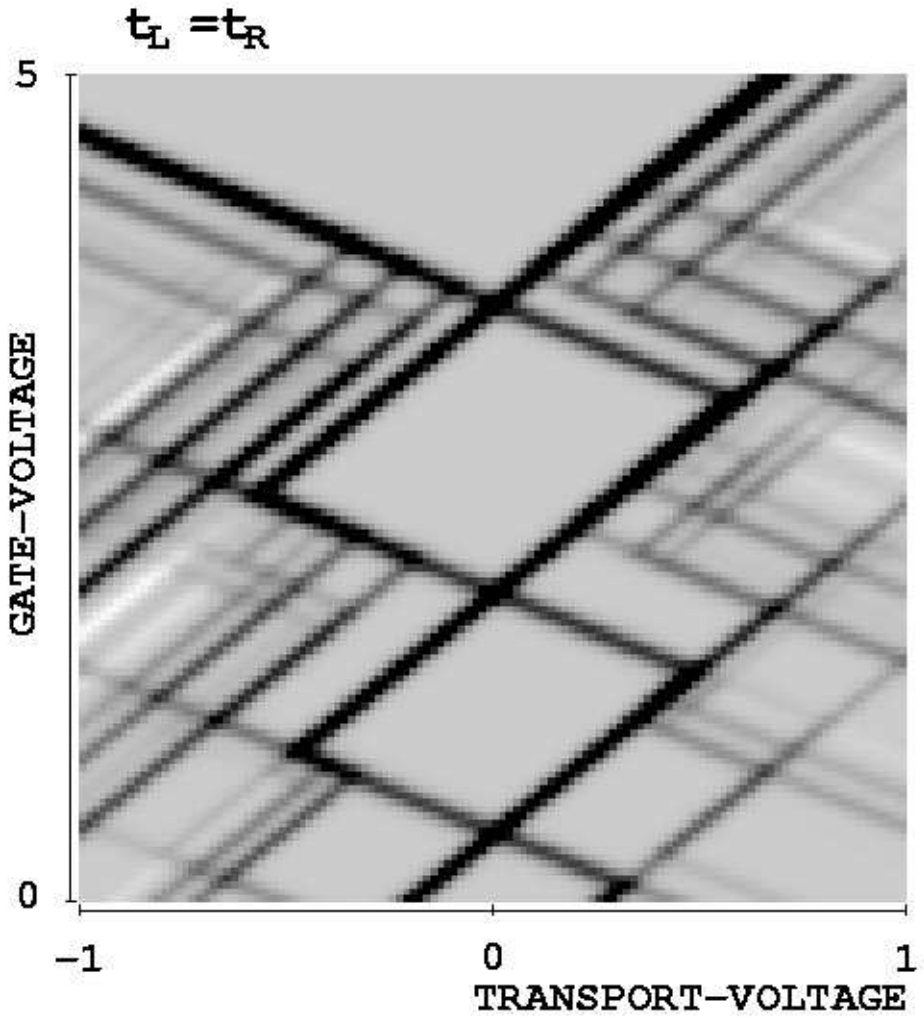

Figure E.14: The differential conductance as a function of transport– and gate–voltage at Zeeman energy $E_{\mathrm{Z}} = g\mu_{\mathrm{B}}B = 0.4\,E_{\mathrm{H}}$.

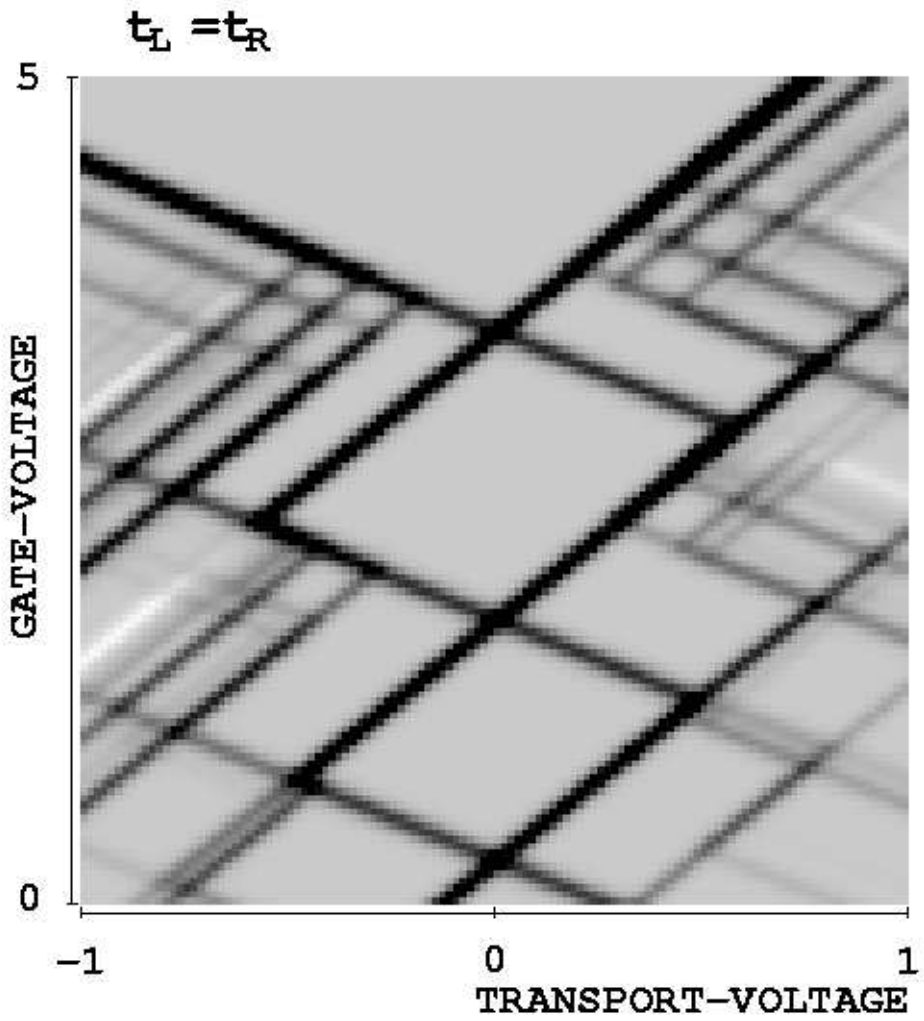

Figure E.15: The differential conductance as a function of transport– and gate–voltage at Zeeman energy $E_{\mathrm{Z}} = g\mu_{\mathrm{B}}B = 0.5\,E_{\mathrm{H}}$.

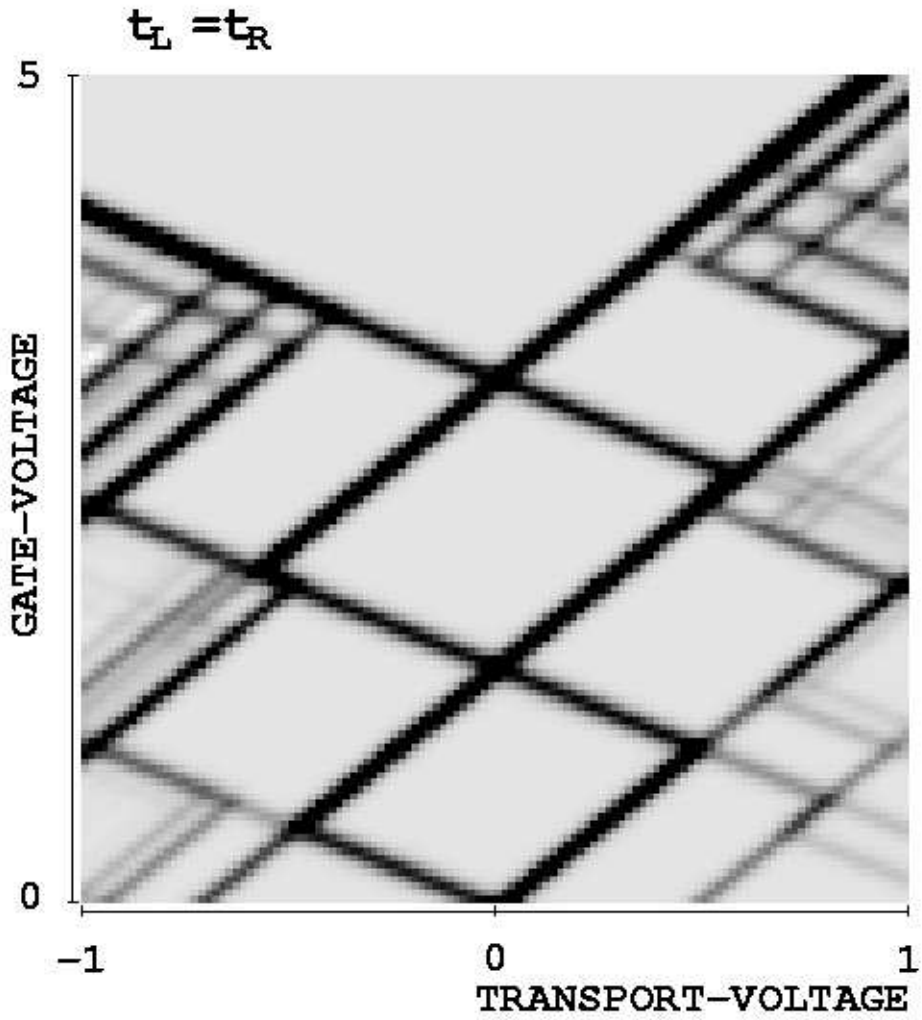

Figure E.16: The differential conductance as a function of transport– and gate–voltage at Zeeman energy $E_{\mathrm{Z}} = g\mu_{\mathrm{B}}B = 0.7\,E_{\mathrm{H}}$.

Bibliography

[1] *Quantum Coherence in Mesoscopic Systems*, ed. by B. Kramer, NATO ASI Series B **254** (Plenum Press, New York 1991).

[2] B. Kramer, *Festkörperprobleme / Advances in Solid State Physics* **30**, 53 (1990).

[3] G. Bergmann, *Phys. Rep.* **107**, 1 (1984).

[4] B. Kramer, A. MacKinnon, *Rep. Prog. Phys.* **56**, 1469 (1994).

[5] B. J. van Wees, H. van Houten, C. W. J. Beenakker, J. G. Williamson, L. P. Kouwenhoven, D. van der Marel, C. T. Foxon, *Phys. Rev. Lett.* **60**, 848 (1988).

[6] D. A. Wharam, T. J. Thornton, R. Newbury, M. Pepper, H. Ahmed, J. E. F. Frost, D. G. Hasko, D. C. Peacock, D. A. Ritchie, G. A. C. Jones, *Journ. Phys.* **C 21**, L209 (1988).

[7] D. Y. Sharvin, Y. V. Sharvin, *JETP Lett.* **34**, 272 (1981).

[8] S. Washburn, R. A. Webb, *Adv. Phys.* **35**, 375 (1986).

[9] C. P. Umbach et al., *Appl. Phys. Lett.* **50**, 1289 (1987).

[10] V. Chandrasekhar, R. A. Webb, M. J. Brady, M. B. Ketchen, W. J. Gallagher, A. Kleinsasser, *Phys. Rev. Lett.* **67**, 3578 (1991).

[11] D. Mailly, C. Chapelier, A. Benoit, *Phys. Rev. Lett.* **70**, 2020 (1993).

[12] M. A. Kastner, *Rev. Mod. Phys.* **64**, 849 (1992).

[13] M. A. Kastner, *Physics Today*, p. 24 (January 1993).

[14] D. V. Averin, K. K. Likharev, *J. Low Temp. Phys.* **62**, 345 (1986).

[15] L. J. Geerligs, V. F. Anderegg, P. A. M. Holweg, J. E. Mooij, H. Pothier, D. Esteve, C. Urbina, M. H. Devoret, *Phys. Rev. Lett.* **64**, 2691 (1990).

[16] L. P. Kouwenhoven, A. T. Johnson, N. C. van der Vaart, A. van der Enden, C. J. P. Harmans, C. T. Foxon, *Phys. Rev. Lett.* **67**, 1626 (1991).

[17] L. P. Kouwenhoven, A. T. Johnson, N. C. van der Vaart, A. van der Enden, C. J. P. Harmans, C. T. Foxon, *Zeitschr. Phys.* **B 85**, 381 (1991).

[18] L. P. Kouwenhoven : PhD thesis, University of Delft (1992).

[19] Special Issue on *Single Charge Tunneling* edited by H. Grabert, *Z. Phys.* **B 85**, 317–468 (1991).

[20] M. H. Devoret et al., *Bulletin du Bureau National de Métrologie* **86**, 7 (1991).

[21] M. Devoret, D. Esteve, C. Urbina, *Nature* **360**, 547 (1992).

[22] C. Schönenberger, H. van Houten, H. C. Donkersloot, *Europhys. Lett.* **20**, 249 (1991).

[23] P. A. Lee, *Physica* **B 189**, 1 (1993).

[24] J. Weis, R. J. Haug, K. v. Klitzing, K. Ploog, *Phys. Rev. Lett.* **71**, 4019 (1993).

[25] D. Weinmann, W. Häusler, W. Pfaff, B. Kramer, U. Weiss, *Europhys. Lett.* **26**, 467 (1994).

[26] R. Blick, J. Weis, R. J. Haug, K. v. Klitzing, K. Ploog, preprint (1994).

[27] C. J. P. M. Harmans, *Physics World*, 50 (March 1992).

[28] J. Weis, R. J. Haug, K. v. Klitzing, K. Ploog, *Phys. Rev.* **B 46**, 12837 (1992).

[29] A. T. Johnson, L. P. Kouwenhoven, W. de Jong, N. C. van der Vaart, C. J. P. M. Harmans, C. T. Foxon, *Phys. Rev. Lett.* **69**, 1592 (1992).

[30] N. C. van der Vaart, A. T. Johnson, L. P. Kouwenhoven, D. J. Maas, W. de Jong, M. P. de Ruyter van Stevenick, A. van der Enden, C. J. P. M. Harmans, *Physica* **B 189**, 99 (1993).

[31] J. Weis, R. J. Haug, K. v. Klitzing, K. Ploog, *Physica* **B 189**, 111 (1993).

[32] J. Weis, R. Haug, K. v. Klitzing, K. Ploog, *Surf. Sci.* **305**, 664 (1994).

[33] J. T Nicholls, J. E. F. Frost, M. Pepper, D. A. Ritchie, M. P. Grimshaw, G. A. C. Jones, *Phys. Rev.* **B 48**, 8866 (1993).

[34] E. B. Foxman, P. L. McEuen, U. Meirav, N. S. Wingreen, Y. Meir, P. A. Belk, N. R. Belk, M. A. Kastner, S. J. Wind, *Phys. Rev.* **B 47**, 10020 (1993).

[35] P. L. McEuen, N. S. Wingreen, E. B. Foxman, J. Kinaret, U. Meirav, M. A. Kastner, Y. Meir, S. J. Wind, *Physica* **B 189**, 70 (1993).

[36] J. Weis, *Ph. D. Thesis,* Stuttgart (1994).

[37] D. V. Averin, K. K. Likharev in : *Quantum Effects in Small Disordered Systems*, ed. by B. L. Altshuler, P. A. Lee, R. A. Webb (Elsevier, Amsterdam, 1991).

[38] G. Schön, A. D. Zaikin, *Phys. Rep.* **198**, 237 (1990).

[39] H. Grabert, G.-L. Ingold, M. H. Devoret, D. Esteve, H. Pothier, C. Urbina, *Z. Phys.* **B 84**, 143 (1991).

[40] T. A. Fulton and G. J. Dolan, *Phys. Rev. Lett.* **59**, 109 (1987).

[41] M. Devoret, D. Esteve, H. Grabert, G.-L. Ingold, H. Pothier, C. Urbina, *Phys. Rev. Lett.* **64**, 1824 (1990).

[42] A. N. Cleland, J. M. Schmidt, J. Clarke, *Phys. Rev. Lett.* **64**, 1565 (1990).

[43] D. B. Haviland, L. S. Kuzmin, P. Delsing, T. Claeson, *Europhys. Lett.* **16**, 103 (1991).

[44] P. Delsing, K. K. Likharev, L. S. Kuzmin, T. Claeson, *Phys. Rev. Lett.* **63**, 1861 (1989).

[45] I. Giaever, H. R. Zeller, *Phys. Rev. Lett.* **20**, 1504 (1990).

[46] M. Büttiker, H. Thomas, A. Prêtre, *Phys. Lett.* **A 180**, 364 (1993).

[47] U. Eckern, G. Schön, V. Ambegaokar, *Phys. Rev.* **B 30**, 6419 (1984).

[48] E. Šimánek, *Journ. Phys. Soc. Jap. Lett.* **54**, 2397 (1985).

[49] F. W. J. Hekking, Y. V. Nazarov and G. Schön, *Europhys. Lett.* **14**, 489 (1991).

[50] F. W. J. Hekking, Y. V. Nazarov and G. Schön, *Europhys. Lett.* **20**, 255 (1992).

[51] F. W. J. Hekking, *Ph. D. thesis*, University of Delft (1992).

[52] T. Heinzel, S. Manus, D. A. Wharam, J. P. Kotthaus, G. Böhm, W. Klein, G. Tränkle, G. Weimann, *Europhys. Lett.* **26**, 689 (1994).

[53] Y. Meir, N. S. Wingreen and P. A. Lee, *Phys. Rev. Lett.* **66**, 3048 (1991).

[54] Y. Meir and N. S. Wingreen, *Phys. Rev. Lett.* **68**, 2512 (1992).

[55] G. D. Mahan, *Many–Particle Physics, 2nd edition* (Plenum, New York, 1990).

[56] S. Doniach, E. H. Sondheimer, *Green's Functions for Solid State Physicists*, Benjamin, Reading, Massachusetts (1974).

[57] R. Kubo, *Can. Journ. Phys.* **34**, 1274 (1956).

[58] D. S. Fisher and P. A. Lee, *Phys. Rev.* **B 23** 6851 (1981).

[59] A. D. Stone and A. Szafer, *IBM J. Res. Dev.* **32**, 384 (1988).

[60] B. Kramer, J. Mašek, in *Quantum Fluctuations in Mesoscopic and Macroscopic Systems*, ed. by H. A. Cerdeira, F. Guinea, U. Weiss, World Scientific, Singapoore (1991).

[61] Y. Fu, S. C. Dudley, *Phys. Rev. Lett.* **70**, 65 (1993).

[62] J. Mašek, unpublished (1991).

[63] B. Velický, J. Mašek and B. Kramer, *Phys. Lett.* **A 140**, 447 (1989).

[64] J. Mašek and B. Kramer, *Z. Phys.* **B 75**, 37 (1989).

[65] B. Kramer and J. Mašek, *Z. Phys.* **B 76**, 457 (1989).

[66] M. H. Cohen, L. M. Falicov, J. C. Phillips, *Phys. Rev. Lett.* **8**, 316 (1962).

[67] R. E. Prange, *Phys. Rev.* **131**, 1083 (1963).

[68] I. S. Gradshteyn, I. M. Ryzhik, *Table of Integrals, Series and Products*, Academic Press, London (1979).

[69] J. D. Jackson, *Classical Electrodynamics*, second edition, Wiley, New York (1975).

[70] E. H. Hauge, J. A. Stovneng, *Rev. Mod. Phys.* **61**, 917 (1989).

[71] P. Hänggi, in *Path Integration, Trieste 1991*, edited by H. A. Cerdeira, S. Lundqvist, D. Mugnai, A. Ranfagni, V. Sa-yakanit, L. S. Schulman, p. 352 (World Scientific, Singapore, 1993).

[72] R. Landauer, T. Martin, *Rev. Mod. Phys.* **66**, 217 (1994).

[73] A. Messiah, *Mécanique Quantique, Tome 1* (Dunod, Paris 1969).

[74] E. N. Economou, C. M. Soukoulis, *Phys. Rev. Lett.* **46**, 618 (1981).

[75] R. Landauer, *IBM Journ. Res. Dev.* **1**, 223 (1957).

[76] R. Landauer, *Phil. Mag.* **21**, 863 (1970).

[77] M. Büttiker, *Phys. Rev. Lett.* **57**, 1761 (1986).

[78] D. Weinmann, unpublished (1992).

[79] H. Grabert, *Z. Phys.* **B 85**, 319 (1991).

[80] T. Brandes, *Ph. D. Thesis*, Universität Hamburg (1994).

[81] M. Büttiker, A. Prêtre, H. Thomas, *Phys. Rev. Lett.* **70**, 4114 (1993).

[82] L. J. Geerligs, C. A. van der Jeugd, J. Romijn, J. E. Mooij, *Europhys. Lett.* **10**, 79 (1989).

[83] T. Brandes, D. Weinmann and B. Kramer, *Europhys. Lett.* **22**, 51 (1993).

[84] T. Brandes, W. Häusler, K. Jauregui, B. Kramer, D. Weinmann, *Physica* **B 189**, 16 (1993).

[85] E. N. Economou, *Green's Functions in Quantum Physics*, Springer, Berlin (1990).

[86] N. W. Ashcroft, N. D. Mermin, *Solid State Physics* (Saunders College, Philadelphia PA, HRW int. edition 1976).

[87] V. Špička, J. Mašek and B. Velický, *J. Phys.(Cond. Matter)* **2** 1569.

[88] J. Mašek and B. Kramer, *Solid State Comm.* **68** 611 (1988).

[89] C. Jacoboni, P. J. Price, *Solid State Comm.* **75**, 193 (1990).

[90] J. Iñarrea, G. Platero, C. Tejedor, *Semicond. Sci. Technol.* **9**, 515 (1994).

[91] L. Lévy, G. Dolan, J. Dunsmuir, H. Bouchiat, *Phys. Rev. Lett.* **64**, 2074 (1990).

[92] M. Büttiker, Y. Imry, R. Landauer, *Phys. Lett.* **96A**, 365 (1983).

[93] Y. Imry, in Ref. [1], p. 221.

[94] V. Ambegaokar, U. Eckern, *Phys. Rev. Lett.* **65**, 381 (1990).

[95] V. Ambegaokar, U. Eckern, *Phys. Rev. Lett.* **67**, 3192 (1991).

[96] U. Eckern, A. Schmid, *Europhys. Lett.* **18**, 457 (1992).

[97] A. Müller-Groeling, H. A. Weidenmüller, C. H. Lewenkopf, *Europhys. Lett.* **22**, 193 (1993).

[98] D. Loss, *Phys. Rev. Lett.* **69**, 343 (1992).

[99] G. Kirczenow, talk at the *ICTP–NATO Workshop on Submicron Quantum Dynamics*, Trieste (June 1994).

[100] D. Mailly, private communication (1994).

[101] K. Jauregui, D. Weinmann, W. Häusler, work in progress (1994).

[102] A. Aldea, *Z. Phys.* **244**, 206 (1971).

[103] Ch. Sikorski, U. Merkt, *Phys. Rev. Lett.* **62**, 2164 (1989).

[104] B. Meurer, D. Heitmann, K. Ploog, *Phys. Rev. Lett.* **68**, 1371 (1992).

[105] D. Heitmann, J. P. Kotthaus, *Physics Today* p. 56 (June 1993).

[106] W. Kohn, *Phys. Rev.* **123**, 1242 (1961).

[107] R. C. Ashoori, H. L. Stormer, J. S. Weiner, L. N. Pfeiffer, S. J. Pearton, K. W. Baldwin, K. W. West, *Phys. Rev. Lett.* **68**, 3088 (1992).

[108] U. Meirav, M. A. Kastner, S. J. Wind, *Phys. Rev. Lett.* **65**, 771 (1990).

[109] J. J. Palacios, L. Martin–Moreno, C. Tejedor, *Europhys. Lett.* **23**, 495 (1993).

[110] L. P. Kouwenhoven, N. C. van der Vaart, A. T. Johnson, W. Kool, C. J. P. M. Harmans, J. G. Williamson, A. A. M. Staring, C. T. Foxon, *Z. Phys.* **B 85**, 367 (1991).

[111] W. Pfaff, D. Weinmann, W. Häusler, B. Kramer, U. Weiss, submitted to *Z. Phys.* **B** (1994).

[112] D. Weinmann, W. Häusler, B. Kramer, preprint (1994).

[113] W. Häusler, K. Jauregui, D. Weinmann, T. Brandes, B. Kramer, *Physica* **B 194-196**, 1325 (1994).

[114] J. M. Kinaret, Y. Meir, N. S. Wingreen, P. A. Lee, X.-G. Wen, *Phys. Rev.* **B 46**, 4681 (1992).

[115] D. V. Averin, G. Schön in Ref. [1], p 531.

[116] C. W. J. Beenakker, *Phys. Rev.* **B 44**, 1646 (1991).

[117] D. V. Averin, A. N. Korotkov, *Journ. of Low Temp. Phys.* **80**, 173 (1990).

[118] D. V. Averin, A. N. Korotkov, K. K. Likharev, *Phys. Rev.* **B 44**, 6199 (1991).

[119] W. Häusler, B. Kramer, J. Mašek, *Z. Phys.* **B 85**, 435 (1991).

[120] W. Häusler, B. Kramer, *Phys. Rev.* **B 47**, 16353 (1993).

[121] W. Häusler, preprint (1994).

[122] D. V. Averin, A. A. Odintsov, *Phys. Lett.* **A 140**, 251 (1989).

[123] D. V. Averin, Yu. V. Nazarov in *Single Charge Tunneling*, ed. by H. Grabert, M. H. Devoret (Plenum, New York, 1991).

[124] U. Weiss, *Quantum Dissipative Systems* (World Scientific, Singapoore, 1993).

[125] C. Bruder, H. Schoeller, *Phys. Rev. Lett.* **72**, 1076 (1994).

[126] P. W. Anderson, *Phys. Rev.* **124**, 41 (1961).

[127] Y. Meir, N. S. Wingreen, P. A. Lee, *Phys. Rev. Lett.* **70**, 2601 (1993).

[128] D. Weinmann, W. Häusler, unpublished (1993).

[129] D. Weinmann, unpublished (1993).

[130] V. I. Fal'ko, *Europhys. Lett.* **8**, 785 (1989).

[131] U. Merkt, J. Huser, M. Wagner,*Phys. Rev.* **B 43**, 7320 (1991).

[132] D. Pfannkuche, R. R. Gerhards, *Phys. Rev.* **B 44**, 13132 (1991).

[133] V. Halonen, T. Chakraborty, P. Pietiläinen, *Phys. Rev.* **B 45**, 5980 (1992).

[134] P. A. Maksym, T. Chakraborty, *Phys. Rev. Lett.* **65**, 108 (1990).

[135] K. Jauregui, W. Häusler, B. Kramer, *Europhys. Lett.* **24**, 581 (1993).

[136] W. Häusler, private communication (1993).

[137] D. V. Averin, Y. V. Nazarov, *Phys. Rev.* **B 47**, 9944 (1993).

[138] K. Jauregui, W. Häusler, unpublished (1994).

[139] G. W. Bryant, *Phys. Rev. Lett.* **59**, 1140 (1987).

[140] N. C. van der Vaart, M. P. de Ruyter van Steveninck, L. P. Kouwenhoven, A. T. Johnson, Y. V. Nazarov, C. J. P. M. Harmans, C. T. Foxon, *Phys. Rev. Lett.* **73**, 320 (1994).

[141] F. Stern, *Phys. Rev. Lett.* **21**, 1687 (1968).

[142] A. Messiah, *Mécanique Quantique, Tome 2* (Dunod, Paris 1964).

[143] G. Hendorfer, preprint (1994).

[144] D. Pfannkuche, private communication (1994).

[145] E. Lieb, D. Mattis, *Phys. Rev.* **125**, 164 (1962).

[146] F. Bolton, *Phys. Rev. Lett.* **73**, 158 (1994).

[147] D. Pfannkuche, V. Gudmundsson, P. A. Maksym, *Phys. Rev.* **B 47**, 2244 (1993).

[148] D. A. Wharam, private communication (1994).

Curriculum vitae

Name:	Dietmar Weinmann	
Born:	January 13, 1965	
Birth place:	Stuttgart–Degerloch, F. R. Germany	
Parents:	Paul and Klara Weinmann	
School:	1971 – 1975	Zeppelin–Grundschule in Echterdingen
	1975 – 1984	PMH–Gymnasium in Echterdingen
	June 1984	Abitur
Military:	1984 – 1985	in Weingarten
University:	1985 – 1991	Physics studies at the University of Stuttgart
	1990 – 1991	Diploma thesis at the II. Institut für Theoretische Physik under the guidance of Prof. Uli Weiss. Title: On the relationship of the dissipative two–level problem with the Kondo–problem
	June 13, 1991	Diploma
Doctorate:	1991 – 1994	Preparation of this thesis under the guidance of Prof. Uli Weiss (Stuttgart) and Prof. Bernhard Kramer (Braunschweig/Hamburg)
	Since Oct. 1991	Employee at the II. Institut für Theortische Physik, Universität Stuttgart
	1991 – 1993	Stay at the Physikalisch–Technische Bundesanstalt, Braunschweig
	1993 – 1994	Stay at the I. Institut für Theoretische Physik, Universität Hamburg